Study to Characterise the Performance of Micro Tubular Solid Oxide Fuel Cells by the Invention of an Avant Garde Experimental Apparatus and Computational Modelling.

• Candidate: Vincent Lawlor Dip Eng. B. Eng (hons)

•.

• Dr. A.G. Olabi School of Mechanical & Manufacturing Engineering, Dublin City University, Ireland

• Submitted: September 2010

Declaration Page

I hereby certify that this material, which I now submit for assessment on the programme of study leading to the award of Ph.D. is entirely my own work, that I have exercised reasonable care to ensure that the work is original, and does not to the best of my knowledge breach any law of copyright, and has not been taken from the work of others save and to the extent that such work has been cited and acknowledged within the text of my work.

Signed: _____ (Candidate) ID No.: _____ Date: _____

Abstract

The content of this PhD thesis deals with the development of Micro Tubular Solid Oxide Fuel Cells (MT-SOFCs) and provides a body of information for any future MT-SOFC stack or testing apparatus design. This information has been achieved through a combination of experimental work, CFD modelling and numerical analysis. CFD models with an additional fuel cell module have been compared to experimental results for single cells with relation to oxygen concentration, fuel utilisation, I/V curves and external cell temperature profiles. All of the above multi physical phenomena match very well to the experimental results.

A key finding of the thesis is the importance of including radiation equations in the CFD models. Neglecting radiation can result in temperature errors of up to 200°C for a single cell in cross flow inside a high temperature wind tunnel. . This is interesting information as most modelling work in the field to date has neglected radiation effects. 3D models that include the experimental apparatus and radiation equations have been completed. These models show how the experimental apparatus or stack design may cause large temperature losses if not properly designed. Furthermore the radial temperature gradient across the cell has been experimentally measured using an impedance spectroscopy technique. A thermographic photography technique has been developed to measure the temperature profile on the cathode wall of a MT-SOFC in cross flow within a high temperature wind tunnel.

Other simplified 3D CFD models have been compared to numerical calculations to predict the conditions when buoyant flows may occur in bundles of MT-SOFCs in cross flow. The results show that a stack oxidant flow rate, even greater than a few mm per second, can dramatically inhibit the effect of buoyant flows to the point where they will not occur. This is important information that should be useful when designing MT-SOFC stack flow channels.

The measurement of the concentration around the perimeter of a MT-SOFC in cross-flow has also been attempted. While it has not been shown conclusively that a method developed in this thesis surely works, it has been shown that there is massive potential for it to work.

Acknowledgements

The past three years from the beginning of the application to begin this study until now, as I put the final piece to this Ph.D. thesis, has been nothing short of a most extraordinary and worthwhile experience. As much as I admit that lots of hard work and persistence has gone into the production of this thesis, there have been several people without whom no amount of perseverance on my behalf would have made this thesis possible.

During a particularly difficult time in the course of this thesis funding was cut and it really seemed as if this thesis could grind to a halt. Prior to this event, but even more remarkably after, Dr. Gerhard Buchinger made 100% sure, even while he was trying to finish his own Ph. D. thesis and find new work opportunities for himself, that I had the best opportunity to finish my studies though a grant application and other internal options that he made possible. He now also has the responsibility of this project and also working in combination with his own work. I offer him my deepest gratitude for taking all the extra work involved in the running of the project.

I cannot find better words than to describe his input into my life and studies better than that of an older brother who has always made himself the available and cared more than the normal course of duty. He has also been a pillar stone of this thesis and I thank him unreservedly for the time he has given for discussion during the course of this thesis and most of all for being such a good friend.

I would like to thank one of the researchers that I admire most not only for his renowned research skills but also for his kind friendship, support and the enthusiasm that he has shown in me and my work. Prof. Dr Dieter Meissner allowed me the opportunity three years ago to begin my post graduate studies through research and has been a key role model in my development as a researcher. Dieter pushed me to make my first oral presentation in Rome when I really felt that I was not ready and also convinced me at the time when I was less than convinced that I was up to the standard to make such research. These events and many others concerning him have pushed me to achieve things that I never even imagined.

I would also like to thank DI Stefan Griesser for his friendship and input into this thesis especially during the period when the review paper was written. He has taken plenty of time to do administration tasks during the course of this project and has been a valuable source of ideas to test concepts and a good friend.

Prof Dr. Christoph Hochenaur has also been very important contributor to both my professionalism with regard to numerical and CFD simulation and validation and has also been a key

driving force in the publicity of my work. He has also been a good friend and has boosted several applications with his name. I would also like to thank Dr. Gerald Zauner for his keen interest in experiments in the thermal camera images and his help thought this section of this work.

I would also like to thank Dr. Abdul G. Olabi my supervisor for taking me on as a student and for the arrangements that he made such that I would have some funding to keep me working in Austria after the time that my funding was cut. Without this funding, to tie me over at the time, I probably would have had to leave Austria before I could figure out how to keep my research going. I also thank him ever so much for arrangements that he has made during the course of my thesis which have made it possible and have been critical for me. I would also like to thank James Carton for helping with proof reading and the co-operations during the past years.

During the past three years living in Austria I have met some extraordinary people all of whom I thank very much for their friendships and often extraordinarily kind deeds towards me. Daniel Neyer and Jacqueline Keckeis have been extraordinary friends who have certainly made living in Austria and away from home much easier through their extremely kind friendship and for always bearing me in mind when different events took place both research wise and socially. I would also like to thank Tomas Stadlier for his kind friendship and introduction to downhill bike riding which I hope to take up again as a hobby after this thesis.

Moving all the way from Ireland to Austria to live was a challenge up until I met my girlfriend Bianca Angerer two years ago. Without her understanding and easy-going nature and of course love, living in Austria alone would have been extremely difficult. I greatly appreciate our friendship and the understandings she has shown and multitude of things she has done for me. I would also like to thank the support of our parents Harold and Annie.

I would also like to thank other co-authors that have been listed on papers for their kind help and support.

I have to leave the small amount of words for those who deserve just as much as those preceding, I would like to thank my family Yvonne, James, Kevin and Aideen for their massive unrelenting support during the past three years, which I can only describe as outstanding and I look forward to spending more time with you now that this thesis is completed!

The majority of the project work done within the framework of this thesis has been funded by the Austrian Science fund (FWF) under the project title HIT-SIM (project number L611-N14) and I offer sincere thanks for their financial support.

The upper Austria University of Applied Sciences campus Wels has provided many of the working materials, labs and many other resources during the course of this thesis and this is gratefully acknowledged.

Papers publications and awards during the time of this work.

Journal papers:

V. Lawlor, S. Griesser, G. Buchinger, A. Olabi, S. Cordiner, D. Meissner - Review of the micro-tubular solid oxide fuel cell (part I: Stack design issues and research activities) - Journal of Power Sources, Vol. 153, No. 2, 2009, pp. 387-399

V. Lawlor, G. Zauner, C. Hochenauer, A. Mariani, S. Griesser, J. Carton, K. Klein, S. Kuehn, D. Meissner, A. Olabi, S. Cordiner, G. Buchinger. -The Use of a High Temperature Wind Tunnel for MT-SOFC Testing- Part I: Detailed Experimental Temperature Measurement of an MT-SOFC Using an Avant-garde High Temperature Wind Tunnel and Various Measurement Techniques. ASME Journal of fuel cell science and technology, (Accepted to be published in next issue)

V. Lawlor, C. Hochenauer, A. Mariani, G. Zauner, S. Griesser, J. Carton, A. Olabi, K. Klein, S. Kuehn, S. Cordiner, D. Meissner, G. Buchinger – A Micro Tubular SOFC and stack testing apparatus: - Energy (Under Review)

Proceedings - Including Talks & Posters:

(Presentation) V. Lawlor, G. Zauner, A. Mariani, C. Hochenauer, J. Carton, S. Griesser, K. Klein, S. Kuehn, D. Meissner, A. Olabi, S. Cordiner, G. Buchinger - Micro-tubular SOFC: Towards a power pack for automotive and auxiliary power supply use - Elevent Grove Fuel Cell Symposiun, London, UK, 2009, pp. 46

(Presentation) V. Lawlor, G. Zauner, A. Mariani, C. Hochenauer, S. Griesser, J. Carton, S. Kuehn, K. Klein, D. Meissner, A. Olabi, S. Cordiner, G. Buchinger – A study to invistage methods to measure the temperature of a MT-SOFC in a high temperature wind tunnel.. - Third European Fuel Cell Technology and Applications Conference - Piero Lunghi Conference, Rome Italy, Italy, 2009, pp.(proceeding published after conference in Dec)

(Presentation) V. Lawlor, A. Mariani, C. Hochenauer, G. Zauner, S. Griesser, D. Meissner, A. Olabi, S. Cordiner, G. Buchinger – A micro tubular SOFC and stack testing apparatus to provide a means of developing highly efficient pertable and axuilary power packs for the future. - Proceedings of SEEP 2009, Dublin, Ireland, 2009, pp. 2-7

(Presentation) V. Lawlor, G. Buchinger, C. Hochenauer, P. Dawson, T. Raab, S. Griesser, A. Olabi, B. Corcoran, D. Meissner - Design of a Micro-Tubular SOFC Rector with CFD and Validations - Proceedings of the 2nd European Fuel Cell Technology and Applications Conference, Rom, Italy, 2007,

(Poster) V. Lawlor, D. Meissner, C. Hochenauer, S. Griesser, S. Cordiner, A. Mariani, G. Zauner, A. Olabi, G. Buchinger - Micro-tubular SOFCs to Measure the Effects of Cross Flow on Mass Transfer Rates Around the Perimeter of a Cylindrical Electrode - ECS Transactions, Vol. 25, No. 2, 2009, pp. 1283-1293

(Presentation) V. Lawlor, C. Hochenauer, G. Zauner, S. Griesser, A. Olabi, D. Meissner, G. Buchinger - Towards an optamised Micro-tubular SOFC reactor core design. - Proceedings of the 3rd Symposium of Austrian Universities of Applied Sciences, Fachhochschule Kärnten, Villach, Austria, 2009, pp. 288-293

(Presentation) V. Lawlor, C. Hochenauer, G. Buchinger, S. Griesser, A. Olabi, D. Meissner - Numerical Simulation and Experimental Validation to Design an Optimised Micro-Tubular Solid Oxide Fuel Cell Reactor. Tagungsband 2. Forschungsforum der Österreichischen Fachhochschulen, Wels, Austria, 2008, pp. 327- 334

(Poster/Presentation) V. Lawlor, C. Hochenauer, G. Buchinger, S. Griesser, A. Olabi, D. Meissner - Towards a micro-tubular SOFC reactor with C.F.D, validation, experiments and a high temperature wind tunnel. - Proceedings of the 11th annual Sir Bernard Crossland Symposium, Limerick, Ireland, 2008, pp. 157

(Poster) V. Lawlor, G. Buchinger, C. Hochenauer, S. Griesser, A. Olabi, D. Meissner - Development Of A High Temperature Wind Tunnel And Numerical Simulations To Optimise The Layout Of A SOFC Micro-Tube Reactor - Proceedings of AGMET 2008: energy and the Irish climate; harnessing the Irish climate for energy, Dublin, Ireland, 2008, pp. 24

As a co-author:

C. Hochenauer, V. Lawlor, E. Spiegl, B. Linimayr - Investigation of the suitability of unused tanks as heat storage accumulators- Proceedings of SEEP 2009, pp 92-97 Dublin, Ireland, 2009

G. Buchinger, T. Raab, S. Griesser, V. Lawlor, S. Potzmann, S. Kuehn, K. Klein, W. Sitte, D. Meissner - Improving the Power Densities and Lifetime of Micro-Tubular SOFCs - Proceedings ot the 2nd European Fuel Cell Technology and Applications Conference, Rom, Italy, 2007, pp. 78

G. Buchinger, J. Kraut, T. Raab, S. Griesser, V. Lawlor, J. Haiber, R. Hiesgen, W. Sitte, D. Meissner - Operating micro-tubular SOFCs containing nickel based anodes with blends of methane and hydrogen - Proceedings: 2007 International Conference on Clean Electrical Power, Capri, Italy, 2007, pp. 450-455

G. Buchinger, P. Hinterreiter, T. Raab, S. Griesser, V. Lawlor, K. Klein, S. Kuehn, W. Sitte, D. Meissner - Stability of micro tubular SOFCs operated with synthetic wood gases and wood gas components - Proceedings: 2007 International Conference on Clean Electrical Power, Capri, Italy, 2007, pp. 444-449

G. Buchinger, S. Potzmann, T. Raab, S. Griesser, V. Lawlor, S. Kuehn, K. Klein, D. Meissner - Entwicklung von mikrotubulären SOFCs - Tagungsband des ersten Forschungsforum der österreichischen Fachhochschulen, Fachhochschule Salzburg, Campus Urstein, Austria, 2007, pp. 50

Awards and achievements.

March 2009

Awarded with Prof. Gerhard Buchinger the “HIT-SIM Project” funded by the FWF.

http://www.fwf.ac.at/asp/projekt_res.asp?L=D&WD_CODE=1307&Typ=W&Text=Chemie%20/%20Elektrochemie&StartRecord=21

September 2009

At the SEEP 2009 Conference: Awarded “Prize for best Presentation”.

http://www.dcu.ie/conferences/seep/prize.shtml

July – September

Review paper submitted to the journal of power sources is number 6 most downloaded document for the Journal of Power Sources during July to September 2009. (Impact factor 3.477)

http://top25.sciencedirect.com/subject/energy/11/journal/journal-of-power-sources/03787753/archive/23/

January 2010

Awarded 2nd place out of 45 in the “Young Researchers Prize” at the Upper Austria University of Applied Sciences

http://www.fh-ooe.at/campus-wels/aktuelles/fh-ooe-news-wels/fh-ooe-news-wels/article/forschungsassistenten-des-jahres/

You don't write because you want to say something; you write because you've got something to say.

~F. Scott Fitzgerald:

Perseverance is the hard work you do after you get tired of doing the hard work you already did.

~Newt Gingrich.

With ordinary talent and extraordinary perseverance, all things are attainable.

~Thomas Foxwell Buxton

Edison failed 10, 000 times before he made the electric light. Do not be discouraged if you fail a few times.

~Napoleon Hill,

Contents

Declaration Page ii

Abstract iii

Acknowledgements iv

Papers publications and awards during the time of this work. vii

Contents xi

Table of figures xv

Table of tables. xxii

Nomenclature table xxiii

Chapter 1 Introduction to fuel cells and the Solid Oxide Fuel Cell ..... - 1 -

1.1 Introduction to fuel cells ..... - 1 -

1.2 The Solid Oxide Fuel Cell and principles of operation ..... - 3 -

1.3 Materials ..... - 6 -

Chapter 2 Literature Review ..... - 9 -

2.1 Part I: The micro-tubular SOFC stack and possible applications ..... - 9 -

2.2 Part II: Review of flow around a cylinder for Reynolds numbers between 0 and 40 - 40 -

2.3 Part III: Mass transfer to a cylinder in cross flow ..... - 56 -

2.4 Part IV Temperature measurement and MT-SOFCs ..... - 58 -

2.5 Conclusions and indication of gaps in the literature ..... - 63 -

2.6 Summary of the goals ..... - 64 -

Chapter 3 An Introduction to CFD and SOFC theory with the fuel cell module.. - 66 -

3.1 What is CFD? ..... - 66 -

3.2 Introduction to the fundamentals of computational fluid dynamics ..... - 68 -

3.3 Fuel cell theory and the fluent fuel cell module ..... - 84 -

Chapter 4 The development stages of the experimental apparatus ..... - 101 -

4.1 Introduction to the development of the experimental apparatus .....- 101 -

4.2 Second developmental stage of the high temperature wind tunnel .....- 102 -

4.3 Solution for the chamber heating.....- 104 -

4.4 Third developmental stage of the high temperature wind tunnel .....- 114 -

4.5 In-House Building of MT-SOFCs .....- 118 -

Chapter 5 Experimental and analytical procedures..... - 121 -

5.1 Introduction to CFD simulation and analytical calculation to estimate the effect of natural convection is a MT-SOFC reactor.....- 121 -

5.2 Method for temperature measurement of a MT-SOFC .....- 128 -

5.3 Modelling of a single MT-SOFC in cross-flow.....- 132 -

5.4 Using MT-SOFCs to measure the rate of mass transfer to a cylindrical electrode in cross-flow .....- 140 -

5.5 Detailed modelling of the concentration of oxygen around the perimeter of a MT-SOFC in cross flow and the fast solving model .....- 151 -

5.6 Measuring oxygen concentrations at higher Reynolds numbers .....- 153 -

Chapter 6 Experimental and analytical results..... - 156 -

6.1 Results of CFD simulation and analytical calculation to estimate the effect of natural convection in a MT-SOFC reactor .....- 156 -

6.2 Results of the method for temperature measurement of a MT-SOFC.....- 165 -

6.3 Results from the modelling of a single MT-SOFC in cross-flow.....- 171 -

6.4 Results of using MT-SOFCs to measure the rate of mass transfer to a cylinder electrode cross-flow .....- 191 -

6.5 Results of detailed modelling of the concentration of oxygen around the perimeter of a MT-SOFC in cross flow and the fast solving model. .....- 199 -

6.6 Results of the development of the system incorporating MT-SOFC's to measure a concentration of oxygen around a larger high temperature electrode in cross-flow. .....- 205 -

Chapter 7 Discussion..... - 210 -

7.1 Summary and discussion on CFD simulation and analytical calculation to estimate the effect of natural convection is a MT-SOFC reactor .....- 210 -

7.2 Summary and discussion on methods of temperature measurement in MT-SOFCs - 213 -

7.3 Summary and discussion of detailed models of a single MT-SOFC.....- 217 -

7.4 Summary of discussion of results of measuring the concentration of oxygen around the perimeter of a MT-SOFC in cross flow.....- 222 -

7.5 Summary and discussion of the 4 mm cathode and suggestion for a new modelling strategy.....- 227 -

7.6 Summary and discussion of simulations for a larger bundle of cells to increase the cylinder diameter. .....- 228 -

Chapter 8 Thesis Conclusions. ..... - 230 -

8.1 Overall Conclusions with reference to the original goals in Section 2.6 .....- 230 -

8.2 Thesis Contribution. .....- 233 -

8.3 Recommendations for Further work.....- 234 -

References: ..... - 236 -

Appendix I

Appendix I Experimental techniques used to improve cell performance.....II

Appendix II Level of research in micro-tubular SOFCs and what is being researched in the field. V

Appendix III-(A) An Initial Study to Design a Device to Test Single MT-SOFCs and Stacks. X

Appendix III-(B) Heat transfer calculations for designing and proofing. XV

Heat transfer estimations. XV

Appendix III-(C) Numerical Results and Comparison to Experimental Data XXIV

Results Related to Pipe Wall Temperature & Outlet Temperature. XXIV

Appendix III-(D) Lab view code to control the experiments for initial design..... XXXI

Appendix III-(E) Code used to estimate the temperature of the first attempt system. .XXXIII

Appendix IV: Development of a single inlet singlet outlet manifolding system.XLVIII

Background.....XLVIII

Reason for and description of the idea. L

Appendix V Introduction to Methods of Temperature Control.....LXI

Appendix VI Control circuitry for the high temperature wind tunnel control.....LXXIV

Appendix VII Labview code for the final version of the high temperature wind tunnel. LXXV

Appendix VIII: Drawings for the final high temperature wind tunnel LXXVIII

Appendix IX Code for single cylinder and bundles in forced and free convection regimes. LXXIX

Appendix X Modelling parameters for the Full cathode simulations. XCI

Appendix XI Modelling parameters for the small cathode simulations. XCV

Table of figures

Figure 1: Operation of a SOFC showing the electrochemical reactions. ..... - 3 -
Figure 2: An exemplarily depiction of the electrochemical processes at a single three phase in the anode [1] . - 5 -
Figure 3: Depiction of the gas and heat flows in a triple layer catalyst-SOFC-catalyst system proposed by Tompsett et al. [20]..... - 12 -
Figure 4: Author's depiction of the current collectors and cell configuration by Sammes and Bove [23] ..... - 14 -
Figure 5: Author's illustration of the cube shaped SOFC cathode structure with embedded electrolyte-anode tubes by Funahashi et al. [24]. ..... - 15 -
Figure 6:Author's illustration of the gas supply system invented by Lee et al. [26]. ..... - 16 -
Figure 7: Author's illustration of the heat exchanger design by Alberta Research Council (CAN) inc.[29]. ..... - 18 -
Figure 8: Author's illustration based upon the description of [39] where the current produced by the fuel cell is very briefly interrupted using a current pulse generator and the initial change in cell voltage, due to losses is measured. ..... - 20 -
Figure 9: Author's illustration based upon the description of [39] on an example EIS result where the amplitude and phase of the signals may be plotted in Nyquist format for analysis and modeling. ..... - 21 -
Figure 10: An array of cells (left) and the damage caused (right) from a small flame in a reactor. ..... - 25 -
Figure 11: Author's depiction of a single module in a multi module system used by Suzuki et al .[71]. ..... - 33 -
Figure 12 Regions of flow around a cylinder in cross flow. ..... - 40 -
Figure 13: Visualization of the flow regime around a cylinder at Re >0.1 [75]..... - 44 -
Figure 14: Pressure distribution in creeping flow [73]..... - 46 -
Figure 15: Photograph of the cylinder in cross-flow take another Re of five [76]..... - 47 -
Figure 16:ymmetric eddies photographed under Re of 24 [84]..... - 49 -
Figure 17:For $12 < Re < 78$ plot of the flow stream around the cylinder for Res 12 to 78 [79]..... - 49 -
Figure 18: Development of the wake between a Re of 20 and 40 [85]. ..... - 50 -
Figure 19: A picture showing the onset of bubble asymmetry at a Re of 40 [84]..... - 51 -
Figure 20: Figure showing the asymmetry in the wake [85],..... - 52 -
Figure 21: Visualization of the development of the wake from $30<Re<60$ [85]..... - 54 -
Figure 22: Vortex shedding behind a cylinder in cross flow where R= Re [94]..... - 55 -
Figure 23: An illustration and commentary showing the different stages involved in the finite volume discretisation method [113]. ..... - 71 -
Figure 24: A 1-D example showing the concept of a gridded domain [114]. ..... - 72 -
Figure 25: A diagram showing a stationary cube containing a single particle in a fluid of mass flowing into the cube must equal the mass flowing out of the cube adapted from [87]..... - 74 -
Figure 26: Single cell used to describe an equation of motion, adapted from [113]. ..... - 77 -

Figure 27 (Top) shows the classic case of flow in a pipe where the boundary layer and flow profile develops over time. (Bottom left) shows that as a point is moved from the wall the viscous stress increase. (Bottom right) shows a cell where the nearest boundary is a wall [115]. - 79 -
Figure 28: Guide for the labelling of a cubic cell adapted from [113]. - 80 -
Figure 29: A plot comparing fuel cell and carnal efficiency as a function of temperature [117] - 85 -
Figure 30: A typical current voltage diagram for a fuel cell indicating the points on the IV curves that correspond to different losses [117]. - 86 -
Figure 31: The solving process and coupling between the Fluent and the SOFC module [118]. - 90 -
Figure 32: Photograph of the coil, 6 coils deep, that was built to enhance the heat transfer to the inlet air. - 103 -
Figure 33: Initial experiments using a coil that had a straight section on the end that was connected into the high temperature wind tunnel. - 103 -
Figure 34: A simple temperature curve over a period of time for a single and two bulbs in a box experiment. The insert shows the bulbs in the box. - 105 -
Figure 35: Concept A wind tunnel design where the cells are indicated by the blue tubes - 105 -
Figure 36: An original concept tested by CFD simulation that shows contours of temperature and velocity magnitude. - 106 -
Figure 37: Image outlining the concept was in the flow heat exchanger from the radiators to the gas via metal plates - 107 -
Figure 38: (A) A numerical simulation result of the heat exchanger (B) that was built - 107 -
Figure 39: Concept B that includes the heat exchanger as outlined in Figure 38 - 108 -
Figure 40: A bundle of MT-SOFC's that was build related to the concept B design. - 108 -
Figure 41: An external view of the concept B wind tunnel design that was built. . - 109 -
Figure 42: Hydrogen fuelling and anode side current collecting of the fuel cells in the concept B high temperature wind tunnel. - 111 -
Figure 43: Concept C looking through the top wall at a bundle of cells inside the wind tunnel. - 112 -
Figure 44: Cell loading case for concept (D). - 112 -
Figure 45: The building of concept C where the layout is shown in (A), Heating system in (B), infra red transparent plastic end cap (C) and outline of problems with the design (D).. - 113 -
Figure 46: A picture showing the layout of the experimental concept (B) - 114 -
Figure 47: The velocities required to increase the Reynolds number on a 1.5cm and 0.3cm tube - 116 -
Figure 48: A sample of an electrolyte support itself that was initially used at the beginning of the study. - 119 -
Figure 49: A picture showing from left to right, (D) a fully made MT-SOFC, (C) one with just the electrolyte after sintering, (B) when with electronic before sintering, and (A) the substrate of the anode prior to sintering. - 119 -
Figure 50: A picture showing the different stages in the process for making electrolyte supported MT-SOFCs. - 120 -
Figure 51: An image of a computer-controlled spraying machine that was initially used to spray the cathode onto the cells. - 120 -
Figure 52: 3D simple representation of an array of horizontal cylinders as in a MT-SOFC stack - 125 -
Figure 53: View of the meshed model though the symmetry walls. The blue mesh shows the inlet. - 126 -
Figure 54: A more detailed look at the meshing of the tubes in the array - 127 -

Figure 55: A more detailed look at the meshing around the cells that is coopered down through the 3D model. ... - 127 -
Figure 56: Schematic of the high temperature wind tunnel..... - 129 -
Figure 57: MT-SOFC and aluminium-oxide cover over a thermocouple for the test chamber temperature regulation (A). Positioning of the thermal camera for image acquisition (B)..... - 130 -
Figure 58: Positioning of the LGT and measurement using a thermocouple. ..... - 131 -
Figure 59: An image showing the basic outline of the meshing and current connection method used in the very first models. ..... - 133 -
Figure 60: Outline of the mesh conditions for the model with a reduced number of cells..... - 135 -
Figure 61: Outline of the mesh used for the faster solving model. Note that the face seen nearest has a symmetry boundary condition applied.. ..... - 136 -
Figure 62: A view of the upper face mesh on the cell that is coopered down through the cell. An important point to note is the relatively few cells used to mesh between the anode and cathode layers..... - 137 -
Figure 63: Experimentally determined values of the electrolyte resistance as a function of the total cell current. Note this current value refers to the total cell current but a half cell was modelled in the model see Figure 60. ..... - 139 -
Figure 65: Illustration showing the proposed architecture of the cathode on a MT-SOFC to measure the concentration of oxygen around the cell's perimeter. ..... - 143 -
Figure 66: An image showing the segmented cathode applied to an MT-SOFC ..... - 145 -
Figure 67: An image showing the duel cathode layer with the electrical connection to one of the cathode strips. . - 145 -
Figure 68: Picture of an anode supported cell and the small testing cathode isolated from the normal cathode which wraps around the back of the cell..... - 147 -
Figure 69: Picture of an anode supported cell with the segmented cathode system complete with electrical connections. ..... - 147 -
Figure 70: Full view of the manifolding to the cell complete with anode reference, anode working (out each end of the silicon inlet tubes and sealed with silicone)and cathode working and cathode reference for each of the cathode strips. ..... - 147 -
Figure 72: The cell is rotated inside the wind tunnel by holding the red silicon sealer in the top of the cell and turning it by hand. The anode working connection is used as a reference as to the collation of the testing strip. ..... - 149 -
Figure 73 A pictorial plot showing the outline of the model and sample results. ..... - 152 -
Figure 74: Image of a cylindrical arranged bundle of MT-SOFCs to detect the concentration difference around the perimeter of a cylinder..... - 153 -
Figure 75 (A) Sample oxygen concentration contour plot qualitatively indicating the mass fraction of oxygen where red indicates high and blue indicates low concentrations. (B) The meshing scheme employed around the bundle of cells. ..... - 155 -
Figure 76: Nusslet number plots for free, forced and combined convection on a single cylinder. ..... - 156 -
Figure 77: A plot of CFD and analytical results for the output temperature for a bundle of cylinders 3 rows deep versus inlet air velocity m/s. ..... - 158 -

Figure 78: For the 1.5mm case (A) contours of z direction velocity on a plane situated in the middle of the bundle and flow path. (B) Contours of temperature on a plane located in the middle of the bundle and flow path. ..... - 158 -
Figure 79: For the 1.5mm/s case (A) velocity contours on a plane situated in the middle of the bundle of cells. (B) Velocity contours situated on a plane located between the first two cells in the bundle ..... - 159 -
Figure 80 For a single cylinder vertical cylinder Gr/Re^2. The 3 red dots are the velocities mentioned in this section ..... - 160 -
Figure 81: For the 1.5mm case (A) contours of z direction velocity on a plane situated in the middle of the bundle and flow path. (B) Contours of temperature on a plane located in the middle of the bundle and flow path. ..... - 161 -
Figure 82: For the 3mm/s case (A) velocity contours on a plane situated on the middle of the bundle of cells. (B) Velocity contours situated on a plane located between the first two cells in the bundle ..... - 161 -
Figure 83: For the 1.5mm case (A) contours of z direction velocity on a plane situated in the middle of the bundle and flow path. (B) Contours of temperature on a plane located in the middle of the bundle and flow path. ..... - 162 -
Figure 84: For the 10mm/s case (A) velocity contours on a plane situated on the middle of the bundle of cells. (B) Velocity contours situated on a plane located between the first two cells in the bundle. ..... - 163 -
Figure 85: Looking between two cells the contours of Z velocity are displayed. (A) velocity is 1.5 mm/s and (B) is 10 mm/s. ..... - 164 -
Figure 86: MT-SOFC under OCV conditions (A) and when producing 1.5 A/cm^2 (B) with colour scale showing the temperatures in °C in the middle. ..... - 165 -
Figure 87: Temperature gradient around the perimeter of the cell caused by the wind tunnel slit ..... - 166 -
Figure 88: The effect of emissivity on the thermal camera measurements. Top 3 lines points on the cathode, middle 4 points on the silver. Bottom line shows the fluctuation in chamber temperature due to the PID heating control. ..... - 168 -
Figure 89: Sample impedance measurement made where the ohmic resistance is measured where the nyquest plot hits the x axis. ..... - 169 -
Figure 90: Comparison of the temperature calculated by the EIS method and wall temperature measured by a thermocouple. ..... - 169 -
Figure 91: The methods are compared on the open cathode zone above the middle silver for a range of current densities produced by the cell. ..... - 170 -
Figure 92: the boundary conditions applied to a 2-D model to investigate the effects of the wind tunnel profile on the temperature gradient around the cell ..... - 172 -
Figure 93: The temperature gradient when radiation model is not applied showing a broad temperature profile. .. - 173 -
Figure 94: A case where a 2 w/cm² heat flux is applied to the cathode wall of the cell. As can be seen the temperature increases 200° above that which we would expect. ..... - 173 -
Figure 95: A simulation result for when a zero flux is applied to the outer wall of the fuel cell and there can be seen that the temperature profiles do not match the results of Figure 86 ..... - 174 -
Figure 96: A flux of 1.1 W/cm² was placed on the inside of the cell because the cell temperature would be too low without it ..... - 175 -

Figure 97: Temperature profile when a flux of 2e8 w/m³ on the electrolyte The simulation results match those of the experimental results. - 176 -
Figure 98: Only the fluid zone was included in the DO fluent model with the wall emissivity and temperatures set as shown.. Note that these values were obtained from experimental measurements using the thermo-graphic camera. - 177 -
Figure 100: I/V and power curve comparison for the cell and the model at a flow rate of 25ml/min. - 179 -
Figure 101: A sample comparison of the voltage and current plots on the outside cathode wall of the MT-SOFC in the wind tunnel. - 180 -
Figure 102: An illustration that shows the temperature profile (Kelvin) in three perpendicular sections along the length of a cell under test. Also the cell wall temperature and gas temperature is shown. - 181 -
Figure 103: An illustration showing the temperature profiles (Kelvin) in the same order as above but without temperature profile on the cathode wall so that the radial temperature across the cell can be seen. - 182 -
Figure 104: The temperature profile (Kelvin) on the outside wall of the cell. (A) depicts a view looking at the rear of the cell and (B) looking at the front. - 183 -
Figure 105: A comparison between a thermographic camera result (A) and a simulated result (B). Note that the temperature scale (Kelvin) applies to both. - 183 -
Figure 106: An illustration that shows the temperature profile (Kelvin) in three perpendicular sections along the length of a cell under test also the wall temperature and indirect gas temperature. - 184 -
Figure 107: An illustration showing the temperature profiles (Kelvin) in the same order as above bust without temperature profile on the cathode wall so that the radial temperature across the cell can be seen. - 185 -
Figure 108: The temperature profile (Kelvin) on the outside wall of the cell. (A) depicts a view looking at the rear of the cell and (B) looking at the front. - 186 -
Figure 109: A comparison between a thermographic camera result (A) and a simulated result (B). Note that the temperature scale applies to both (Kelvin). - 186 -
Figure 110: The thermal heat flux produced by the cell depicted by two colour scale and the resulting temperature profile in the oxidant gas shown in the rainbow scale. The lines seen on the outside wall of the cell refer to the temperature profiles (Kelvin). - 187 -
Figure 111: The current production of the cell into rainbow scale in the mass fraction of oxygen in the two colour scale - 189 -
Figure 112: The mass concentration of oxygen in the fluid flow and molar faction of hydrogen at the electrolyte anode interface. - 189 -
Figure 113: A three-dimensional plot of the mass fraction of oxygen in the gas flow looking at the front of the cell and the current density on the electrolyte cathode interface - 190 -
Figure 114: A three-dimensional plot of the mass fraction of oxygen in the gas flow looking at the back of the cell and the current density on the electrolyte cathode - 191 -
Figure 115: I/V curves showing how as more current is taken from a strip on the cathode the open circuit voltage of the other strip reduces and a initial simulation result for the concentration of oxygen around the cell. - 192 -
Figure 116: Plot showing the effect of the partial pressure of water in the flow on the Nernst potential. - 193 -
Figure 117: I/V plot if the cathode testing and normal strips the first time that the cell was tested. Notice that the testing strip produces higher current densities than the larger normal strip. - 194 -

Figure 118: Measuring the effect of temperature variations within the wind tunnel with 0.9 P(H_20). ..... - 197 -
Figure 119: Comparison of a tested cell in the high temperature wind tunnel and the Fluent model. ..... - 200 -
Figure 120: Plot comparing a simulated and tested cell with 56% mass water in the fuel..... - 201 -
Figure 121: A plot showing a comparison of the tested cell in the wind tunnel under 50ml/min + 56% mass water and 16cm/sec oxygen/nitrogen mix. ..... - 202 -
Figure 122: A simulation result showing the oxygen concentration on the flow plane and current density on the cell wall looking at the front of the cell. ..... - 203 -
Figure 123: A simulation result showing the oxygen concentration on the flow plane and current density on the cell wall looking at the rear of the cell..... - 203 -
Figure 124: Variation of specie concentration in the wake of a cylinder in cross flow at a mass sink rate of 0.44032 kg/m^3s. ..... - 205 -
Figure 125: Contours of Y direction velocity (right to left being –Y) with an overlay of streamlines. ..... - 206 -
Figure 126: A plot of mass concentration of oxygen in nitrogen vs. Re. ..... - 207 -
Figure 127: Velocity measurement along a line from the rear of the cylinder. ..... - 208 -
Figure 128 A view closer to the rear of the cylinder velocity at the rear wall of the cylinder (+Y: direction against the bulk flow) legend the same as Figure 127. ..... - 209 -
Figure 130: A view from the simulations where the front of the cell can be seen showing current density. Please refer Figure 122 for o_2 values. ..... - 224 -
Figure 131: A view from the simulations where the rear of the cell can be seen showing current density. Please refer Figure 123 for o_2 values. ..... - 224 -
Figure 132: Buckle on the wind tunnel after the course of 7 months testing. ..... - 226 -
Figure 133: Average species mole fractions from the gas side to the triple phase boundary zone [1]..... II
Figure 134: Application of the XCT reconstructed geometry to predict the pore-scale species distribution of hydrogen in an SOFC anode using LBM (62). III
Figure 135: 18O- ion images on the surface around Au/YSZ and Pt/YSZ interfaces treated at different cathodic polarization T=773 K, p(O2)=7 kPa for 300 s: (a) Au/YSZ E=0 V, (b) Au/YSZ E=−0.3 V, (c) Pt/YSZ, E=−0.3 V. The depth of the images ranges from ca. 150 nm in YSZ region..... IV
Figure 136: Search results from [1] for articles with the terms c (AND/OR/NOT) a theme in their titles abstracts or subject fields..... VI
Figure 137: Break down of the search results in Figure 136 into the countries of origin of the major contributors. VII
Figure 138: Break down of the search results in [1] using an advances search more specific to MT-SOFCs. ... VIII
Figure 139: Break down of the search results from Figure 138 into percentage publications per nation since 2002. IX
Figure 140 Picture of a gas flow controller used..... XI
Figure 141 the method of measuring the flow rate in the mass flow controllers. XI
Figure 142 A schematic of the components inside the flow controllers..... XII
Figure 143: An illustration depicting the flow of the gases in the initial experimental apparatus. XIII
Figure 144 making the coils on the end of the stainless steel bars. XIV
Figure 145 Side view end view and a view showing the system without any insulation. XIX
Figure 146. An illustration and characteristics of the insulation chamber. XX

Figure 147 Flow of gas through a tube. XXIII
Figure 148: For a 0.75 l/min flow rate of air through the heated pipe the outlet temperature should always equal the pipe wall temperature. XXIV
Figure 149 for a flow rate of 1 litre per minute the outlet gas temperature begins to drop off. XXV
Figure 150 For a flow rate of 2 litres per minute the outlet gas drops well below the wall temperature. XXV
Figure 151 For a flow rate of 2 litres per minute the outlet gas drops only by a small amount below the wall temperature. XXVI
Figure 152: Comparison of experiment, numerical and a quick CFD simulation for the outlet temperature of the pips wrapped with heating tape and PID regulated 1127 Kelvin pipe wall temperature. XXVII
Figure 153 Heat losses through the insulation encasing the heated gas. XXVIII
Figure 154: Simple calculation shows that to make the air deliver large amounts of energy high flow rates would be needed. XXVIII
Figure 155 rates of change of temperature for zero flow rate and the heating tape wrapped around 0.68m of the pipes XXIX
Figure 156 Shows how the pipes cool when no heat flux is applied over a period a time. XXX
Figure 157: Normal method to fuel and collect current from a cell. L
Figure 158: Proposed patentable method to collect current from the anode while fuelling it in a way that reduces temperature losses. LI
Figure 159 Picture with a single inlet and outlet fuelling design and the dual inlet outlet design. LII
Figure 160: Outer view of the parallel connected MT-SOFC stack module. LV
Figure 161 The current can be taken from the cell by blocking the end of the cell with a nickel pin thus jamming the silver wire into the cell. A glued cap is then placed over this. LVI
Figure 162: Section view of the Parallel MT-SOFC module sown in Figure 161. LVII
Figure 163: View of the serial connection cells. LVIII
Figure 164 Sectional view of the serially connected cells. LIX
Figure 165 A simulation result showing on off control with a high hysteresis value and thus low relay switching rates [1]. LXII
Figure 166 Simulation result with reduced hysteresis value and thus a higher switching rate [1]. LXII
Figure 167: Proportional control where it can be seen that increasing the gain “P” to a value under that which would cause instability causes the temperature to fluctuate under the set point. [2]. LXIV
Figure 168 Proportional + Derivative control where increasing the “D” term reduces the ringing in the system but still does not make the controller meet the set point. [2] LXV
Figure 169 PID control where the integral term forces the controller to meet the set point and eliminates the ringing effect in this case [2] LXVI
Figure 170 Heater system and its response against time [3]. LXVII
Figure 171 Temperature controller with proportional feedback [3]. LXVIII
Figure 172 Temperature control system with integral control [3] LXIX
Figure 173 Heater with PI control LXIX
Figure 174 Heating system with PID control [3]. LXX
Figure 175 shows the main control screen where the concentrations of oxidant and fuel in their respected channels are controlled. LXXV

Figure 176 On this screen several thermocouples can be monitored via a multiplexer built on a separate circuit board. LXXVI
Figure 177 This is where temperature programs be programmed into, that the wind tunnel follows. The operate can monitor the temperature profile (big white graph). The oxidant and fuel concentrations may also be manually controlled from this screen. LXXVI
Figure 178 Probably the most complicated screen. The PID controller is tuned here either manually or with an auto tuning function. Regardless of the wind tunnel type this program can be applied to all and tuning parameters may be saved. Also thermocouple readings are saved to disk on this page. LXXVII
Figure 179 This page allows proportional control or just % on off control. LXXVII

Table of tables.

Table 1: Fuel cell types and some of their characteristics. ..... - 2 -
Table 2: Comparison of the researched micro-tubular SOFC stack designs. ..... - 23 -
Table 3: Comparison of the type of electrical connections used by MT-SOFC development groups. ..... - 35 -
Table 4 Estimated Reynolds number for the separation to occur[73]. ..... - 47 -
Table 5: Simulation properties. ..... - 154 -
Table 6 Measurement of the electrical dependence of each of the testing strips. ..... - 192 -
Table 8: The effect of the testing strip and normal cathode on each others OCV when producing current at 90% $P(h_2)$ @50ml/min and 90% $P(h_20)$ 4ml/min air flow ..... - 196 -
Table 9: Measurements taken on the front and rear of cylinder for a flow rate of 16 cm/sec (100%N_2) ..... - 198 -
Table 10: Comparison of oxygen concentration and current density simulated with 1.5% mass oxygen in nitrogen flowing at 16cm/sec and with 55% mass water vapour in 44% mass hydrogen flowing at 5.7kg/s. - 204 -
Table 11. The heating tape's specifications. XVII

Nomenclature table

Symbol	Name	Units
Cp	Mean Pressure	Non dimensional
Cp_o	Pressure stagnation coefficient	Non dimensional
D	Diameter	m
g	Gravity	9.81 m/s
I	Current density	A/m²
m	Molar mass	mol
N	Nernst potential	V
p	Static pressure	Pascal
p∞	Free stream static pressure	Pascal
R_0	Universal gas constant	8.314472(15) J/K.mol
Re	Reynolds number	Non dimensional
Ro	Universal gas constant	
t	Time	s
u	X velocity	m/s
u	Velocity x direction	m/s
v	Velocity	m/s
v	Y velocity	m/s
∀	Volume	m³
V	Velocity	m/s
V	volts	V
w	Z velocity	m/s
z	Height	m
δ	Area	m²
η	loss	
μ	Dynamic Viscosity	kg/m.s
ν	Kinamatic viscosity	m²/s
ρ	Density	kg/m³
σ	electrical conductivity	1/ohms
σe	Conductivity of electrons.	S/m
σi	Conductivity of ions.	S/m
ϕ	electrical potential	volts
Γ	Diffusivity	m²/s
$\dot{m}$	Mass flow rate	kg/s

Chapter 1 Introduction to fuel cells and the Solid Oxide Fuel Cell

1.1 Introduction to fuel cells

Fuel cells are electrochemical devices that convert chemical energy in hydrogen enriched fuels into electricity electrochemically. In the most widely used energy extraction mechanisms of today, such as engines and hydrocarbon fuelled turbines etc, a process of producing heat and converting this heat energy into mechanical work results in thermodynamic limitations such as Carnot efficiency limitations. During the combustion process pollutants are also exhausted and these pollutants add to global warming and are not good for human health.

In the future fuel cells will be a means of producing electricity more efficiently and have the potential of producing environmentally friendly energy with much lower pollutant and CO_2 emissions. There are several types of fuel cell and each is normally identified by its type of electrolyte. Table 1 below, gives a brief outline and states the uses of some of the different types of fuel cells currently being developed.

Although fuel cells are an extremely promising technology for greener energy they are not always considered to be the best alternative to petroleum and battery driven systems. Low temperature fuel cells require platinum as a catalyst and therefore their cost is quite high. Mass production of fuel cells that require platinum may not even be possible because of supply and availability of this precious ore.. Higher temperature fuel cells have the advantage that they do not require platinum. However they operate at high temperatures, which is also problematic. It seems that the main obstacle to the mass production of fuel cells is occurring because of the mass production of , the combustion engine, which has been developed over the last hundred years. The combustion engine does everything that a user requires, it is low-cost, easy and cheap to fuel, has a relatively long lifespan, is tried and trusted and finally in many instances the fuel cell, apart from being a greener energy technology,

does not have any advantages over an engine. However should fuel prices rise enough, the fuel cell may become more desirable. This situation is expected to inevitably occur in the future and drives fuel cell research.

Table 1: Fuel cell types and some of their characteristics.

Type of fuel cell	Electrolyte	Operational temperature	Possible uses	Notes:
Polymer electrolyte membrane (PEM)	Solid Polymer	80°C	Transportation applications and some stationary applications.	Has the advantage of low weight and volume. Requires an expensive platinum catalyst.
Phosphoric acid (PAFC)	Liquid phosphoric acid	150-200°C	Stationary applications and some transportation applications.	Requires an expensive platinum catalyst. Typically large and heavy but many units already in use.
Direct methanol (DMFC)	Polymer	25-100ºC	Ideal for tiny to midsize applications.	Reduced storage issues as methanol is the fuel.
Alkaline	Solution of potassium hydroxide in water	100ºC- 250ºC	Large-scale utility applications.	Easily poisoned by CO_2. The first type widely used in the U.S. space program.
Molten carbonate (MCFC)	Molten carbonate salt mixture suspended in a LiAlO2) matrix	650ºC	Large-scale utility applications.	Does not require an external reformer. The high temperatures and the corrosive electrolyte used accelerate component breakdown and corrosion.
Solid oxide (SOFC)	Hard, non-porous ceramic compound	850-1,000ºC but aiming for 550 - 650ºC	Mainly for utility applications.	Does not require an external reformer. High-temperature operation has disadvantages for sealing.

1.2 The Solid Oxide Fuel Cell and principles of operation

One particular type of fuel cell is the Solid Oxide Fuel Cell (SOFC) ,which has some important characteristics that other types of fuel cells cannot provide. Within a fuel cell, hydrogen rich fuel is fed to an oxidising anode electrode and an oxidant, air or pure oxygen, is fed to a reducing cathode electrode. Sandwiched between the anode and cathode is an ion conducting device called an electrolyte that electrically isolates the anode from the cathode. Figure 1 depicts an illustration of this layout.

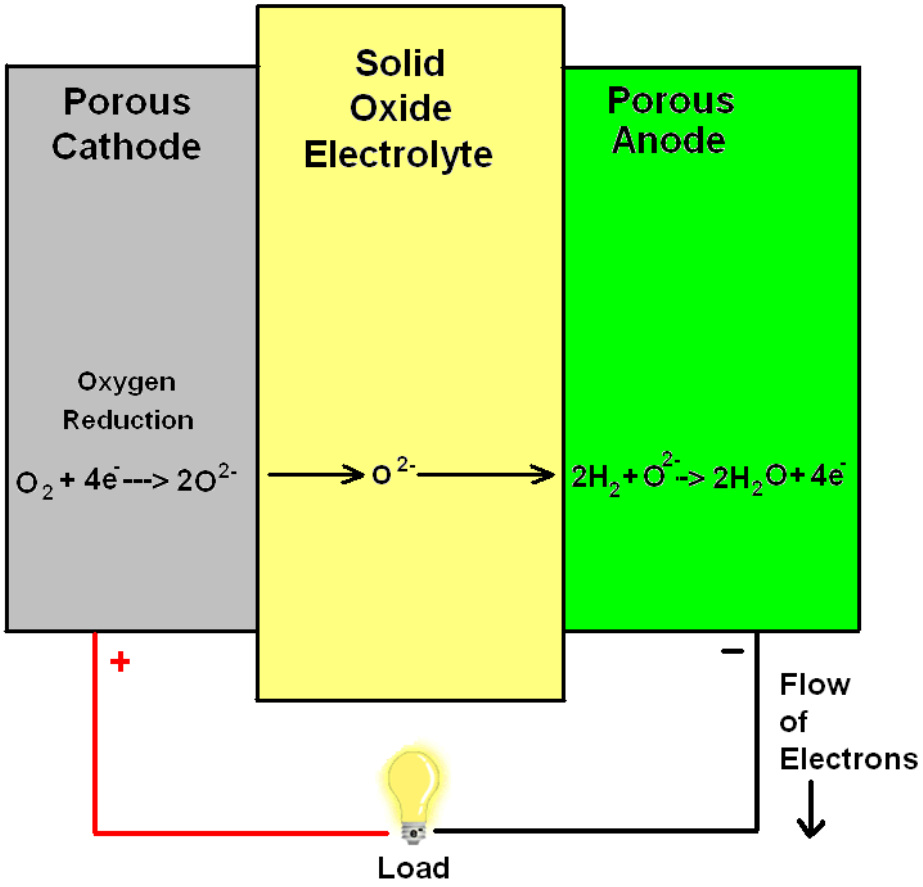

Figure 1: Operation of a SOFC showing the electrochemical reactions.

An important concept in the operation of the SOFC is the triple phase boundary regions, which are places where the oxygen reduction and hydrogen oxidation (red-ox) can only take place. More specifically these are spots where oxygen ions being transported through the electrolyte meet hydrogen atoms flowing through pores in the anode. In these spots there should also be a nickel conduction

path to the external circuit. Thus oxidation can occur on the anode forming water and releasing electrons that can be used for work in an external circuit. These electrons then flow back to the cathode to facilitate oxidation of oxygen, producing the ions for transportation through the electrolyte. These electrons are driven by the voltage generated between the negative and positive electrodes and this voltage is a function of the Nernst equation, which provides a relationship between the ideal standard potential for a cell reaction and the ideal equilibrium potential at other partial pressures of reactants and products. For the overall cell reaction, the cell potential increases with an increase in the partial pressure, gas concentration of reactants and/or a decrease in the partial pressure of products.

The following image, Figure 2, by Seniw and Wilson [1] is a depiction of the electrochemical processes at a single three phase location in the anode. The three dimensional microstructure of the anode and electrolyte layers are shown together as the translucent shades surrounding the red, green and blue tracks. The position where the green, “hydrogen (fuel) supply and water (exhaust) removal pore”, blue , “oxygen ion transportation pore” and red, “nickel electron conduction path” tracks meet is called a three phase boundary. A pore in the anode is depicted as the green track and has an incoming flow of hydrogen and also an exhausting flow of water concurrently. The blue track is an area within the electrolyte where reduced oxygen ions from the cathode flow through it. The red track is nickel that conducts the electrons, released from the oxidation reaction at the triple phase boundary, out to an external circuit where power can be utilised.

The three main advantages of the SOFC over many other types of fuel cells are firstly, that losses associated with the cells that result in heat can be integrated into the heat provision system for the SOFC and can make it thermally self sustaining or at least very efficient once the cells are operational. The second advantage of the SOFC is the fact that at these elevated temperatures internal fuel reforming can also take place at locations where nickel is present in the anode. The internal reforming capability of SOFCs means that a variety of fuels such as hydrocarbons can be used without the need for external reformers. These devices need power themselves to run and take up space reducing the overall efficiency of a fuel cell power plant/pack. The third advantage is that the materials to make the cells are not as expensive as those for other types of fuel cells.

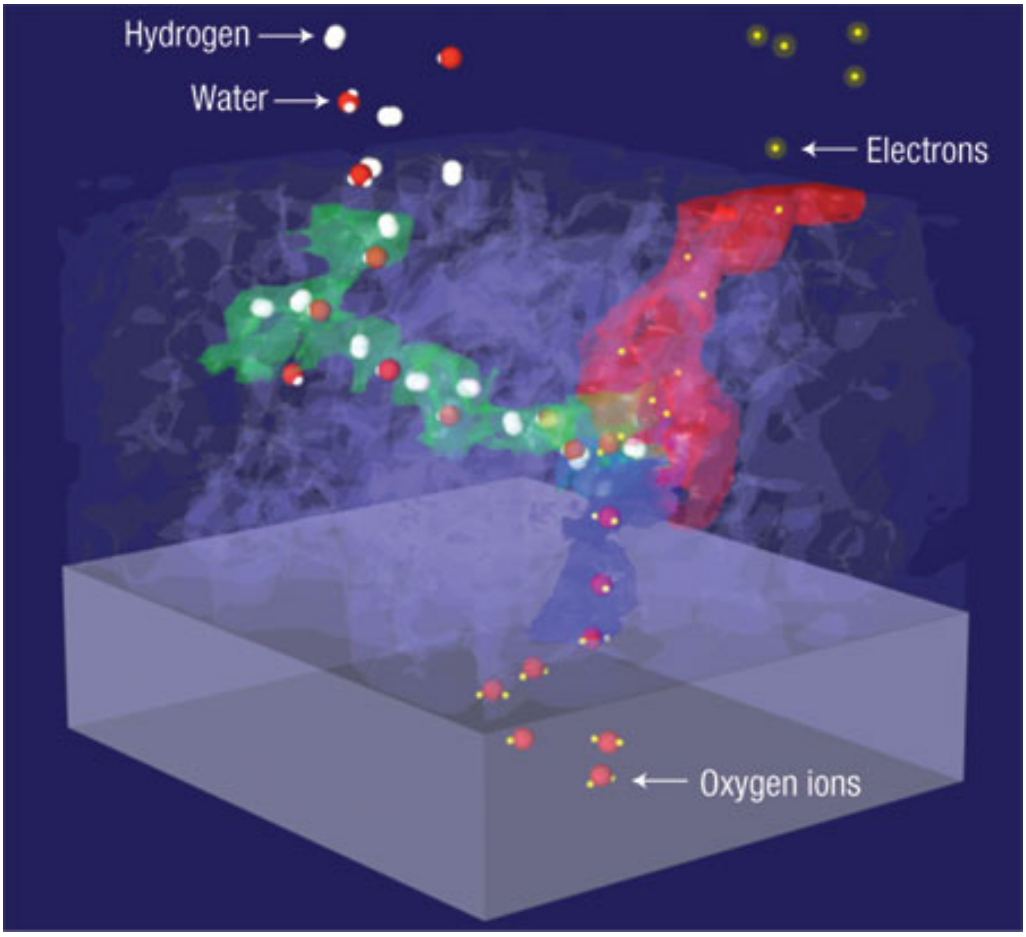

Figure 2: An exemplarily depiction of the electrochemical processes at a single three phase in the anode [1].

1.3 Materials

The Solid oxide fuel cell is composed of solid ceramic materials and this is why they have the name solid oxide, in particular reference to the electrolyte, which in the case of other cells may be liquid or a flexible polymer. According to Bessler [2], Baur and Preis [3] were the first to study a number of important ceramic materials and found that ceria and zirconia based had potential to be oxygen ion conductors or electrolytes. It is interesting to note that even 70 years after that study, these materials are still regarded as the basis for solid oxide fuel cell technology. For more information regarding SOFC materials the reader is pointed to the following texts,[4-9]. These texts include a selection of materials books and review papers that give in depth information about SOFCs materials.

1.3.1 The Anode

Typically the anode material must be a material that contains an ionic conductor, catalyst and metallic elements. It is normally the case that the ionic material is the same as the electrolyte and it consists of materials such as doped zirconia or ceria. To carry the free electrons produced by the electrochemical reactions on the anode side it must also contain a metallic material and copper and nickel are the normal candidates. This system is referred to as cermet (a material comprised of ceramic reinforced by a metal). The composite as a whole is a heterogeneous mixed ionic and electronic conductor (HMIEC) [10]. These materials are selected because they show a high chemical stability in reducing environments and have a high catalytic activity for hydrogen reduction. Nickel doped ceria and copper doped ceria or addition of other metals such as (Pt, Rh, or Pd) may be considered.

1.3.2 The Cathode

Electronically conductive oxide ceramics are generally used in the cathode because the materials used must be chemically stable under hot oxidizing environments. One of the most prominent materials is strontium-doped lanthanum manganite (LSM, $La_{1-x}Sr_xMnO_3$). LSM shows high electronic conductivity (σe > 10 S/cm at 700 °C) and good electro-catalytic activity for oxygen reduction. The porous cathode can consist of LSM only, or of a composite of LSM and the electrolyte material.

The use of a mix conductor may also be used to improve the performance of the cathode similar to the case of the anode. A material widely studied is strontium- and iron-doped lanthanum cobaltite (LSCF, $(LaSr_x)(Fe_{1-y}Co_y)O_3$). Like LSM, this material has a perovskite crystal structure [11]. The crystal structure of a perovskite material is ideally cubic, with a framework of corner-sharing octahedra, containing titanium (Ti) or other relatively small cations surrounded by six oxygen (O) or fluorine (F) anions. Within this framework calcium (Ca) or other large cations are placed, surrounded by twelve anions. Tilting of the octahedra and other distortions often lower the symmetry from cubic, giving the materials important ferroelectric properties and decreasing the coordination of the central ciation . This flexibility gives the structure the ability to incorporate ions of different sizes and charges. Perovskite materials can have very high electron conduction and ion conduction properties. These materials are also renowned for their high catalytic activity practically with oxidation reactions. For more information on this class of material for the SOFC field the reader is pointed to [12].

1.3.3 The electrolyte

The electrolyte is an extremely important component in the makeup of a solid oxide fuel cell. The electrolyte must conduct oxygen ions and the traditional material has been yttria-stabalised zirconia [6] (YSZ, $Y_{2x}Zr_{1-2x}O_{2-x}$, where x = dopant concentration in mol-% Y_2O_3 in ZrO_2). This material was first tested by Baur and Price in 1937 [3] and is still today the most widely used electrolyte material because of its high performance at high temperature. Another key advantage of this material is that it is very stable under both oxidizing and reducing environments. Doping

exchanges the ZrIV cations of the ZrO_2 host lattice with YIII cations. This leads to both, the formation of oxygen vacancies resulting in ionic conductivity, and the stabilization of the cubic phase of Z_rO_2 down to room temperature (hence, the name). YSZ has a high conductivity for O^{2-} ions only at relatively high temperatures (σi ~ 0.1 S/cm at 1000 °C, ~0.01 S/cm at 700 °C) [2]. Other dopant atoms (Sc, Ca, Mg, Nd, Sm, Yb) are also being used [9].

Current research in the electrolyte field tends to be aimed at reducing the operating temperatures to below 600°C. Gadolinium-doped ceria is generally regarded as the most promising candidate for having a high ionic productivity and also having a high electrical resistance at the 600°C temperature range. The ionic conductivity is around five times higher than that of YSZ (σi ~ 0.05 S/cm at 700 °C) [13]. However at low oxygen partial pressures and at higher temperatures ceria is partially reduced and the material becomes an electronic conductor which of course is undesirable.

Zirconia and ceria-based electrolytes have a cubic, fluorite-type crystal structure. With this structure they allow high mobility of the large oxygen ions. Oxides with perovskite structure have also been used, for example strontium- and magnesium-doped lanthanum gallate (LSGM, $(La_{1-x}Sr_x)(Ga_{1-y}Mg_y)O_{3-\delta}$) [14]. Recently, proton-conducting materials (e.g. barium cerate, BaCeO3) have been studied as electrolytes, opening up a completely new type of solid oxide fuel cell [15].

Chapter 2 Literature Review

The Literature review has been divided up into 4 different sections. The first section, Part I is a review of the literature available for MT-SOFCs relating to stack design and is intended to introduce the reader to the MT-SOFC field. The second section, Part II, reviews the literature available for fluid dynamics and heat transfer around a cylinder in cross-flow and this section in intended to inform the reader about this much researched and applicable field to the MT-SOFC as it is also a cylinder in cross-flow experiencing the same fluid dynamic, heat transfer and also mass transfer phenomena. Part III of the literature review investigates the available literature for temperature measurement and the effect thereof on the performance of a MT-SOFC. A very important gap in the literature was found in this section and forms a major part of the research in this thesis. Part IV of the literature review studies the literature available for mass transfer to cylinders in cross flow. The focus of this section was to see if previous studies had been made on this topic and could the performance MT-SOFCs in cross flow be affected. The final section of the literature review summarises the first three parts of the review and outline areas deemed eligible for research and forms the topics dealt with in this thesis.

2.1 Part I: The micro-tubular SOFC stack and possible applications

2.1.1 Introduction

The demonstration in the early 90s of the extrusion of thin YSZ ceramic tubes, with wall thicknesses of between 100 and 200 μm, which could be used as the electrolyte for SOFC operation, opened up the Micro-Tubular SOFC (MT-SOFC) research field [14]. Soon after this achievement Kendall et al. [16] demonstrated the first operational 20, 200 and 1000 cell reactors. Alston et al. [16] described the 1000 cell reactor that was used to produce electricity from the cells directly and to heat water

with the heat losses. The reactor was made up of 40 modular stacks that are joined together to make a master stack. They reported that the hot air alone fed to the reactor was sufficient to heat up the cells to their operating temperature and that these cells could withstand temperature increases of 200°C min^{-1}. The reactor produced only 82 mW cm^{-2} but this achievement proved that the MT-SOFC system was feasible.

Currently the most commonly used cell architecture for the MT-SOFC is a deviation from the original electrolyte supported type called the anode supported MT-SOFC. To reduce the ohmic losses and impedance to ionic transport, a thin electrolyte layer is spread upon the anode. In this case the anode is much thicker than the electrolyte and it is the support body for the electrolyte and cathode. This form of cell was also pioneered by a group including Kendall [17]. Cutting edge experimental techniques such as impedance spectroscopy, X-ray computed tomography in combination with modelling techniques, oxygen stable isotope labelling and subsequent secondary ion mass spectrometry analyses are some examples of the novel approaches for improving the cell performance can be seen in Appendix I.

In 2000 a paper by Van Herle et al. [18], investigated the application of the SOFC for vehicles. It was presumed at the time by the authors that SOFC technology could not meet the requirements needed by a vehicle power plant, i.e. a massive reduction in size, enhanced strength and resistance to fast thermal heat up, may be short-sighted and incorrect. They recommended that cells based on thin small tubular ceramics had the potential to overcome the problems listed above and that the inherent advantages of the SOFC over engines and other types of fuel cells (mainly economic) made the MT-SOFC very attractive for this scale of power plant.

Several designs for the use of SOFCs for automotive use have since been suggested for example by Winkler and Lorenz [19]. Their suggestions include a SOFC-GT (Gas Turbine) power train system, a SOFC-GT power train system with external cooling and a SOFC-Stirling cycle. The authors specifically point to the MT-SOFCs as the most feasible type of SOFC for mobile applications coupled with a Stirling engine because of the expected high system efficiency, low specific volumes and the present availability of small units.

The heat extraction of the SOFC by a Stirling engine does not affect the combustion reaction because the coolant is the separated working fluid of the Stirling engine. They also recommend that the exhaust temperatures of the SOFC-Stirling engine should be much lower than that of a SOFC-GT system indicating better heat recovery. These initial studies indicated that the design problems of such cycles should be solvable. The micro-GT is a very simple device compared to the Stirling engine and the inclusion, for example, of turbo-chargers in the exhaust flow of the Stirling engine system, to increase its efficiency, also increases its complexity. However the authors pointed out that more research in this area could be valuable in the long term.

Tompsett et al. [20] in another application for MT-SOFCs describe the integration of a micro-SOFC stack and standard gas burner to produce both electricity and heat by putting a cell inside a 3-catalyst burner. Figure 3 illustrates the concept where the platinum combustion catalyst provides heat (900°C) for the operation of the MT-SOFCs and the pre-heating of the ruthenium pre-reforming catalyst to 700°C. The catalytic reformer produces hydrogen gas for the fuel cell operation and the mixing of some air into the fuel gas prevents carbon build up on the fuel cell anodes, by oxidising the carbon. Finally the air that is utilised in the fuel cells is fed back to the pre-burner fuel mix to preheat the fuel giving a faster reaction time.

This prototype unit produced a very meagre 1.5 W, but the demonstration alone showed the versatility of the MT-SOFC stack. The authors also pointed out other possible applications such as a vehicle battery charger. In this case the fuel cell could be used to recharge a battery and the battery life would be extended due to smaller discharge depth, ultimately reducing the costs of the number of replacements. The usable time of the vehicle would be increased due to the continuous recharging from the fuel cell, when in use. They also point out how a power pack from a MT-SOFC would not intrude on such products as golf trolleys, bicycles and wheel chairs.

Instantaneous start-up, similar to that of an engine or battery, is an unavoidable condition, for the commercial success of MT-SOFCs, not only in the automotive field but also in the auxiliary power supply sector. Systems using battery and super capacitor start-up heating mechanisms have been envisaged for the start up of the MT-SOFC stacks, but the volume occupied by such a system, that generates an

equivalent power, is prohibitive for many applications. Originally Kendall [16] demonstrated with his 1000 cell reactor that MT-SOFCs could be heated up to their operational temperature of 850°C at a rate of 200°C min^{-1} and other authors have since shown much faster heat up times.

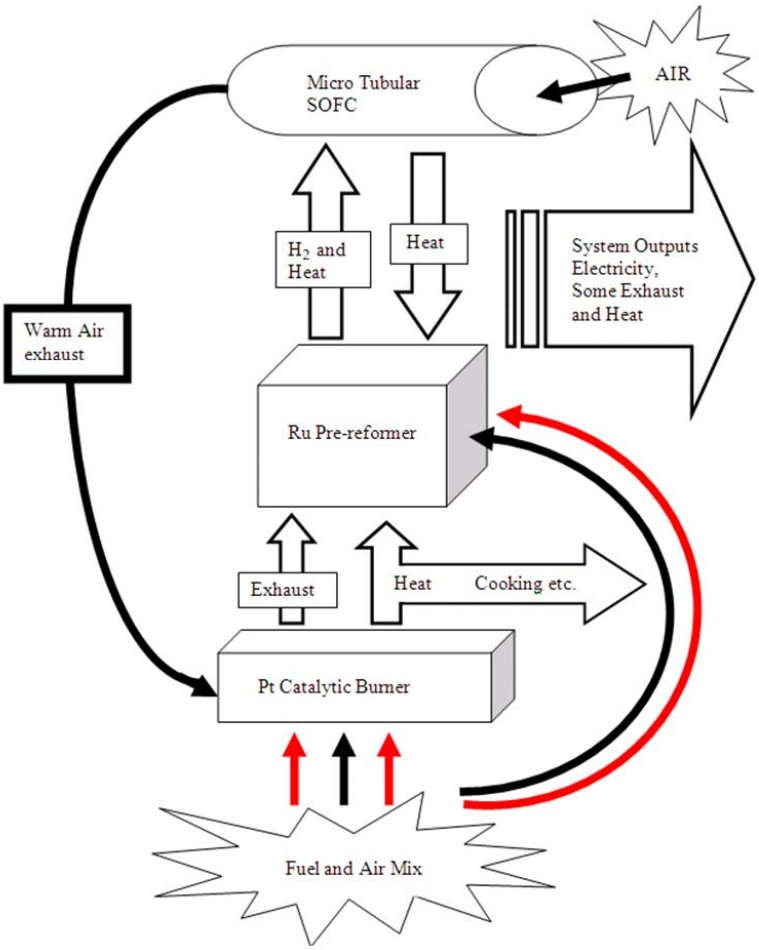

Figure 3: Author's depiction of the gas and heat flows in a triple layer catalyst-SOFC-catalyst system proposed by Tompsett et al. [20].

In 1996 Prof. Kendall also set up the first MT-SOFC company called Adelan (UK) Ltd. Bujalsk et al. [21] with these Adelan cells have shown that MT-SOFCs could be consistently ramped to operational temperature at a rate of 4000°C min^{-1} without any structural damage or power degradation. This would mean that the cells would be at their operational temperature after 12 seconds. An important result of these tests was the finding that these cells could also be allowed to cool extremely fast to 300°C within a few seconds and not become damaged or incur losses of

performance after a 50 cycle test. Of course it should be noted that the apparatus used to perform these tests was specifically designed for single cell tests and a stack of these cells will have its heating up and cooling down rates further limited by the thermal stresses induced by the reactor housing and seals of the cells. Nonetheless it has been shown that the cells themselves can be very thermal shock resistant.

Very recently Du et al. [22] showed with their cells (Nano-dynamics USA, Inc.) that regardless of single cell tests or stack tests that thermal cycling of their cells did not cause any degradation of them. They recommended that their stacks can be heated up at rates of 550°C min^{-1} and that their cells produced the normal operational power as soon as it reached the operational temperature of 800°C. It was very interesting that their single cell tests just comprised of putting the cells into preheated ovens for heating up and simply removing them for cooling down. This is another example of how robust these cells can be. Another interesting aspect of the work of Du et al. [22] were the outcome of experiments where they heated up different generations of their cells in stacks. In these experiments the start-up heating rate was 550°C min^{-1}. They found that no performance losses or structural damage occurred even though the cell size was scaled up 2.7 times. The sizes of these cells were not found in any of the published literature associated with the company. However this is a demonstration the robustness of stacks containing MT-SOFCs.

2.1.2 Reports of micro-tubular SOFC stack designs and considerations

In the literature there are only a few design concepts described for MT-SOFC stack design. The most standard design is an array of MT-SOFCs with hydrogen flowing inside each cell in the array and air flowing around the outside of the cells. The lack of stack designs and optimisation of the arrays in the literature is probably for two reasons. The first being that the problems associated with single cells have not been totally eradicated by most groups. Thus they will be focusing their efforts on single cells. The second reason is that groups associated with industrial partners will be guarding their stack designs carefully to keep their innovations hidden from their competitors. However there are some interesting reactor designs described in both the literature and patents for MT-SOFCs.

To begin with, Sammes and Bove [23] show a concept for a 40 cell stack where the cells are connected together with current collectors in planar multi-cell arrays. The main feature of this design is that these single rows of tubular cells can be electrically connected in series or parallel and physically connected as parts of a larger stack comprised of these individual modules. Silver is used to braze the cells to the current collectors and the brazing process takes place inside a furnace. Figure 4 illustrates an example of the current collection and sealing mechanism for serially connected cells where the terminal on the left of the flat plate connector contacts the cathode and the terminal on the right to the anode providing a serial connection that builds up the voltage.

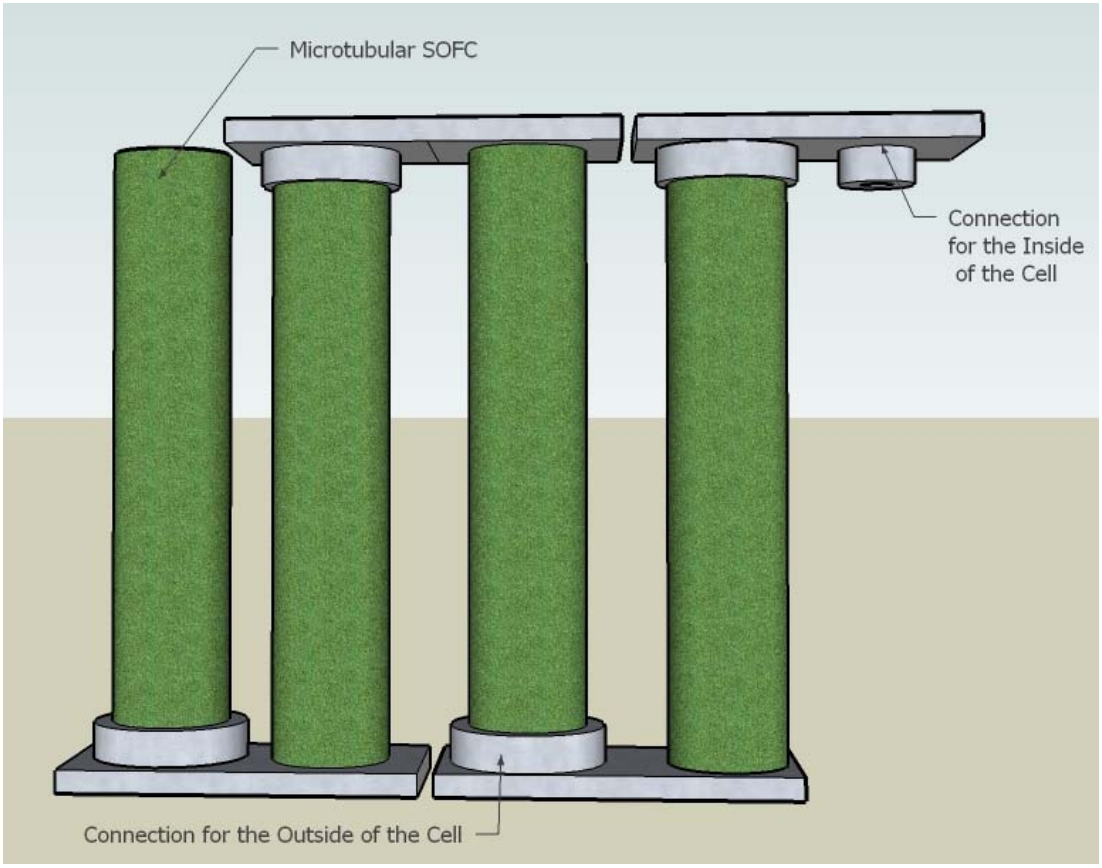

Figure 4: Author's depiction of the current collectors and cell configuration by Sammes and Bove [23]

Funahashi et al. [24] describe the fabrication of a cube shaped MT-SOFC bundle that can be seen in Figure 5. The reactor components were successfully assembled into a cube shaped MT-SOFC bundle (3cm×3cm×3cm) with 36 tubular cells each having a diameter of 2.0 mm. In this type of MT-SOFC stack design, the cathode consists of blocks of matrices with several grooves that hold the MT-SOFCs. The cathode matrices are used as the current collectors, the guide for cell arrangement and the oxidant flow path. This original design is also an example of a stack where cells are connected in parallel and recently the same group [25] have shown an innovative technique to connect these cells in series.

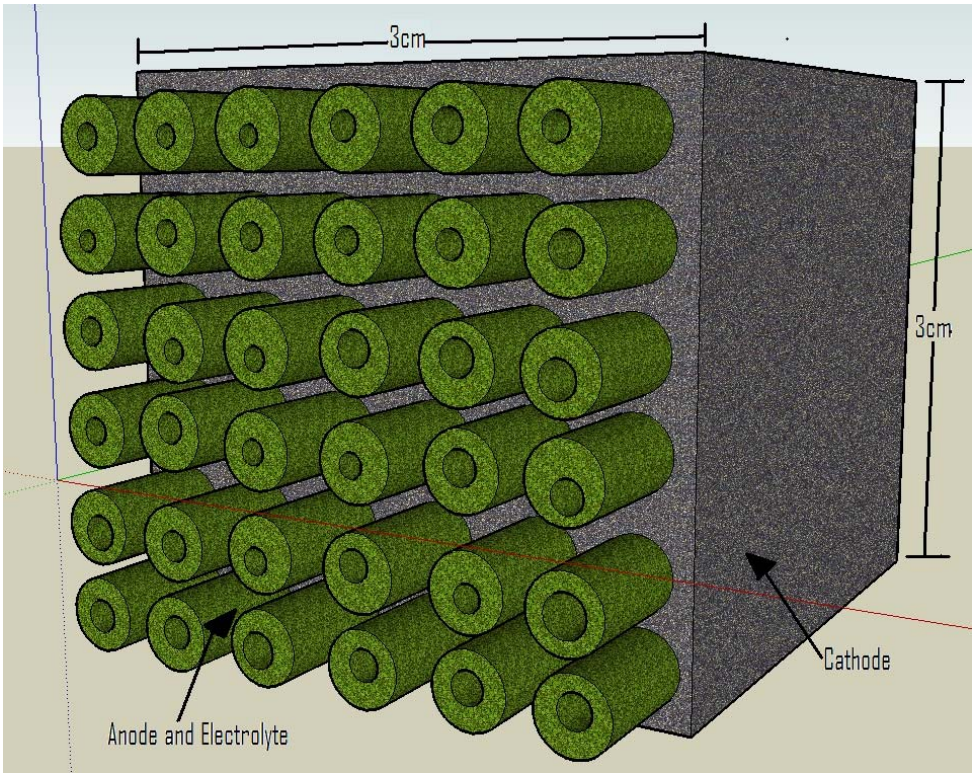

Figure 5: Author's illustration of the cube shaped SOFC cathode structure with embedded electrolyte-anode tubes by Funahashi et al. [24].

They recommend that when the cathode matrix has a gas penetration coefficient of 1.68×10^{-4} mℓ cm^{-2} s^{-1} Pa^{-1}, it is possible to flow 600 mℓ /min of air in a cubic cell (1 cm^3) under a 0.1 MPa difference between the inlet and outlet. The air flow rate of 470 mℓ min^{-1} was estimated to meet the target power density of

2 W cm^{-3}, and indeed these cathode matrices appeared to be suitable components for the cube to achieve targeted performance.

The flow of fuel to the anode is also an important area to be optimised in a MT-SOFC reactor design. Currently most groups send the fuel in one end of the micro-tubular cell anode and out the other end. The electrical connections are made via wires lodged inside the anode, meshes lodged inside or brazed connections to areas of the anode not covered by the electrolyte. Recently Lee et al. [26] have demonstrated their 700W anode supported SOFC stack for APU applications. It has a novel combined approach of supplying the fuel and electrical connection by using a conductive inlet pipe, illustrated in Figure 6 as a "red" fuel inlet pipe and wires located between the inlet pipe and anode, illustrated as orange nickel wires in Figure 6. Their cells are 10mm in diameter and they are 160mm long, which is at the larger end of the MT-SOFC scale.

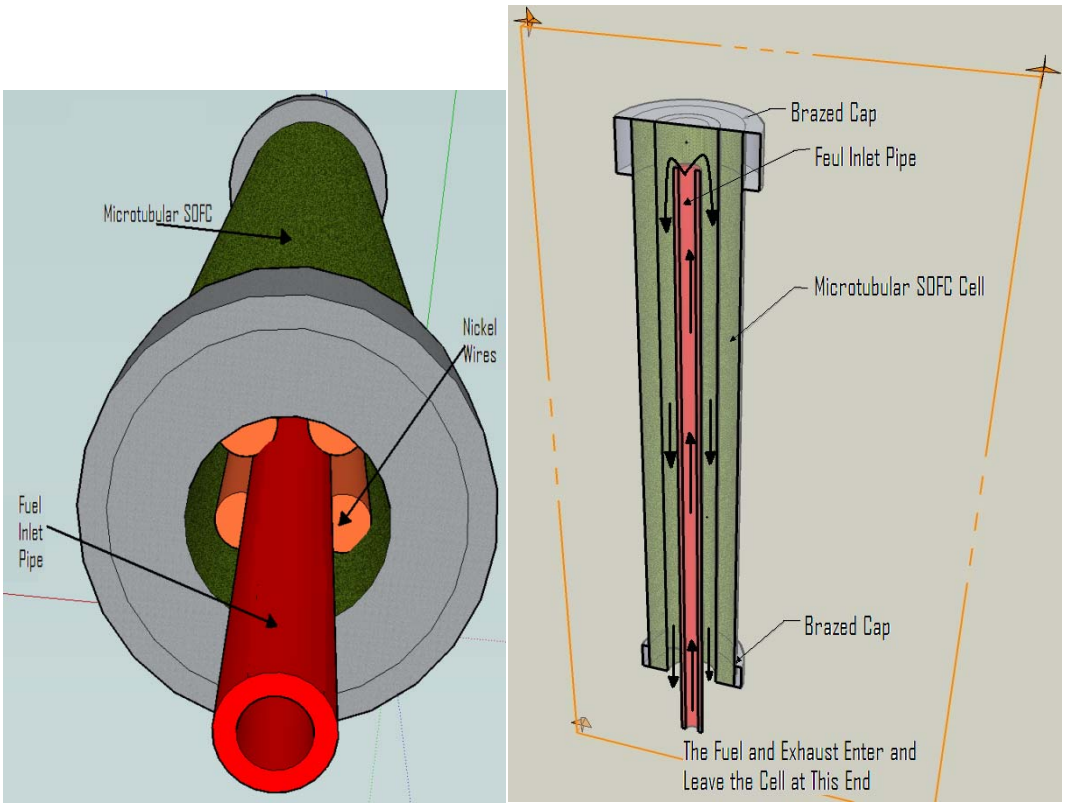

Figure 6:Author's illustration of the gas supply system invented by Lee et al. [26].

A novel feature of this design is that the inclusion of a metallic pipe, nickel wires and layer of nickel felt inside the anode, enhanced the fuel utilisation efficiency by reducing the volume of the gas flow channel inside the anode. Importantly this system may simplify the fuel inlet and exhaust manifolds because both the fuel and exhaust enters and leaves the cell at the same end. It may also be the case that the heat transfer from the hot exhaust to the cooler inlet gas in this system also improves the overall system efficiency. They report a dramatic increase in the power output of their cells from 0.24W cm^{-2} up to 0.54W cm^{-2} with a fuel utilisation of 45%. The reasons suggested for this increase in performance are attributed to this new fuel supply system, a reduction in ohmic losses and a reduction in contact resistance between the anode and the current collector.

A very interesting part of this paper examines the gas supply to a 6 cell stack. They use a computational fluid dynamics program to design their gas supply systems and by varying the size of the gas entrance slit within the fuel supply chamber and the angle of the inclined wall of the fuel exhaustion chamber, they make sure that each cell in the reactor receives the same amount of fuel. The length of the current paths within their stack was also designed so that the length of the current collection wires in hot zones was minimised. This was because of the increased power losses from these wires at higher temperatures. Their final stack contained 36 cells produced a total of 700 W at 750 °C with a fuel utilisation of 49% and 0.39 W cm^{-2}. This method may be applicable to the smaller diameter cells as there are micro-sized capillary pipes available on the market made from pure silver and indeed nickel, available from various manufacturers.

The prior mentioned stack designs only relate to the physical structure of the reactors and there are some examples of detailed accounts of whole systems that include the key topic of thermal-self-sustainability. For example Zheng et al. of the Alberta Research council [27] issued a patent in 2004 that includes the design for the operation of a MT-SOFC stack and heating system. The system was actually quite simple. The un-reacted fuel is used to supply the required burn temperature from the exhaust to control the temperature inside any of the reactor modules and this is electronically controlled. These burners can also be used to maintain any individual module at a standby temperature.

The invention contains 4 modules of cells or sub-stacks with different numbers of cells in each, any of which can be activated or deactivated in any combination to satisfy the power demand. Also a novel type of insulation from Aspen Aerogels .Inc (USA) [28] is utilised to thermally insolate the system. This seems to have a very low thermal conductivity, which would be extremely advantageous for holding heat within the modules. In the patent application there is a lot of detail about the workings of the stack and sub-stack systems and the reader is referred to the patent [27] for more information.

Another patent also by Sarkar et al. of the Alberta Research Council [29] also describes the operation of a MT-SOFC stack with a novel heat exchanger design as seen in Figure 7, where it should be noted that the oxidant outlet from the top of the stack is connected to the oxidant outlet in the heat exchanger. The system comprises of a cylindrical array of SOFC cells encased by a heat exchanger that wraps around the fuel cell stack and comprises of a flexible, thermally conductive first layer and an overlapping flexible, thermally conductive second layer spaced from the first layer. The first and second layers define adjacent annular oxidant supply and oxidant exhaust channels when wrapped around the stack. The exhaust channel is communicative with heated exhaust oxidant flowing from the stack. The oxidant supply channel is communicative with supply oxidant that flows to the stack and is heated by hot exhaust oxidant in the adjacent oxidant exhaust channel and from heat radiating from the stack.

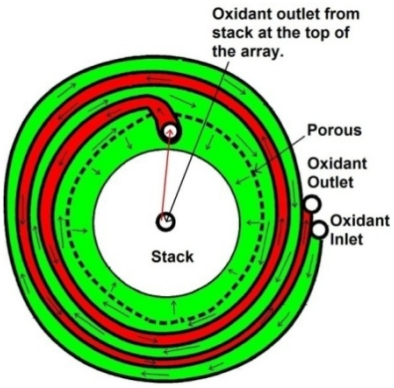

Figure 7: Author's illustration of the heat exchanger design by Alberta Research Council (CAN) inc.[29].

This is just a design and there are no performance data available on how well the heat exchanger works but it seems that it could work quite well. Indications of the advantages of similar coiled heat exchangers, such as better heat transfer from the walls of the pipe to a gas and reduced heat exchanger size, has been shown elsewhere [30-33]. The most notable difference between a coiled pipe heat exchange system and a simple straight pipe system is that in the coiled pipe system circumferential forces act on the fluid as it travels inside the coil and this causes two rotating swirl motions to occur. The end result is that these extra motions, inside the coiled pipe, improve the heat transfer from the coiled pipe walls significantly.

Another addition of this system could be to burn the exhaust hydrogen to also heat the incoming oxidant and fuel lines, which should increase the overall efficiency. Because the oxidant gass exits the oxidant supply manifold at one point inside the MT-SOFC holding chamber, this could potentially cause areas inside the reactor where the inlet gas is not refreshed. A possible solution could be to reverse the direction of the flow and allow the gas to exit at the porous material rather than the single point. A very interesting additional adaptation of this design would be to supply the fuel rather than the oxidant to the cells through this heat exchanger with the anode layer on the outside of the cells. This may make it much easier to make electrical connections to the anode and the fact that the hydrogen would be confined inside this chamber could also be advantageous and a novel approach.

Most of the previous reactor concepts are designed to operate at high temperatures but many groups are working to reduce the operating temperature of the cells. The use of intermediate temperature MT-SOFCs, operating under 650°C, can decrease material degradation, prolong stack-lifetime and reduce stack material costs by utilizing common metal materials. In the past few years results published by several authors [13, 34-38] have reported promising intermediate temperature MT-SOFCs. The reduction of the operating temperatures also reduces the diversity of the fuels that can be used in these cells. Internal reforming requires temperatures in excess of 700°C and so it may not be possible without external reformers operating at higher temperatures than the cells themselves. So there is a possibility that high temperature cells will always be needed for hydrocarbon fuel utilization.

A very important part of a MT-SOFC reactor design will be the temperature management of the stack. This has been studied recently by Hashimoto et al. [39]

experimentally and with some analytical techniques. The principle behind the technique, used in this study, is that the reduction in electrical potential of a MT-SOFC, as the amount of current drawn from the cell is increased, can be accounted for by mainly ohmic and polarisation losses associated with the electrolyte. The ohmic part of these losses should obey Ohm's law and thus be a linear function. However, if the resistance of the cell is relatively high compared to the current level, or if the cell has difficulty in radiating heat away fast enough, the cell will lose the linearity between ohmic potential drop and current. This is due to heat generation within the cell, which lowers the resistance of the electrolyte. This would imply that the electrical potential drop due to ohmic losses is related to the temperature of the cell.

To measure the ohmic losses and polarization losses two methods were used. The current interrupt method is an AC technique that very briefly interrupts the fuel cell current and rapidly measures the terminal voltage before and during the interruption. A current pulse generator is used as an electric load and pulse source. An electrometer that has a high input resistance is connected to the potential sensing terminals of the cell under test. Using the electrometer the potential pulse can be measured by using an oscilloscope and thus the ohmic drop of the cell can be measured at any cell current.

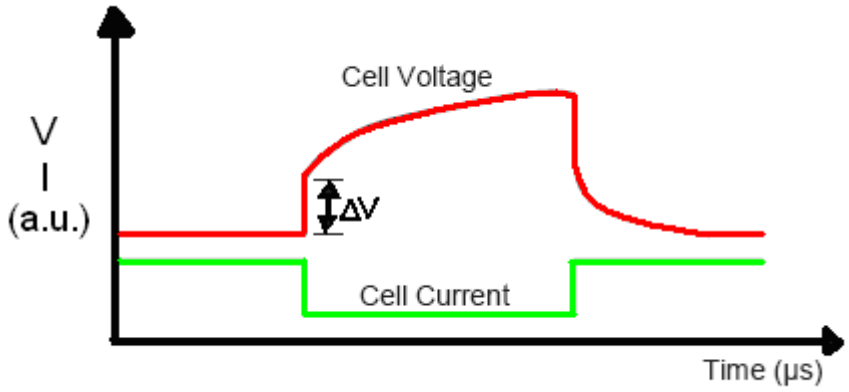

Figure 8: Author's illustration based upon the description of [39] where the current produced by the fuel cell is very briefly interrupted using a current pulse generator and the initial change in cell voltage, due to losses is measured.

The second method to measure the ohmic losses was Electrochemical Impedance Spectroscopy (EIS). This method involves imposing the AC perturbation over a broad range of frequencies normally from10 kHz to 1 Hz or lower. By monitoring the resulting variations in magnitude and phase of the cell voltage and current with a frequency response analyzer the complex impedance (Z' and Z") of the fuel cell can be found. This produces a detailed data set and several parameters may be extracted including the ohmic losses from the cell, kinetics and mass transport within the cell. They report no differences in ohmic measurement results between the two methods indicating that the much less expensive current interrupt method is just as effective as the costly EIS method.

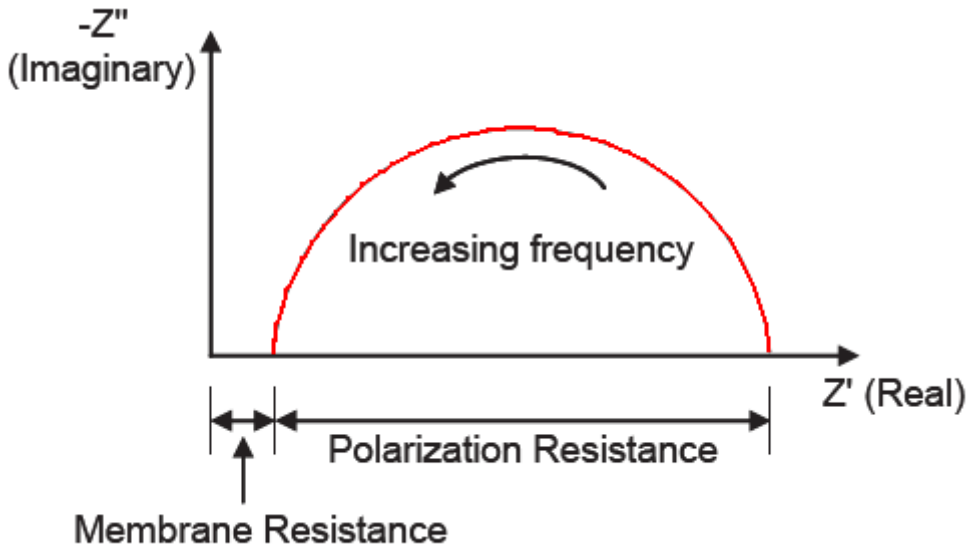

Figure 9: Author's illustration based upon the description of [39] on an example EIS result where the amplitude and phase of the signals may be plotted in Nyquist format for analysis and modelling.

The steps to define the cell temperature as a function of the current drawn from the cell are as follows. Firstly, polarization of the cell during power generation is measured by EIS or the current interruption method. The ohmic potential drop as a function of current is obtained and the ohmic resistance at each current is calculated. Secondly, the temperature dependence of the cell resistance at OCV or in the low

current density region, where the ohmic potential drop follows Ohm's law, is measured. By applying the change in ohmic resistance in the cell, the cell temperature as a function of current can be estimated.

While experimentally validating their theory they found a dramatic reduction in the ohmic resistance of the electrolyte of a cell as the current density was increased. This would mean that there should also be a large increase in temperature around the cell. Compared to their electrochemical technique for measuring the temperature, the experimental results matched quite well, where there was the same slope in temperature gradients, but 10 °C less in the experimental result. This was most likely caused by the distance of the thermocouple away from the cell.

The methods used by this group could be a very useful non-intrusive method to measure the temperature of cells within bundles or stacks where the temperature at points within the reactor is related to the current being drawn from a cell. The authors make suggestions for the improvement of the measuring methodology. These include, better positioning of the potential sensing terminals, the addition of other potential sensing terminals and making a regular measurement of the dependence of the testing cell's electrode resistance to temperature.

Table 2 summarises some of the qualities of the MT-SOFC stacks that were found during the course of this research paper. Probably the most advanced micro-tubular reactor has been made by Nano-dynamics (USA) Inc. which is already being commercialised. This system runs on propane/natural gas and reforms the fuel via partial oxidation (POX) reformation. There are currently 50 and 60 watt systems for battery recharging. While there are some papers dealing with improving the performance and optimisation of the micro-tubular cells from this company, there is very little information available on the stack design and system operation.

Table 2: Comparison of the researched micro-tubular SOFC stack designs.

Name of Group	**Cell Dia. mm**	**Support**	**Stack Power W (# of cells)**	**Development Stage**	**Oper. Temp. °C**	**Heat up time °C** min^{-1}
Adelan (GBR)	~2	Electrolyte/Anode	500 (1000)	Demo. model	850	200
AIST (JPN)	0.8	Cathode	2 (20)	R&D	500	83
Alberta Research Coun. (CAN)	~2	Anode	20 (~ 30)	Thermally self sustaining model.	800	N/a
Korea Inst. of Tech.(KOR)	10	Anode	700 (36)	Demo. model.	750	6
Nano-dynamics (USA)	n/a	Cathode	250	50 and 60W models on the market.	800	550
TOTO (JPN)	n/a	N/a	43 (14)	N/a	700	N/a
Uni. Connecticut (USA)	13.2	Anode	100 (40)	Demo model.	850	40°C
Upper Austria Uni. App. Sci. (AUT)	~2	Anode	3.5 (7)	Early experimental stacks.	850	N/a

A key component in MT-SOFC reactor design for commercialisation has been addressed by Sammes et al. [40]. Once the performance of the stack has been decided the choice of the optimal active surface or number of MT-SOFCs has to be decided based upon economic reasoning. This is divided into investment/buying cost versus operating cost. Increasing the current density should lead to a lowering of the initial investment cost because less cells will be needed. However at the same time the increased current density reduces the fuel efficiency resulting in an increased operating cost. So a trade off will be required between the buying cost and the running costs. This will determine the optimal size of the active surface and consequently the number of MT-SOFCs. Due to the fact the MT-SOFC stack is at such an early stage in its development there are probably very few groups considering this. But it is a critical reactor design consideration when stacks for the consumer market should be made.

2.1.3 Sealing of micro-tubular SOFC stacks

MT-SOFC sealing is more difficult than the sealing of the larger planar, tubular and monolith types. In these larger types the seal would be located in a specific large area. However with the MT-SOFCs, sealing occurs in small amounts to connect each of the individual cells to its gas feed and exhaust ports. This results in many more possibilities of seals being or becoming defective and thus a much higher risk of fuel leaks. For example groups such as Serincan et al. [41] have already shown the extent of possible temperature variations across the MT-SOFC. So the possibility of a substantial temperature gradient across the position where the seal may be is a very important consideration. This thermal gradient is likely to occur at the sealing location because the active heat producing cells will be joined to passive manifolds at this position.

Typically hydrogen travels through the inside of the cell and air will travel around the outside of an array of cells, because this is a much easier way to contain the hydrogen and control the fuel supply to the cells. Flowing the oxidant through the

inside of the cell could mean that very high flow rates of air inside these thin tubes would be required because of the high concentration of N_2 in the air. Leaks of hydrogen into the air flow can be catastrophic for the performance and durability of a MT-SOFC stack. When hydrogen leaks at high temperatures it causes a flame, which is both safety-wise unacceptable and also causes damage by overheating and vaporisation of seals as seen in Figure 10. The flame removes oxygen from the stack and can also melt the metallic current collectors attached to the cathodes. This leak also increases the possibility of the re-oxidation of the anode which is fatal for a cell's power producing capability.

Figure 10: An array of cells (left picture) and the damage caused (right picture) from a small flame in a reactor.

As sealing is such an important component in the operation of a MT-SOFC, companies seem to guard their sealing methods and so the only literature available at present is not specifically for MT-SOFCs but may be applied. One of the only cases where the sealing was explicitly described for MT-SOFCs was by Hashimoto et al. [42],used for pressurised tests on MT-SOFCs. They used a combination of Aron C and CC (Toagosei Japan Ltd.) ceramic glues to seal their cells to aluminium oxide tubes and then tested their cells and seals under pressures of 0.7MPa finding the seal to work very well

In many instances the sealing will be located between a zirconia electrolyte and a high-temperature resistant metal frame, which has the advantage that the electrolyte acts as an electrical insulator. Seals can also be from an electrode, normally the anode to a metal interconnect, which can act as a flow path for the free electrons produced by the cell if the seal is metallic. Depending on the stack operating conditions, this seal can potentially be exposed to operating temperatures of about 750–850 °C. This seal will always be exposed to an oxidising atmosphere

on the cathode side. On the anode side the seal will be exposed to a wet fuel gas, containing various ratios of hydrocarbons (e.g., CH_4, H_2, CO, CO_2, and H_2O) and the seal will always be between these two conditions. The housing material can also be as important as the sealing material itself. Crofer E-brite (26Cr-1 Mo) and heat treated 430 stainless steel are some of the materials being considered.

Strong metal to ceramic seals seem to be quite difficult to realise even at ambient temperatures and the extreme temperatures required by MT-SOFC stacks make the sealing problem substantially more difficult. Glasses are most widely used to make metal–ceramic seals [43] because they can be modified to have a very close match of thermal expansion with other fuel cell components. These seals show good hermeticity and good thermal and environmental stability.

In a very comprehensive review paper Raj [44] breaks down the different sealing approaches into groups. Outlined in his own research are alloys like FeCrAlY (Fe 22% Cr, 5% Al, 0.2% Y) as a metal for sealing by brazing to YSZ. Other methods that use glasses that crystallize either during processing or during use in an SOFC stack, thereby forming a more rigid glass seal are also discussed. The author states that these seals are hermetic because they have a very small crystalline phase but require a close match of the coefficient of thermal expansion (CTE) and may be less forgiving against seal fracture under thermal transients. Self healing glass was studied by creating cracks in seal samples and then observing the healing at elevated temperatures. It was found that some of the glass seals performed quite impressively even after as many as 300 thermal cycles between room temperature and 800°C. Along with the stability, the glass seals retained their ability to self-heal even after very long exposure times of more than 3000 hours at higher temperatures.

Raj also talks about a number of more novel sealing concepts that are being investigated by groups, such as using polymers of Si–C–N to make seals to SOFC components and a novel approach of mica and mica–glass hybrid compressive seals.

In another review paper, Lessing [43] discusses some types of sealing methods. Glass-ceramics are a common type of sealing method, where compositions of glasses that are amorphous when liquefied. These glasses are liquefied by mixing glass powder with a thinner, which evaporates upon heating the seal. This allows the glass to be positioned initially in a liquid state, for example with a brush. Moreover this liquid state allows the glass to be sucked into narrow spaces via capillary action

and form fully tight seals. This allows the possibility of tight seal not otherwise achievable unless the seal is heated well above its melting point to make it extremely viscous. Extremely high temperatures that are needed for melting the glass will cause undesirable thermal expansion in stack housings and possible re-oxidation of the MT-SOFC anode. These materials are specifically designed to partially or fully crystallize and become opaque when held in a high temperature range that is below the melting/solidification temperature range. Lessing also gives an in-depth analysis of this type of sealing stating its problems.

Metal seals are also a very interesting and a plausible solution to the sealing problem for MT-SOFCs but the types of metals that are suitable are limited because of their oxidation at high temperatures or insufficient melting points. Silver is a possible solution, however based on experimental observations of Singh et al. [45] it was concluded that silver may not provide adequate long-term structural stability under a dual oxidation reduction environment. It is suggested that porosity formation in the silver seals is related to the formation of gaseous H_2O bubbles due to simultaneous diffusion of hydrogen and oxygen followed by subsequent interaction resulting in the formation of steam. Abernathy et al. [46] attached silver wire to a patterned $La_{0.8}Sr_{0.2}MnO_3$ cathode. This cathode was put into a regulated temperature and atmosphere chamber that was filled with Cr-containing vapor. Using Raman spectroscopy they found silver chromate, Ag_2CrO_4, on the surface of the silver at 500°C and at 625°C the Ag_2CrO_4 was deposited by vapourisation across the LSM surface. The evidence of this contamination means that choosing the type of metallic interconnect is a serious consideration to be made especially in MT-SOFC systems with silver components.

Tucker et al. [47] have shown that Ticusil (68.8Ag–26.7Cu–4.5Ti) even after complete oxidation could be a sealing solution. The brazed strength, sealing ability and conductivity of this material remains sufficiently high after application. This material oxidises rapidly in air above 700°C and sample Ticusil joints were exposed to fuel/air dual atmospheres. After exposure the joints remained robust and free of voids. They found, even after very rapid cycling, that no de-lamination or cracking was observed in the vicinity of the joint. This enabled 30 rapid thermal cycles of a braze-sealed metal-supported tubular cell with no loss of open circuit potential. Based on these observations they concluded that silver-based brazed alloys filled with low CTE particulates are strong candidates for use as the seal or interconnect in

SOFCs operating at 700 °C. These types of seals could be suitable for MT-SOFC stack designs because of the ease of application and dual role as a gas tight seal and current collector.

Recently Kim et al. [48] have shown the high-temperature tolerance of silver–copper oxide air braze filler metals under dual oxidizing reducing atmospheres at 800°C. Regardless of the filler metal composition or brazing temperature employed, none of the specimens that were tested for 100 h displayed any signs of hydrogen embrittlement. Specimens exposed for a longer period of time, 1000 h, did exhibit evidence of internal porosity and the extent of this was limited to less than half the width of the joint. According to Kim et al. while the issue of hydrogen embrittlement remains a concern with respect to the long-term stability of silver-based brazes under dual oxidizing/reducing environment, its development in the Ag–CuO filler metals is much slower than was previously reported in high-purity silver. This is both due to the longer diffusion path in the braze joints and the buffering effects that CuO reduction appears to afford. Kim et al. [49] have also investigated the possibility of a Ag–Al–Cu and Ag–Al brazes. However they report that while the Al improves the atmospheric tolerance it also weakens the joint strength. Lessing [43] in his review also points to the work of ceramic-composite seals being investigated by Sandia National Laboratory (USA) and NexTech Materials, (USA Ltd). According to Lessing [43] Sandia's stated composite approach is to produce a deformable seal based on using a glass above its normal glass transition point with control of the viscosity and CTE modified by using ceramic powder additives. The aim is that the composite should be rigid enough to remain in the joint, but have a low enough viscosity to slightly flow to relieve stresses and heal cracks.

Lessing [43] reports that NextTech Materials are using BaO–CaO–Al_2O_3–SiO_2 candidate glass compositions (e.g., 15 BaO 25 CaO 7.5 Al_2O_3 45 SiO_2) together with powders of mica, talc, alumina, or zirconia fibers as an additive to increase the seal viscosity.

According to Lessing [43] historically, both alumino-silicate cements and alumino-silicate cements plus glass were used during the early 1990s by various developers. High temperature cements are easily available from a variety of commercial sources. However after curing and firing, they are typically very porous and lack good wetting/bonding with metal interconnects and the ceramic surfaces

that are needed to produce hermetic seals. Therefore, in some cases, glass was added to the cement in an effort to fill the porosity and aid wetting. This combination then becomes a ‘‘glass–ceramic’’ seal, when the mixture is fired to sufficient temperature to melt the glass. Sealing cements can also be produced by combining ceramic powders (e.g., zirconia) with chemically bonded ceramics.

2.1.4 Modelling and micro tubular SOFC stack design

Producing electricity at high temperatures electrochemically has been studied by a large number of authors by modelling the coupled electrochemical and physical phenomena. Computation Fluid Dynamics (CFD) packages such as FLUENT (ANSYS, Inc. USA), CFD-ACE (ESI Group, Inc. USA) and Star-CD (CD-adapco Ltd. USA) all have their own inbuilt electrochemical models and indeed some academic groups have built their own models such as DETCHEM [50, 51] to work with FLUENT or stand alone CFD codes. While some information can be gathered by using models without the electrochemical and mass transfer of the cells, the best models will certainly contain the electrochemical and mass transfer reactions.

For example Lockett et al. [52] have used some very simple features in the FLUENT modelling package to characterise heat transfer inside arrays of MT-SOFCs in counter flow. The purpose of these simulations was to identify possible stack designs and methods for efficient stack thermal management. This paper describes a 20 cell test system and claims to be the first of its kind for modelling flow around MT-SOFCs in a stack. This was a very basic attempt to use CFD to model the flow regimes within a stack. This model neglected radiation modelling, species removal and all of the electrochemistry. With a constant heat flux of 0.5 watts on each cell it cannot be certain how the cells would work in reality because of the missing modelling variables. While the authors express that an experimental device has been built, the CFD results are not compared to any experimental values and no further publication has been produced.

While some studies such as Jasinski et al. [53] try to discover how these processes affect the cells through experimental approach, the vast majority of authors are developing models on the nano scale / molecular dynamics Lehnert [54] and Qi

et al. [55] macro scale, / fluid dynamics Tanaka et al. [56] and Bhattacharyya et al [57] and system scale / system dynamics Ivers-Tiffee et al. [58] and Xue et al. [59]. A paper by Hong [60] has shown how all the afore mentioned scales of models and their associated dynamics, can culminate into a real time simulation package for a vehicle fuel cell power plant.

Some of the fundamentals of the electrochemical processes in SOFCs are still not understood. Indeed the effects of the multi physical phenomena surrounding the electrochemical processes on a high temperature electrode have not been entirely resolved in the literature. The electrodes on either side of the electrolyte reduce the concentrations of the fuel and oxidant through red-ox reactions, producing thermal and electrical energy. The oxidant and fuel concentrations and thermal gradients surrounding MT-SOFCs and the power output of them should ideally be uniform for a cell that does not experience any other mass transfer or thermal disturbances. It is unspecified and not fully resolved in the literature to what degree the fluid, thermal, mass transfer and geometrical dynamics affect the performance of the electrodes.

An example of how models are ever evolving and giving a more accurate account for what is happening in the nano scale can be seen in the improvement in the modelling of the anode. Older studies which include models such as Lehnert et al. [54] have shown that there is a concentration gradient within the anodic electrode. It is suggested that the reaction zone size is 50 μm out stretched from the electrolyte. This layer is treated as a boundary condition and the fuel concentration through the anode appears as an exponential function. Hussain and Dincer [61] also suggested that the anode reaction zone is 50 μm but they consider the reaction zone as a volumetric continuum rather than a boundary condition and their result is more like a bi-linear function. They also show that considering the reaction zone as a boundary condition leads to over predicting the concentration over-potential at all loads.

The effect of radiation within reactors is a very interesting topic and is discussed by Vandersteen and Pharoah [62] who have shown that for both planar and tubular models that neglecting radiation effects in modelling results in overestimating the reaction rates, material properties and also the maximum theoretical voltage. Tanaka et al. [56] also concur with this statement and add that modern CFD packages are easily capable of including radiation models. However Daun et al. [63] state that due to the minor effect of thermal radiation on the

temperature field in planar SOFC cells, that thermal radiation can be excluded from a detailed CFD analyses of a planar anode supported SOFC. To the contrary Murthy and Fedorov [64] found that ignoring radiation effects caused errors of 100°C in the surrounding temperature fields.

Damm and Fedorov [65] studied radiation with a 2 dimensional model of an anode supported SOFC. This study found, in contrast to that of Daun et al. [63] that the effect of radiation accounts for a few degrees in the cell temperature field and states that heat is predominately removed from the cells by convection. The authors remark that their opposite hypothesis to that of Murthy and Fedorov [64] is because of the different SOFC geometries involved. So it can be concluded that the geometry within a MT-SOFC reactor can have a huge bearing on the radiation effects.

Qi et al. [55] modelled with finite volume methods the effects of transport dynamics of the fuel and oxidant. Their main objective was to measure how all of the macroscopic transport phenomena affect a cell's power producing performance. They only model a small 3d section of a tubular cell and apply step responses to inlet temperatures and velocities. The results include dynamics from the diffusion, inherent impedance, flow and heat exchange processes including radiation and internal shift processes. The results clearly show that fuel flow inlet pressure and temperature have large effects on the dynamic performance of a SOFC, especially with regard to its temperature response. It was also shown on the cathode side that the temperature of the incoming air has the most significant effect on SOFC solid phase temperature and performance when compared to other inlet flow properties. They report that the effect of flow velocity is not as significant as inlet pressures and temperatures. Their results also pointed out that the transient response of a SOFC was mainly controlled by the temperature dynamics. This would be a critical inadequacy of models that just apply a heat flux to the cells. For example Locket et al. [52] recommend an air inlet temperature of 400°C, which may well be correct for dummy cells outputting a constant flux, but this air temperature will have a huge affect on the thermal flux that the cells output. This is an example of why electrochemical models are a necessity when modelling a MT-SOFC stack design.

Comparisons in the literature of the co-, counter- and cross-flow methods, can only be found for big SOFC tubes and planar cells. Recknagle et al. [66] examined

the effects of these three different methods with a validated electrochemical code and combined it with CFD software.

However for the MT-SOFC, it is interesting to note that Xue et al. [59] and Lockett et al. [52] both assume a counter flow configuration. In both simulation results it seems that the counter flow operation results in lower cell structure temperatures at the inlets and outlets. This would be advantageous for the MT-SOFCs because high temperature seals are required in these positions. An area which is totally neglected in the literature is the performance of the MT-SOFCs or its larger predecessor mounted in the cross flow position. The tubular SOFC in cross flow is a very interesting research topic because of the wakes at the rear of the tubes.

The role of the flow regime between and around cells within arrays and also through them internally is a very important consideration in a MT-SOFC stack design. This issue has been addressed to some degree by several authors. For example recently Fazil-Serincan et al. [41] have investigated the steady state behaviour of a MT-SOFC inside an oven in a very comprehensive and enlightening 2D model.

The fuel modelled in this paper is a mix of 25% H_2 in N_2 having a flow rate of 100 mℓ min^{-1}. The temperature of the fuel in the anode rose by about 110°C between OCV and 0.2V. Such a temperature response should affect the system response. Also they found temperature gradient field ranges of 18 and 40°C on the cathode and anode sides. In their model the electrolyte temperature is slightly higher than the electrodes, ranging from 0.1°C at OCV to 0.9°C at 0.2V. This is probably because of the reactions taking place in that vicinity. Fuel mixtures of H_2 and N_2 are not expected to have dramatic effects on the temperature distribution across a cell, even with different ratios of each because of their similar molar (volumetric) heat removing capacities. However the use of hydrocarbon fuels flowing inside the anode containing extra un-reacted mass should be an issue to be considered for the temperature profile across a cell.

Making a MT-SOFC stack that is thermally self sustaining is a very important characteristic to have for high system efficiency. A critical consideration is how close should the tubes be stacked together and what are the effects on the flow regimes and heat transfer through bundles of cells? In an attempt to answer this question Lawlor et al. [67, 68] performed a numerical analysis on high temperature

flows through an array of cylinders. It was found that for a particular arrangement of MT-SOFCs exposed to flow rates expected inside a reactor that buoyant flows could be an issue for extremely low flow rates. However these effects could be negated by forced oxidant flows over a single mm sec^{-1} through this array of cells.

Chouikh et al. [69, 70] studied the spacing distances between cylinders and the effects of heat transfer by natural convection. They concluded that the distances between the cylinders are paramount to the heat transfer and flow regimes of heated cylinders causing natural convection. Even though there are no detailed models in the literature on this topic Suzuki et al. [71] made manifold design and stack housing system which did not have a forced flow of oxidant between the cells. This reactor was placed inside an oven for the tests and natural convection and/or diffusion of oxygen from the surroundings must have been the oxidant refresher to the cathodes. From visual observations of the images of the cell stacking it in the paper, similar to Figure 11, it seems that these cells are very close together, which is interesting with regard to the refreshing of oxygen to the cells.

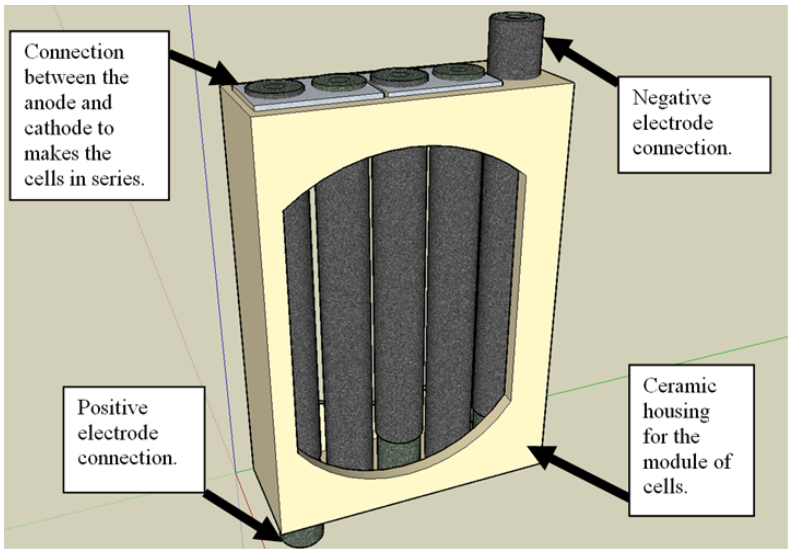

Figure 11: Author's depiction of a single module in a multi module system used by Suzuki et al .[71].

The range of literature for flow around arrays of cylinders is wide and varied but none of it deals specifically with high temperature, laminar flow, around arrays

of cylinders wrapped with wires, with electrical contacts, being affected by mass transfer.

2.1.5 Electrical connection and efficient power extraction from stacks

Current collection from the MT-SOFCs is critical for achieving high power densities from the cells and high fuel efficiency. There are many variables that effect the collection of current from the cells including, contact resistance, temperature, amount of current in the contact wires, means of connecting cells together (parallel or serial), choice of materials and geometry and scale of the cells. Most groups generally use a winding of silver around the cathode and nickel meshes or wires as the means of connection to the anode. These materials have high melting points, resistance to oxidation and corrosion and high electrical conductivity. To reduce the contact resistance on the cathode side, silver paste is normally used as a transition between the silver wire wrappings on the cathode and the cathode itself. Indeed Serincan et al. [72] have performed some numerical simulations where coating the entire cathode surface with silver was suggested as a viable current collector for MT-SOFCs.

The crucial question is, are there mass transport limitations when a layer of silver is coated over a whole cell? To find this out the silver coating on the cathode was given different porosities using a simple model which incorporates mass, momentum and charge balances as well as the species transport. The results suggest that for a broad range of porosity values, mass transport losses are negligible due to the small scale of the fuel cell. They also compared this design with a more common type of current collector arrangement with silver paste on the cathode that utilizes several pasted strands of silver, length ways along the cathode as seen in Figure 10.

In this case the potential losses were found to be negligible for the same reason related to the small scales of the system. A non-uniform current density distribution inside the cathode was predicted by the model, which would lead to a non-uniform reaction rate and temperature distribution along the cathode.

The authors conclude that such a non-uniform temperature distribution maybe severe enough to cause mechanical failures such as warping and distortion of the

cathode and the separation of the silver paste from the cathode. However there is no experimental data to back this up. Table 3 presents a summary of the different methods of electrical connections used by the main groups in the field.

Table 3: Comparison of the type of electrical connections used by MT-SOFC development groups.

Name of Group	**Cathode Connection.**	**Anode Connection.**	**Connection profile and architecture.**
Adelan (GBR)	Silver wire wrapped around the cells	Internal wire-mesh contact to the anode.	Modules containing cells in parallel
AIST (JPN)	a. Silver wire wrapped around the cells b. Cells impressed in cubic cathode matrix	Connection to one end of the anode.	a. Modules with serially connected cells connected in parallel. b. Parallel or serial connection of all cells within the module.
Alberta Research Coun. (CAN)	Gold or silver layers applied by a sintering technique.	Gold or silver layers applied by a sintering technique	Modules with cells, connected in parallel connected in series.
Korea Inst. of Tech.(KOR)	Silver wires wrapped around the cells	Capillary pipe provides fuel and current collection.	Parallel.
Nano-dynamics (USA)	N/A	N/A	N/A

TOTO (JPN)	N/A	N/A	N/A
Univ. Connecticut (USA)	Brazed seal at one end of the cell which also collects the current.	Brazed seal at the other end of the cell which also collects the current.	Serially connected cell modules connected in serial or parallel thereafter.
Upper Austria Univ. App. Sci. (AUT)	Silver wire wrapped around the cells	Internal wire contact to the anode	Several methods under test

Connecting the cells in parallel or series has advantages and disadvantages. When cells are connected in series the voltage is increased incrementally, while the current is limited by the worst performing cell. However a break in the connection, for example by a damaged cell or broken wire, leads to a failure of current collection among all the cells in serial connection. Connecting the cells in parallel of course will not cause all the cells to stop providing current if one malfunctions unless there is an electrical shortcut. In this case the current rather than the voltage increments up. This is un-desirable because of the associated wires losses. A combination of both serial and parallel connections should be used to extract the current from the reactor. Current collection is an area in the literature which has not received any meaningful attention with regard to what combinations work best. Some authors [16, 27, 71] have presented the cells connected in series within smaller modules and then these modules are connected in parallel to make larger stacks. The other approach is to connect modules of cells initially in parallel and then in series or parallel. Initially the AIST (Japan) Inc. group connected their cells in parallel [37] but recently they have invented a serial approach [25] which they hope to use to increase the power production of their stack modules by reducing the losses through resistance.

Of course the numbers of cells in the modules will be determined by the size of the stack, but there should be a balance between, efficiency, costs and probability of a cell becoming defective to decipher the most optimised stack electrical configuration.

For example if every cell is connected individually to external power conditioning hardware a lot of wires will be needed, thus increasing the total system cost. If all the cells are just connected in series to build up a high voltage, then the amount of wiring is reduced but the probability of a cell failure causing the failure of the system or a part failure is increased. This is an area which deserves addressing and is essential for the cost of these systems vs. reliability. Keeping the electrical wires and contacts out of the hot zones or at least as short as possible in them is advantageous because in these hot zones the wires will have higher resistances and also sufferer degradation faster. So an appropriate geometry design with consideration for the electrical current collection should also improve the system efficiency and reliability. The attempt by several groups to reduce the operating temperature of the MT-SOFCs should also reduce the electrical losses.

The power coming from a MT-SOFC reactor will have to be conditioned through the use of an inverter unit, especially if it is used as an auxiliary power pack or for an electric motor. The inverter should be compact and highly efficient. Since driving an Electric Vehicle (EV) motor requires a large current, the heat generated by the power module in the inverter, has been a problem impeding the achievement of compactness and high efficiency. The transistor switching losses increase and Free Wheel Diode (FWD) reverse recovery losses increase linearly with the switching frequency while the total loss increases quadratically as the current increases. In other words, a higher switching frequency and current both induce more power module loss and heat generation and this reduces the efficiency of the system.

To cope with this heat generation requirement a larger power module and a cooling system is required, which is also undesirable. Attempting to suppress the current would compromise the performance. Isolated Gate Bi-polar Transistor switching (IGBT) technology is used for breakdown voltages above 1000V, while the Metal Oxide Semiconductor Field Effect Transistor (MOSFET) is used for device breakdown voltages below 250V. Between 250 and 1000V, there are many technical papers available from manufacturers of these devices, some preferring MOSFETs and some IGBTs. However, choosing between IGBTs and MOSFETs is very application-specific and cost, size, speed and thermal requirements should all be considered. To optimise the total system conversion chain, the output voltage and current of the MT-SOFC stack, which will be determined by the parallel and serial arrangement of the cells within the stack, should be also considered.

Also to be considered is the costs. The size of the components involved in the power inverter depends on the output frequency and current. As the frequency is reduced the size of the capacitance and inductive components must be increased to store larger amounts of power between charge and discharging. It is also desirable to keep the frequencies above 20 KHz so that the switching is not audible. Increasing the voltage would seem to be the solution but then undesirable ripple voltages occur and wire insulation can become an issue.

2.1.6 Stack Design Conclusions

This section of Chapter 2 has discussed the topics of MT-SOFC stack design and application. In the process a broad range of scientific disciplines, including materials sciences, chemistry, thermo-fluid engineering and mechanical engineering and of course electro-chemistry have been included. Scientific and engineering content has been discussed in the areas of the optimisation of the cell performances within reactors, sealing within reactors, rector design and a review of some of the modelling taking place, which can be applied to MT-SOFC stack design.

In Appendix II a study of the range of literature associated with MT-SOFCs can be found. In this Appendix the methodology used to find group the literature is described. Also the status of research areas within the field such as cell design, stack design, sealing etc. has also been analysed. The findings show that the compared to the large SOFCs the MT-SOFC field has not been so widely researched. However interest in the field is growing slightly year after year even though only a tiny fraction of total SOFC research is MT-SOFC specific. Also literature related to critical key areas within the MT-SOFC field have scarcely been published. For example MT-SOFC specific sealing, control systems and interconnects have scarcely been publicised. Regions of MT-SOFC research are pinpointed via published literature to mainly Japan, USA and Korea with several EU nations also publishing significant quantities of literature in the field.

An important conclusion of this literature review section is that while there are some products on the market using MT-SOFCs, their potential as power producing devices for a whole range of applications has yet to fulfil its potential.

With so many technological advances possible and the diverse range of scientists and companies researching in the field it is highly possible that this type of SOFC may have a bright future as more efficient power generating mechanisms become in demand. But also this form of SOFC could turn out to be extremely profitable, when alternative inexpensive methods of producing APU and vehicle power are required, because of the relatively small scientific community and industrial partners advancing it.

However to reach this goal it is suggested that targeted research is required in the area of sealing, manifold design and optimisation of the fuel and oxidant flow regimes. A key area that has not received quality research is the electrical connection regimes. For example should these cells be connected in parallel or series or which combinations of these is most effective in reducing power losses while also reducing the effect of a single cell failure on the whole stack. While the reduction of the operating temperature of these cells offers the advantages of less thermal stresses and a wider range of materials suitable for sealing, frame material and electrical connections. However lower operating temperatures negates the internal reforming attribute of the MT-SOFC and reduces the system efficiency when hydrocarbon fuels are to be used. High temperature operation of MT-SOFC stacks that run on hydrocarbons should certainly not be forgotten amidst the recent trend of lower temperature stacks.

2.2 Part II: Review of flow around a cylinder for Reynolds numbers between 0 and 40

2.2.1 Description of the flow around a cylinder

The distributed flow around a cylinder has been divided into 4 regions with regard to flow around a cylinder as outlined by Zdravkovich [73] and shown in Figure 12.

The four regions are detailed as follows:

i. A narrow region of retarded flow in the oncoming flow.
ii. Two boundary regions attached to the surface of the cylinder.
iii. Two side wise regions of sidewise and accelerated flow.
iv. The downstream region behind the cylinder called the wake.

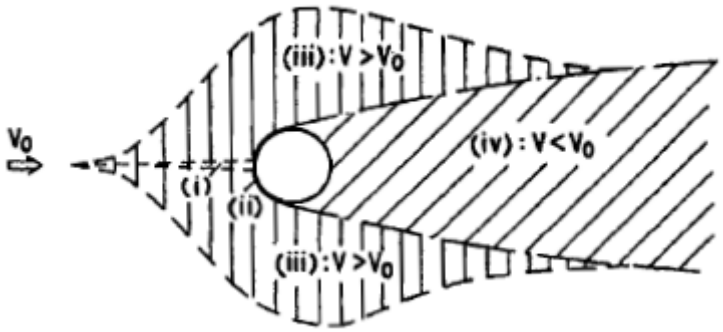

Figure 12 Regions of flow around a cylinder in cross flow.

2.2.2 Some points on the different methods used for visualizations

As it was thought that visualisation of flow regimes within bundles of MT-SOFCs may need to be visualised for CFD validation the following section was researched in order to acquire some techniques for the visualisation. All of the methods researched seem to rely on the addition of foreign matter (granulates, smokes or dies) into the flow stream. There are four methods briefly outlined below. Examples of the techniques outlined below by A. Shapiro may be seen in video format at [74].

1. **Streamlines:** Video recording can be used during a short time span to monitor the path of individual particles that are randomly spread within the test fluid. Arrays of streaks are obtained that represent the velocity vector field. By visual or numerical integration the streamline pattern at a given time can be translated to this velocity vector. The particles introduced into the flow stream are normally solid, liquid or gaseous (hydrogen/oxygen bubbles produced by electrolysis).

2. **Streaklines:** Involve the continuous release of foreign substances into the flow from the cylinder wall or injectors placed in specific locations within the stream. This method results in streak-line patterns.

3. **Time lines**: Making visible a continuous line of the flowing fluid particles, by instantaneous production of a line of smoke or hydrogen bubbles from a wire. Another method for this case includes a luminescent dye or photochemical process like photo-chromism. The results of these methods give time lines. Photo-chromism is the reversible introversion of a chemical species between two states with different absorption spectra. This change is usually brought about by absorption of light. Thus by taking pictures at regular intervals, how they distort may be seen after defined periods of time. The velocity profiles can be deduced either around the obstacle or in any section of the flow.

4. **Path-lines**: The Path-line method is the recording of the path of single particles with long time exposures. This method gives the path line of the particles but is unsuitable for unsteady flows.

Shaporo [74] states that the streamline method is the most regularly used and that all the methods give identical results when the regime is steady state with Reynolds numbers below 40. When the Reynolds number is increased beyond this for the flow regime the different methods give varying results and the Particle Image Velocimetry (PIV) has been used by many authors to study turbulent flow regimes.

2.2.3 The Reynolds number and disturbances

The Reynolds Number "Re", which represents the ratio of inertial to viscous forces, is really the only governing parameter for undisturbed flow around a cylinder. It is also used to estimate the flow regime within a pipe and is a dimensionless number.

$$\mathrm{Re}.d = \frac{\rho * V.mean * di}{\mu.air} \qquad (2\text{-}2\text{-}1)$$

The Reynolds number while is generally accepted as the standard unit to define flow regimes within certain values the conditions of the fluid flow must be adequately observed. This is the case because there is a succession of transitions from laminar to turbulent flow within in the distributed flow and these transitions are sensitive to even very small disturbances [73]. These disturbances can initiate transitions at lower Reynolds numbers that indicate separation from a cylinder wall, "Re_s", than expected and also can significantly modify the resulting flow patterns. These disturbing parameters are also known as influencing parameters with the Re being the governing parameter. But these influencing parameters such as, turbulence, surface roughness, wall blockage, wall proximity, end effects and oscillations, can indeed become the governing parameters in some transition states when they surpass a certain magnitude. This adds a whole range of possible inconsistencies and so detailed experimental parameter data can be very necessary.

Free stream turbulence is generally considered as being the most common form of disturbance. Surface roughness, K/D, (roughness factor/diameter) the effect of wall blockage G/D, (width of walls/diameter) the effect of the walls above and below the cylinder L/D (length/diameter) and the stream wise oscillations are also very prevalent disturbances. It is obvious then that experiments need to be designed and described with the, afore mentioned disturbances accounted for. The effect of boundary walls on the onset of vortex shedding is discussed in more detail in the experimental section 4.4.

2.2.4 Introduction to the laminar flow regime

Zdrakovich [73] divides the laminar flow state with regard to flow around a cylinder into three basic flow regimes and these will be explicitly explained in the following sections.

Creeping flow. $0 < Re < 4\text{-}5$

Closed near wake regime. $4\text{-}5 < Re < 30\text{-}48$

Periodic laminar regime. $30\text{-}48 < Re < 180\text{-}200$

From some initial calculations using the Reynolds number and molar content of air it is expected that single cells will definitely be in the creeping flow regime while large bundles of cells experience the closed near wake regime, see 6.3.7 The periodic laminar regime is not expected to be seen in MT-SOFC bundles but is of academic interest with regard to mass transfer as outlined in section 2.3.

2.2.5 Reynolds number below 0.1

In cases where the Reynolds number is very low, for example under 0.1, the inertial effects are insignificant and consequently vorticity should be dominant. In such a case as seen below Figure 13 the flow fits exactly the shape of the cylinder perimeter. The effect of these kinds of flow regimes on the availability of oxygen to the cathode of a MT-SOFC is an interesting parameter that should be addressed.

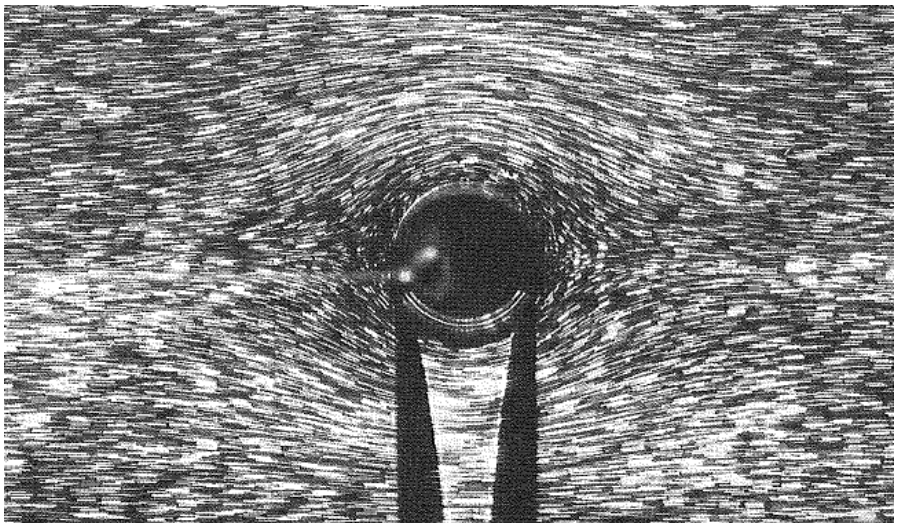

Figure 13: Visualization of the flow regime around a cylinder at Re >0.1 [75].

2.2.6 Reynolds numbers between 0.1 and 4.5

Countaceau and Defaye [76] refer to flows past a cylinder in cross flow between a Re of 0.1 and 4.5 as "Fore-aft asymmetrical flow without separation". When Re increases, the vorticity convection increases compared with diffusion. However up to Re equal to 4.5 the surrounding streamlines outline a cylinder perimeter. In the downstream part, behind the cylinder, they sequentially move away from the axis as the Re increases showing a reduced velocity in the downstream fluid.

Zdravkovich [73] calls this creeping flow and states that there is a trail of steady and symmetric laminar shear layers. A separation of the oncoming flow occurs at Re_s between 4 and 5. This separation induces the formation of a steady symmetric and closed wake behind the cylinder. While the creeping phase exists, all the distributed regions remain laminar due to the fact that viscous forces are

dominant. The size of the retarded region of flow is about 20 times the cylinder diameter wide and 8 times the cylinder diameter in front and behind the cylinder. This is an important rule of thumb to be remembered for the simulation stages of this work. There is not a massive increase or decrease of velocities around the cylinder because there is a pushing and dragging of the shear layers and these two actions produce a large resistance force. White [77] recommends that even in a container with the side walls spaced 500 times the diameter of the cylinder under test the walls still affected the flow at such low Re_s. The effect of enclosure walls close to the cylinder tend to squeeze the flow between the cylinder and these walls and thus accelerate the flow such that it is greater than the free stream velocity. This should be an important consideration when designing any wind tunnels.

At low Re_s, such as those that MT-SOFCs should be subjected to, the velocity field around a cylinder is connected to a characteristic pressure distribution around the circumference of the cylinder. Cp is the mean pressure and it is a non dimensional number.

$$Cp = \frac{P - P\infty}{0.5 \times \rho \times V^2} \qquad (2\text{-}2\text{-}2)$$

Where

p is the local static pressure.

p∞ is the free stream static pressure.

½ pV² is the free stream dynamic pressure.

At the frontal stagnation position Cp_0, the pressure stagnation coefficient, is expected to be 1 with regard to the in-viscid Bernouldi equation. However from the experimental work of others [78] an improved approximation has been suggested because the Cp_0 value is always greater than 1:

$$Cp_0 = 1 + \frac{6}{\mathrm{Re}_p} \qquad (2\text{-}2\text{-}3)$$

Where Re_p is based on the Pitot-tube diameter.

Zdravkovich [73] compared the results of Thom [79], Underwood [80] and Homann [81] in Figure 14 below. There was a good agreement between the results of Thom [79] and Homann [81]. These results show a favourable pressure gradient extends up to 115° at a Re of 3.5 followed by a small pressure gradient that is that is too small to induce a separation. The curve from Underwood's results [80] are from computations. Another term worth noting is the resistance coefficient, which represents the ratio of the resistance and viscous forces while the drag coefficient is the ratio of the drag and inertial forces.

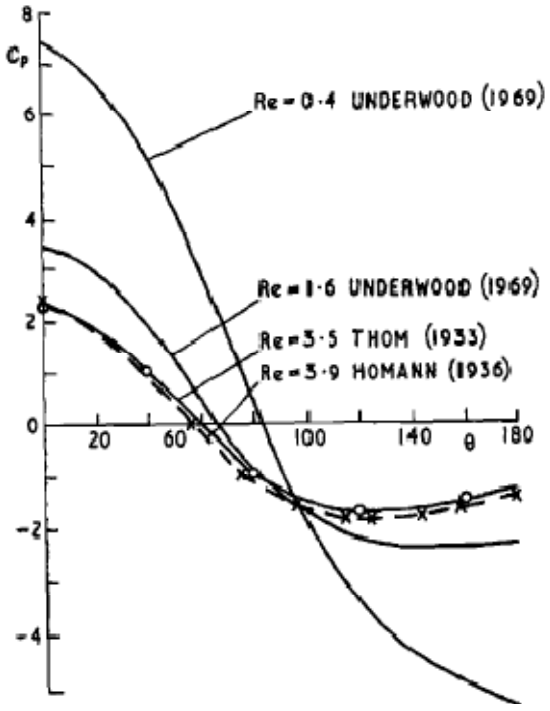

Figure 14: Pressure distribution in creeping flow [73]

2.2.7 Reynolds number between 4 and 5

As the Re increases from 0.1 up to about 4.5 the vorticity conversion increases compared with diffusion. However as the flow continues downstream, as seen in Figure 15, the streak lines tend to progressively move off from the axis as the Re increases showing a reduced speed of the downstream fluid compared with the upstream part[73].

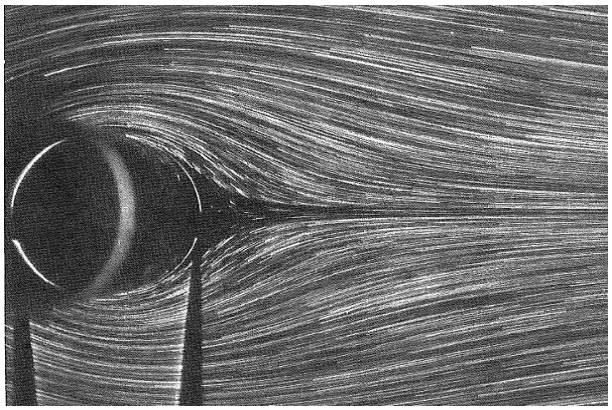

Figure 15: Photograph of the cylinder in cross-flow take another Re of five [76]

The magnitude of viscous forces decreases with increasing Re until at Re_s, separation of the boundary layers occurs. It can be very hard to state exactly when this separation occurs because the size of the near wake is small and separation occurs at a region where the velocity is also small. The following table from Zadrakovich [73] lists the estimated Re for the separation to occur.

Table 4 Estimated Reynolds number for the separation to occur[73].

Author	D/B	Re_s
Nisi and Porter [82]	0.015	4.3
Homann [81]	0.067	6.0
Taneda [83]	0.01	5-6
Coutanceau and Bouard [84]	0.012	9.6
	0.07	7.2
	0.02	4.4

The separation is strongly influenced by the blockage that the flow sees as it passes the cylinder. It has been found that the separation point varies quite a lot at lower Re_s. For example in the range of 6> Re >20 the variation is 15° while for 20 > Re > 40 the variation is only 5°. This would mean that at high Re_s the near wake widening is negligible when compared with its elongation. A noticeable change in the pressure distribution can be seen because of a steady separated region confined in a closed and symmetric near wake.

A point called the inflection point occurs because the adverse pressure gradient must be relieved by separation. When the Re increases so also does the Cp minimum value. This causes the separation point to move towards the shoulder of the cylinder and indeed up stream[73]. Countaceau and Defaye [76] state that if dye is released into the wake behind the cylinder it will remain there for a Re up to roughly 35 meaning that there influx of the bulk flow into the wake should be low. This is a very interesting observation and leads to the question how does this affect the mass transfer to the rear of the MT-SOFC and cross-flow?

2.2.8 Reynolds number from 5 up to 35

Because of an unfavourable pressure gradient caused by the deceleration of the near downstream fluid, a backward flow is induced that deflects the oncoming stream and removes it from the cylinder wall. As the Re is increased the separation points are located up stream along the cylinder wall away from the rear stagnation point. Two separated shear layers meet at an increasing distance from the cylinder on the downstream axis, enclosing a rotating bubble that grows in size related to the Re, see Figure 16. There is a tail leading off from behind these eddies and this is the prolongation of the double layer. The length of the bubble behind the cylinder increases linearly with the Re, whereas the width of the bubble tends to evolve at $Re^{1/2}$, Countaceau and Defaye. [76]. Figure 17 shows the development of the wake during the phases from where the eddies form and are symmetric until they become non symmetrical and unstable

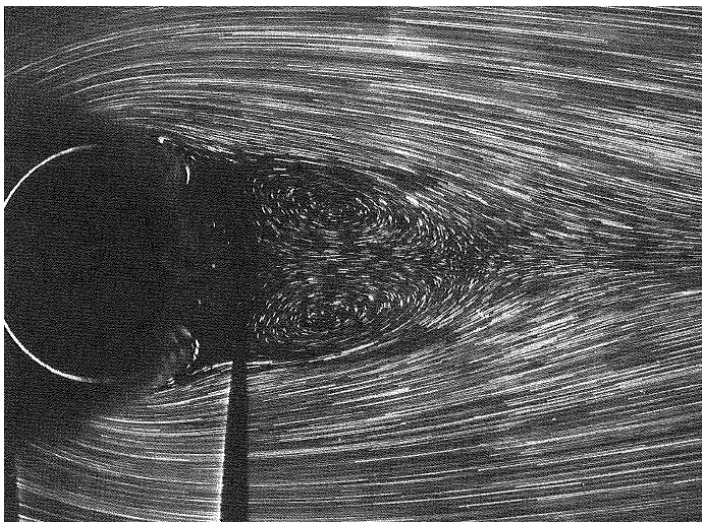

Figure 16:ymmetric eddies photographed under Re of 24 [84]

.

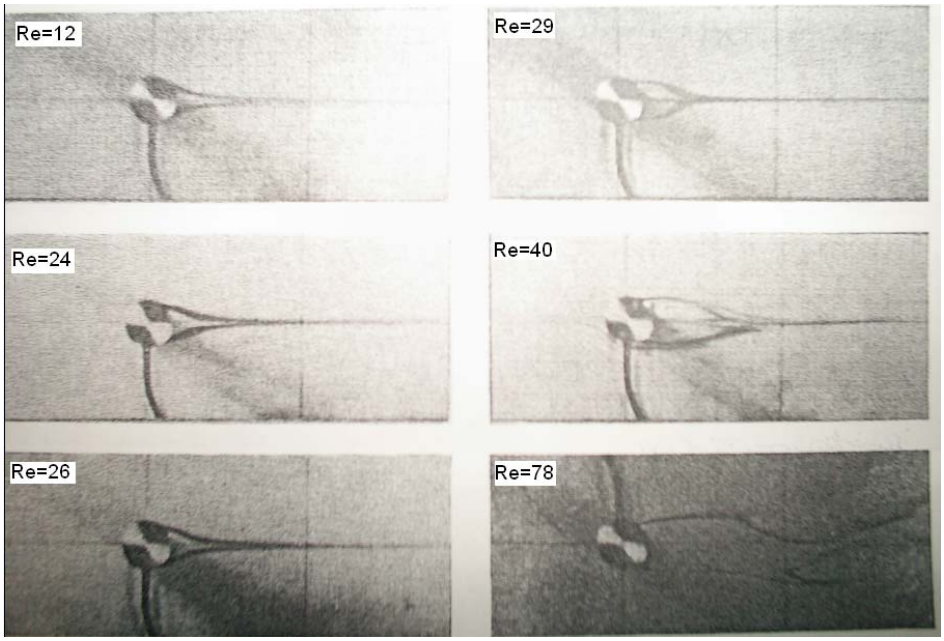

Figure 17:For 12 < Re < 78 plot of the flow stream around the cylinder for Res 12 to 78 [79]

Camichel [85] photographed a set of metamorphosis of the near wake from values of 20 < Re < 40 as seen in Figure 18. This is the example used by Zdravkovich [73] where he explains the pictures as follows; 1,2 and 3 being the elongation and pictures 4 and 5 being the obliteration of the initially closed near wake. It is suggested that a new wake is made by the secondary separations of the

free shear layers as shown in 4, 5 and 6 from the near wake illustrated in Figure 18. This new wake is then gradually filled with dye as the shear layers gradually approach each other and merge as seen in 9 of Figure 18.

In the figures below by Camichel [85] clearly show a metamorphosis of the near wake behind a cylinder, it is not stated in the book of Zdravkovich [73] but this metamorphosis maybe for a sudden increase of velocity from Re 20 to 40. This may support his statement that the metamorphosis proves that the intensity of the eddies must be quite weak because if they were strong then they should not show much deformation and indeed certainly not obliteration. This must be the case because there is a plot [73] depicting how the cores of the wakes move from Re 5 to 40.

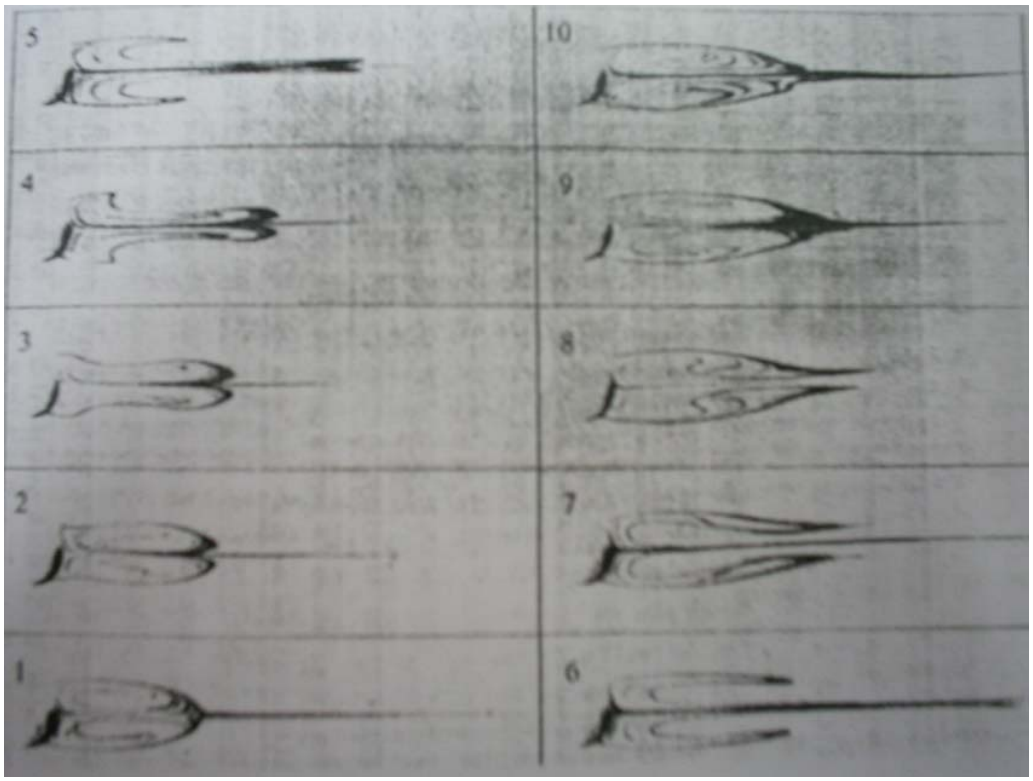

Figure 18: Development of the wake between a Re of 20 and 40 [85].

MT-SOFCs are not expected to see flow regimes in this range. However these interesting flow patterns may have some effect on the mass transfer to a cylinder in cross-flow and to measure these effects, the MT-SOFC maybe applicable.

2.2.9 Reynolds number from about 35 up to 60

As the Re becomes greater than 35 the width of the recirculation zone is about half the cylinder diameter and its length approaches twice the diameter. The centres of the two standing eddies begin to shift a little causing a very slight asymmetry of this bubble [76]. Further down the stream of the wake, it becomes wavy and thus the tail behind the wake now undulates in adherence approximately with time and stream wise distance [84]. This undulation can be seen initially far away from the eddies and comes closer to them with an increasing amplitude as the Re increases. This wave has been suggested to be caused by a convective type instability by Triantafyllou et al. [86]. In this analysis however the visualised spikes on the bubble boundary are not taken into consideration and the effects of this in the wake are also not considered

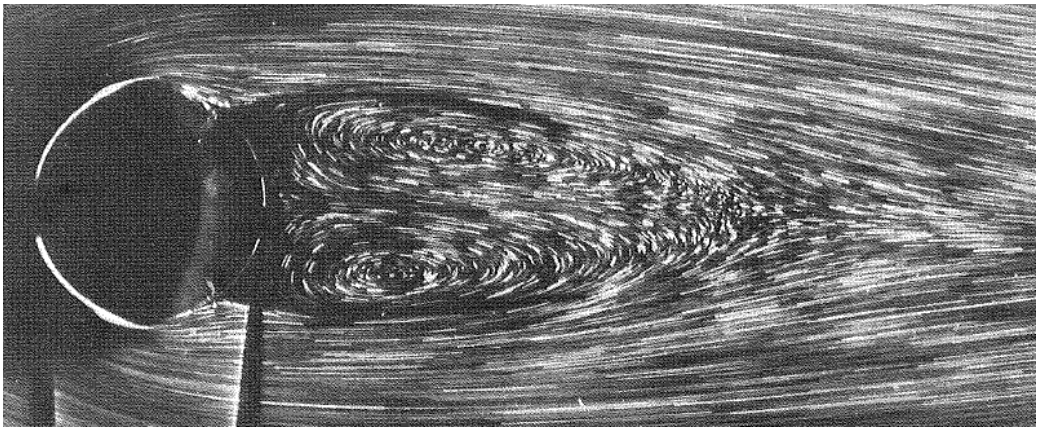

Figure 19: A picture showing the onset of bubble asymmetry at a Re of 40 [84]

Numerical integration of the Navier Stokes equations produces stable flows for flows without an artificial disturbance introduction [87]. Another important point with this regime is that it corresponds to the beginning of mass transfer into the bubble. Zdravkovich [73] shows pictures from Fague [88], Camichel [85] and Teissie Sodier [89] that a spiralling motion in the near wake at Re = 38. This motion is due to an inward flow of particles from the ends of the cylinder towards the centre of the cylinder. From a Re of about 35, although the width of the re-circulating zone is about the same size as the cylinder diameter and its length is roughly twice its diameter, the centres of the eddies begin to shift a little causing a slight asymmetry of

the wake dimensions. Camichel [85], Tom [79], Taneda [83] and Gerrard [90] all visualised this similar to that shown in Figure 20 below.

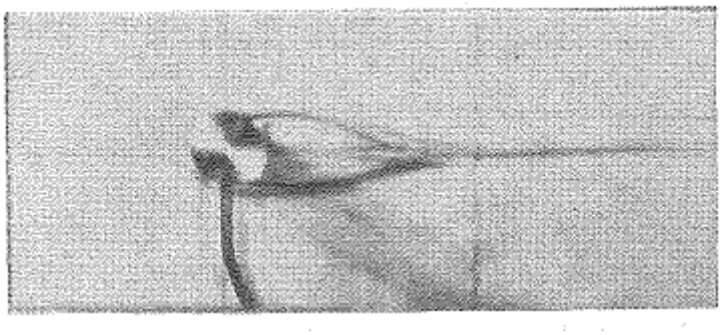

Figure 20: Figure showing the asymmetry in the wake [85],

Countaceau and Defaye [76] state that when dye is released from the wall, ahead of the separation points, initial irregularities or spiked points can be seen on the wake boundary. Taneda [83] called these "gathers" and they first appear at the downstream end of the near wake border line then move towards the rear end of the near wake and then tremble there for a while and die away. Before these gatherers form, the tail of the wake tends to oscillate in a sinusoidal manner. Gerrard, [90] gave a theory to the contrary stating that the periodic gathering of the gathers resulted in the wavy tail.

Also Countaceau and Defaye [76] state that this regime corresponds to the beginning of mass transfer into the bubble. They claim that if a die is realised into the wake behind the cylinder it will not all remain entirely within the two eddies and then the die seeps and is shed into the wake. The double eddy boundary is slightly opened at its downstream extremity. This is noticeable by the "z" notch which can be seen in Re = 40, as seen in Figure 20. Obviously then mass must enter the bubble from the oncoming flow. This is stated as being because while one of the eddies is still completely attached to the cylinder wall by two half saddle points, the second is slightly shifted downstream and is slightly detached from the cylinder wall. Thus a trickle of fluid from the up-stream flow runs between the cylinder wall and this eddy and on then between the two circling eddies and is ejected from the rear of the wake.

The transition from laminar to fully turbulent flow past a cylinder can be separated by three distinct transitional states, which take place one after the other in the different disturbed regions. In the first transition, stated by Roshko [91], the wake behind the cylinder transforms from a laminar to turbulent state by becoming turbulent “down-stream” in the wake and gradually creeping up along the wake until it is fully turbulent. This turbulence remains in the wake and on either side of it the shear layers remain laminar. The second transition occurs in the free shear layers. After a certain Re, as the velocity is increased the transition region moves along the free shear layers. This has an effect on the length and width of the near wake also causing the separation point from the cylinder to move further to the rear of the cylinder.

In this transition phase there is a sudden decrease in the drag force and this is related to the transition in the boundary layers around the separation. This transition in the boundary layers begins as stated at the rear separation points and then moves forward towards the front stagnation point with increasing Re. At a point all the regions will be fully turbulent when the stagnation point is reached. The effect of disturbances on these three transitional regimes can be that, when they become the governing parameters, the flows may become displaced, obliterated and even some times new flow regimes can be created [85] as seen in Figure 21.

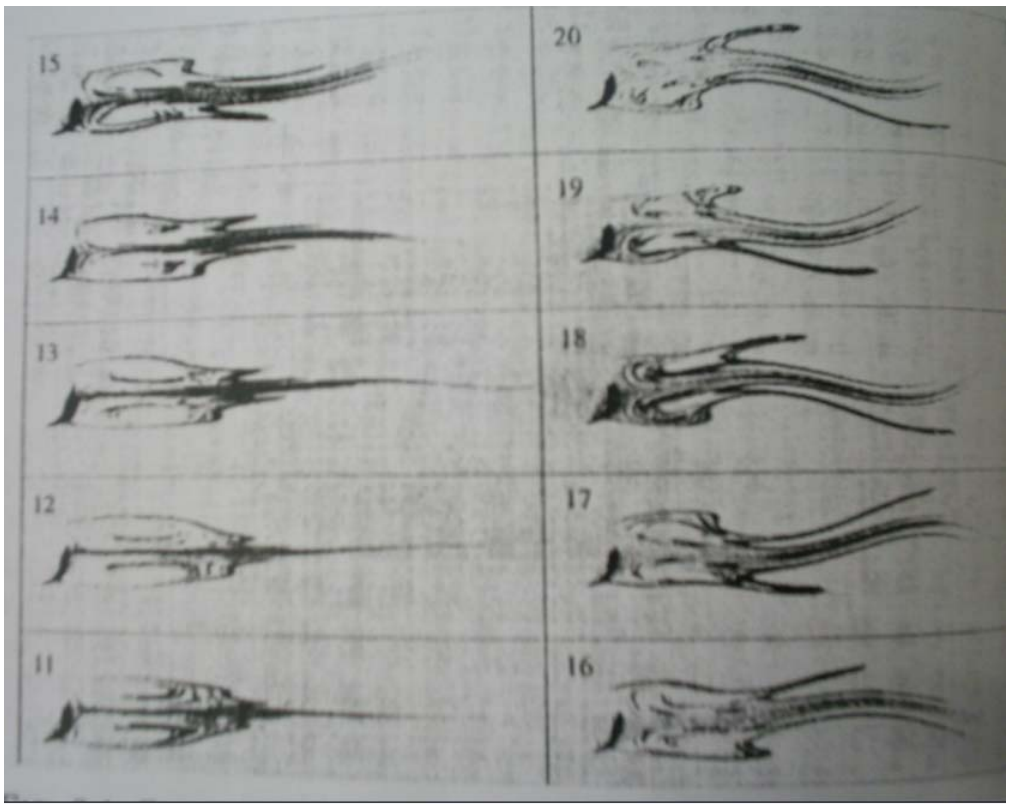

Figure 21: Visualization of the development of the wake from 30<Re<60 [85]

An interesting effect on the onset of the oscillations in the wake of a cylinder in cross flow is the effect of flow containment walls near the cylinder under test. In summery the nearer the top and bottom walls are to the cylinder under test the higher the $Re_{s.}$ Gerrard [92] states, for example the critical value for the first appearance of the naturally occurring oscillations in the wake is dramatically increased by the walls of the wind tunnel and gives an example from Shair [93] that the onset of these oscillations can be withheld up until a Re of 135 by a confinement of up to 20%. Also, with these confinements, if the wall distance from an asymmetric wake is varied a bifurcation point can be seen. This would be absent without interference from the side walls. Gerrard [92] also mentions the difference between a stationary cylinder in a wind tunnel and a towed cylinder in the fluid. He mentions that in the towed method generally causes the onset of vortex shedding to occur at Re_s of 35 due to non constant velocities.

2.2.10 Reynolds numbers higher than 60.

. The pictures shown in Figure 22 show how the oscillations described in the previous section develop for Reynolds numbers higher than 60. The effect of mass transfer in the wakes of cylinders in such regimes should be very interesting. The Von Karman vortex street is a well studied phenomena in the fluid dynamics field but is not of interest in the SOFC field because of the high velocities required to produce this effect.

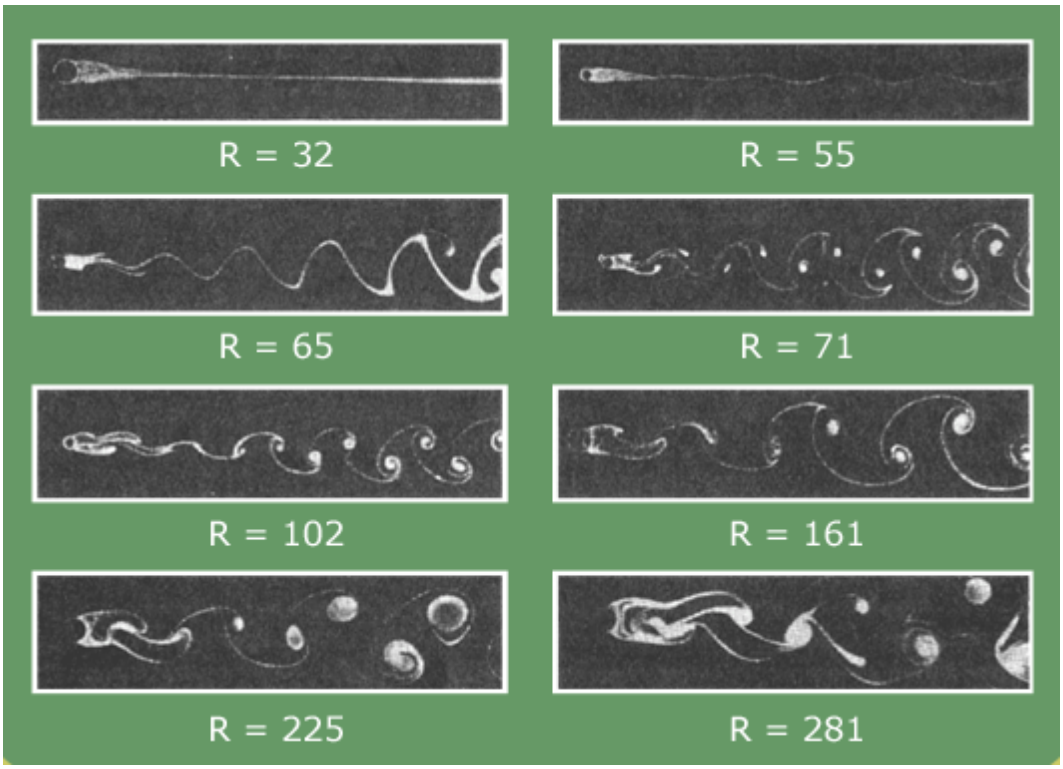

Figure 22: Vortex shedding behind a cylinder in cross flow where R= Re [94]

2.3 Part III: Mass transfer to a cylinder in cross flow

Knowing about the flow regimes within a bundle of MT-SOFC tubes could help in predicting where the diffusion limited losses may occur and more importantly how to maximise the usage of oxygen in the reactor while removing heat where necessary. While researching the literature using the Compendex data base it was found that there is very little literature dealing specifically with mass transfer to electrochemical cylindrical electrodes in cross flow.

The only paper found that seemed to be relevant enough to the MT-SOFC in cross flow was Newmann [95] who provides a correlation for the mass transfer Nusselt number (Sherwood number) for a cylinder in cross flow with high Schmidt numbers. The Schmidt number in a MT-SOFC reactor should be in the order of 0.65 to 0.8 [96] and thus the correlation in this paper is not relevant. However some other interesting papers were found even though it is difficult to assess their merit to the present study at this early stage without relevant literature for the MT-SOFC in cross flow.

A very interesting paper by Sedahmed and Nirdosh [97] investigates the behaviour of mass transfer to an array of vertical copper electrode cylinders immersed in a solution of $CuSO_4$. This paper investigates the effects of natural convection that is induced by the concentration difference caused by the mass transfer to the electrodes in the $CuSO_4$ solution. A copper anode and copper cylindrical cathodes were used and even though the Sherwood numbers are much higher than those on the cathode side of a MT-SOFC bundle, the authors point out some interesting findings through the analysis of their results.

They found [97] that the total mass transfer within a reactor depended upon the diameter of the electrodes and the number of electrodes in the reactor. One would presume however that the greater the number of electrodes the higher the rate of mass transfer but to the contrariety the authors found that when increasing the number of electrodes from a single to many the mass transfer coefficient initially reduced to below that of a single cylinder and then changed when the number of cylinders was increased enough. This initial drop in performance, which can cause a 31.5 % loss in performance, is attributed to the dominance of the reduced concentration effect. When enough cylinders are added the natural convective flows induced the velocity of the solution flowing towards the electrodes to increases and this enhances the mass transfer. This is something that one would not expect to see in a MT-SOFC reactor because of the lower Sherwood numbers. The authors point out that with a cylinder spacing of 9/8 electrode diameter a total of 6 cylinders would be required to produce mass transfer coefficients higher than that of a single cylinder.

Cordiner et al. [98] have already shown that reducing the spacing between MT-SOFCs can dramatically increase the mass transfer coefficient. With MT-SOFCS another factor must be considered. High performing cells generate a lot of heat and the cell wall temperatures should not exceed the melting point of the cathode current collectors (e.g. 961°C for silver). These wires when carrying high current will also have substantial undesirable ohmic losses.

What may be very relevant however in the findings of Sedahmed and Nirdosh [97] is that in their case closer spaced cylinders have a lower mass transfer coefficient than arrays with cylinders spaced wider apart. However the fact that closer spaced cylinders will have a higher volumetric mass transfer coefficient means that there is an optimum balance between overall mass transfer coefficient and volumetric mass transfer coefficient to be resolved for optimised array productivity.

Sobera et al. [99] investigate the mass transfer to a cylinder sheathed by a porous layer. While this study is very far from the MT-SOFC theme, because its aimed at mass transfer through clothing in highly turbulent conditions.. Their discussion and illustration of meshing around the cylinder and in particular their meshing of the porous zone around the cylinder is very interesting and a good

starting point for meshing CFD models. They illustrate very clearly the differences between the mass transfer coefficient at the rear and front of the cylinder due to pressure differences.

2.4 Part IV Temperature measurement and MT-SOFCs

MT-SOFCs have received some attention with regard to heat transfer and thermal gradients that the cells can be exposed to without damaging them. Some studies on the temperature production of MT-SOFCs have been performed by several authors. For example Serincan et al. [100] show that as the temperature of a MT-SOFC is increased so also does the mass transfer rate and the catalytic activity whilst the ionic conductivity of the electrolyte also increases. Serincan et al. [41] also provide detailed information about specie distribution and temperature gradients around and within their cells. An interesting conclusion of their study suggests that shorter cathodes on longer anodes may be beneficial to reduce high temperature induced stresses at the seals of the MT-SOFC. Bujalsk et al. [21] show that the thermal cycling of the MT-SOFC is a massive advantage that the larger types cannot achieve because the sharp thermal gradients and induced stresses can cause cracks. Thus these longer anodes suggested by Serincan et al. [41] may be essential for stack designs specifically made for rapid start up to improve the reliability and longevity of seals. Locket et al. [52] and Cordiner et al. [98] investigate the thermal gradients across electrolyte supported cells and Lawlor et al. [67] investigate the heat removal from a MT-SOFC in cross flow. In the literature there are plenty of models that calculate the temperature gradients in MT-SOFCs but substantially less detailed experimental results are available.

With regard to temperature measurement infrared photography should be a very useful tool to visualise the temperature gradients across MT-SOFCs in ways that other methods cannot and have not in the literature been satisfactorily achieved. Thermal camera measurements have been performed by Du et al. [22] on MT-SOFCs where they examine hot and cold cells in cold and hot ambient conditions. The shown images however are not very detailed and do not include images to compare a cell under OCV and loaded conditions. Brett et al. [101] use thermographic cameras to evaluate the temperature profile on a pellet type solid oxide fuel cell however

these images are extremely pixelated and the resolution is affected. Very recently published work done by Pomfret et al. [102] use Si-charge-coupled device (CCD) thermal camera investigations during feeding hydrocarbons to a SOFC button cell. In the MT-SOFC field published infrared measurements have remained more or less neglected by the vast majority of groups. This is probably related to the design of the testing apparatus used by these groups that does not allow for such measurements and maybe also the lack of exposure to the benefits of this type of method. Additionally there is a high risk of measurement errors in the case of lack of experience in this field, so that this type of investigation is quite difficult to accurately make without an experienced thermal camera operator. Thermocouple measurements are commonly used by many groups for example [22, 39, 42, 52, 103] to measure the wall temperature of MT-SOFCs.

Normally Electrochemical Impedance Spectroscopy (EIS) is used by fuel cell material scientists to improve the performance of their electrodes and electrolytes and investigate degradation effects and attributes [24, 38, 104-107]. The use of EIS for temperature measurement is explicitly described by Hashimoto et al. [39] for MT-SOFC temperature monitoring. They use this method to measure the ohmic losses of the tested cells to estimate the cell temperature. In the shown procedure of Hashimoto et al. [39] the temperature is calculated once the ohmic loss is measured using EIS or current interrupt method. This value is then compared with a thermocouple placed 2 mm from the cathode wall. They conclude that this is a suitable method for temperature measurement and found that the EIS measurements and current interrupt readings agree. In this paper by Hashimoto et al. [39] they use the EIS method solely as a means to monitor the cell temperature, which in itself is a groundbreaking idea. A key point that could be addressed that has not been directly measured in their paper, because the thermocouple did not touch the outer electrode, is the difference in cathode wall temperature and the core temperature inside a MT-SOFC. It is thought that this is of special interest in order to provide data for MT-SOFC models for simulation.

The temperature radially through a cell has only been measured by Hashimoto et al. [39] in their EIS approach where they show huge temperature gradients through the cell. The fact the no cathode wall temperatures are made means that the temperature radially through the cell has not been defined and such information would be very useful for modelling. The electrolyte region, which is generally 10 microns thick,

must get much hotter than the electrodes that it is sandwiched between. This is because the amount of electrons that conduct through the electrolyte have a massive effect on its temperature. Zitouni et al. [108] in a numerical model show that the temperature of the electrolyte regardless of whether the cell is electrode or electrolyte supported will be the zone that has the highest temperature in the cell because of joule heating effects. This high temperature increase, which seems to be about 60°C, when 1.5 A/cm^2 is drawn from the cell, is dissipated very fast into each of the much cooler electrodes. The anode and even the cathode have many times the mass of the electrolyte. Thus this high temperature zone in comparison to the overall cell size is small. But compared to the size of the cathode the size of the electrolyte is similar, it being roughly a fifth of the electrolyte in the cells used in these tests.

In a very informative paper by Daan and Cui [109], where they investigate 3 different methods of current collection at the anode and asses the current transfer and heat generation through the cell, they show that collecting current at the centre of the anode is vital for a high performance and efficiency of a MT-SOFC. With regard to the heat profile across the radius of the MT-SOFC they concur with Zitouni et al. [108] that the dominant means of heat generation in the anode supported MT-SOFC is in the electrolyte. However they add information regarding the heat transfer profile radially across the cell by stating that the anode and cathode entropy heat fluxes are opposite to each other. At the cathode electrolyte interface heat is generated because of the reduction reaction while at the anode heat is removed by the oxidation reaction. This is a also critical point that the fluent CFD software does not seem to include as it dumps 50% of the heat generated into the anode and cathode sides respectively.

In the temperature gradient results of Serincan et al. [41, 100] from their 2d model these high gradients between the electrolyte and electrodes are not shown. However Serincan et al. [36] in their 2d model show that a 40°C cell temperature rise in their cell temperature should be expected when generating 2A and display an interesting plot that indicates that as the geometry of a MT-SOFC is increased the temperature of the cell should also increase. Cordiner et al. [98] show that for an electrolyte supported cell the temperature rise for a cell producing 1.1 W, at 2A, as seen on the active surfaces should be about 30°C with an ESC and no radiation included in the model. The results of Cordiner et al. [98] seem a bit strange because

unless they are removing heat in their model vial walls without the radiation included in the model the cell temperature should increase to a much higher value.

The temperature from the outer wall of the cathode to the reduction reaction points increases and increases more rapidly closer to the electrolyte wall because of gained entropy from the reduction reaction. Then the temperature rises through the electrolyte to a maximum just before the oxidation points and falls a bit because of loss of entropy caused by the Oxidation reaction. The temperature in the anode is highly dependent on the temperature of the gas and electrical contact points. It is expected that the connection the cell with the used current collection methods is actually quite good and that there are several contact points along the anode from a little past the middle of the cell to the inlet. It is also thought the anode reference connection touched the anode working connection inside the cell meaning a reliable voltage measurement. When the connections were reversed in the experimental setup i.e anode reference cable switched with the anode working cable and vice versa, the change in temperature on the outer wall of the cell, as measured by the thermographic camera, did not result in the drastic temperature differences as predicted in [109], where; when the current tapping points are switched so also did the direction of the high and low temperature gradient along the cell.. This indicates that the location of the anode current collector does not have a prominent effect on the overall cell temperature profile.

The effect of the electrodes on the temperature have to be quite small because the resistance of the cell reduces drastically in the impedance measurements see Figure 63. This is because of the resistance of the electrolyte being dominant.

Fischer et al. [110] using a novel modelling approach attempt to break down the heat generation components, zones and mechanisms in a tubular SOFC. A method for the estimation of the required single-electrode entropy changes from Seebeck coefficient data was presented and applied to a SOFC. This was a spatially discretised model that took into account mass transport and reactions in the gas channels and porous electrodes, charge transfer, and transport in the electrodes and electrolyte, as well as convective, conductive, and radiative heat transfer. A clear result of their findings is that there is a temperature gradient through their cell where the cathode side reduction reactions add entropy while the anode oxidation reaction reduces entropy.

The problem in comparing these results with MT-SOFCs is that the current produced per area of the cell modelled is much lower than that MT-SOFCs. 0.35A/cm^2 maximum for their cell as opposed to over 1.6A/cm^2 in the MT-SOFC case and thus the temperature increase is very low in their case. Nonetheless they clearly show that there is a temperature gradient radially through the cell. The temperature gradient in the electrolyte is strongly affected by the location of the reversible heat sources, which is probably due to the magnitude of the related heat source terms. For a specified operating point at 0.6 V with a set fuel and oxidant temperature and concentration the maximum radial temperature gradient in the electrolyte was computed to be −4425 K/m in the case of the simplified assignation of the heat source, while it was −4715 K/m when the separate electrode reaction were taken into account. The difference rose towards lower cell voltages and this resulted in higher current densities and thus in a higher electrochemical conversion rate.

Kanamura et al. [111] who also modelled a tubular solid oxide fuel cell taking into account the entropy changes also show a similar temperature gradient across the cell similar to the z=0.3 case of Fischer et al. [110] where the cell is producing maximum power and thus has a positive temperature gradient across the cell. However both these are large tubular SOFCs and are producing substantially less power per cm^2. Thus the ohmic resistance of the electrolyte possibly has a smaller role in the temperature increase than the electrochemical reactions. However similar temperature profiles are shown in these two papers but with much higher gradients across the cell should be expected for MT-SOFCs with the electrolyte zone being much hotter than the cathode and anode zones. This has to be the case if the EIS and cathode wall measurements of Figure 90 are correct, which we presume is the case.

To support this claim Hashimoto et al. [39], at 650°C operating temperature, show that the estimated temperature from electrochemical analysis shows that the cell temperature should rise by 100°C when 2.5A/cm^2 is drawn from the cell. Their thermocouple measurement read a change in temp of 30°C. This 30°C is slightly higher than our measurement at the same current density possible because ions are driven though the electrolyte at the same rate, but their electrolyte has a higher resistance at lower operating temperature, which may imply more Joule heating than our cell at 725°C which had an electrolyte resistance of 0.08 Ohms. It seems that the electrical connection to the cell is very important because Hashimoto et al. [39] conclude that poor electrical contacts easily cause Joule heating and causes a

temperature increase from OCV 650°C to over 1000°C at 2A/cm^2. Such high amounts of heat generation could be usefully for small stacks that would need extra heat to be thermally self-sufficient and would negate the need for extra haters increasing the efficiency of such a system. Possibly by using a combination "active" and under heat up conditions "passive wirings" on the MT-SOFCs this extra heat produced by lack of adequate current collection could be used to increase the temperature of the stack. To vindicate this statement simulation and experimentation would be required. However it should also be considered that the cells environment played an important role in the excessive temperature increase. It seems from visual inspection that their experimental apparatus confines the cell in a tight space. Lawlor et al. [67] have shown that under no flow conditions, the temperature of a cell producing 0.5W joule heat is very high compared to the same cell even experiencing flow in the range of several mm/s$^-$

2.5 Conclusions and indication of gaps in the literature

The first part of this literature review discussed in section 2.1 is an outline of the stack design in the MT-SOFC field. Designs and literature form the main research groups and companies in the field have all been outlined and discussed. During this study it became very clear that many groups had directly jumped into stack design without detailed single cell studies. This fact has been outlined in detail in section 2.1.4 . None of the models found in the literature comprehensively provided critical information that would be required in advance to make informed decisions when making multi-cell stack designs. A hypothesis of this thesis is that a high-quality stack design can be best realized after performing a detailed study of the multi-physical phenomena and how they affect a single MT-SOFC.

The second part of this literature review in section 2.2 is a review and an introduction to literature dealing with a cylinder in cross-flow. It was found in the literature review of section 2.1 that with the exception of Cordiner eat al. [98] there is no literature that deals specifically with an MT-SOFC in cross-flow. It has also been found in this literature study that there is not a single study whereby all the multi-physical phenomena, especially radiation and electrochemistry, are included in a single model that has subsequently been validated by experiments for MT-SOFCs.

Having studied in depth the literature available for flows around the cylinder in cross-flow it became evident that in this generally well-established field of research, there is also a gap in the literature with regard to mass transfer and cylinders. Section 2.3 follows on from the previous section that investigates flows around a cylinder in cross-flow and focuses specifically on literature available for mass transferred to a cylinder in cross-flow. A MT-SOFC in cross-flow is an example of a rare case where mass transfers to a cylinder occurs and this phenomena may be a very important for the optimal performance of the device especially at lower concentrations of oxygen. The MT-SOFC furthermore us a device that can potentially be used to study mass transfer to a cylinder in cross flow.

The final section in the literature review in section 2.4 investigated a topic that has also been pointed out from the initial literature review study. Outlined in section 2.1 is a literature study of temperature measurements made by the other authors and groups in the field. In high-temperature fuel cells regulation of the temperature is an extremely important factor. This review also showed that some very obvious temperature measurement technologies have not been used to map the temperature profile of MT-SOFC's. The literature review also pointed out that no groups had developed a high temperature experimental apparatus either solely or partially for the purpose of measuring the MT-SOFC's. Most groups either used standard high temperature ovens adapted slightly to make their experimental measurements.

2.6 Summary of the goals

Upon summarizing the goals of this thesis it is relevant to note that the goals subsequent to the realization of an apparatus that could test the cells were highly dependent on the effectiveness of this apparatus. Originally an important goal was to build a high temperature apparatus capable of testing bundles of cells to broaden the scope of the experiments that could be performed.

However it was found after several attempts to build such a system that the effort required to build control and monitor the cells within such an apparatus would consume most of the time of the thesis. Thus a more targeted approach using a

device to test single cells would more likely result in much more scientific information. The following list of goals is actually a scaled-down version of the original goals of the thesis but in hindsight was the most sensible way to get the maximum scientific information out of a three-year study.

Aim 1: Establish if and when natural convective flows are likely to occur in a bundle of MT-SOFCs

Aim 2: Design and build an apparatus capable of creating the conditions for MT-SOFC testing. These conditions should include variable fuel and oxidant flows to the cell, the ability to test the cell at various temperatures up to 850°C and should allow thermo graphic images to be taken either through a window or opening.

Aim 3: A variety of measurement techniques to measure the temperature profiles on a MT-SOFC in cross flow should be performed

Aim 4: CFD models should be developed that accurately predict the behaviour of an MT-SOFC in cross flow. Experimentally acquired I/V curves and temperature measurements should be realised to compare and asses the validity of the CFD predictions.

Aim 5: The concentration of oxygen and current density profiles on the cathode electrolyte interface should also be predicted using the CFD software and experimentally validated.

Aim 6: The effect on mass transfer to a cylinder in cross flow as the wake develops behind the cylinder as a function of the Reynolds number should be assessed.

Chapter 3 An Introduction to CFD and SOFC theory with the fuel cell module.

3.1 What is CFD?

Computational fluid dynamics (CFD) is a numerical code that contains equations within various models to describe various multi-physics phenomena. As the name suggests the software is mainly used to model fluid motion including gases and liquids but it may also be used to model heat transfer, species transport, chemical reactions, multi phase flows, solidification and melting and various other multi-physical phenomena. These models may be coupled together to solve physical problems simultaneously. Computational thermodynamics is a good industry at the moment and there are several big players including ANSYS Inc. the owners of the fluent software package, which has been used for the modelling in this thesis.

There are three main reasons why an engineer or researcher would use computational fluid dynamics.

1. When the device or system being studied is difficult to build or analyze for economic, logistic, time or difficulties in making measurements. CFD allows engineers to model and often very accurately predict what occurs in the system or design.

2. If the system has been modelled and somehow validated, an engineer can adapt the model geometry or boundary conditions to try to improve or analyze a design or system.

3. The insight and foresight that CFD offers can allow the engineer to design equipment or systems to be more efficient, ensure industrial compliance, and may increase the design cycle of products.

As a summary CFD is a tool for compressing the design and development cycle of a product for future rapid prototyping. However CFD is not only a useful tool for industry it may also be used by researchers to study various systems and indeed fundamental science questions. In this study CFD was used to model fluid flow, heat transfer, mass transfer and the electrochemical reactions within the fuel cell. For more information on CFD modelling with regards to SOFCs the readers pointed to the following section 3.3.

The main stages of the CFD simulating process involve:

Pre-processing:

This is where a computational mesh would be generated which is downloaded into the CFD software and boundary conditions and appropriate models are applied to the problem.

Simulation solving:

This is where the CFD software uses discretization of the governing equations to calculate the fluid properties within the mashed model considering all the boundary conditions and application of the selected models.

Post-processing:

This is where the engineer must use reports provided by the CFD software in the form of contour plots, vector plots and flux reports to analyse if solution is correct or not. Often the CFD software results are loaded into a separate post-processing program that allows more advanced post-processing techniques to be applied to the results Thus allowing better visualization or analysis not provided by the CFD software.

Only a basic knowledge of the working equations in CFD software may be useful for engineers using CFD software. It would be more important for developers of the code for researchers involved in the fundamental researching of fluid flow and fluid properties to have a much more detailed understanding.

Having said this it is commonly said in the CFD field that without validation of CFD models, instead of having “Computational Fluid Dynamic” results the engineer or operator may just have “Colourful Fluid Dynamic” results [112].

Without a skilled user who can make concise educated guesses and apply learned reasoning to any set of CFD results the results may be wrong and indeed unphysical. For this reason this section will very briefly introduce the reader to some of the governing equations and focus more concisely on the skills that an operator should be aware of when using CFD software. The knowledge that will be listed in the following sections has been learned during the duration and the simulation work in this thesis.

3.2 Introduction to the fundamentals of computational fluid dynamics

3.2.1 The Navier-Stokes Equations and CFD

The Navier-Stokes equations are named after L.M.H Navier (1778-1836) a French mathematician and an Irish-English Scientist G.G. Stokes (1819-1903). These equations are based upon equations for motion and mass conservation and can provide a complete mathematical description of the movement of incompressible Newtonian fluids. The beauty of the equations is that they have only four unknown terms *u, v and w* which are the velocity components in the x,y and z directions and ρ the density. The Navier-Stokes equations are quite complex and the reader is pointed to the following texts for more information [87, 112]. The equations deal with the following key points.

- Conservation of mass
- Conservation of linear momentum
- Conservation of angular momentum
    - Symmetry of the stress tensor
- Conservation of energy
    - Conservation of mechanical energy
    - Conservation of internal energy
- Hydrostatic and viscous stress tensors

The Navier-Stokes equations are nonlinear, second-order, partial differential equations and are generally quite complex. Exact mathematical solutions except in a very few instances are not one hundred percent possible. However in the cases where solutions have been obtained and compared experimental results the results have been in close agreement [112].

3.2.2 Mechanical principles

When a mass is at rest, pressure forces balance weight [113] this can be written mathematically as:

$$\Delta P = -\rho g \Delta z \qquad (3\text{-}2\text{-}1)$$

or

$$\frac{dp}{dz} = -\rho g \qquad (3\text{-}2\text{-}2)$$

Equations (3-2-1) and (3-2-2) can also be applied in the case of a fluid where articulate acceleration does not exist, in a case where vertical acceleration is much smaller than gravity. In the case where density remains constant equation (3-2-3) may be written as:

$$p' = p + \rho g z = const. \qquad (3\text{-}2\text{-}3)$$

By using the piezometric pressure gravitational forces may be eliminated when a flow of liquid at a constant density is without a free surface. Temperature pressure and density may be connected in what is referred to as an equation of state. An important example of this coupling is described in the ideal gas law:

$$p = \rho R T \qquad (3\text{-}2\text{-}4)$$

where

$$R = \frac{R_0}{m} \qquad (3\text{-}2\text{-}5)$$

R_0 refers to the universal gas constant and m is the molar mass. T in this case refers to the absolute temperature. The dynamics of fluid motion contain a set of governing equations that are fundamental for describing fluid motion [113] .

1. Mass: Change of mass = 0.
2. Momentum: The rate of momentum = force.
3. Energy: Change of energy = work + heat.

For a fluid containing multiple species

4. Species: Each of the specie constituents should be conserved.

Energy plays a different role in the cases of compressible and incompressible fluid flows. In most cases in CFD the assumption that the flow is incompressible is made. This means that there is no need to solve a separate energy equation. Mechanical energy principle states that the change of kinetic energy is equal to the work done and is formally equivalent to the momentum equation in the case of incompressible flow.

3.2.3 Discretization of a Domain

A point to note is that there are several methods of discretization that may be applied to this kind of modelling. They include the finite difference method, the finite volume method and the finite element method. The finite element method is often used in solid mechanics because of the considerable geometric flexibility that it allows and because general-purpose codes can be used for a wide variety of physical problems. The finite volume method however is used most often in CFD because it rigorously enforces conservation, it is flexible in terms of the geometry, the variety of physical phenomena it can handle and it is directly related to both the physical

quantities such as mass flux. The figure below, Figure 23 shows different stages within a finite volume method.

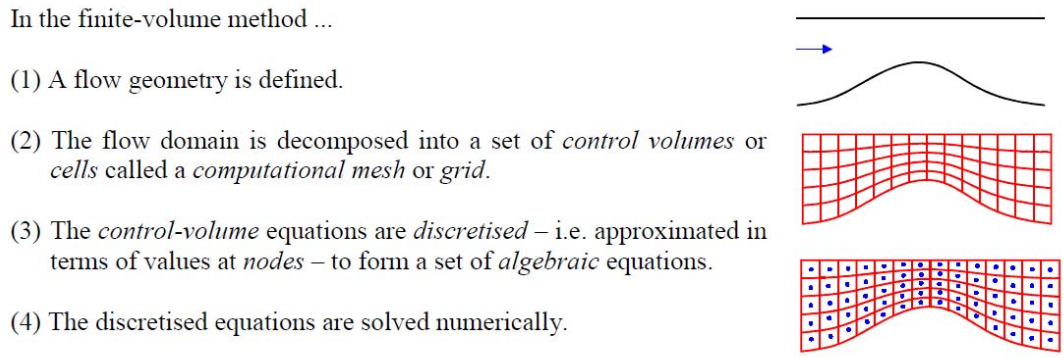

Figure 23: An illustration and commentary showing the different stages involved in the finite volume discretisation method [113].

Fluid motion can be described by applying the fundamental laws of mechanics including the conservation of mass and momentum equations to the motion of a fluid. When the conservation of energy equation for heat is also applied the combined equations from a set of coupled nonlinear partial differential equations. These coupled equations are used within a discrete gridded domain to solve a continuous problem as shown below in Figure 24. If it is taken, for example, that between X=0 and X=1 is a space that contains physical property such as pressure, velocity, temperature etc. in a continuous domain. If we take pressure as an example the domain could be described as:

$$p = p(x),\ 0 < x < 1 \tag{3-2-6}$$

Correspondingly in a discreet domain the pressure would be defined at each grid point thus:

$$p = p(x_i),\ i = x_1, x_2 .... N \tag{3-2-7}$$

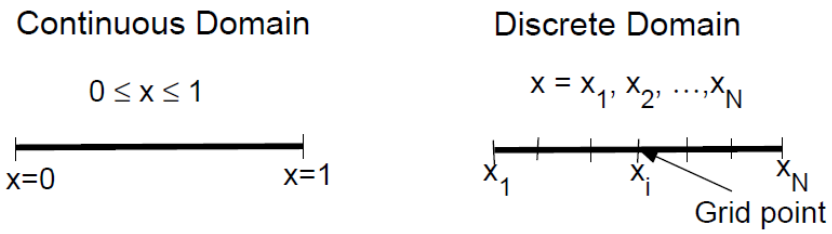

Figure 24: A 1-D example showing the concept of a gridded domain [114].

The fundamental elements of the CFD simulation are:

1. The flow field is discretised where variables such as density pressure and velocity are approximated by their values as a finite number of nodes within the modelled zone.
2. The equations of motion are discretised where the continuous control volume or differential equations are converted to discrete algebraic equations.
3. The resulting system of algebraic equations are solved to give values at the nodes within the model.

3.2.4 Expressing Fluid flow equations

Mass inside in a volume may be considered in two different ways. In CFD, continuum mechanics considers changes to the total amount to some physical quantity, for example mass, momentum, energy, species within specified regions of space is known as the control volume. Another way to consider mass inside a volume would be practical mechanics. For an arbitrary control volume the change in mass of a physical quantity over an interval of time is:

$$\Delta Mass = \sum Entering\ \ mass - \sum Outgoing\ \ mass + \sum created\ /\ lost\ \ mass \qquad (3\text{-}2\text{-}8)$$

In fluid mechanics the equation above would normally be expressed in a rate form by dividing by the time interval and transferring the net amount passing through the boundary to the left-hand side of the previous equation (3-2-8) [113].

$$\left[\underset{\text{Inside the volume}}{\text{Change Rate}}\right]+\left[\underset{\text{Out the boundary}}{\text{Net flux}}\right]=\underset{\text{Inside the volume}}{\text{Source}} \qquad (3\text{-}2\text{-}9)$$

The rate of transport across the surface is known as the "Net flux" and is the sum of the advection and diffusion phenomena. Advection implies a movement with the fluid flow and diffusion refers to transportation of mass within a flowing liquid or gas by random molecular or turbulent motion. Regardless of whether the physical quantity has mass momentum or chemical content for example, a single genetic scalar transportation equation of the form (3-2-9) is applied.

3.2.5 Conservation of mass/continuity equation

The conservation of mass requires that the mass of a system should stay the same as that system moves through a flow field. If the controlled volume approach is used to solve fluid flow problems the conservation of mass is written as:

$$\frac{\partial}{\partial t}\int_{cv}\rho.d\forall+\int_{cs}\rho V.\hat{n}\;\;dA=0 \qquad (3\text{-}2\text{-}10)$$

Where:

$\forall$ = Volume

V = Velocity

$\hat{n}$ =is the outward unit normal vector that is used to describe the orientation of the control surface.

This is commonly referred to as the continuity equation and is applied to a finite control volume (cv) that is bounded by a control surface (cs) [87]. The control volume integral term represents the rate at which the mass contained in the control

volume is changing. The control surface term represents the rate that the mass is flowing out through the control surface. That is the rate of mass outflow minus the rate of mass inflow. The differential form of the continuity equation can be derived when stationary cubical element is used as shown below Figure 25 (a). In the centre of the cube the fluid density is represented and the three directional related velocity components are represented by the v,u and w terms. The particle is considered small and may be expressed as:

$$\frac{\partial}{\partial t}\int_{cv}\rho \; d\forall \approx \frac{\partial \rho}{\partial t}.\delta x.\delta y.\delta z \qquad (3\text{-}2\text{-}11)$$

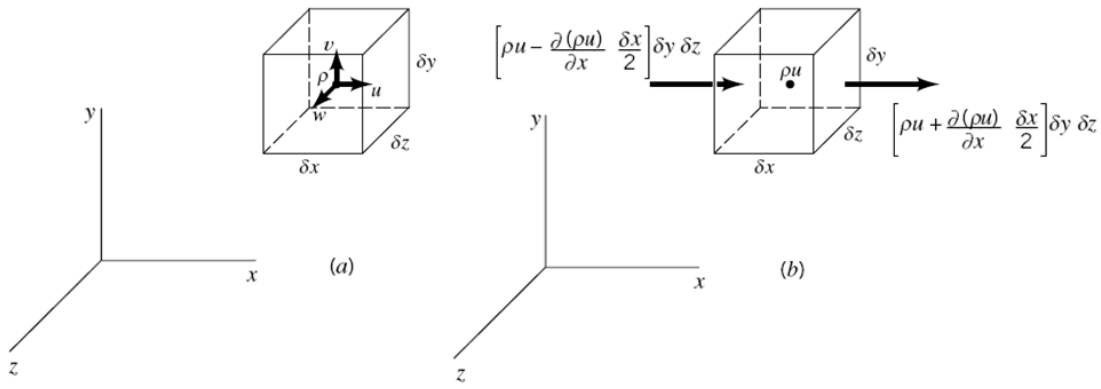

Figure 25: A diagram showing a stationary cube containing a single particle in a fluid of mass flowing into the cube must equal the mass flowing out of the cube adapted from [87].

If the flow is considered in each of the co-ordinate directions separately the mass flow through the surfaces of the element can be deciphered [87]. In Figure 25 (b) the flow in the x direction is shown. Letting "ρu" represent the x component of the mass rate of flow per unit area at the centre of the element then

on the right face:

$$pu\,|_{x+(\delta.x/2)} = pu + \frac{\partial(pu)}{\partial x}\frac{\delta x}{2} \qquad (3\text{-}2\text{-}12)$$

and on the left face:

$$pu\,|_{x-(\delta.x/2)} = pu - \frac{\partial(pu)}{\partial x}\frac{\delta x}{2} \qquad (3\text{-}2\text{-}13)$$

.

3-2-12 and 3-2-13 are really a Taylor series expansion of "ρu" but neglecting the higher order terms. When the right hand terms of the above equations are multiplied by the area δy and δz the mass flow rate flowing from the right face to the left of the cube can be calculated. This can be seen in Figure 25 (b). The total rate of mass flowing ($\dot{m}$)from the element through the two surfaces is:

$$\sum \dot{m}_x = \left[pu + \frac{\partial(pu)}{\partial x}\frac{\delta x}{2} \right]\delta y.\delta z - \left[pu - \frac{\partial(pu)}{\partial x}\frac{\delta x}{2} \right]\delta y.\delta z \qquad (3\text{-}2\text{-}14)$$

$$\sum \dot{m}_x = \frac{\partial(pu)}{\partial x}\delta x.\delta y.\delta z \qquad (3\text{-}2\text{-}15)$$

There is also flow occurring in y and z directions, so only flow in the x direction has been considered in 3-2-14 and 3-2-15. But they are simply found by using the previous analysis, but in their respective directions. The result is as follows [87].

$$\sum \dot{m}_y = \frac{\partial(pv)}{\partial y}\delta x.\delta y.\delta z \qquad (3\text{-}2\text{-}16)$$

$$\sum \dot{m}_z = \frac{\partial(pw)}{\partial z}\delta x.\delta y.\delta z \qquad (3\text{-}2\text{-}17)$$

The total mass outflow ($\dot{m}$) is found by adding the total mass flow rates in the x, y and z directions.

$$\sum \dot{m}_{x,y,z} = \left[\frac{\partial(pu)}{\partial x} + \frac{\partial(pv)}{\partial y} + \frac{\partial(pw)}{\partial z} \right] \delta x.\delta y.\delta z \qquad (3\text{-}2\text{-}18)$$

From the controlled volume approach formula, the differential continuity equation and the total mass flow rate in all directions formulate the equation for the conservation of mass [87] that is given in equation 3-2-19 and is also known as the continuity equation. This equation is a fundamental equation in fluid mechanics and is used for steady or unsteady flow and for compressible or incompressible fluids.

$$0 = \frac{\partial \rho}{\partial t} + \frac{\partial(\rho u)}{\partial x} + \frac{\partial(\rho v)}{\partial y} + \frac{\partial(\rho w)}{\partial z} = \frac{\partial \rho}{\partial t} + \nabla \bullet \rho V \qquad (3\text{-}2\text{-}19)$$

Just to note there are two interesting cases for steady flow of compressible fluids [112]. Density is not a function of time for steady flow but it can be a function of position as expressed in equation 3-2-20:

$$0 = \frac{\partial(\rho u)}{\partial x} + \frac{\partial(\rho v)}{\partial y} + \frac{\partial(\rho w)}{\partial z} = \nabla \bullet \rho V \qquad (3\text{-}2\text{-}20)$$

For incompressible fluids the fluid density p is constant everywhere within the flow field [112] and the continuity equation can be described as in equation 3-2-21:.

$$0 = \frac{\partial u}{\partial x} + \frac{\partial v}{\partial y} + \frac{\partial w}{\partial z} = \nabla \bullet V \qquad (3\text{-}2\text{-}21)$$

This equation can be used for both steady and unsteady flow of incompressible fluids.

3.2.6 Conservation of momentum

The conservation of motion equations for flows through the computational domain form a very important part of the Navier-Stokes equations. Again the reader is pointed to the following texts for more concise explanation [87, 112-114] and a very brief summary is given below.

With regard to the conservation of momentum Newton's second law is a very important concept where the rate of change of momentum is equal to force. The total change of momentum for a fluid passing through a control volume consists of two determinants.

1. The time rate of change of the total momentum inside to control volume.
2. The net momentum flux which is the difference between the rates at which a momentum leaves and enters a control volume.

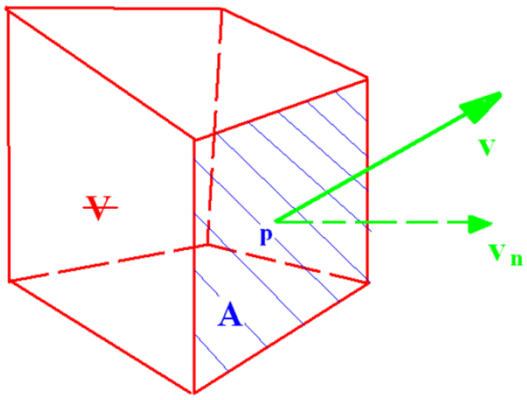

Figure 26: Single cell used to describe an equation of motion, adapted from [113].

The momentum in the cell display above in Figure 26, which contains a typical volume "$\forall$" and a typical area "A" may be described with the following equations 3-2-22 to 3-2-25 [113].

Momentum in the cell

$$= \ mass \times V = (\rho \times \forall)V \tag{3-2-22}$$

Momentum flux

$$= \ mass \ \ flux \times V = (\rho v \bullet A)V \tag{3-2-23}$$

From the prior two equations 3-2-22 and 3-3-23 the following equations 3-2-24 and 3-2-25 may be derived [113]. These equations describe the relationship between the rate of change of moment in a cell and force imposed on the fluid in the cell causing acceleration of the fluid and is the basis for Newton's second law..

$$\underbrace{\frac{d}{dt}(momentum) + net \ \ out \ \ momentum \ \ \ flux}_{total \ \ rate \ \ of \ \ change \ \ of \ \ momentum} = \ force \tag{3-2-24}$$

$$\frac{d}{dt}(m \times V) + \sum_{faces}(mass \ \ \ flux \times V) = F \tag{3-2-25}$$

In equation (3-2-25) the momentum, velocity and force terms have three components and are vectors.

There are two types of fluid forces that need to be considered in the conservation of momentum equations. Surface forces are proportional to the area and act on the control volume faces. Body forces are proportional to the volume [87]. Surface forces are generally expressed in force per unit area, or in other words stress. The main surface forces include pressure and viscous stresses. Pressure (p) will always act normal to the surface and fictional forces, viscous stresses (τ) arise from relative motion.

Figure 27 (top) shows the classic case of flow through a pipe where the flow regime takes time and distance before the flow becomes fully developed. The shear stress at the wall is zero and in fluid dynamics this is said to be the "no slip condition" that may be applied to a wall boundary condition. What it really means is

shown in detail in Figure 27 (bottom left) where at the wall the shear stress is zero, the velocity at the wall should also be zero. As a point is moved away from the wall the viscous stresses increase and the velocity of the bulk flow also increases.

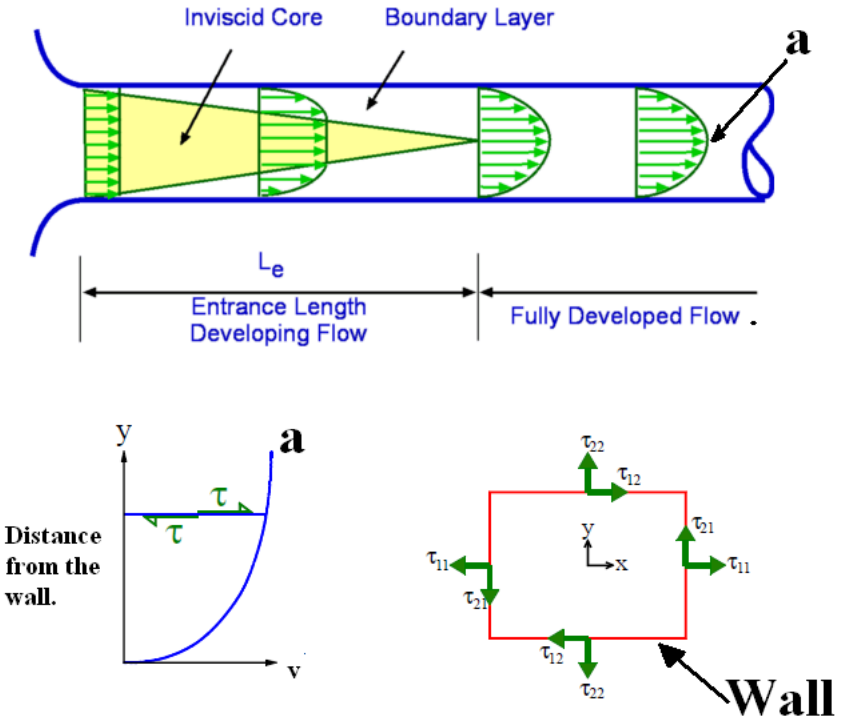

Figure 27 (Top) shows the classic case of flow in a pipe where the boundary layer and flow profile develops over time. (Bottom left) shows that as a point is moved from the wall the viscous stress increase. (Bottom right) shows a cell where the nearest boundary is a wall [115].

For a simple shear flow there would be only one zero viscous stress component situated directly at the wall and therefore please refer Figure 27 (bottom right). Equation 3-2-26 describes how a liquid, depending on its dynamic viscosity μ and velocity gradient through the fluid, will oppose motion within the fluid body perpendicular to the shear layers formed in the fluid:

$$\tau = \tau_{12} = \mu \frac{\partial u}{\partial y} \qquad (3\text{-}2\text{-}26)$$

However in general τ is a symmetric tensor with a more complex expression for its components. in an incompressible flow is described below in 3-2-27 [87]:

$$\tau = \tau_{i,j} = \mu(\frac{\partial u_i}{\partial x_j} + \frac{\partial u_j}{\partial x_i}) \qquad (3\text{-}2\text{-}27)$$

To mention briefly there are other forces that a fluid may experience including body forces (gravity is an example) and centrifugal and Coriolis forces.

3.2.7 Differential equations and fluid motion

If a fixed Cartisian control volume, with sides shown in Figure 28, is fixed ,conservative differential equations for momentum may be derived as seen in equation 3-2-27 [113].

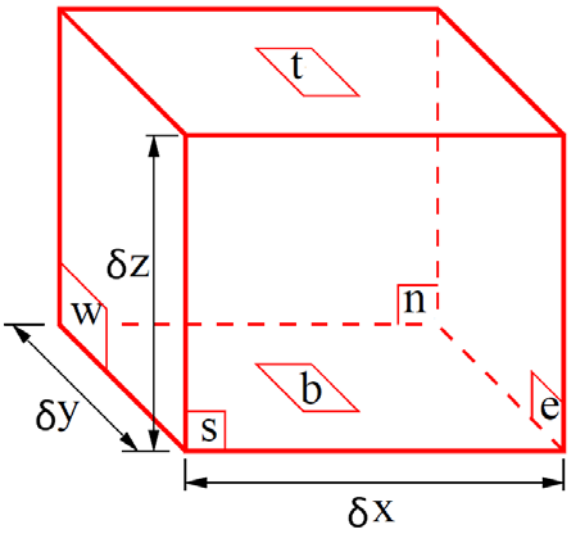

Figure 28: Guide for the labelling of a cubic cell adapted from [113].

$$\underbrace{\frac{d}{dt}(\rho \forall u)}_{\frac{\Delta momentum}{\Delta t}} + \underbrace{(\rho uA)_e u_e - (\rho \upsilon A)_w u_w + (\rho \upsilon A)_n u_n - (\rho \upsilon A)_s u_s + (\rho \upsilon A)_t u_t - (\rho \upsilon A)_b u_b}_{\Sigma Outward\ \ momentum\ \ flux} = \underbrace{(p_w A_w - p_e A_e)}_{pressure\ \ x\ \ dir} + forces$$

(3-2-27)

Where u is the velocity components in the x direction and ν is the kinematic velocity defined below in equation 3-2-38.

$$\upsilon = \frac{\mu}{\rho} \qquad (3\text{-}2\text{-}28)$$

When the cell dimensions are implemented in the volume and area terms,please refer to Figure 28 for the indexing of the functions equarion 3-2-29 discribes in more detail the differential equations describing momentum in the cell:

$$\frac{d}{dt}(\rho\delta_x\delta_y\delta_z u) + [(pu)_e u_e - (\rho u)_w u_w]\delta_y\delta_z + [(pu)_n u_n - (\rho u)_s u_s]\delta_x\delta_z + [(pu)_t u_t - (\rho u)_b u_b]\delta_x\delta_y = (p_w - p_e)\delta_y\delta_z + viscous\ \ and\ \ other\ \ \ forces$$

(3-2-29)

Divideing by the volumetric dimensions and change the order of p_e and p_w results in equation 3-2-30 which is a useful simplification of equation of 3-2-29:

$$\frac{d(pu)}{dt} + \frac{(\rho uu)_e - (\rho uu)_w}{\delta_x} + \frac{(\rho vu)_n - (\rho vu)_s}{\delta_y} + \frac{(\rho vu)_t - (\rho vu)_b}{\delta_z} = -\frac{(p_e - p_w)}{\delta_x} + other\ \ forces$$

(3-2-30)

Introducing limits on the area dimensions δx, δy & δz → 0 and a viscous term causes a futher simplification, equation 3-2-31, of the differential equations describing momentum in a controlled volume:

$$\frac{\partial(\rho u)}{\partial t} + \frac{\partial(\rho uu)}{\partial x} + \frac{\partial(\rho vu)}{\partial y} + \frac{\partial(\rho wu)}{\partial z} = -\frac{\partial p}{\partial x} + \mu\nabla^2 u + \ forces$$

(3-2-31)

∇^2 refers to the Laplace equation and in-viscid incompressible ir-rotational flow fields are governed by this equation. This function is also an important term in the stream function that applies for 2-d flows. The forces term refers to buoyancy or density by gravity where the direction of gravity should be considered. For more information on this component please see [87]. The pressure force per unit volume in the *x* direction is given by (minus), the pressure gradient in that direction. Also to

note removing the viscosity term results in Euler's motion equations and when these equations include the viscosity term and are re-arranged such that the acceleration terms appear on the right and force terms on the left the result is the Navier-Stokes equations which are the differential equations used in CFD to describe fluid motion as seen below.

(x direction)

$$\rho\left(\frac{\partial u}{\partial t}+u\frac{\partial u}{\partial x}+v\frac{\partial u}{\partial y}+w\frac{\partial u}{\partial z}\right)=-\frac{\partial p}{\partial x}+\rho g_x+\mu\left(\frac{\partial^2 u}{\partial x^2}+\frac{\partial^2 u}{\partial y^2}+\frac{\partial^2 u}{\partial z^2}\right)$$

(y direction)

$$\rho\left(\frac{\partial v}{\partial t}+u\frac{\partial v}{\partial x}+v\frac{\partial v}{\partial y}+w\frac{\partial v}{\partial z}\right)=-\frac{\partial p}{\partial y}+\rho g_y+\mu\left(\frac{\partial^2 v}{\partial x^2}+\frac{\partial^2 v}{\partial y^2}+\frac{\partial^2 v}{\partial z^2}\right)$$

(z direction)

$$\rho\left(\frac{\partial w}{\partial t}+u\frac{\partial w}{\partial x}+v\frac{\partial w}{\partial y}+w\frac{\partial w}{\partial z}\right)=-\frac{\partial p}{\partial z}+\rho g_z+\mu\left(\frac{\partial^2 w}{\partial x^2}+\frac{\partial^2 w}{\partial y^2}+\frac{\partial^2 w}{\partial z^2}\right)$$

(3-2-32)

3.2.8 Accounting for advection and diffusion.

Because the fuel cell module will be used in this thesis as will be described in 3.3 it is important to also have a basic understanding of species transport and how CFD accounts and calculates specie concentrations. A basic concept for the movement of species is that a specie within a gas volume will tend to spread evenly within the gas. When a higher quantity of a specie is located in one part of the volume than another, a potential is generated measured by the partial pressure of the specie. This potential drives some of the specie at the higher concentration into the zone where the species is at a lower concentration. This is refered to as pure diffusion mass transfer. In reality this may also occur in a fluid in motion and then the diffusion potential must be combined with the forces causing the fluid to move which will aid or hinder the diffusion of the species and this is referred to as advection. A similar equation to 3-2-32 may be derived for any physical quantity that is advected or diffused by a fluid flow. For each such quantity an equation is solved for the concentration (i.e. amount per unit mass), for example, the concentration of salt, sediment or chemical constituent. Diffusion occurs when concentration varies with position. It typically involves transport from regions of high concentration to regions of low

concentration, at a rate proportional to area and concentration gradient. For many scalars it may be quantified by Fick's diffusion law [113] as seen below in equation 3-2-33:

$$rate\ of\ \ diffusion = -diffusivity \times gradient \times area \quad rate\ of\ \ diffusion = -\Gamma \times \frac{\partial \phi}{\partial n} \times A \tag{3-2-33}$$

Equation 3-2-33 is often referred to as gradient diffusion. A common example is heat conduction or in the case of fuel cells partial pressure gradients in the oxidant and fuel channels.

For an arbitrary control volume the mass of a specie inside a cell can be described as the mass inside the cell multiplied by the concentration inside as seen in equation 3-2-34.

$$Amount\ in\ the\ cell\ \ \times\ \ V \times \phi \tag{3-2-34}$$

The advective flux of a specie inside a cell can be described by multiplying the mass flux by the concentration of the specie as seen in equation 3-2-35.

$$Advective\ \ flux = C \times \phi \tag{3-2-35}$$

The diffusive flux of a specie inside a cell can be described by the diffusivity of the specie in the mixture times the gradient of the concentration of the specie within the mixture multiplied by an area. This is described more clearly below in equation 3-2-36.

$$Diffusive\ flux = -\Gamma \times \frac{\partial \phi}{\partial n} \times A \qquad (3\text{-}2\text{-}36)$$

The quantity of a species produced or removed in a cell can be determined by multiplying the source/sink density by the volume, seen below in equation 3-2-37.

$$Source = S \times V \qquad (3\text{-}2\text{-}37)$$

Balancing the rate of change against the net flux through the boundary and rate of production yields the scalar-transport or (advection-diffusion). Please refer [87, 112, 113] for more information, section is just to introduce the reader to terms that will apply to the fuel cell module with regards to mass transport of species.

3.3 Fuel cell theory and the fluent fuel cell module

3.3.1 Fuel cell efficiency

In fuel cells chemical energy contained in a fuel can be directly converted into electricity at theoretically higher efficiencies than all other common fuel conversion methods. The Carnot efficiency limit that affects combustion and heat engines does not apply to fuel cells. When chemical energy is converted to electricity as in combustion for example the heat of the maximum theoretical efficiency is limited by the operating temperatures [20]. This fact is expressed below in equation 3-3-1.

$$\eta = \frac{T_{\max} - T_{\min}}{T_{\max}} \qquad (3\text{-}3\text{-}1)$$

Theoretical efficiency for fuel cells can be expressed as a relationship between mechanical energy available, free energy change of the fuel cell reaction ΔG in the higher heating value of the fuel cell reaction, enthalpy change of the fuel cell reaction ΔG [116].

Fuel cells potentially have a higher efficiency and over a large temperature and power range as shown below in Figure 29. Combustion and heat engines are well

suited for operation under constant conditions because they have a limited maximum power range. Should this range be exceeded their efficiencies drop quite fast. This is where fuel cells have a large advantage, because they have a high efficiency over a high a range of powers and temperatures. This makes them perfect for dynamically load cycles [117]. The high efficiency at very low loads is particularly useful.

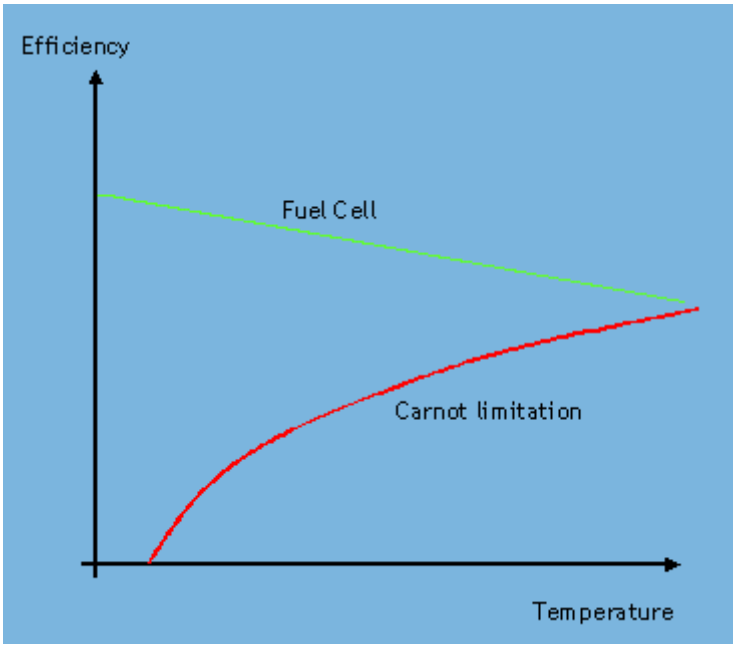

Figure 29: A plot comparing fuel cell and carnal efficiency as a function of temperature [117]

3.3.2 The losses in fuel cells

The losses in fuel cells are a very important concept to understand for the following sections in this work. The losses in fuel cells are related to the power produced by the cells. The more current that is drawn from a cell, the higher the losses from the cell would be. This is the reason why the voltage of the cell reduces as more current is drawn from the cell. This ideal cell voltage (E_{rev}) of a fuel cell can be calculated from the available free energy, ΔG [116]. This equation is shown below in equation 3-3-2:

$$E_{rev} = \frac{\Delta G}{nF} \qquad (3\text{-}3\text{-}2)$$

Where ΔG is the free Gibbs energy, n is number of electrons transferred in the electrochemical reaction and F is the Faraday constant (94685 C/mole) [116]. The E_{rev} is also dependent on operating conditions like temperature, pressure and concentration of reactants.

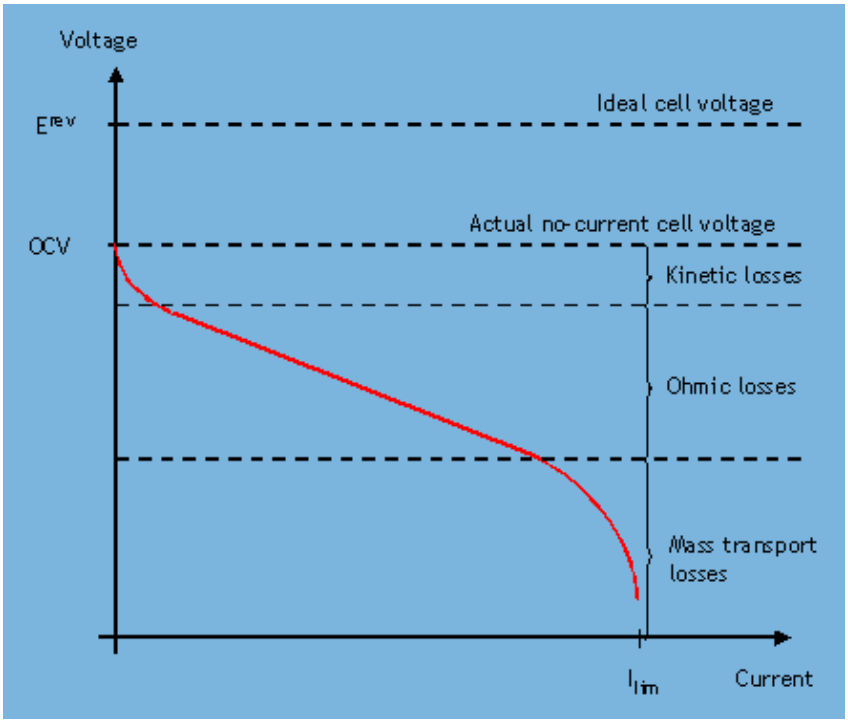

Figure 30: A typical current voltage diagram for a fuel cell indicating the points on the IV curves that correspond to different losses [117].

The term overvoltage refers to the difference between the ideal cell voltage and the operating cell voltage. This in due course represents the losses in the cell. The relationship between the theoretical E_{rev} and the actual operating voltage (E_{cell}), expressed in equation 3-3-3, is a more correct way to express the efficiency of a fuel cell [117].

$$\eta = \frac{E_{cell}}{E_{rev}} \qquad (3\text{-}3\text{-}3)$$

Fuel-cell losses may be divided into the following types of losses:

- Fuel crossover.
- Internal currents.
- Activation losses.
- Ohmic losses.
- Mass transfer losses.

In theory the electrolyte should only transport ions, however in practice a certain amount of fuel an electron crossover will occur. Although the fuel and internal current crossover losses are small they are the reason that the real open circuit voltage does not match with the theoretical value.

Activation/polarization losses occur because of the slowness of the electrochemical reactions taking place on the electrode surfaces. Electrochemical reaction kinetics cause the voltage to decrease and these losses can mainly be seen in an IV curve as the cell begins to produce current, as seen on the left-hand side of Figure 30.

The electrolyte has a resistance to the flow of ions within it and this coupled with losses caused by travelling electrons within the electrodes and current connectors result in ohmic losses that produce heat. The major proportion of the losses within a fuel cell occur as more current is drawn from the cell as seen in Figure 30 (middle part of the plot). These losses are due to ohmic losses and are directly proportional to the current taken from the cell.

When the reactant concentration depletion reaches a certain value, at the surface of the anode or cathode, from either fuel utilization or poor refreshing of the reactants, mass transfer losses will occur. This literally means that the reactants are not available for the electrochemical reactions to maintain a high performance and this can be seen at the tail end of the IV curve in Figure 30.

Understanding these fundamental concepts of losses in the fuel cell and the terminology used to describe them is essential for understanding the following sections of his work.

3.3.3 Introduction to the fluent fuel cell module

The solid oxide fuel cell module is an extra set of equations that have been defined by the fluent company in user-defined function form for the modelling of Solid Oxide Fuel cells. The fluent module allows the following be calculated [118]:

- Electrochemical reactions that contain elements for the electric field, mass species and energy transport.
- In all solid cell components the electric field solution including ohmic heating in the electrodes and electrolyte.
- A tortuosity term for the porous electrodes is also included.
- It is also possible to include an arbitrary number of electrochemical cells similar as in an array or in a stack.
- It also allows geometric flexibility meaning that as long as the model is set up in the correct way almost every type of geometry can be solved for.

To achieve the above points, the following must be achieved [118]:

- Fluid flow, heat transfer and mass transfer in the front channels and porous electrodes must be accounted for.
- The transportation of current and potential field in the porous electrodes and solid conducting regions must be modelled.
- The redox reactions must be modelled at the electrodes, electrolyte and gas species interfaces.

3.3.4 Outline of the electrochemical model

The current density distribution and the transport behaviour of a fuel cell are very dependent on external effects. This is because the local Nernst potential is dependent on the composition of the flows directly in the vicinity of the electrolyte inside the anode or cathode. Additionally the activation and limit losses associated with the electrolyte are a function of the current density. In the electrochemical module either side of the electrolyte is partitioned by local potential difference. The Nernst potential, the ohmic losses in the electrolyte and the activation losses associated at the electrode electrolyte interfaces provide the terms required to calculate this potential difference.

Equation 3-3-4 represents the aforementioned calculation as a potential difference between the anode in the cathode [118].

$$\delta E = N - i\rho_{ele}.t_{ele} - \eta_{act}(i) \qquad (3\text{-}3\text{-}4)$$

Where "i" is the the local current density, "ρ"is the Ohmic resistance of the electrolyte, "N" is the Nernst potential, "δE" is the difference in potential, "t" is the temperature and "η_{act}" are the activation losses.

The fluent module assumes the ideal case where there is a uniform contact between the electrodes and highly conductive current connectors. When the module is asked to solve for cell voltage rather than the system the previous equation is used to calculate the current density distribution on the anode and cathode respectively.

Figure 31 is a graphical portrait depicting how the fluent CFD software is coupled with the SOFC module. While fluent monitors and calculates the species momentum energy and electric potential field, the SOFC model is calculating the Nernst voltage the current distributions and over potentials at the electrolyte and the electric potential field boundary conditions. Fluent passes information about the local species concentration and temperature to the SOFC module, which uses these data for its calculations and passes out species and heat flux values at boundaries within the model.

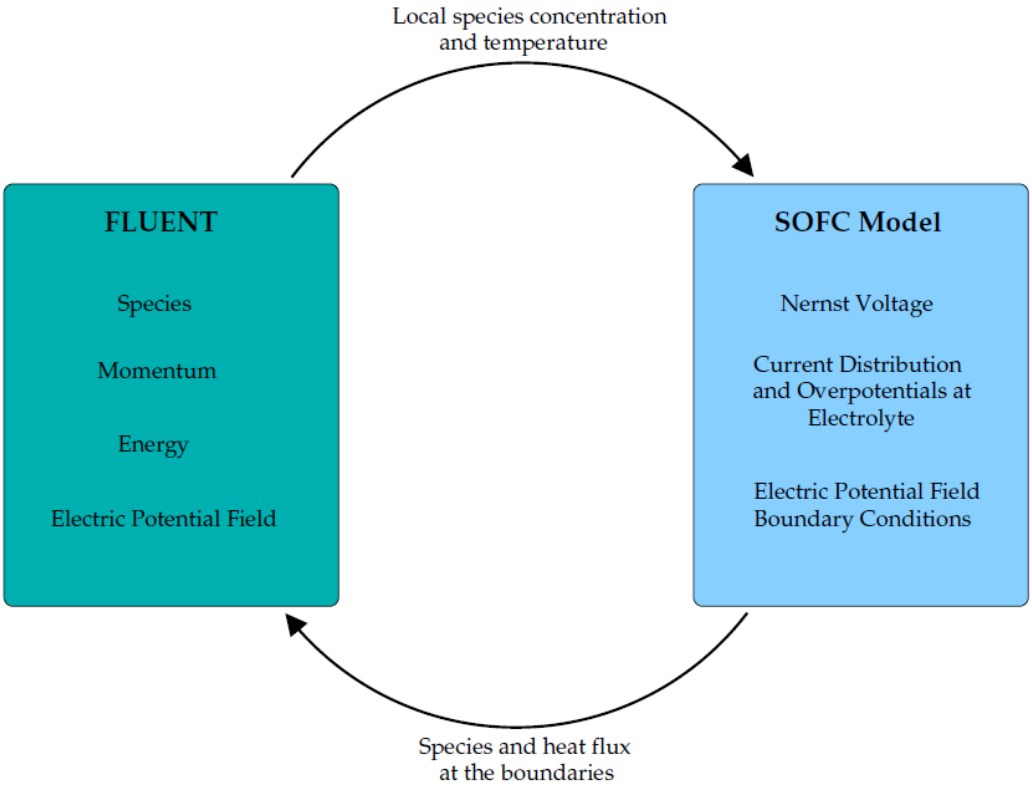

Figure 31: The solving process and coupling between the Fluent and the SOFC module [118].

Fluent handles all aspects of the fluid flow heat transfer and mass transfer in the flow channels and porous electrodes. Fluent also uses its multi-component diffusion model to calculate the mass diffusion coefficient of a specie in the oxidant and fuel mixtures.

3.3.5 Modelling of the current transport and potential field

Three-dimensional electrical conduction is directly analogous to the calculation of heat transfer and fluent uses this concept as a means to calculate the electric field. The conservation of charge is the basis for the calculation of the potential field throughout the conducting regions of a model. This is expressed below in equations 3-3-5 and 3-3-6:

$$\nabla \cdot i = 0 \qquad (3\text{-}3\text{-}5)$$

where

$$i = -(\sigma \nabla \phi) \qquad (3\text{-}3\text{-}6)$$

"σ"electrical conductivity "ϕ"electrical potential and "i" is the current density

Therefore the Laplace equation is the governing equation for the electric field [118] and is described below in equation 3-3-7..

$$\nabla \cdot (\sigma \nabla \phi) = 0 \qquad (3\text{-}3\text{-}7)$$

The following attributes are all combined to make the electric field potential calculation [118]:

- In all the conducting materials including the electrolyte, electrodes and electrical conductive materials the ohmic losses are calculated.
- Where contacts exist between different materials the contact resistance is considered.
- As a result of the current density throughout the domain ohmic heating occurs and is accounted for.

3.3.6 Treatment of the activation over potential

The Fluent SOFC module uses a Taylors serious expansion where previous value for current density i_{old} is used [118]. The Butler-Volmer equation for the activation potential is nonlinear and this Taylors Series expansion may be used to make a locally linearised form as described in equations 3-3-8 to 3-3-10. This allows a more complete account of the electrochemistry and above all else allows for a better model stability for improved convergence.

$$\eta_{act}(i) \approx \eta_o - \eta_1 (i - i_{old}) \qquad (3\text{-}3\text{-}8)$$

$$\eta_o = \eta_{act}(i_{old}) \qquad (3\text{-}3\text{-}9)$$

$$\eta_1 = -\frac{\partial \eta_{act}}{\partial i} \Big| i = i_{old} \qquad (3\text{-}3\text{-}10)$$

Using this approximation the voltage jump across the electrolyte may be formulated as shown in equation 3-3-11:

$$V \approx \underbrace{\left[N - \eta_o + \eta_1 i_{old}\right]}_{Constent} - \underbrace{i\left[\rho_{ele} t_{ele} + \eta_1\right]}_{Liner\ with\ local\ i\ density} \qquad (3\text{-}3\text{-}11)$$

The activation over potential is considered as a direct reduction of the voltage and as an additional effect of resistance. While the calculation is running, this formulation caters for the activation over potential to vary to changes in cell current density. This linearized form of the Butler Volmer equation becomes more accurate as the solution reaches its final convergence and is exact at convergence.

3.3.7 The cell potential

Within the fluent fuel cell module the electrode reactions are assumed to occur in a single step. The rate limiting step for the electrode reactions is the charge transfer reaction. Oxygen is electrochemically reduced at the triple phase boundary at the cathode electrode expressed in equation 3-3-12: $\frac{1}{2}O_{2,cathode} + 2e^- \Leftrightarrow O^{2-}$ *(3-3-12)*

The oxygen ion at the triple phase boundary on the anode electrode is electrochemically re-oxidised expressed in equation 3-3-13:

$$O^{2-} \Leftrightarrow \frac{1}{2}O_{2,anode} + 2e^- \qquad (3\text{-}3\text{-}13)$$

The Nernst equation describes the electromotive force or a cell voltage under equilibrium conditions as shown in equation 3-3-14. In other words this means in the absence of an electrical load the oxygen activity on both sides of the electrolyte is fixed by the respective chemical potentials:

$$\phi_{ideal} = \frac{RT}{4F}\ln\left(\frac{Po_{2,cathode}}{Po_{2,anode}}\right) \quad (3\text{-}3\text{-}14)$$

The anode reaction is outlined below in equation 3-3-15:

$$H_2 + O^2 \Leftrightarrow H_2O + 2e^- \qquad (3\text{-}3\text{-}15)$$

Thus at equilibrium the Nernst potential can be described as shown in equation 3-3-16 [118].

$$\phi_{ideal} = \phi^\circ + \frac{RT}{2F}\ln\left[\frac{\{P(h_2).P(\frac{1}{2}o_2)\}}{P(h_2o)}\right] \qquad (3\text{-}3\text{-}16)$$

Where P is the designation for partial pressure which is a dimensionless unit equal to or less than 1.

An important term in the fuel-cell field is the Open Circuit Voltage (OCV), which is the term given when the potential measured between the anode and cathode is in the equilibrium condition or in other words a cell with no load applied. Normally the main reason why the theoretical OCV may not be reached can be due to electrical leakage across the electrolyte or poor performing electrodes. When a load on the cell is applied the cell voltage drops caused by polarization losses at the electrodes.

The fluent fuel cell module considers that the electrochemistry takes place at the electrolyte interfaces with the electrodes. At this stage it is important to note that the fuel cell module does not treat the electrolyte as a 3-D zone but rather as an imaginary 3-D zone sandwiched between two walls or interfaces. This means that when the electrolyte is drawn into meshing software it is a simple wall face in fluent that breaks into a wall and shadow. In other words two faces on either side of an imaginary 3-d zone that is normally used in heat transfer calculations so that the wall need not be meshed.

This impermeable wall has a “jump” condition applied to each side to simulate the electrochemistry. All of the electrochemical effects are included in this condition to closely couple the electro chemical behaviour. The voltage jump due to Nernst, the voltage reduction due to activation losses, the ohmic losses due to the resistivity of the electrolyte and the voltage reduction due to activation losses are all

accounted for in this step. This interface condition relates the potential on the anode and the cathode side of the electrolyte and has the following form

$$\phi_{cell} = \phi_{jump} - \eta_s \qquad (3\text{-}3\text{-}17)$$

Where ϕ_{jump} is the potential relating to either side of the impermeable electrolyte wall. η_s is the ohmic loss in the solid conduction regions.

Equation 3-3-17 can be broken down into more comprehensive equations as shown in equations 3-3-18 and 3-3-19 which provide a better dicription of the processes being modelled.

$$\phi_{jump} = \phi_{ideal} - \eta_{ele} - \eta_{act,a} - \eta_{act,c} \qquad (3\text{-}3\text{-}18)$$

$$\eta_s = \eta_{ele} - \eta_{act,a} - \eta_{act,c} \qquad (3\text{-}3\text{-}19)$$

Where η_{ele} is the ohmic overpotential of the electrolyte, $\eta_{act,c}$ is the cathode overpotential, $\eta_{act,a}$ is the anode overpotential and ϕ_{ideal} is the is the Nernst potential.

Fluent uses the Laplace equation for potential flux field. The computational domain is divided into control volumes and the flux conservation is enforced at each cell. On the electrolyte boundary flux from one cell to its neighbour is given by ohms law.

$$\vec{i} = -\sigma \nabla \phi \qquad (3\text{-}3\text{-}20)$$

An approximation is made by utilizing the numerical difference in each of the cells of the values of ϕ.

Ohms law in combination with the voltage difference must be used at the electrolyte interface. There are three separate voltage relations that fluent uses for the normal flux calculation. These three separate relations couple the anode computational cell center voltage to the anode/electrolyte face voltage. The cathode center cell voltage is also coupled to the cathode/electrolyte face voltage and both are coupled to the electrochemistry jump condition [118].

$$\phi_{centroid,anode} = \phi_{anode,wall} - i\rho_{anode} D_{anode} \quad (3\text{-}3\text{-}21)$$

$$\phi_{centroid,cathode} = \phi_{cathode,wall} - i\rho_{cathode} D_{cathode} \quad (3\text{-}3\text{-}22)$$

$$\phi_{anode,wall} = \phi_{cathode,wall} - i(\rho t)_{eff} \quad (3\text{-}3\text{-}23)$$

Where D_{anode} and $D_{cathode}$ are the distances from the electrode computational cell center to the electrolyte.

The normal current flux, *i*, is calculated by solving the three linear equations above and is based on the values of the electric field in the anode and in the cathode computational cells. These linearised forms of the electrochemical equations provide a solution of the electric field that directly includes variations in specie concentrations, true Nernst variations, resistive response of the electrolyte and an approximate response to changes in activation losses.

3.3.8 The electrolyte interface

As described earlier the electrolyte in fluent is more or less an imaginary three-dimensional zone. When one draws the model, the electrolyte is not drawn but is rather a two-dimensional wall used to separate the anode and cathode and this wall in fluent software is given a certain thickness between it and its shadow zone. This in effect means that electrolyte supported cells may not be modelled in this version of the software. This condition also means that heat profiles through the electrolyte may not be calculated. In the case of this work the cells used were anode supported and the thickness of the electrolyte was in the range of 10 μ. This ultimately means that using the electrolyte interfaces the way fluent allows for should not affect any model results, particularly the temperature and current profiles. However the ability to calculate the temperature profile inside the electrolyte is not possible in the 6.3.26 version of Fluent.

The CFD software imposes a flux balance between computational cells that share a common face. This calculation is what the solution procedure hinges on and where fluent has made some special interface modifications in their UDS solution. In fact when you run the fluent module and when you want to run the residuals for the SOFCs electrochemistry one monitors this UDS term. For more information and the derivation of this solution process in these modifications the user is pointed to the fluent fuel cell module manual [118] where it is detailed.

As a summary however the solution process can be broken down into the following [118]:

- Using Cartesian cells the current flux from cell (volume) centroid to the electrolyte interface centroid (face) must be calculated.
- At the discontinuity, the electrolyte interface, the values of potential change discontinuity and the current may be deduced.
- A set of equations are then manipulated to solve the current values in the face and the potential values are eliminated.
- Fluent uses this definition of the current flux to build a system of linear equations to start a potential field. For an interface that has a constant resistance and voltage jump the prior formulation would be valid.

- Fluent includes these general flux computations into its UDS solution scheme and this provides the ability to compute the electrolyte/ jump resistance and to calculate the contact resistance of any interfaces.
- The energy equation also needs some special treatment to account for the heat generated by the cell that is lost as a result of the electrochemistry over potentials. One half of this value is applied as a source term to the energy equation of the anode computational cell adjacent to the electrolyte and the other half is applied as a source to the cathode side.
- The result is an arbitrary destruction and generation of heat applied to a cell adjacent to the electrolyte interface.
- To find the activation over potential at the anode and the cathode the Newton method can be used to solve the full version of the Butler-Volmer equation [116]:

$$i = i_0 \exp\left[\frac{\alpha \eta_{act} zF}{Rt}\right] - \exp\left[-\frac{(1-\alpha)\eta_{act} zF}{Rt}\right] \qquad (3\text{-}3\text{-}24)$$

Where, $\boldsymbol{i}$ is the current density (A/m^2), $\boldsymbol{i_0}$ is the exchange current density (A/m^2), α is the transfer coefficient (-), α η the activation polarisation (V), $\boldsymbol{z}$ the number of electrons transferred per reaction (-), $\boldsymbol{R}$ is the Universal gas constant and F is Faradays constant (is the magnitude of electric charge per mole of electrons 96485.3399 C mol^{-1}). The transfer coefficient is considered to be the fraction of the change in the polarisation which leads to a change in the reaction rate constant and for fuel cells its value is usually 0.5 [118]. The exchange current density is the (equal) forward and reverse electrode reaction rate at the equilibrium potential and can be determined experimentally by extrapolating plots of log j versus η to η = **0**. High exchange current densities mean a high electrochemical reaction rate and hence the possibility of good fuel cell performance. This is a key volume in determining/manipulating the performances of fuel cells in the SOFC module.

Exchange current densities describe intrinsic rates of electron transfer between electrodes. Such rates provide structural and electronic insights into these elements (anode and cathode) and in general, the exchange current density depends

on the composition of the electrode, the state of the electrode surface (e.g., surface roughness, presence of oxides, adsorbed species on the surface), concentration of the electro-active species in the solution (both the reduced and oxidized form), the composition of the electrolyte, and temperature.

Fluent uses the following formula to include the exchange current densities[118].

$$i = i_0\left[e^{\frac{\alpha_{anode}(\phi-\phi_0)F}{Rt}} - e^{-\frac{\alpha_{cathode}(\phi-\phi_0)F}{Rt}} \right] \quad \textbf{(3-3-25)}$$

Where

η_{act} = $(\phi - \phi_0)$

ϕ_0 = the potential field at the cell centroid.

ϕ = is the ideal cell potential.

- Using the electrical current information when calculated, Fluent's SOFCs model then applies species fluxes to the electrode boundaries thus sinking oxygen and hydrogen and also sourcing water in the appropriate flow channels.

Section 3.3 has introduced the reader to the basic operation of the fluent SOFC module and how it operates. Using this model without a the basic understanding of how it operates is very important to understand its limitations. The most important limitation is the fact the electrolyte is not actually included in a 3d form as has been discussed in detail earlier in this chapter. A key point in tuning the models is the i_o, current exchange density values as outlined in equations 3-3-24 and 3-3-25. The current exchange density is a value that is very difficult to measure and it was decided that when modelling the MT-SOFCs that these values would be fitted after every other value was found.

The fluent model also does not include equations to allow electron transport through the electrolyte as a function of temperature. This would be very important

for modern ceria based electrolytes. Modern SOFCs are now often built using several layers of anode and cathode with various current collection and catalytic properties. Should anodes or cathodes with these layers be modelled then questions will arise about the suitability of the models presented in this section. In particular as described in equation3-3-4 and equations 3-3-30 the active zones inside the cell are attributed to the electrolyte/cathode and electrolyte/anode faces. However in reality these zones actually spread into the anode and cathode are certainly 3d in nature measuring 50 microns or more. This means that in reality the SOFC module is using a much simplified assumption of the actual conditions within a MT-SOFC and it was the aim of this section to present the modelling method to the reader. Although these models are simplified the scale of on which these simplifications would have to be included, ie. the electrolyte thickness and 3phase boundary thickness, to accurately model would require extremely small meshed cells and thus CFD may not be the best approach for such detailed modelling anyway. Regardless CFD has been used in the field for stack design with much success. For more details please refer to section 2.1.4.

Chapter 4 The development stages of the experimental apparatus

4.1 Introduction to the development of the experimental apparatus

The majority of the work carried out during the initial half of the duration of this thesis work was focused almost completely on the development of the high temperature apparatus. The scientific content of this phase, even though it took much longer than expected to realize and required some backtracking with regard to the original goal of building a device that could contain bundles of MT-SOFC's, has been deemed not as significant to the outcome of the final goals of the thesis.

Therefore the main quantity of the initial work that was performed before the concept of a high temperature wind tunnel was conceived can be found in Appendix II (A-D). In this appendix the reader will find the outline of an original concept to test single cells and stacks. Also to be found in this section is a set of numerical calculations derived to perform the function of estimating the outlet temperature of the flow of air through a pipe. The original concept was that the airflow alone could provide enough heat to allow operation of the tested cells.

The result of this initial numerical and experimental study clearly showed up the need for balance between the inlet flow rate in some kind of test chamber heating. These initial calculations also showed that the heating demand of such a system or to be shortly thereafter conceived a high temperature wind tunnel, would be massive somewhere in the order of 7 to 8 kW. Normal ovens used in the labs at the Upper Austria University of Applied Sciences generally are heated to 800°C with 4 to 5 kW of power so it became abundantly clear that the high temperature wind tunnel system should be small in volume and highly powered. This clearly meant a three phase power would have to be used.

4.2 Second developmental stage of the high temperature wind tunnel

With the main conclusion of the previous section being that the air alone would not provide enough energy to heat up the reactor housing. It was decided to experiment with different methods to try to force more heat into the incoming air and different methods to maintain the testing chamber temperature. Originally the use of equipment available for heating the incoming gas and testing chamber was limited by two very tight constraints. The first constraint was that open flames were undesirable and the second constraint was that the cost of the heating elements had to be kept to an absolute minimum because of funding constraints at the time.

In the previous section it was found that the heat absorbed by the air flowing through a straight pipe would not be enough to supply substantially enough heat to a test chamber, see details in Appendix III – (C). The only way to realise a condition where the testing chamber would be 850°C with only heat provided by the pipe would be to keep the walls of the air inflow pipe at temperatures much higher than 850°C. However because of the low airflow rates this would have hardly any effect on the output temperature of the air.

Subsequently from a very brief literature review it was found that an inlet pipe made out of a coiled pipe may help the absorption of heat into the gas at low flow rates [30-33]. Figure 32 is an illustration of a pipe that was used to increase the heating performance. The pipe was heated with a 1 kW heating tape the same as those outlined in Appendix III - (A) wrapped around the coiled pipe that also contained one of these heating tapes located inside the coiled pipe. However this method did not increase the temperature of the air at the end of the pipe sufficiently.

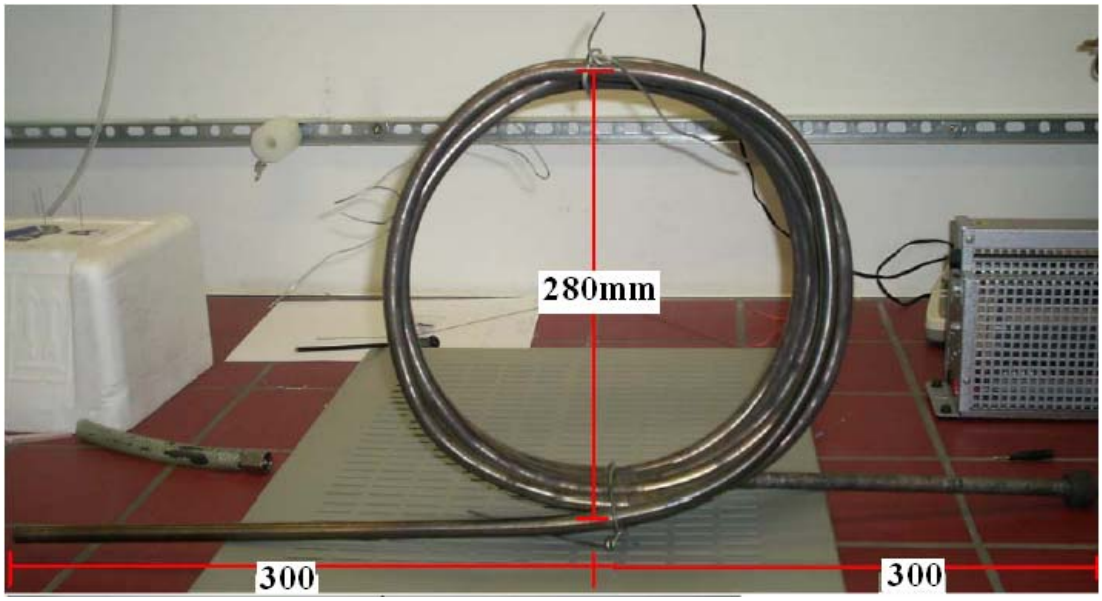

Figure 32: Photograph of the coil, 6 coils deep, that was built to enhance the heat transfer to the inlet air..

Figure 33: Initial experiments using a coil that had a straight section on the end that was connected into the high temperature wind tunnel.

4.3 Solution for the chamber heating

Using standard quartz halogen light bulbs (Quartz infrared Halogen – IR lamps Philips N.V. Holland) within a metal box open at either side, the following heating rates as shown in Figure 34 were obtained from a simple test. The bulbs used were standard 500 Watt rated and it was found that two bulbs in the box seemed sufficient to heat up the box to just below 900°C. Due to the relatively low cost of these bulbs and their impressive heating output it was decided that future designs would be based around this heating element. It was found that as long as the connections at either end of the bulbs were kept cold, as in below 500°C the bulbs could be heated up too above 1000°C.

The basic principle of operation of these heating elements is that they radiate heat to a surface thus increasing its temperature. It was conceived that this principle could be adapted in two ways to act as the means of heat generation in the high temperature wind tunnel. Firstly if the heating elements were placed in the oxidant flow path and a substantial metallic heat exchanger comprising of a multitude of flat surfaces to absorb radiation was developed, this method could be used to transfer to radiation heat into the oncoming gas. A second method involving placing the light bulbs outside the gas flow and allowing the radiators to heat the top and bottom walls of the testing apparatus. These top and bottom walls would not only radiate heat to the fuel cells under test but also convect heat into the air stream in the high temperature wind tunnel.

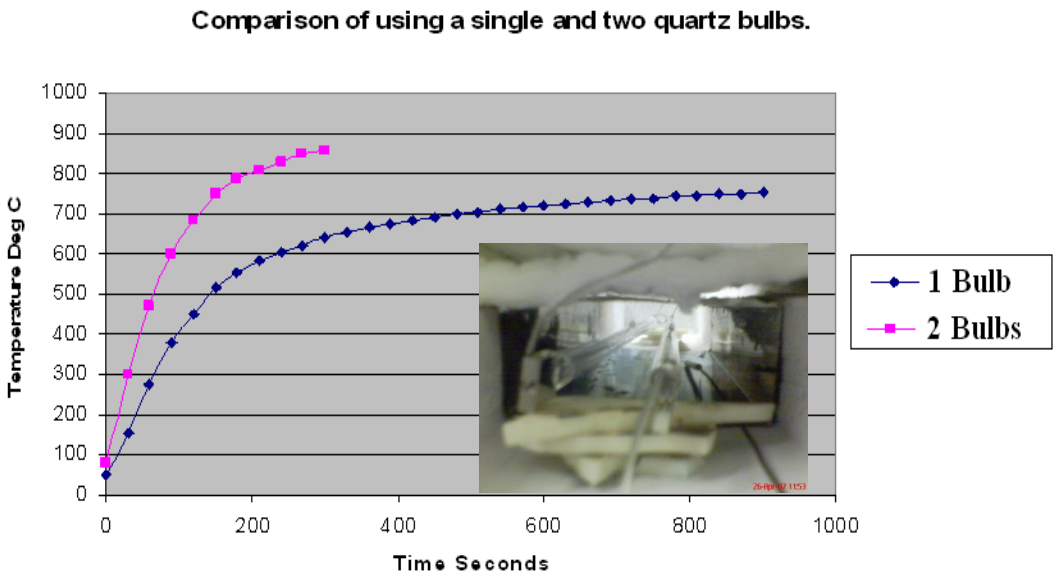

Figure 34: A simple temperature curve over a period of time for a single and two bulbs in a box experiment. The insert shows the bulbs in the box.

Figure 35 briefly shows an outline of an original concept that was tested using CFD software. In Figure 36 the top two pictures show the physical structure and meshing of that structure for this brief simulation. The red and blue tubes represent a stack of MT-SOFC's. The positions where holes can be seen running perpendicular to the cells are the positions of the light bulbs described above.

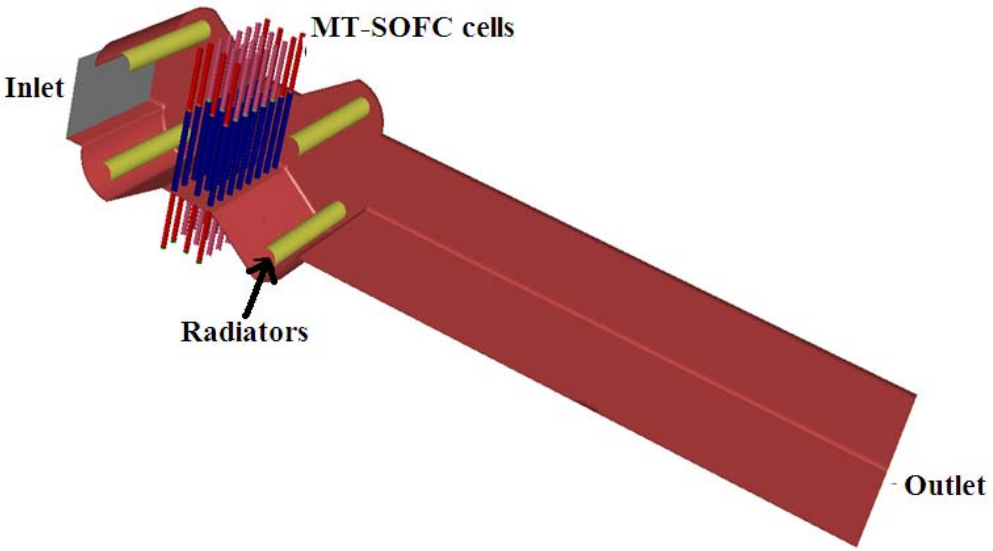

Figure 35: Concept A wind tunnel design where the cells are indicated by the blue tubes.

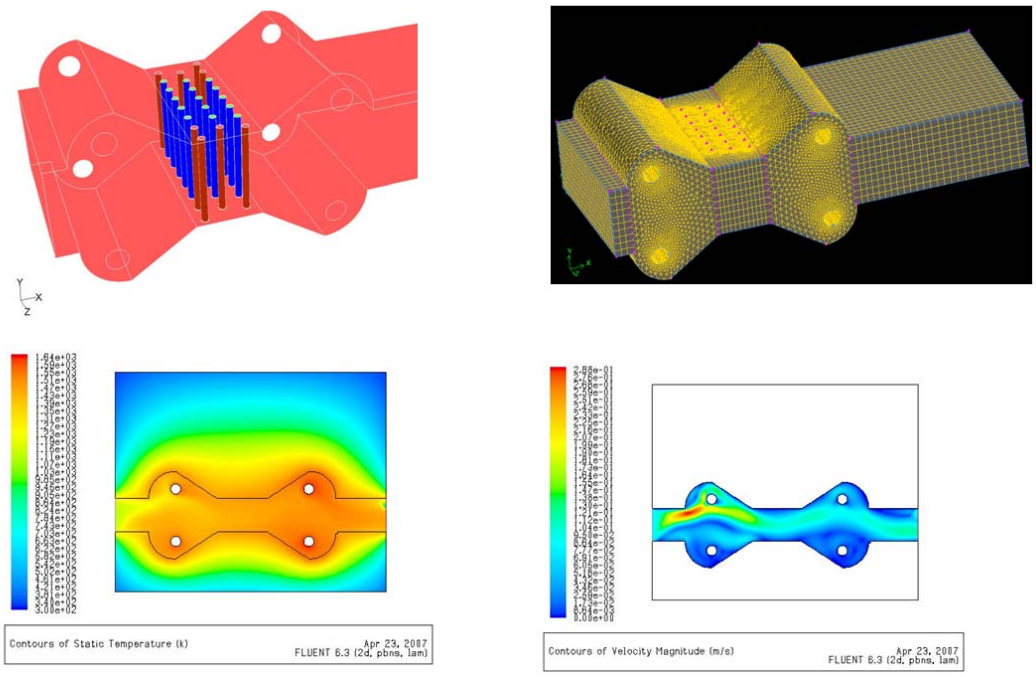

Figure 36: An original concept tested by CFD simulation that shows contours of temperature and velocity magnitude.

These light bulbs radiate heat onto the cells and also help to heat the incoming gas. However as it can be seen in the bottom left (contours of static temperature) and bottom right (contours of velocity magnitude) where the temperature profile would be relatively homogeneous the flow pattern would certainly not. This is because of the protrusions where the light bulbs must be located allowed unwanted velocity profile movements especially in slow flow regimes. A possible solution could be to seal off these bulb heating chambers with quartz glass but it was decided that this would complicate the design too much by having to join metallic and non metallic materials together.

A subsequent design involved the generation of a heat exchanger built around the bulbs that would be directly placed in the gas flow path. The principle of operation of this device was that the light bulbs should radiate heat to the flat plates which, then allows air passing into channels between the plates to conduct heat. This air, containing heat, would then be driven into the test chamber. This combination of external chamber heating and heat exchanger would provide the heat to test the cells.

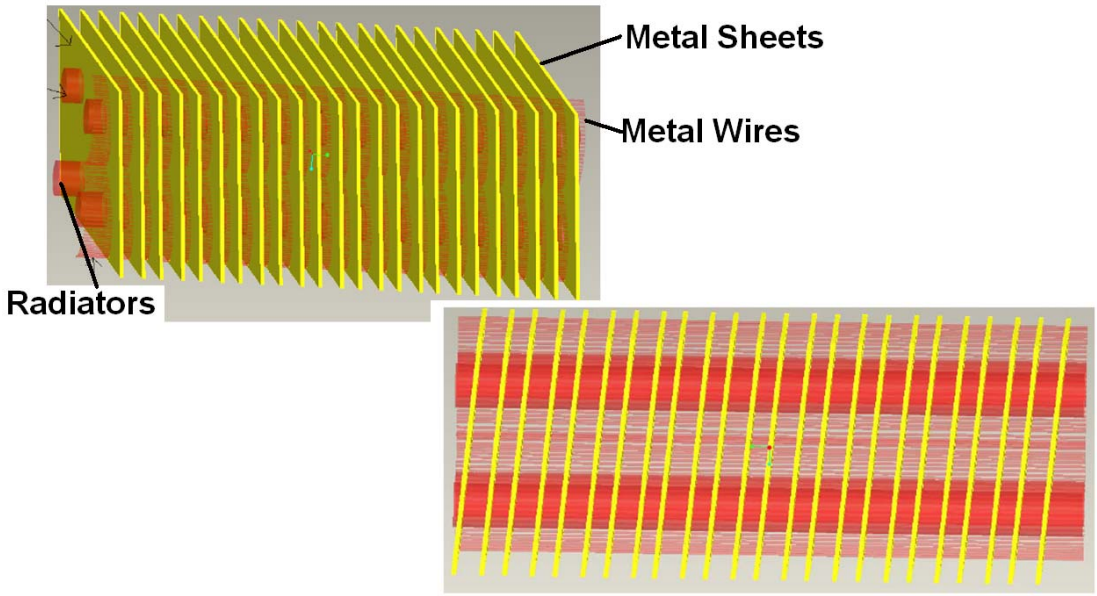

Figure 37: Image outlining the concept was in the flow heat exchanger from the radiators to the gas via metal plates.

Illustrated above is a concept drawing of the heat exchanger where it should be noticed that the metal sheets are staggered to absorb as much radiation as possible from the light bulbs. This heat exchanger was built and tested and was used in an experimental apparatus that contained the first attempt at experimenting with a bundle of cells. Numerical data of its performance was not noted. From experience it can be said that exchanger worked extremely well as it provided an additional function as a diffuser see Figure 38 below. However it was probably more suitable to higher air flow rates on the order of 100cm/s or more.

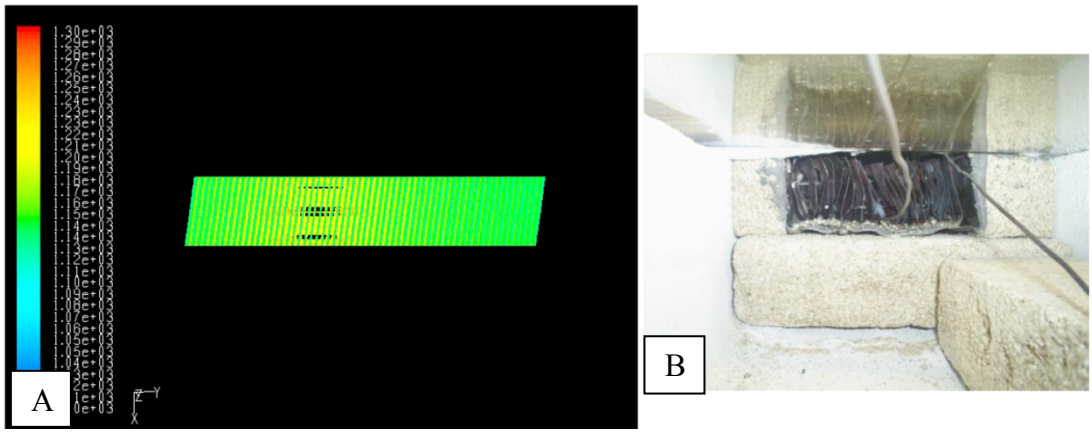

Figure 38: (A) A numerical simulation result of the heat exchanger (B) that was built.

Shown below in Figure 39 is a concept that was tested and used to perform the first test on the bundle of MT-SOFC's. This concept included both the heat exchanger as described previously and also radiators placed above and below the testing chamber. However there were many problems with is its design that would not be seen until later on in the study. A main problem was sealing the wind-tunnel to be gas tight.

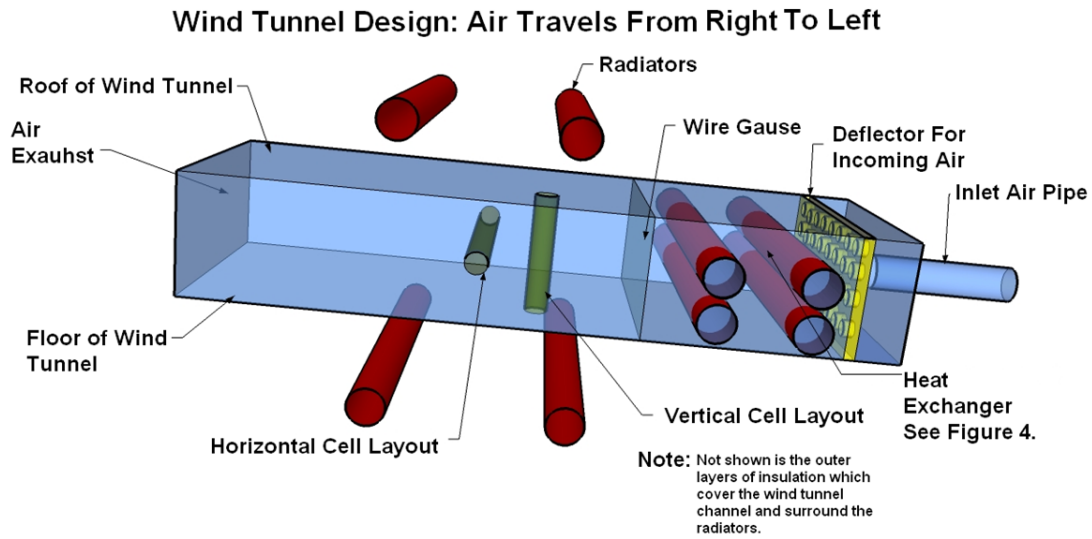

Figure 39: Concept B that includes the heat exchanger as outlined in Figure 38

Figure 40: A bundle of MT-SOFC's that was build related to the concept B design.

Figure 40 shows the first ever and consequently final attempt to build a bundle of MT-SOFC's into a high temperature wind tunnel during this study. In this case, six out of the seven cells worked. However many problems were found related to the high temperature wind tunnel design. Most notably the current connection from the cells proved to be extremely difficult. The fact that the wind tunnel was not designed gas tight made it easier to feed the cathode side wires out of the wind tunnel. However in a design that would require the wind tunnel to be gas tight, such wiring conditions would not be possible. A key point of these bundle tests were that each cell should be monitored and this meant that serial or parallel connection was impossible and the reason for the complicated wiring.

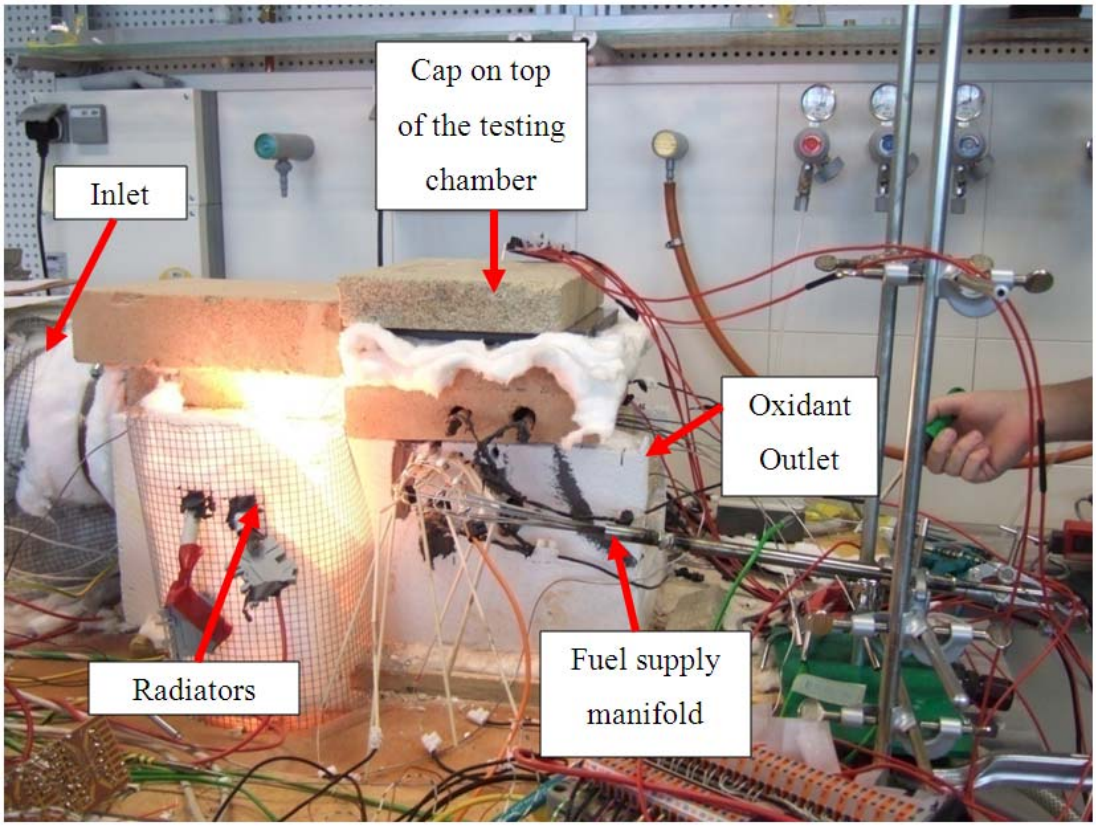

Figure 41: An external view of the concept B wind tunnel design that was built. .

Figure 41 shows the outside of the high temperature wind tunnel described in concept (B). This wind tunnel contained 8 X 1000 W radiators. Two of these radiators were placed above and below the testing chamber and four were placed inside the heat exchanger that can be seen in the right areas in the photograph

(produced by the light bulbs). In hindsight this was a very crude way to build the wind tunnel. However it functioned but had so many problems that it became clear that testing bundles of cells would not be feasible. This was attributed to two reasons. The first reason being that the cells often had to be replaced and this was extremely difficult to do without disturbing the other cells because they were all connected to the same of gas feed shown in

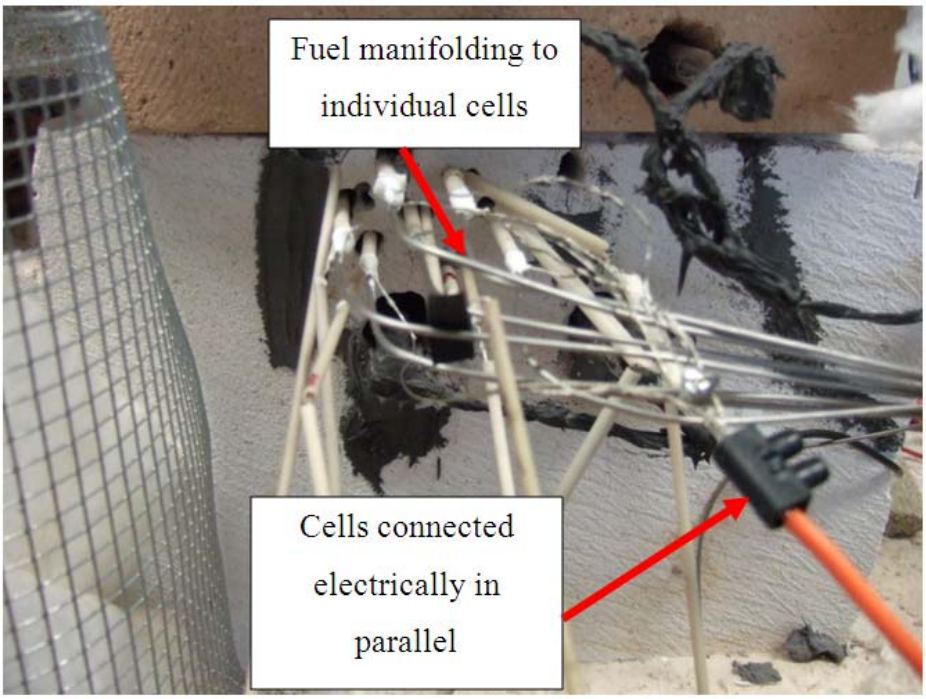

Figure 42. The second reason is that at this stage the techniques used to seal cells were very crude and constantly leaks occurred. Leaks of hydrogen result in flames, which then damages cells in the vicinity. The wiring of the cells as outlined above was also extremely difficult and monitoring of the cells proved just as difficult.

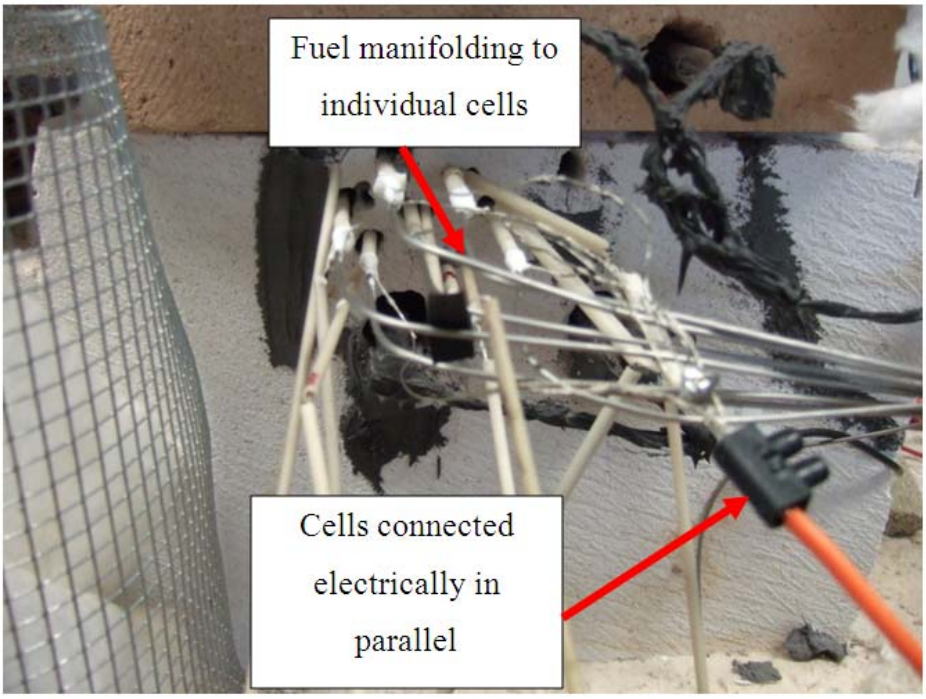

Figure 42: Hydrogen fuelling and anode side current collecting of the fuel cells in the concept B high temperature wind tunnel.

Following the attempts to realize concept (B), a further concept, concept (C), as shown in Figure 43 and Figure 44 was envisaged. The idea hinges around two key points. The first point is that cold sealing would be used to seal the cell in a cold zone at below 250°C using a high temperature silicone (Fischerwerke GmbH Germany). The second key point is that the cells, instead of each individually being loaded into the wind tunnel as was the case in concept (B), each of the cells would be fixed by a combination of holes in a set of four guide plates and the cold silicone sealing as described before would be used on the outermost plate.

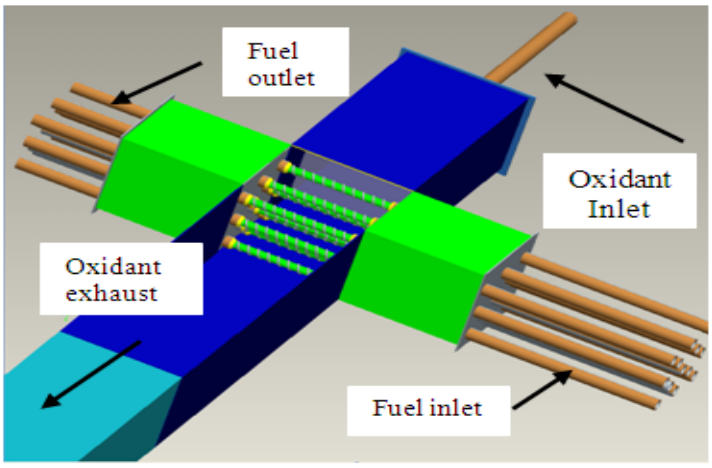

Figure 43: Concept C looking through the top wall at a bundle of cells inside the wind tunnel.

Figure 44 (A) shows the tray that would slide into the wind tunnel- This sliding in and out of a tray of cells would be achieved by either using a new and novel single inlet and outlet fuelling exhaust system (see Appendix IV), as shown below in Figure 44 (B) , or by using the old single inlet single out the method. The black substance on this picture is a high temperature sealant (Kamin + Ofen Dichtmasse UHU GmbH & co Germany) that was conceived to be used to hold the cathode wires and also the anode reference wire, which is taken outside the cell.

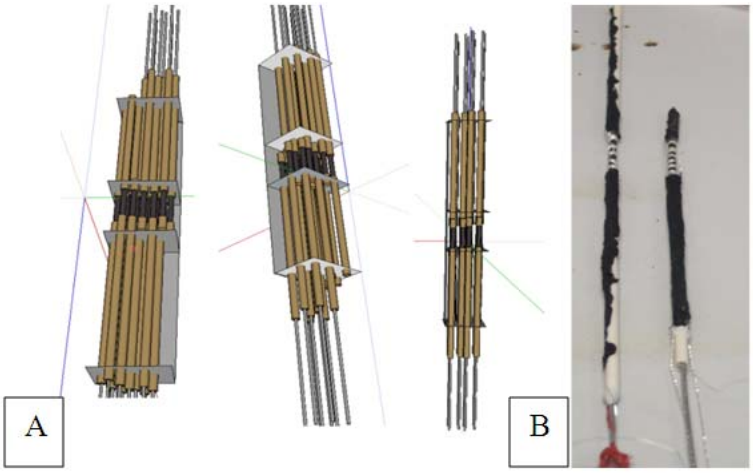

Figure 44: Cell loading case for concept (D).

However as shown below in Figure 45 (D) even though the concept may have seemed quite good, in practice it was later found that the buckling of the wind-tunnel walls from the thermal stresses induced by the radiators above them, meant that the wind-tunnel body would not stay in a reliable shape. So facilitating the sliding in and sliding out at the loading tray of fuel cells could not be guaranteed. One of the most detrimental attributes of the way that this wind tunnel was built, because of cost saving, was that the silver braising used to join the sheets of metal together tended to weaken and also become porous. This meant that back diffusion effects of oxygen into the high temperature wind tunnel would mean that when using low concentrations oxygen, by using high concentrations of nitrogen in the chamber, oxygen diffusion into the wind tunnel was difficult to avoid. Please note that in the Figure 45 (B) below the light bulbs are positioned parallel to the wind tunnel body rather than transversely, which had been the norm up to this build. This new layout

of the light bulbs meant that they radiated over a larger area of the wind tunnel and no extra inlet air heating was needed.

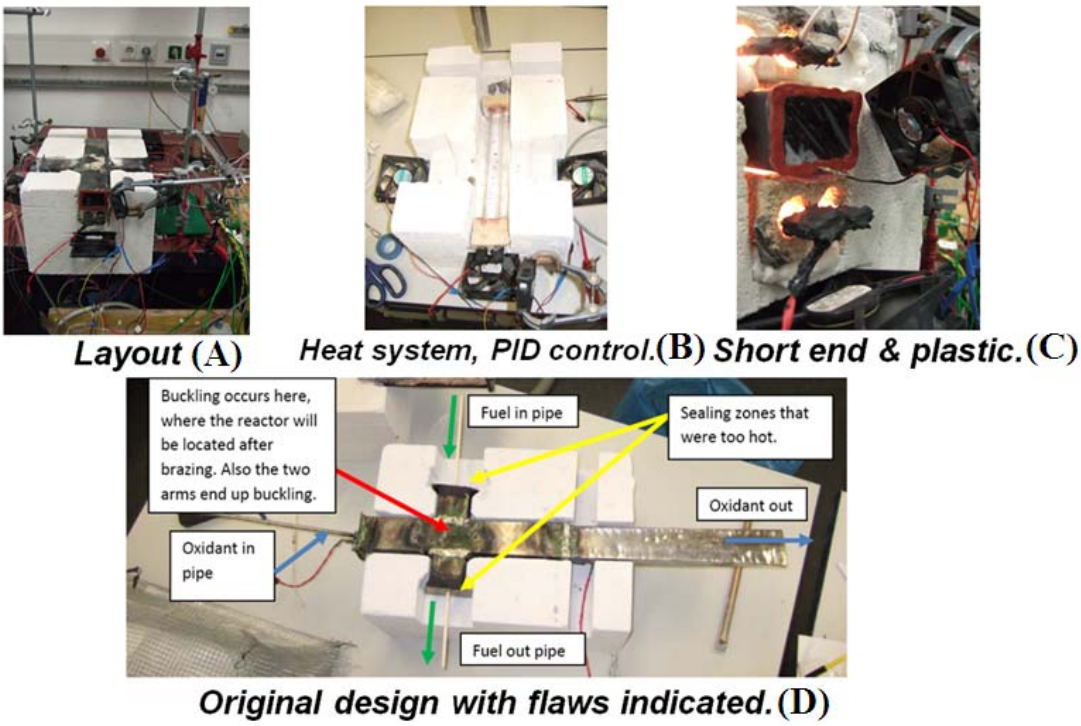

Figure 45: The building of concept C where the layout is shown in (A), Heating system in (B), infra red transparent plastic end cap (C) and outline of problems with the design (D)..

As also illustrated in Figure 45 (C), attempts were made to block the end of the wind tunnel with a high temperature plastic (Oven bags, Reynolds Kitchens® USA) that would allow infrared radiation to pass through for thermal camera imaging and also block back diffusion through the end of the wind-tunnel. This blocking could be achieved by piercing small holes in the plastic sheet and initially seemed viable until it became clear that the blocking would melt as soon as reasonably large flow rates were introduced. Another attempt as shown in Figure 45 bottom was to extend the length of the end of the wind tunnel. However this helped in a very small way to prevent oxygen back diffusion, because of the poor silver, leaking oxygen still diffused into the wind tunnel. Also extending the end of the wind tunnel made it difficult to get good thermographic images.

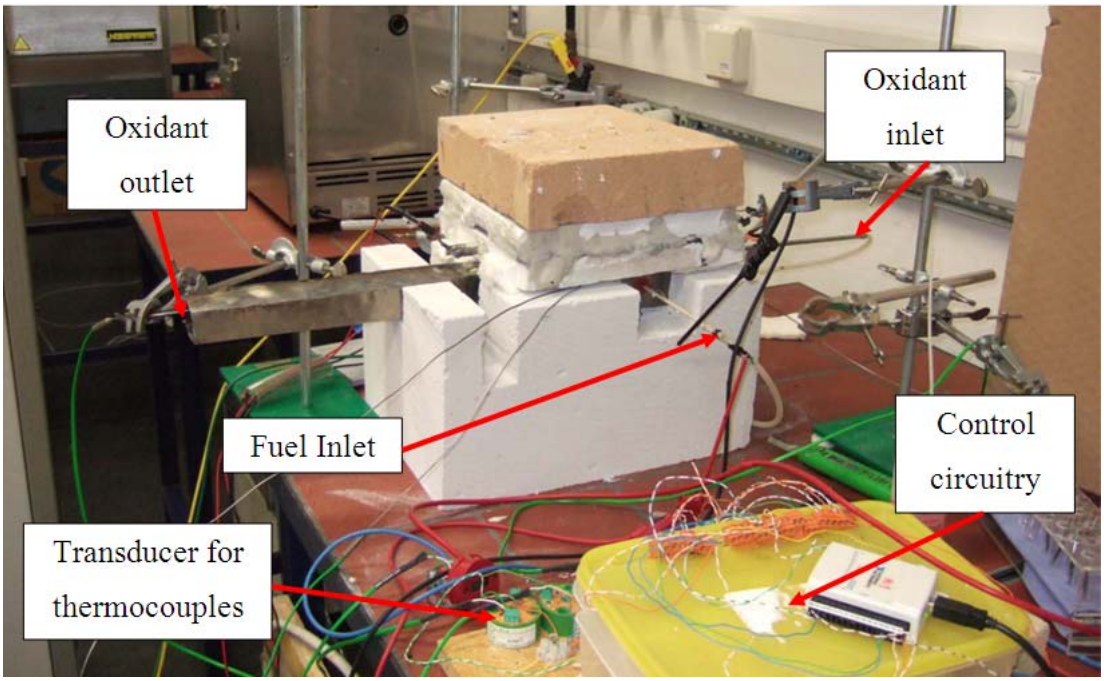

Figure 46: A picture showing the layout of the experimental concept (B)

At this stage having seen the difficulty in building a low-cost apparatus that could easily allow assemblies of MT-SOFC bundles to be tested. It was decided that it was sensible to just focus on single cell validations to get good science out of the amount of time that was left in the study. Information about the heating control system software developed during this study over 3 years and circuitry for the high temperature wind tunnel can be found in Appendix III (D) and a introduction to PID control that also had to be researched for the implementation of the code and tuneing of the controllers is can be found in Appendix V VI and VII.

4.4 Third developmental stage of the high temperature wind tunnel

At this point in the study it was considered that a high temperature wind tunnel had to be designed in such a way that single cell measurements could be guaranteed. It was also decided that because a goal of the thesis was to examine both single MT-SOFC's in cross-flow and larger bundles thereof, to examine the effects of the wake at the rear of the cylinder at higher Reynolds numbers, that the final wind tunnel should be oversized a bit.

Before attempting to resolve the mass transfer questions for a single 2.5 to 5mm diameter MT-SOFC experimentally, it was thought that a good approach would be to first attempt to simulate and then experiment with a larger "cylinder diameter" to increase the resolution of the mass concentration measurements around the perimeter. To realize this larger "cylinder diameter" it was planned to build a bundle of MT-SOFC that will surround a ceramic tube.. For more information on the challenges of designing a high temperature wind tunnel please refer to [119]. The bundle of MT-SOFCs was to be inserted into the newly designed high temperature wind tunnel that is designed to measure Reynolds numbers from 0 to 120 for this 0.0175 m diameter cylinder.

To indicate possible wind tunnel dimensions two main factors have to be taken into consideration. Both of these factors are related to the volumetric flow of gas through the wind tunnel. The first factor is related to the range of wake dimensions and internal flow regimes that can be studied. Ideally the generation of a wide range of Reynolds numbers that would allow the development of the wake from creeping flow all the way up to Von Karman vortex shedding would be desirable. However a simple calculation will show that the volumetric flow rates required in the wind tunnel, that would hold the MT-SOFCs, the MT-SOFC's having a height of 40 mm and the diameter 3.5 mm, would be massive and unrealistic given the size of the equipment available at the Upper Austria University of Applied Sciences Figure 47 shows how the Reynolds number will increase as a function of bulk gas velocity. It can be seen that with a cell diameter of 0.3 cm would never provide a broad range of wake geometries and effects. The 1.5cm diameter tube causes a larger increase in Reynolds number for the same bulk gas velocities. However the problem is not so easy to solve because note that this means a balance between volumetric flow and heat provision is required. Also the walls of the wind tunnel retard the wake development.

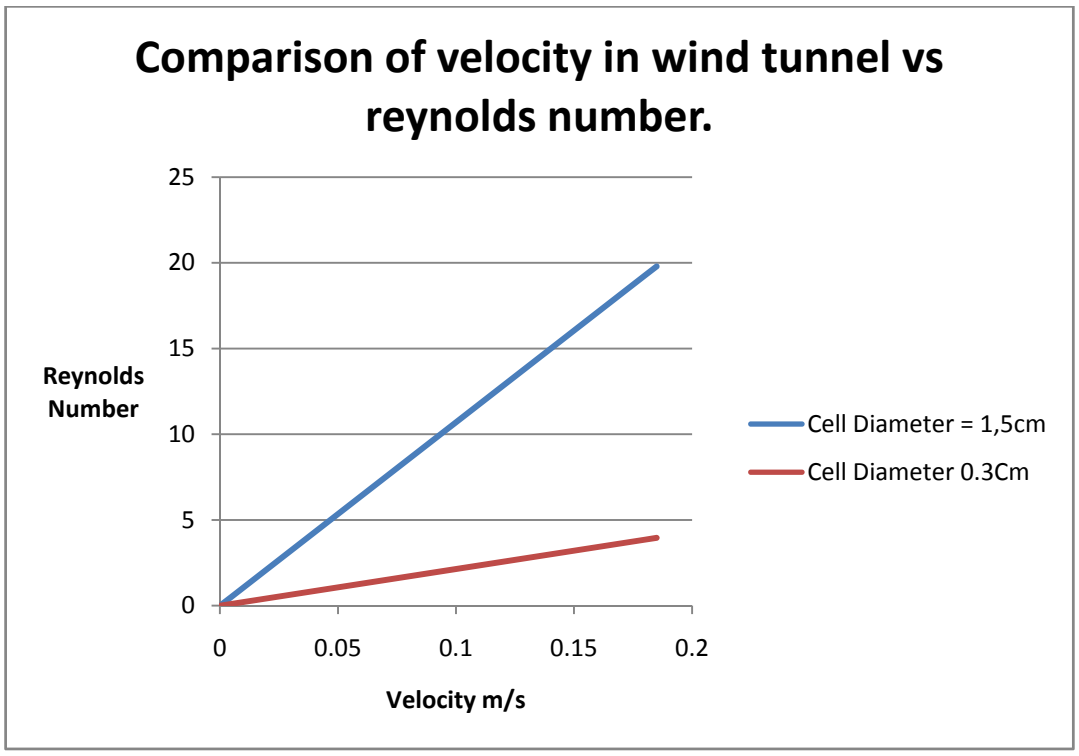

Figure 47: The velocities required to increase the Reynolds number on a 1.5cm and 0.3cm tube.

. Zdravkovich pointed out that the onset of the Von Karman vortex shedding is mildly delayed by the side walls [73] and that they are strongly retarded by the top and bottom walls [120]. Two useful plots can be found these references that give very useful information about how the wake development can be retarded by the top and bottom walls of a wind tunnel.

A value of Re = 70 has been selected as a desirable Re for the onset of von Karman shedding because [120] indicates that after a L/D of 10 (cylinder length/ cylinder diameter) the effect of the top and bottom walls has a massive retardation effect per m height. Surprisingly the side walls do not have such a drastic effect [120] and to reach a Re of 70 a D/B (diameter of the cell / width of the side walls) value of 0.1 would seem appropriate. To make concentration measurements from creeping flow regimes to the onset of vortex shedding the ideal wind tunnel size for a cylinder with a diameter of 0.0175 m, according to the plots in the previous two references, would be about 0.175 m high (L/D=11.42) and 0.175 m wide (D/B = 0.1). At the absolute maximum 100 l/min flow restriction, in such a wind tunnel, the Re

would be 22.7 meaning that Von Karman vortex shedding would not occur and the heating losses from the wind tunnel wall surface area would be very high.

Thus reducing the cell diameter would seem to be an option to reduce the effect of the walls but reducing the cell diameter increases the flow rate required to onset the vortex shedding as seen in the reynolds number formula. For a cell diameter of 0.01 m and with reference to the plots discribed in the previous paragraph in reference [120] the the dimensions should be about 0.1 m wide and 0.1 m high with the max Re possible being 44 and for a diameter of 0.005 m the height should be about 0.05 m and the width 0.05 m and the max possible Re with the 100 l/min restriction would be 88. Such a wind tunnel may be built in the future but for now the increased resolution capability with the wide diameter cylinder will be used in a small wind tunnel 0.04 m high and 0.10 m wide.

Engineering drawings and construction of the metallic part of a high temperature wind tunnel can be found in Appendix VIII. Figure 56 shows an illustration of this wind tunnel including the heating system and insulation.

4.5 In-House Building of MT-SOFCs

While the building and manufacture of micro-tubular solid oxide fuel cells is not a key theme of this work the cells had to be built in house by the Ph D candidate. The type of cell used most often and through the entirety of the end of the study was the anode supported cell. For this type of cell a substrate, the anode, was provided by Alpps GmbH, Austria or Ezelleron Gmbh, Germany. The cathode and electrolyte was then coated onto the substrate using methods privy to these companies at the Upper Austria University of Applied Sciences by the Ph. D. candidate. However some work done in the initial phases of this thesis was done using electrolyte supported cells (Adelan, UK) and in this case the anodes and cathodes were coated onto the electrolyte.

During the course of this work the cells were changed from the electrolyte supported type to the anode supported type because of the availability of this type of cell and also because of the higher powers they could produce. Figure 48 below shows an example of an electrolyte supported cell and a cracked cell where the anode can be seen beside an AAA battery for comparison. Figure 49 below shows the anode supported cells used. Figure 50 shows a schematic of the of the manufacturing processes involved in anode supported cell manufacture. Figure 51 shows the spraying machine that was used to coat the cathode onto both the electrolyte and anode supported cells. Dip coating was later used to make these coatings and through a combination of trial and error and measurements made with an electron microscope they thicknesses of the layers were made to be the same as spray coating layers.

Figure 48: A sample of an electrolyte support itself that was initially used at the beginning of the study.

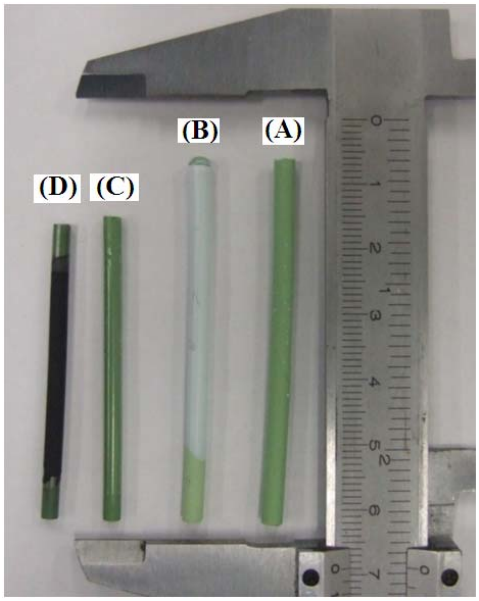

Figure 49: A picture showing from left to right, (D) a fully made MT-SOFC, (C) one with just the electrolyte after sintering, (B) when with electronic before sintering, and (A) the substrate of the anode prior to sintering.

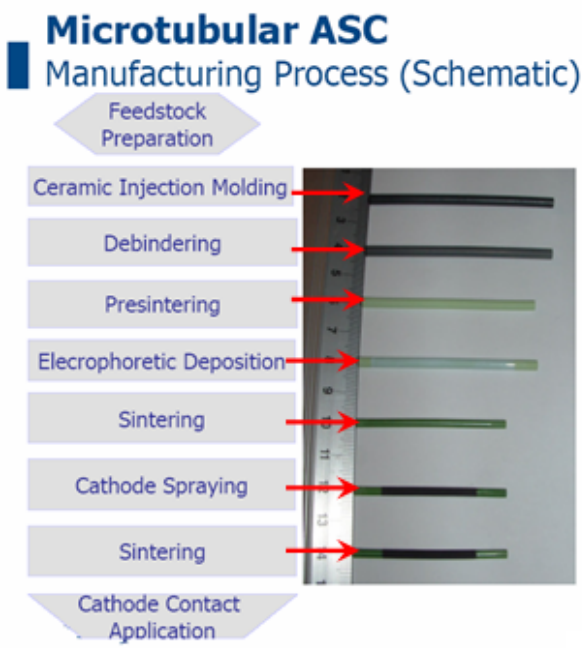

Figure 50: A picture showing the different stages in the process for making electrolyte supported MT-SOFCs.

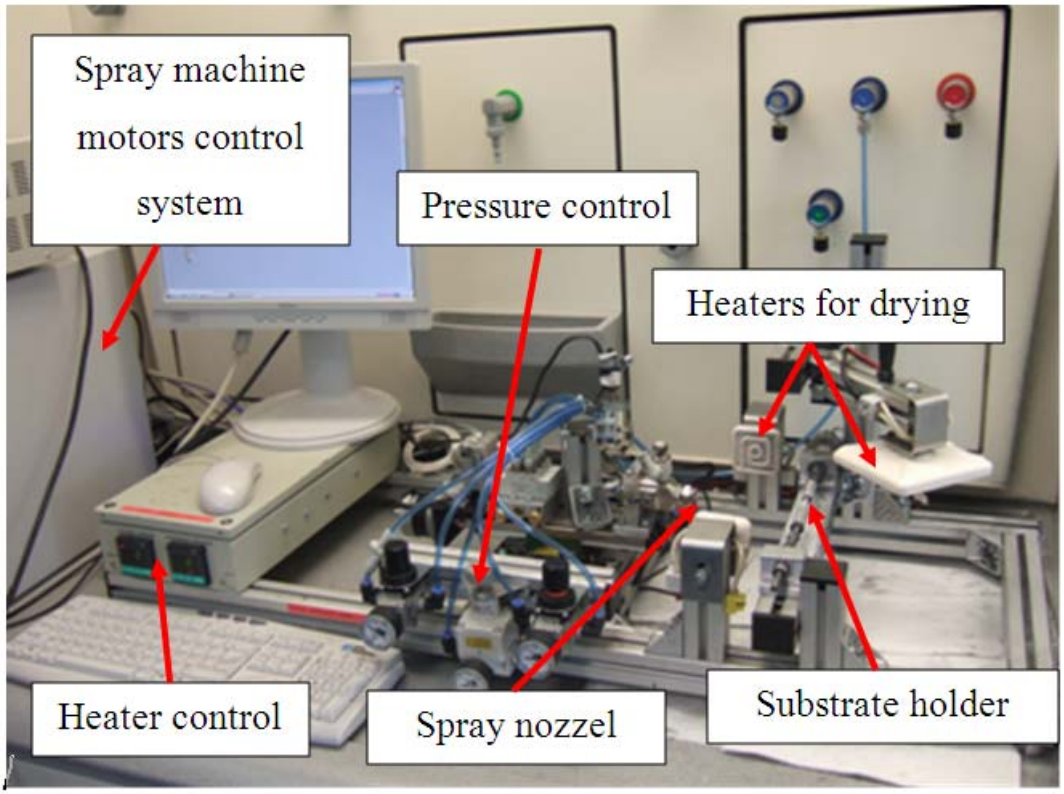

Figure 51: An image of a computer-controlled spraying machine that was initially used to spray the cathode onto the cells.

Chapter 5 Experimental and analytical procedures

The next 3 chapters, Chapter 5; Experimental and analytical procedures, Chapter 6; Experimental and analytical results and Chapter 7; Discussion on each of the studies, cover the following listed below sequentially:

1. Effect of buoyant flows in a MT-SOFC reactor.
2. Investigation of temperature measurements of MT-SOFCs
3. Modelling of a MT-SOFC in cross flow
4. Using a MT-SOFC the measure the concentration of o_2 around a perimeter.
5. Modelling the concentration around the perimeter of a MT-SOFC.
6. An attempt to measure the O_2 concentration around a larger cylinder and modelling.

The numbering is designated in this order, in each chapter, to allow the reader to quickly follow a theme, as the themes have been broken up to fit the chapter titles listed above.

5.1 Introduction to CFD simulation and analytical calculation to estimate the effect of natural convection is a MT-SOFC reactor

Cylinders are often used for heat transfer purposes especially for heat exchangers because of the extended surface they afford. Heat exchangers such as tube-fin, plate-fin are examples of some alternatives. Heat transfer from and to cylinders fall into the categories of either free of forced convection. Free convection implies that the movement of the fluid is due to buoyancy, gravity and variable densities within a heated fluid. Forced convection, the second category, is where buoyancy, gravity or variable densities are not the main causes of the motion of the fluid, but rather the fact that the fluid is driven by an external source normally a fan, compressor or

blower. The isothermal flow of a viscous fluid, with the free stream velocity being less than the speed of sound, are highly dependent on the associated temperature fields that depend on the Prandtl, Grashof and Nusselt numbers.

The Prandtl number, called after Ludwig Prandtl a German scientist, is a dimensionless number approximating the ratio of momentum diffusivity (viscosity) and thermal diffusivity [112]. In heat transfer analysis, thermal diffusivity (symbol: α) is the ratio of thermal conductivity to volumetric heat capacity. These two parameters have a decisive effect on the extent of the temperature and boundary layers and also the rate at which heat is transferred under free and forced convection conditions.

$$\mathrm{Pr}=\frac{\rho.\upsilon Cp}{k} \qquad (5\text{-}1\text{-}1)$$

Where "ρ" is the fluid density, "Cp" is the fluid specific heat capacity, "υ"is the fluid kinematic viscosity and "k" is the thermal conductivity.

The Grashof number is a dimensionless number in fluid dynamics, which approximates the ratio of the buoyancy to viscous force acting on a fluid. It was named after the German engineer Franz Grashof [87].

$$Gr=\frac{D^3.g(Tw-To)}{\upsilon^2.To} \qquad (5\text{-}1\text{-}2)$$

Where "*D*" is the cylinder diameter, "g" is gravity, "T_w" is the cylinder wall temperature "T_o" is the fluid temperature and "*v*" is the kinematic viscosity.

In the majority of applications it is not necessary to have exact values for the local temperatures and velocity fields. The overall heat transfer "Q" between the body and fluid field can be expressed through the Nusselt number, using the following equation [120]:

$$Q = \frac{\overline{N}u.(Tw - To)\kappa A}{D} \qquad (5\text{-}1\text{-}3)$$

Where $\overline{N}u = \overline{\alpha}.D/\kappa$ and $\overline{\alpha}$ is the mean heat transfer coefficient. K is the heat transfer coefficient. The Nusselt number is another dimensionless number that measures the enhancement of heat transfer from a surface that occurs in a 'real' situation, compared to the heat transferred if just conduction occurred. Typically it is used to measure the enhancement of heat transfer when convection takes place. The bar over the top of the Nusselt number indicates the mean Nusselt number over the whole surface of the cylinder and the unaltered script, the local Nusselt number, along the circumference.

It follows from the dimensionless energy equation [112] that:

$$Nu = f(\mathrm{Re}.\mathrm{Pr}.Gr) \qquad (5\text{-}1\text{-}4)$$

Where f = the frequency of shedding and Re is the Reynolds number.

These equations can be simplified when used in specific applications. If the heat transfer is confined to free convection the Re has little influence as no free stream will be present. Thus it can be neglected [112]:

$$Nu = f(\mathrm{Pr}.Gr) \qquad (5\text{-}1\text{-}5)$$

Then it can also be stated that when a free stream exists, such that forced convection is present, then the forces due to gravity and variable densities in the fluid are negligible, so the Grashof number can be ignored [112].

$$Nu = f(\mathrm{Re}.\mathrm{Pr}.) \qquad (5\text{-}1\text{-}6)$$

The latter two equations are very useful for the free and forced convection heat transfer regimes with regard to cylinders.

The role of natural convection within a bundle of cylinders has been studied by many other authors such as Chouikh et al. [69, 70] and Fowler and Bejan [121]. However it is important to know what to expect within a bundle specifically of MT-SOFCs especially for stack design considerations, to establish if there is evidence that highly buoyant flows could be possible within a stack of cells in cross flow and what effect this could have.

Initially in this study analytical calculations were undertaken on a single cylinder and an important number to consider is the Nusselt number (*Nu*). This is a dimensionless number and gives an indication of how well heat is being transferred from a surface into a gas or liquid. The following relates to a case where a heat flux of 0.5W for a cell is applied to its outer wall. A Nusselt number for forced and free convection cases must be uniquely calculated and then combined in a formula, equation (1), as recommended by von Böckh [122]:

$$Nu_{combined} = \sqrt[3]{Nu_{forced}^{3} + Nu_{free}^{3}} \qquad (5\text{-}1\text{-}7)$$

Such equations are useful to describe imperially what flows to expect around single cylinders but their application for bundles of cylinders must be quantified. It may be the case that these simple equations can be used to estimate the flow regime also within bundles. To establish the applicability of these equations it was decided to compare their predictions with the predictions of a CFD code. The power of CFD can calculate the heat-transfer, flow regimes and a whole lot more detail such as

boundary conditions. Such detail cannot be included in analytical calculations with the same accuracy and detail. This is done much more efficiently and accurately than any analytical attempts could ever achieve. It is very important to confirm that the CFD results are comparable to established analytical or experimental results and this is a reason for the prior and following analytical results. The point is that the CFD and analytical results should complement each other and this is a good indication that the models are correct. Of course an experimental analysis is the optimal methodology that should be used but no corresponding results for this specific case or apparatus was available to make the measurements. Thus it was decided that comparing two models based on sound scientific principle was sufficient to make an educated predictive analysis on the flow regimes within the bundle. The following calculations were performed on a bundle of staggered cylinders with a volumetric heat flux on each cell comparable to that of a micro-tubular SOFC of 2.6×10^6 W/m^3. This is illustrated in with the cylinders being of diameter 3mm and 10mm spaced apart from their centres. The results of these simulations can be found in section 6.1.

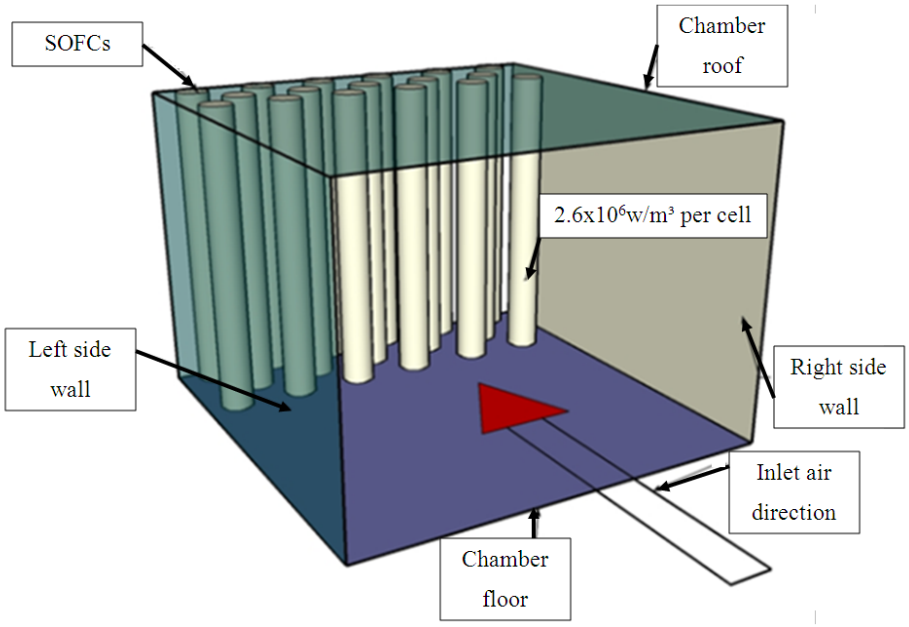

Figure 52: 3D simple representation of an array of horizontal cylinders as in a MT-SOFC stack.

5.1.1 Modelling parameters for the CFD models

The following conditions were applied to the CFD model.

- Periodic conditions without radiation.
- Volumetric heat flux of 2600000 W/m^3 this is equal to roughly 0.5 watts per cell.
- 3rd order discritizations, gravity enabled and the PRESTO! scheme for density were used in the CFD model.
- The inlet air temperature was set to 1100 K.
- The distance between the cells, in both the transverse and longitudinal directions, was 1 cm from their centres.
- The mesh contained 400,000 cells and the exit is 400 mm away from the working area and 50 mm in height to negate the exit effects on the area of interest.

Figures 54 to 56 show the meshing of the model.

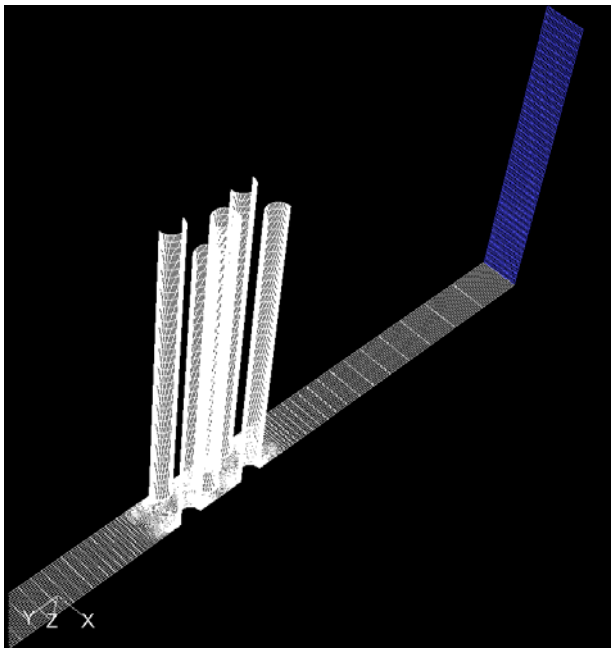

Figure 53: View of the meshed model though the symmetry walls. The blue mesh shows the inlet.

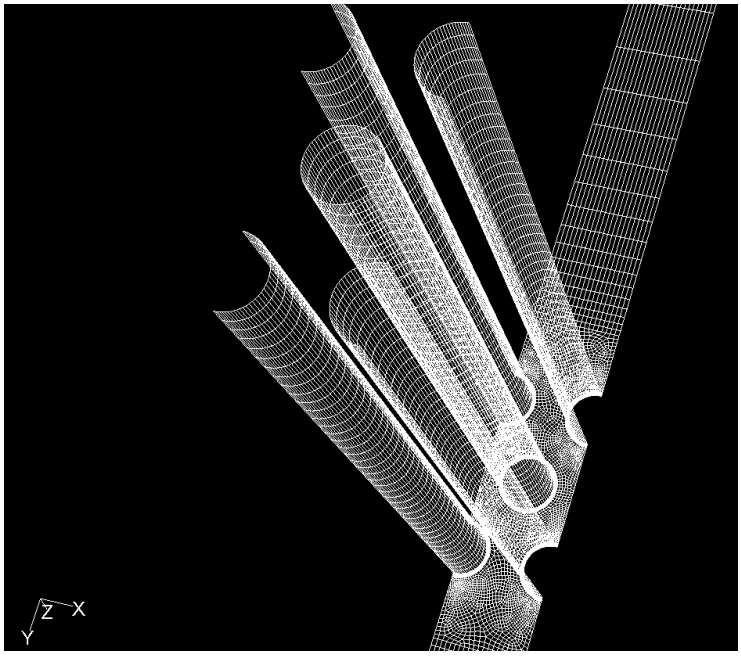

Figure 54: A more detailed look at the meshing of the tubes in the array.

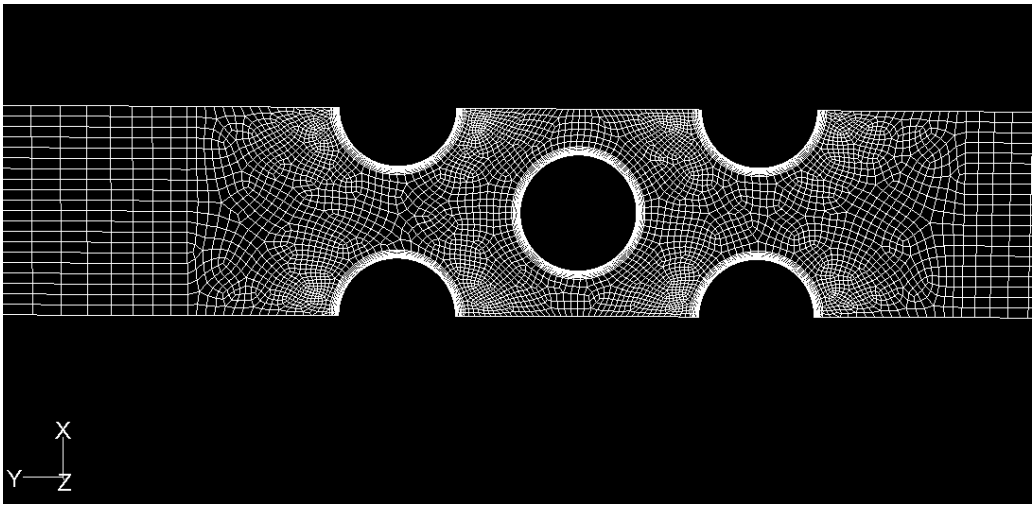

Figure 55: A more detailed look at the meshing around the cells that is coopered down through the 3D model.

5.2 Method for temperature measurement of a MT-SOFC

5.2.1 Introduction

The purpose of the first part of this study was to compare four different temperature measuring methods. The application of these tools for possible temperature monitoring or calibration of monitors of MT-SOFCs is explored. It was found that a thermographic camera is very useful to visualise the temperature gradient on the outside of a cell, while an electrochemical impedance spectroscopy method was useful for estimating the core temperature of a test cell. A standard thermocouple was also used in combination with the previous two methods. Furthermore an inexpensive laser guided thermometer was also tested for MT-SOFC temperature measurement.

This initial study has opened up a range of questions not only about the effect of the experimental apparatus on the measurement results, but also about the radial temperature distribution through a MT-SOFC in loaded mode. Both of these topics will be further studied through a computational fluid dynamic (CFD) study. This should provide additional interesting information about any differences between testing single cells and those within a bundle of cells. The discussed results are expected to be mainly temperature related which should have direct consequences on power output and optimised gas inlet temperatures.

5.2.2 Experimental apparatus

A high temperature wind tunnel for the sole purpose of MT-SOFC single cell testing has been developed as outlined in Chapter 4. During the development stage the performance and applicability of this device dramatically improved to the point where a +/- 1 °C temperature fluctuation at every temperature between 25-850 °C with flow rates between 0-30 l/min can be precisely regulated with the use of PID control. Figure 56 is an illustration that shows the layout of the wind tunnel where the wind tunnel body made of Crofer 22APU and Conicro 5010 W both from ThyssenKrupp AG Germany, The other area show the outside body of the wind

tunnel which consisted of top insulation (Porextherm GmbH Ultra board, Germany), bottom insulation (regular porous concrete block) and heating bulbs (Philips GmbH, Germany). The testing chamber and cell position are shown in Figure 57 (A).

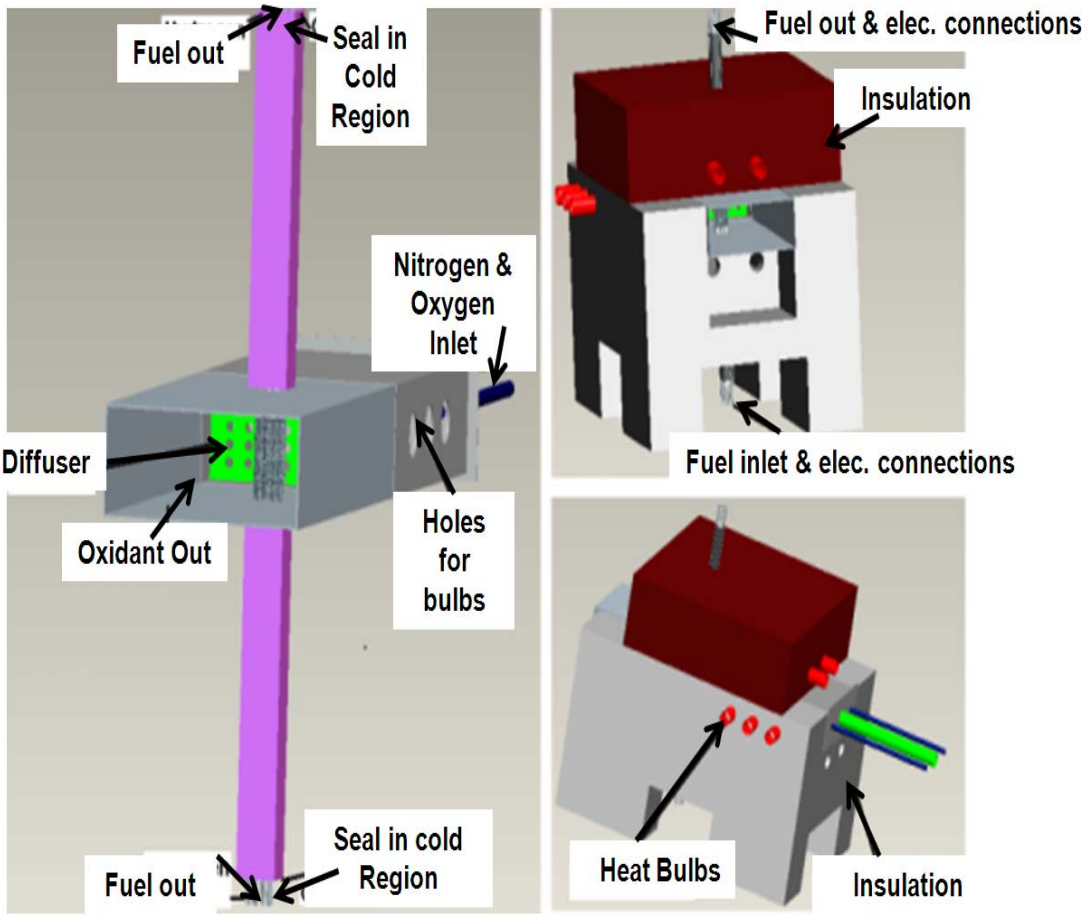

Figure 56: Schematic of the high temperature wind tunnel.

The equipment used to make the thermal measurements include thermo couples (Type K and LCD display unit TC Direct, UK) (Accuracy +/-1.5% or about 10°C at 750°C), laser guided thermometer (LGT) (Infrared Thermometer TP6 TROTEC GmbH & Co. KG, Germany), Thermal Camera (FLIR PM695 FLIR Systems, Inc, Germany) and a potentiostat with an impedance analyzer (Bio-logic SAS, VSP and Vm3 booster, France). The end of the wind tunnel was packed with insulation leaving a 2cm slit so that the measurements could be made, as shown in Figure 57 (B). To achieve good images the thermal camera had to be quite close to the end of the wind tunnel, also seen in Figure 57 (B). In order to prevent damage to the camera the insulation and an additional fan were used to maintain the camera lens

at a safe operating temperature. Note that all of the devices were calibrated by comparing their measurements to that of the thermocouple and adjusting emissivity values, for example, to get the best fit.

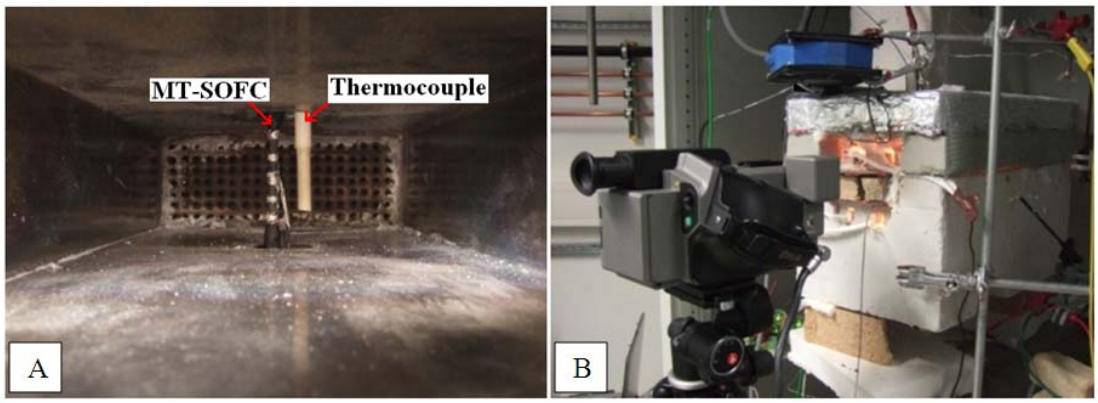

Figure 57: MT-SOFC and aluminium-oxide cover over a thermocouple for the test chamber temperature regulation (A). Positioning of the thermal camera for image acquisition (B).

5.2.3 Procedure

Thermocouple contact measurements were made through this opening at the rear of the wind tunnel. Whereby being able to visually see the MT-SOFC is necessary to make good contacts in multiple locations on its surface. To show that there was no effect from hydrogen leaks or short circuits a set of thermal camera images were made for low and high concentrations of hydrogen, in nitrogen, in the fuel channel. From the analysis of the images no temperature difference was observed, meaning that no short-circuits or hydrogen leaks had a visible effect on the measurements. It was found that pressing the thermocouple with force against the cathode of the MT-SOFC did not damage or affect the performance of the cell. The laser guided thermometer also required a view of the cell to perform its measurements and these were also made through this opening as seen in Figure 58. The EIS measurements did not require this slit or any blocking but the insulation condition was maintained nonetheless to guarantee comparable results.

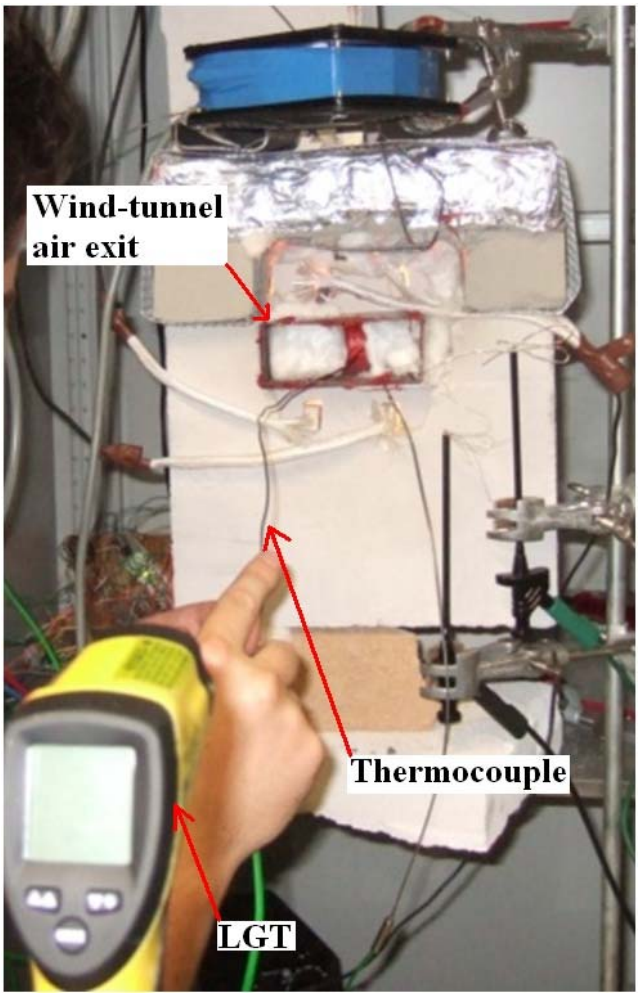

Figure 58: Positioning of the LGT and measurement using a thermocouple.

The thermocouple was assumed to make the most accurate reading and the LGT and thermal camera were calibrated to match temperatures read, at certain points along the length of the cell, by the thermocouple. Measurements were made through the opening at the end of the wind tunnel, as seen in Figure 58. Calibration was performed by simply changing the emissivity values, of the two devices, until the temperatures measured at the point initially measured by the thermocouple matched those indicated by the LGT and thermal camera. The EIS measurements were also made in conjunction with a thermocouple placed on the cathode wall. The concept for the use of the electrochemical method is described in detail elsewhere [39]. As a brief summary the theory behind the method is based upon the fact that the ohmic resistance of the cell is a function of temperature. So in a first step the ohmic resistance under OCV or a working point near OCV, where (nearly) no heat is

produced by the cell, is measured. The cell temperature is dependent on the oven temperature when it is in this state and several resistance readings are recorded at various oven temperatures. These values act as calibration points. Then the ohmic resistance under load is compared to these values which, then gives the correlation to the temperature.

Calibration of the thermographic camera, LGT and EIS was performed using the same thermocouple to make sure each device is calibrated to the same standard. The visible cathode wall of the MT-SOFC in the wind tunnel was the surface that was used for each of these calibrations. For the EIS and LGT methods the calibration was made on the cathode in a location situated above the central silver winding, see Figure 86 as a reference.

5.3 Modelling of a single MT-SOFC in cross-flow

The following section describes attempts made to validate single cell models of MT-SOFCs by using the I/V curves and temperature profiles from section 5.2. A variant of these models with a smaller cathode is described in section 5.5 where the fuel and oxidant concentrations are varied and results in the I/V curves, both in the models and experiments, are noted.

5.3.1 The first modelling attempt.

(a) Introduction

In this section the first set of models using the solid oxide fuel cell module in fluent is described. Only some very basic data will be described for these very first models because while they worked, they were very difficult to tune because of the long iteration times. The time between each iteration was so long that tuning the models took far too much time and required too much effort to be a realistic solution for

achieving high quality models within a reasonable period of time. In section 5.3.2 a detailed account of a model with high accuracy and iteration time is provided.

(B) Meshing the model

Shown below in Figure 59 is the layout and meshing of the cell modelled. This model contained over 1million cells The anode, cathode and the electrolyte dimensions are all the same as a single anode supported MT-SOFC. The method of current connection on the cathode, the 4 cathode connections, does provide a good representation of the current connection on a single MT-SOFC. This is because normally wires are wrapped around the cell. As can be seen in Figure 59 lengths of current connector are fitted along the cell i.e. parallel to the length of the cell with no consideration for current connection perpendicular to the cell.

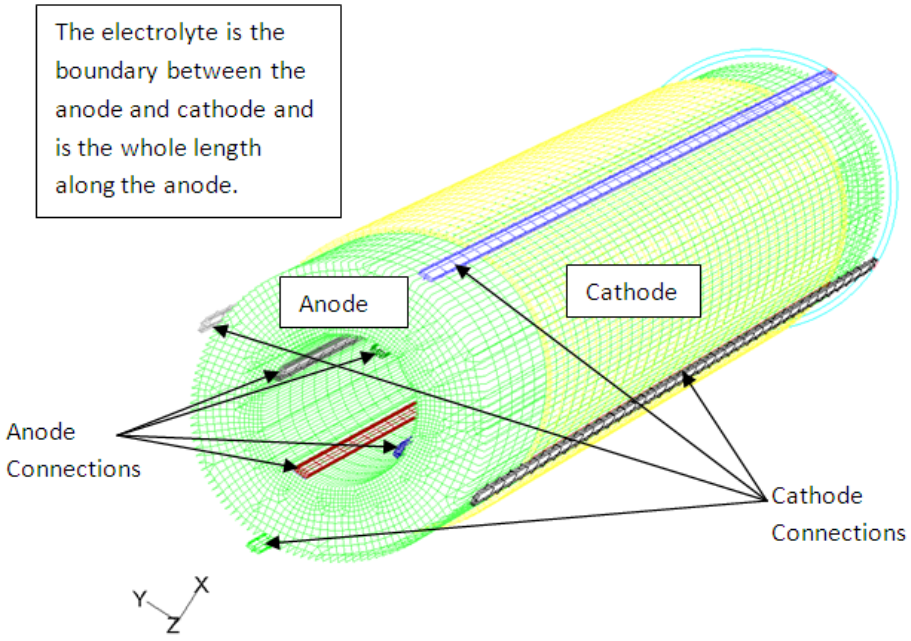

Figure 59: An image showing the basic outline of the meshing and current connection method used in the very first models.

The problem with these models was that they took far too long to solve and this method of simulating was abandoned.

5.3.2 The second modelling attempt

(A) Introduction

Having observed the effects of the previous model, with regard to the number of cells, on the solution time and the ability to tune the model, it was decided that attempts should be made to reduce the number of cells in the model drastically. This was achieved by using a combination of symmetry in the geometry and of course a reduction in the number of cells in the mesh.

(B) Meshing the model

For the first attempt it was decided that the total number of cells should not exceed 100,000. To reduce the number of cells in the model down to a number as low as possible, without losing resolution within the simulation, two techniques were applied. The first technique was to use symmetry boundary conditions. This meant that the size of the model could be effectively cut in half. As there was no evidence that the fuel-cell module would work with this type of boundary condition it was quite a risky approach. The second technique used was, when the meshing was being applied to each of the volumes that made up the large cell volume, the number of cells was consciously recorded and quick calculations were made to estimate what total number of cells in the model would be. Being able to estimate the cell count made it much easier to reduce the number of cells than by simply using at trial and error method. The error between the two approaches was negligible with a less than 1% change in current density, specie concentration and pressure. This indicated that in the second attempt, enough cells were used and grid independence was confirmed.

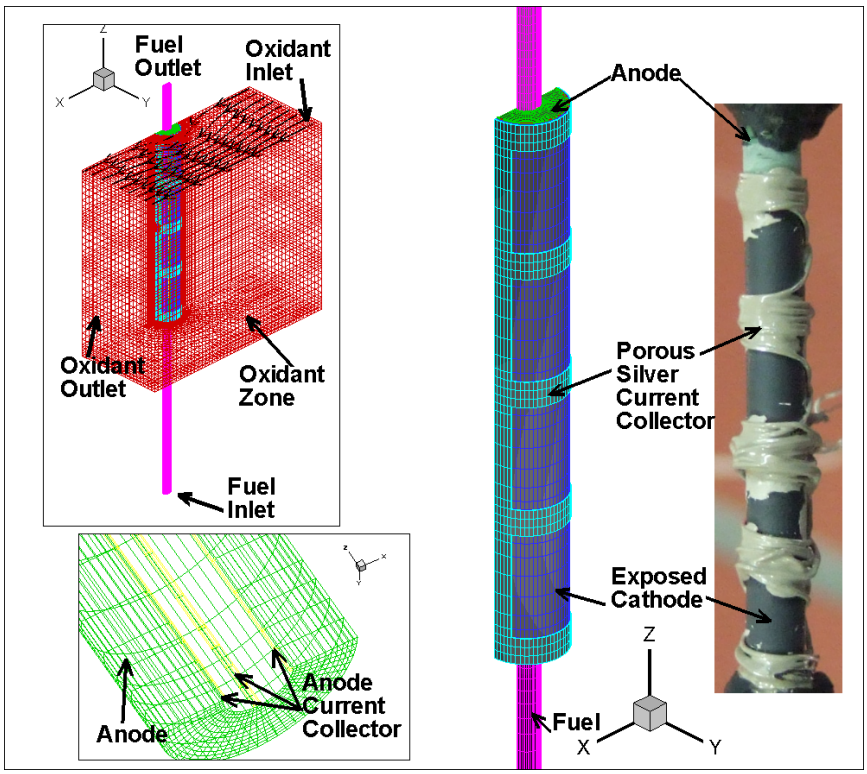

Figure 60: Outline of the mesh conditions for the model with a reduced number of cells.

Figure 60 shows the concept behind the meshing, including the symmetry boundary condition. It is important to note how the electrical connections have been made in the model and how it compared to the experimental setup. A porous silver zone is applied to the outside wall of the MT-SOFC cathode. This is roughly the same condition on the cell that was used for the validation of these models. Note that there are rings of silver at five intervals along the body of the cell. These rings are interconnected by a link of silver wires and paste that is positioned parallel to the cell. The set up of the model was designed to be as similar as possible to the cell used in the experimental setup. The current collectors that were attached to the anode were designated as a nickel zone and they lay parallel to the anode, as indicated by the yellow mesh in the green meshed anode seen in Figure 60

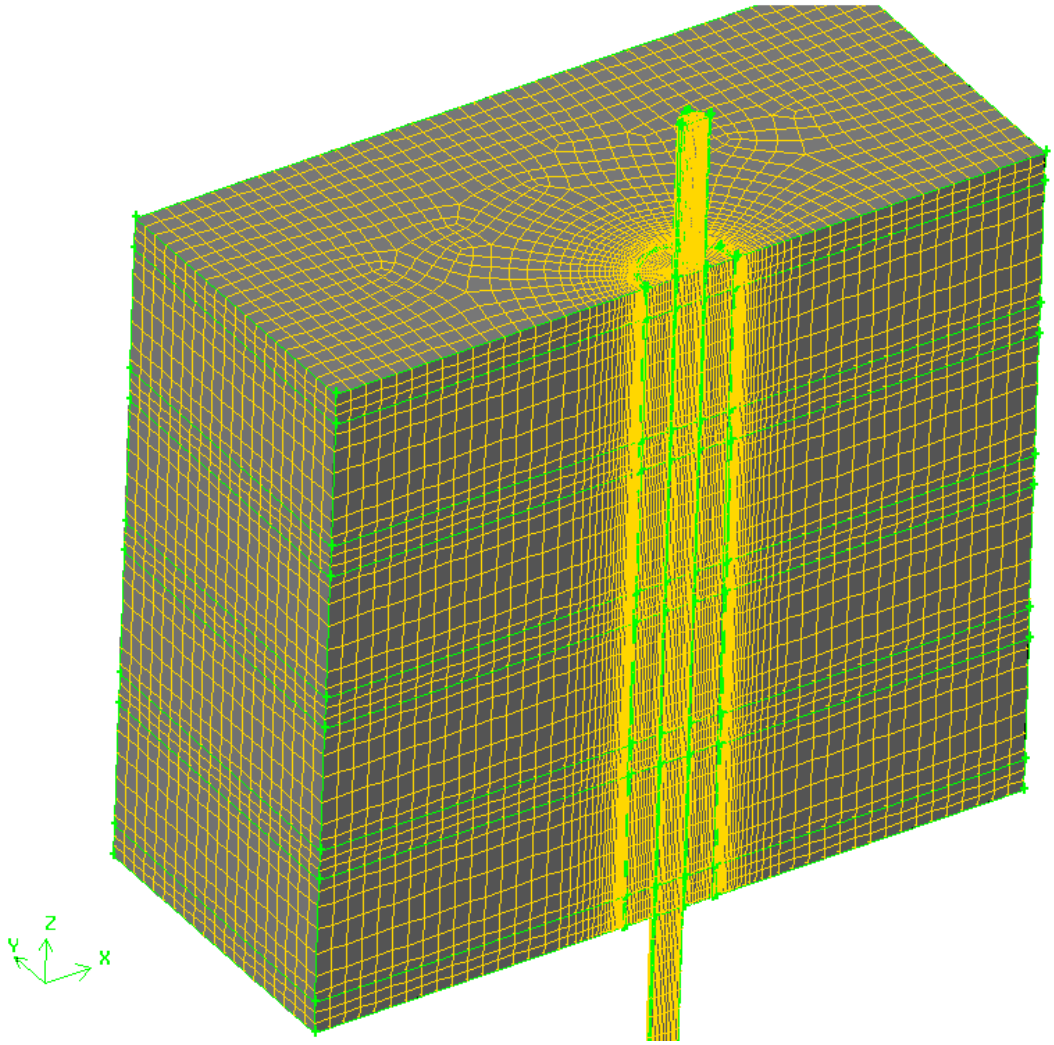

Figure 61: Outline of the mesh used for the faster solving model. Note that the face seen nearest has a symmetry boundary condition applied..

Figures 61 and 62 show a more detailed view of the meshing. In this case the total number of cells summed up to 95,755 cells. The quality of the mesh is extremely high, which is important for quick solving models, where the worst elements had an equsized skew of not more than 0.44, an equi-angle skew of not more than 0.46, an aspect ratio of 44. The cells used to construct the mesh were of the hexahedral type, which is much more desirable than the tetrahedral type.

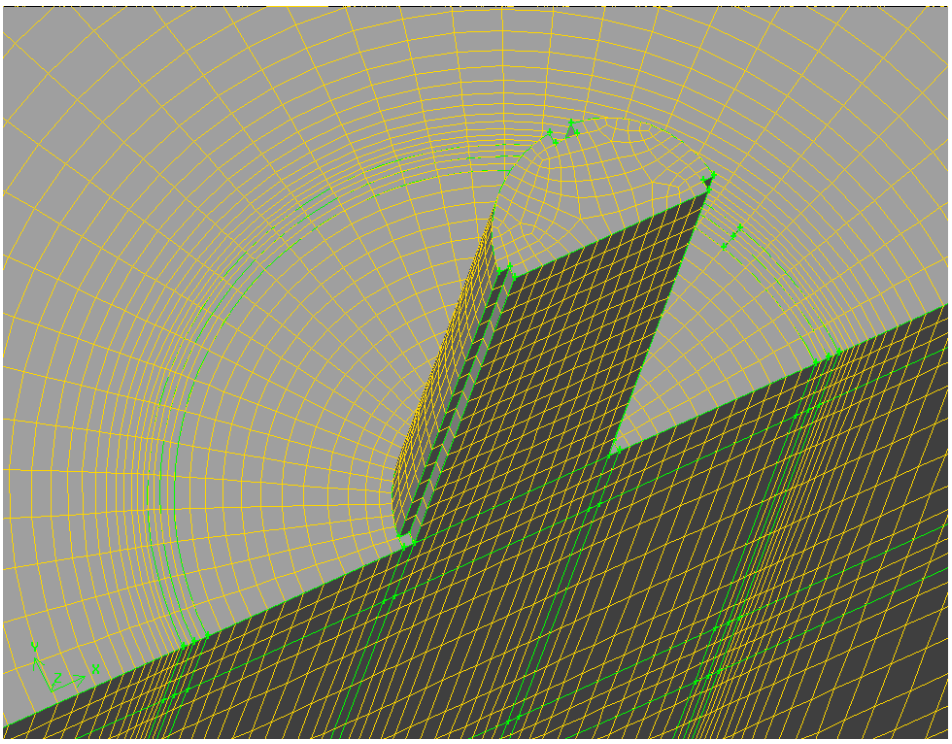

Figure 62: A view of the upper face mesh on the cell that is coopered down through the cell. An important point to note is the relatively few cells used to mesh between the anode and cathode layers.

It was found that the only method to solve the models included beginning to solve the model first at OCV i.e. when no current is produced. Following this, small currents could be drawn from the modelled cell in steps of 0.25A up to 1A. After 1 amp the currents drawn from the cell were increased by 0.05A as for some reason when drawing larger currents the model would diverge. The model took up to 6 hours to solve initially and then as the current was increased in small steps it took about an hour per step to solve. The model solving time was long for such a small number of cells because of the inclusion of the radiation model, which is computationally intensive.

(C) Modelling parameters

The modelling parameters used in this set of simulations are the same as those outlined in a Appendix X. The material properties for the anode and cathode were taken from [109] and are presented in the Appendix X. The reason that these materials were left the same as the standard materials, as was used in [109], is that

from reviewing the literature for an LSM or LSCF cathode or NI-YSZ anode, material properties such as density, thermal conductivity, specific heat capacity and electrical conductivity all generally tend to be in ranges similar to those found in Appendix X.

(D) Model tuning

The models were tuned by defining some of the parameters to remain constant as a function of temperature and others variable. The elements that remained constant were all the material properties except for the resistance of the electrolyte and probably the most important curve fitting parameter the current exchange density. The current exchange density was set to $3.4x10^{10}$ Amps (anode) [123] and (4000) cathode [124] initially. Note that in Fluent the units allocated for the exchange current density are "Amps" however after questioning Fluent on the issue, it was acknowledged that these units should be "Amps/m²). During the rest of this thesis the exchange current densities will be described as A/m². This current exchange density should normally be highly temperature dependent but given that the cell was used in a high temperature wind tunnel and radiation losses were high. The temperature of the cell never increased above 13 K compared to the OCV condition temperature. This meant that the temperature dependence effect of this parameter on the current densities was deemed negligible and thus the values listed above remained constant. Through trial and error these current exchange densities were varied until points on the experimental curve matched those predicted by the simulation. The attuned values of the anode and cathode current exchange densities settled to 2400000 A/m² and 1000 A/m² respectively.

It should be noted that the electrolyte sub conductivity model was not activated. The resistance of the electrolyte was changed in accordance with the values determined experimentally with impedance spectroscopy on the cell used for validation and the resistance values are shown below in Figure 63. These values were manually changed when the system current was changed in the modelling and corresponded to the measured values as a function of temperature.

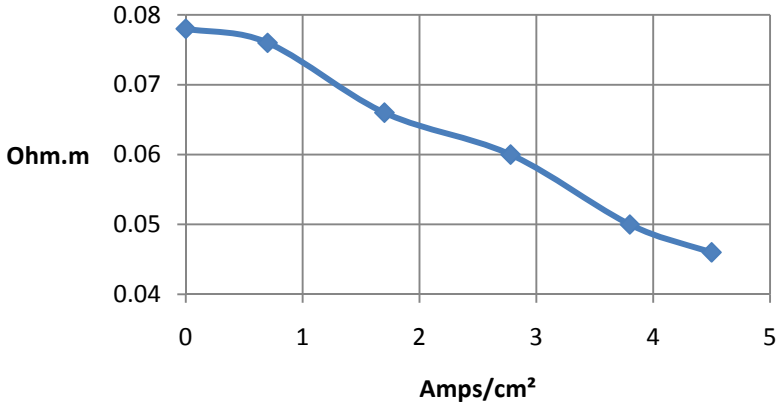

Figure 63: Experimentally determined values of the electrolyte resistance as a function of the total cell current. Note this current value refers to the total cell current but a half cell was modelled in the model see Figure 60.

The following steps were taken to solve the models

1. A very low system current was applied to the cell in the region where it was expected to get a value of around 1 V as a corresponding voltage on an IV curve for the cell being modelled.
2. When the solution converged, the volumetric heating model and discrete ordinate radiation model was switched on and the SOFC model was run again until it converged.
3. Then in steps of 0.25 amps the model was repeatedly converged until 1A is drawn from the cell. (Note: these step sizes may have to be smaller especially when diffusion limitations occur.)
4. After this 1 amp system current, the model was solved for 1.1 amp 1.15 amp 1.2 amps 1.25amps 1.3 amps 1.35 amps and 1.4 amps. Note that the correct electrolyte resistance, measured experimentally, was applied at each of these current density values.
5. Then when 1.4 amps was applied (the max current produced in the experiments) the current exchange densities were varied until the current and voltage values match those of the experimental curve.

It was found that the best way to tune the models, by altering the current exchange densities, was to use the method described above. Following these steps, when the maximum achievable current density was produced by the model, in the case described 1.4A, the current exchange densities were changed slightly to make the voltage correspond to the voltages measured in the experimental I/V curve. If the exchange current densities were tuned at a low current density, the error at the high current densities was found to be high. To minimise this error and to make sure that the new exchange current densities matched the experimental results, the I/V curve was plotted a second time and the error between the simulated and experimental I/V curves was always found to be negligible. In summary if the current exchange densities were tuned at the low current densities, large errors occurred in the high current density part of the I/V curve. However if the exchange current densities were tuned in the high current density zone the errors in the low current density zone were negligible.

5.4 Using MT-SOFCs to measure the rate of mass transfer to a cylindrical electrode in cross-flow

To ascertain the effects of; mass flow rates and flow direction; forced, free and radiation heat transfer; cell geometry and orientation on the concentration gradients of oxygen around and along there perimeter of a cathode electrode, the MT-SOFC is a unique and convenient tool. It could be used, after calibration even at high current densities, to measure the concentration of oxidant and fuel species and furthermore to validate a set of operation parameters for the multi physical simulation parameters discussed previously. Under operational conditions when the current produced by the cell is mainly limited by diffusion (availability of the species), the electrical performance gives a precise measurement indicating the quantity and availability of the supplied reactants.

5.4.1 Development of a Novel System to Measure the Concentration of oxygen around a MT-SOFC in Cross-Flow

The measuring principle to indicate the concentrations of oxidant around the perimeter of the cathode that was hypothesised is as follows. In Figure 64 (A) where there are no external pressure differences acting on the cell. It is assumed that the cell has an infinite supply of oxygen molecules, through natural diffusion from the environment. Below this image, in Figure 64 (A), is the expected effect of adding external pressure differences to the system, whereby a velocity is applied from top to bottom in the image.

If for example this was the cathode, on the outside of the cell, then the blue regions could indicate regions where the cell could be affected by a concentration over potential caused by a possible lack of oxygen.

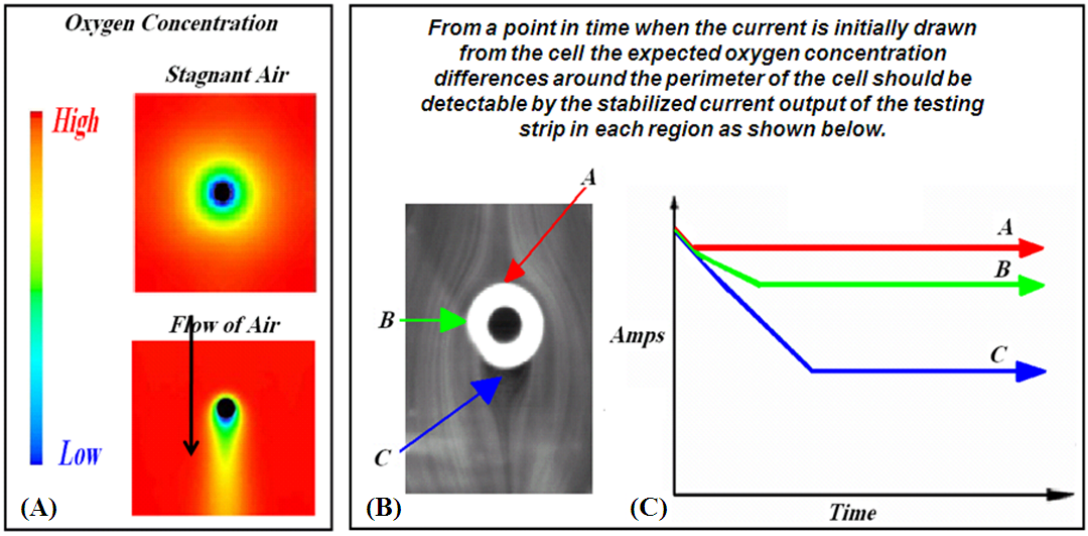

Figure 64: (A) The expected gradients of oxidant concentration in air for the case with no external flow and below for a case with laminar external flow. (B) A high speed camera image of a wake behind a tube and labels for (C), which is a plot of the expected time dependent effect on current output from certain zones around the cell.

Figure 64 (B) shows different possible testing positions of the outer electrode electrically isolated strip, please refer to Figure 65 for more detail on this "testing" strip. Depending on the position around the perimeter of the cathode there may be a

time dependent current output similar to the plot shown in (B) in Figure 64. At time zero a current is drawn from the cell and in case “A”.As the pores in the electrode are full of a ready supply of oxidant, initially the current density will be a maximum which will decrease and level off at some point. However, the gas supply in the pores will mainly be controlled by diffusion rate, the electrode thickness and density, the temperature and the produced current may experience fast decline.

At position “B” on the side of the cell, the oxidant specie supply may not be as concentrated as in position A and therefore a second slope can be found in the “Amps versus Time” plot, Figure 64 (C). This indicates a small diffusion limitation outside the pores. In the case “C” the position of the testing strip is at the rear of the cylinder and again there is an initial drop due to a supply oxidant in the pores. But in this case the second slope could be greater, as the flow regime could cause a greater lack of refreshment of the fuel or oxidant in the wake resulting in a low oxidant specie concentration. These results should only be considered as estimates, as they are fundamentally unknown. The proposed “testing strip” can be orientated not only longitudinally, but also laterally across the micro-tubular SOFCs which could potentially provide more information about the oxidant species concentration along the length of the cathode.

To measure the concentration around the perimeter of the cathode (or potentially anode electrode should the architecture of the cell be reversed) one of the possible solutions is depicted in Figure 65. An electrically isolating strip of the outer electrode, the anode or cathode depending on the test configuration, as a segment of the total electrode could be used to perform the measurements. The specie concentration of oxidant, should the cathode be used, can be quantified by measuring the electrical behaviour of it. If the two cathode layers are electrically isolated and the fuel utilisation is extremely low then the current produced by the cell is directly proportional to the concentration of oxidant. This method provides a direct measurement for different positions around the perimeter of the electrode of the reactant concentrations through the measurement of current generated in this testing strip.

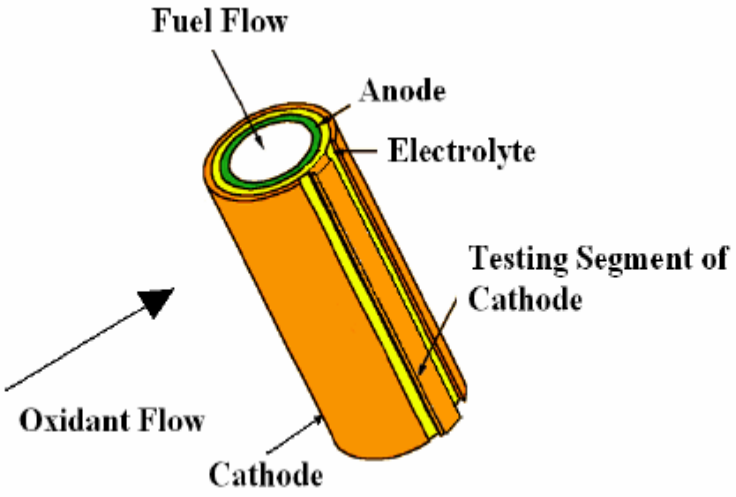

Figure 65: Illustration showing the proposed architecture of the cathode on a MT-SOFC to measure the concentration of oxygen around the cell's perimeter.

Thus this gradient may be measured for a whole range of the possible multi physical conditions that can occur for a single cell, under different flow conditions and orientations or potentially on different cells in different positions within arrays of cells. Multi physical parameters that occur in a stack can be changed, such as oxidant concentration and temperature, even temperature gradients around the cell perimeter and then using this new experimental method to validate the multi physics in a CFD simulation, a validated model incorporating all of the parameters can be realised. This model can then be used to predict the performance of the cell under a wide range of conditions with the advantage of the measuring technique being that a portion of the cathode can be measured, which can provide detailed information about the current density, oxygen concentration and temperature gradient profiles around the perimeter of the cell.

Hussain and Dincer [61] suggest that the magnitude of the concentration over potential is less significant at the loads they considered, 0.3, 0.7 and 1 A/cm², in their experiments and that the over potentials of the activation and ohmic losses must be predicted to evaluate the true performance of the anode under various operating and design conditions. Concerning these results impedance spectroscopy seems to be an essential tool to evaluate the electrical losses due to diffusion under certain working conditions. Jasinskiet et al. [53] for example have shown how impedance spectroscopy can be used to measure the electrode over potentials in a single planar

cell. They show that impedance spectroscopy can be used to isolate the polarization losses due to the different components and processes within the cell and thus isolate the losses due to concentration gradients causing concentration over potentials. Thus a combined study using the dual cathode method described previously and impedance spectroscopy could provide a lot of fundamentally new measurement data to the MT-SOFC field.

5.4.2 Construction of electrolyte supported cells with dual cathode and dual anode layers

Initially it was thought that to eliminate the electrical coupling between the two cathode strips that each strip should have its own separate and directly oppositely located anode strip. To make such cells, an electrolyte supported cell would have to be used and the cathodes and anodes would have to be coated onto the cells. An attempt was made to achieve this by spraying the cathode onto the cell and using small strips of sticky tape, which can be taken away after spraying to reveal the electrolyte. This concept was used to segment the two cathode strips from each other. A similar method was also attempted to separate two corresponding anode segments, located directly under the cathode segments, on the inside of the electrolyte tubes. However this proved almost impossible to achieve because the anodes were and must be coated onto the inside of the cells in several layers with sintering steps between each layer. (The details of this cell production method are privy to Ezelleron GmbH and more detail cannot be given). Keeping the anode segments electrically isolated proved to be impossible. The only way that it may be possible to achieve a segmented anode would be to use larger electrolyte tubes and these were not available. The electrolyte tubes that were used were 5mm and 3mm in diameter and both sizes were not sufficiently big enough to allow easy removal of the tapes inserted inside the cell to allow electrical isolation.

5.4.1 Construction of anode supported cells with an electrically isolated duel cathode layer

To make measurements of the concentration of oxygen at the rear of the cylinder it was decided that a duel cathode layer would probably suffice and anode supported cells could be used. Originally the duel cathode layers, as shown in Figures 66 and 67 were made by spraying the cathode onto the cell with special sticky tape used to block where the cathode should not be sprayed to provide the electrical isolation. This method proved to be extremely time consuming taking weeks to build a batch of cells and the reliability of the cell's performance tended to be extremely low due to the experience of the operator on the spraying machine i.e. Ph.D. candidate.

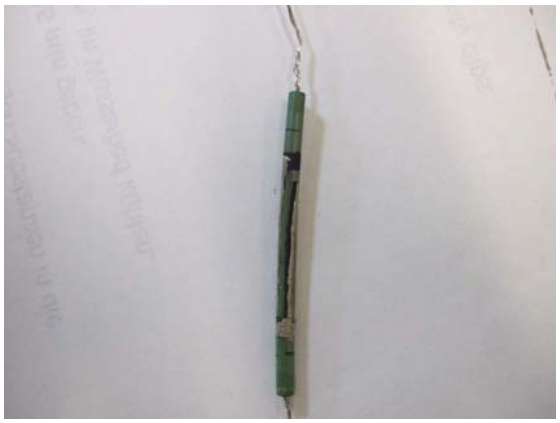

Figure 66: An image showing the segmented cathode applied to an MT-SOFC

Figure 67: An image showing the duel cathode layer with the electrical connection to one of the cathode strips.

5.4.2 Construction of cells with small cathodes and details about the experimental setup

As will be seen in section 6.4.2 it was decided that the size of the cathode should be reduced to increase the resolution of the measurement. Rather than re-making anode supported cells with these small cathodes by spraying. it was decided that an approach where; the cathode of previously made cells, with full cathodes, would be scraped off was attempted and this method proved successful in producing high powered cells with a small cathode. All of the cells that had a small cathode were made using this "scraping off the cathode" method and an example of a cell that had a 2mm X 4mm testing cathode strip and 4mm X 4.2mm normal cathode is shown in Figure 69

In Figures 69 and 70 the electrical connection and full layout of the testing cell and manifold can be seen. This cell was then placed into the high temperature wind tunnel as described in Section 4.4. Figure 71 gives some more detail about the experimental set up, where the apparatus holding the cell under test and peripherals are displayed. Figure 72 shows how the cell is rotated inside the wind tunnel. The cell is turned by simply turning it by holding the hydrogen inlet manifold and turning the cell.

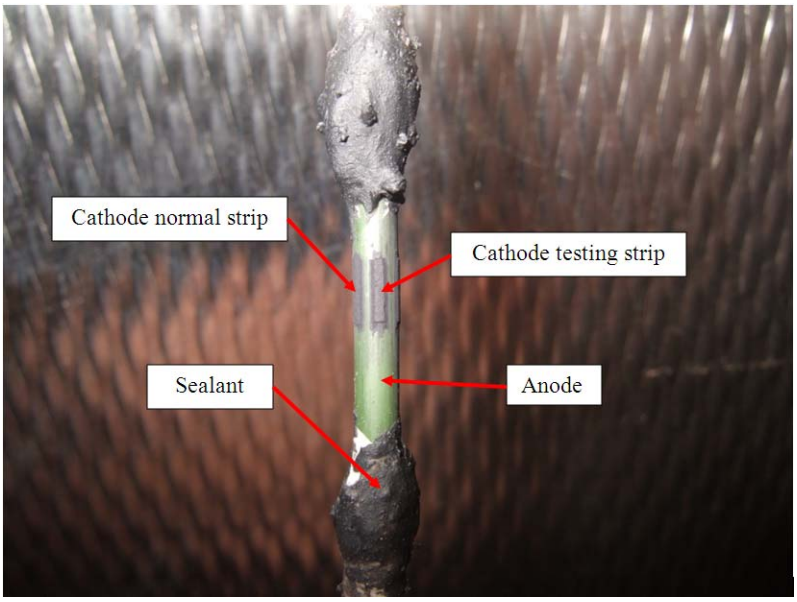

Figure 68: Picture of an anode supported cell and the small testing cathode isolated from the normal cathode which wraps around the back of the cell.

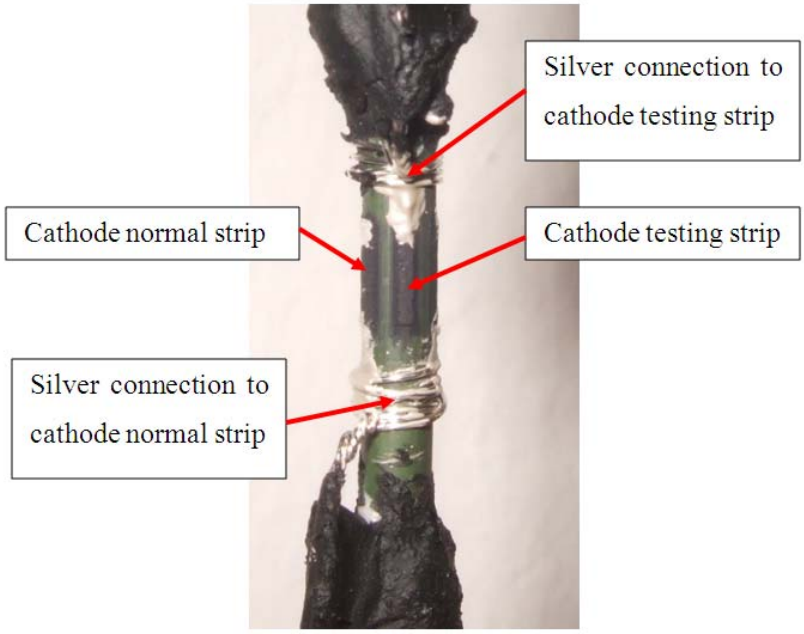

Figure 69: Picture of an anode supported cell with the segmented cathode system complete with electrical connections.

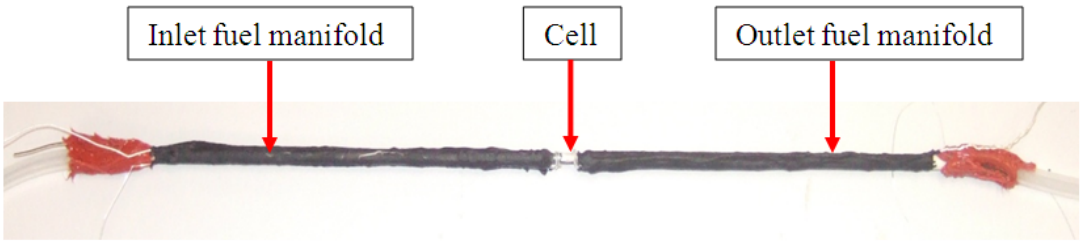

Figure 70: Full view of the manifolding to the cell complete with anode reference, anode working (out each end of the silicon inlet tubes and sealed with silicone)and cathode working and cathode reference for each of the cathode strips.

The Humidifier used in these experiments was a Bronkhorst 5g/hr system (Bronkhorst H.V. Netherlands) and the fuel was piped through it. After being humidified the fuel was then sent through a set of heated pipes where to make sure no condensation occurred the pipes were maintained at 110°C.

The flow rate of the fuel for all experiments using the small cathodes was 50 ml/min hydrogen. This was supposed to be humidified, to cause a 0.5 $P(H_2)$ however it was found that the maximum humidification, before the cell became blocked, was 0.075 $P(H_2)$ which was much less than the specified amount and the effect of which is outlined in section 6.4.

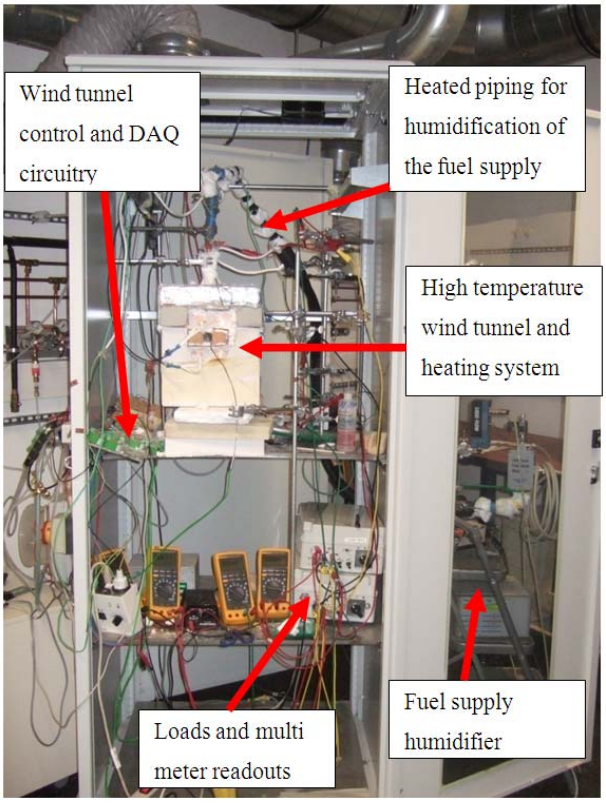

Figure 71: Some details about the experimental set up for the oxygen concentration measurement tests.

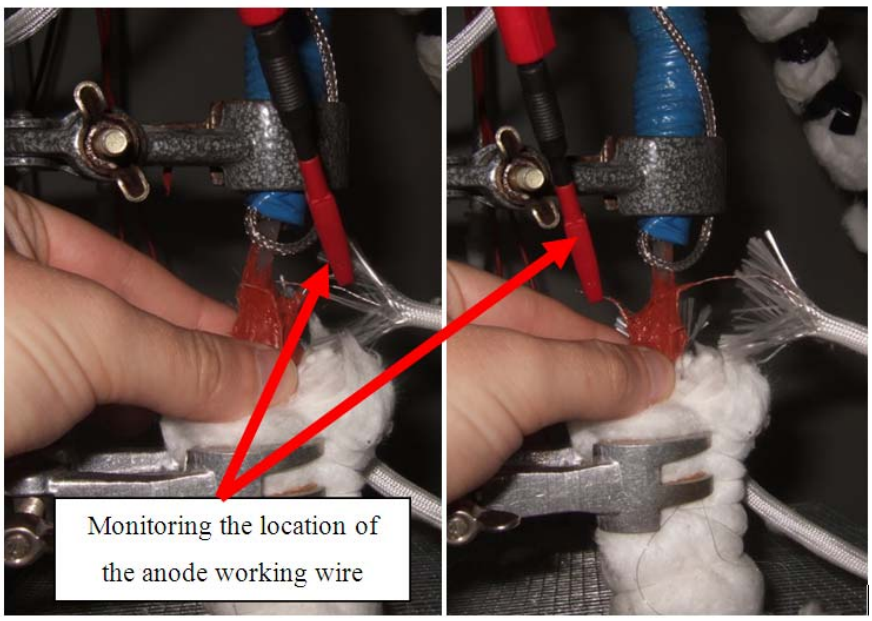

Figure 72: The cell is rotated inside the wind tunnel by holding the red silicon sealer in the top of the cell and turning it by hand. The anode working connection is used as a reference as to the collation of the testing strip.

5.4.3 Procedure to detect the concentrations using the dual cathode method

As the amount of current produced by the testing strip is directly proportional to the concentration of oxygen, when the strip; is electrically uncoupled from the normal cathode strip, is un related to the fuel (ie. when the cell is in a low fuel utilisation at high currents) and is diffusion limited on the cathode side (because of the availability of oxygen) the following procedure was considered appropriate to make the measurements.

1. Make sure that no matter how the cell is twisted that temperature effects do not change the current produced by the cell.
2. Measure the electrical dependence of the two cathode strips on each other, by changing the current drawn on one cathode and monitor the OCV on the other.
3. Reduce the concentration of oxygen in the wind tunnel and make measurements when the testing strip faces the oncoming flow and then when it is positioned in the wake of the cell. Both the cathode testing strip and

normal strip should regulated to 0.55V as this is a low enough voltage that will not damage the cell and draws a high enough current to reduce the oxygen concentration sufficiently to make concentration measurements.

4. Use impedance spectroscopy to make sure that the measurements in point 3 relate to mass transfer of oxygen to the cathode.
    a. Change the anode gas concentration to isolate the part of the Niquest plot associated with the anode.
    b. Make the same measurements as in point 3. Use impedance measurements on the cathode testing strip in both oncoming flow and when it is located in the wake. Changes in the Nyquest plot between the two positions of the testing strip will indicate if the cell is experiencing reduced concentrations of oxygen. This proves that the measurements of point 3 are really showing oxygen concentrations.

These results should then be compared to the CFD simulations.

5.5 Detailed modelling of the concentration of oxygen around the perimeter of a MT-SOFC in cross flow and the fast solving model

As will be discussed in section 6.4.2 it was decided that the length of the cathode should be reduced to increase the resolution of the oxygen concentration measurement. Thus for the simulations the size of the cathode was reduced.

5.5.1 Outline the model

Because all of the previous models, simulated in Fluent to model the MT-SOFCs, took such a long time to solve, it was decided that a drastic reduction in the model size should be made. The models outlined in (first attempt and second attempt) had 1 million and 100,000 cells and solving times ranged from the order of days to 4-5 hours to make complete I/V curves. While the second attempt made the curve fitting in the model easier to handle, for full cells, it was not sufficient for rapid tuning of the model. This fact hindered both the learning objective and the accuracy of the model. It was hoped that if a rapid solving model could be successfully generated and validated, it could also be used to tune the models of sections one and two at a later date.

The quick solving mode consisted of the 4mm high, section of cathode immersed in an oxygen flow field section also 4mm high. The top and bottom walls of this continuum had a symmetry boundary layer applied. This meant that no wall effects were present, as should be the case in the experiments because the top and bottom walls were located some distance away. More detail about the model parameters can be found in Appendix XI. Figure 73 shows the meshing and outline of this model with some initial results are inserted.

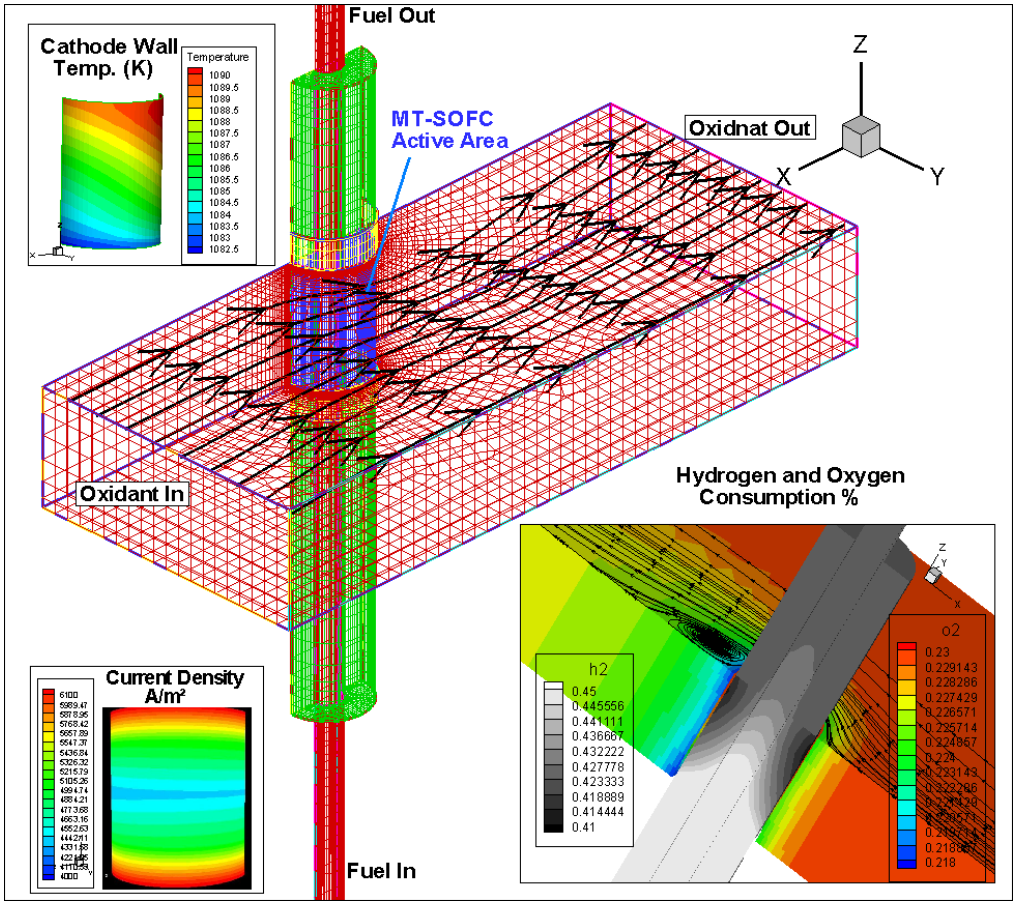

Figure 73 A pictorial plot showing the outline of the model and sample results.

It was found that some of the modelling parameters must be fitted and the most important of these is the exchange current density which is described in Section 3.3.4 in detail. A similar procedure as outlined in 5.3.2 (D) was used to tune the models to match I/V curves and the results may be seen in section 6.5

5.6 Measuring oxygen concentrations at higher Reynolds numbers

The following section contains the introduction to an attempt that was made to measure the concentration of oxygen around a larger cylinder. Unfortunately this larger cell was never realised and so only model results are presented.

5.6.1 Measuring the concentration of oxygen around the perimeter of a high temperature electrode

To measure the concentration of oxygen around the perimeter of a cylinder, a stack of cells with a cylindrical shape as shown in Figure 74 was intended be built. Using a cylinder with a larger diameter of several cm (compared to mm for a MT-SOFC) is discussed in more detail in the following section. However it should be pointed that the larger diameter was selected for a more academic than practical reason to study the mass transfer to a cylinder in cross flow in more detail than allowable with a single MT-SOFC.

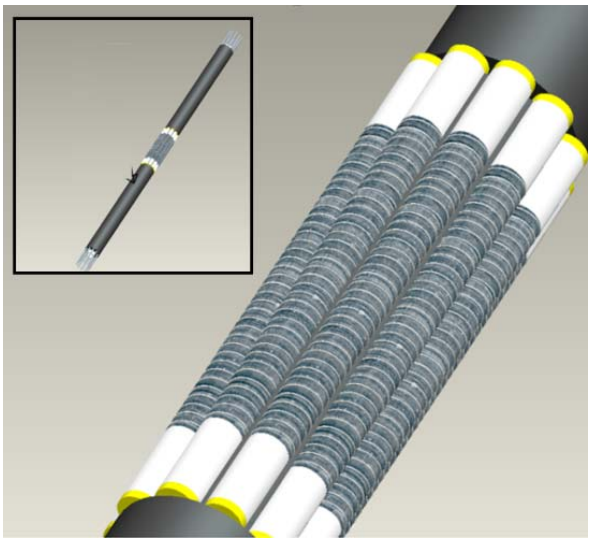

Figure 74: Image of a cylindrical arranged bundle of MT-SOFCs to detect the concentration difference around the perimeter of a cylinder

5.6.2 Simulations and the effect of wakes behind cylinders on mass transfer

To get an idea of the results to expect this design was simulated using the CFD code. The simulations that were performed were just the calculated for the case where 1 % oxygen and 99 % nitrogen in an air flow existed. The range of Reynolds numbers studied was 10 to 120 and the walls of the wind tunnel were included in the simulation. Omitting the wind tunnel walls would result in wake geometries that would not represent any future experimental endeavour that was planned at the time and is discussed also in the following section. Table 5 gives an overview of the parameters used for the simulation.

Table 5: Simulation properties.

Property	Value
Wind tunnel dimensions	100mm L X 40mm H
Viscosity 1% O_2	4.49×10^{-5} N.s/m^2
Mass diffusivity	Kinetic theory calculation.
O_2 Diffusion sink rate	0.44032 kg/m^3.s
Density N_2	0.3062 kg/m^3
Specific Heat N_2	1187 J/kg.K
Density O_2	0.3490 kg/m^3
Specific Heat O_2	1090 J/kg.K
Temperature	1100 K

5.6.3 Meshing the model

To give an indication of the shape of the 3D model including the bundle of MT-SOFCs Figure 75 (A) shows a sample image of the outline of the cathodes of twelve 2.8 mm diameter MT-SOFCs located around a support tube. Also depicted in this image is a sample contour plot showing a gradient of oxygen concentration caused by the sinking of oxygen induced by the bundle. The key point of interests is what occurs to the oxygen concentration in the wake of the bundle of cells as the velocity of the oxidant gas is increased. Figure 75 (B) shows the meshing scheme that was used on the x/y plane perpendicular to the cells. Notice that the gird is tightly meshed in the vicinity of the MT-SOFCs and that the grid is coarsened from this region into the bulk flow regions. This coarsening never exceeds a volumetric increase of "1.2" from cell to cell and this is crucial for good meshing. The grid used in these simulations was adapted to increase the cell numbers by a factor of 8 and little difference was found in both the convergence patterns or numerical results. This conferred that the coarse mesh was "grid independent" and sufficiently meshed.

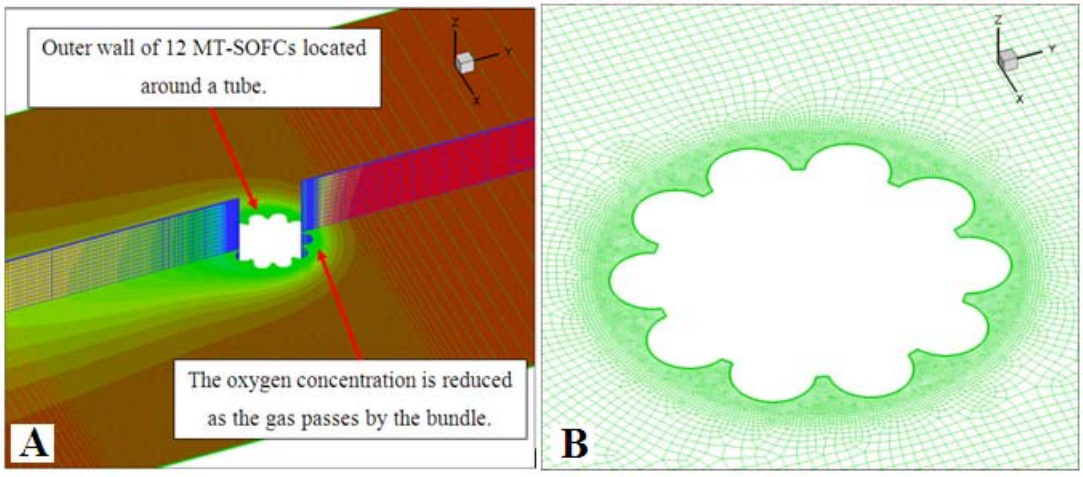

Figure 75 (A) Sample oxygen concentration contour plot qualitatively indicating the mass fraction of oxygen where red indicates high and blue indicates low concentrations. (B) The meshing scheme employed around the bundle of cells.

Chapter 6 Experimental and analytical results

6.1 Results of CFD simulation and analytical calculation to estimate the effect of natural convection in a MT-SOFC reactor

In Figure 76**Error! Reference source not found.**, which has been calculated using a combination of equations 5-1-4, 5-1-5 and 5-1-6, it can be seen that the Nusselt number for free convection is the major part of the combined Nusselt number at miniscule gas velocities around and under 2.25mm/s bulk flow velocities. This indicates that free convective heat transfer is dominant below this bulk flow velocity. However as soon as faster flows of air flow around the cylinder occur, more heat is removed from the MT-SOFC walls. The temperature difference between the wall and the air reduces and so the free convection component is reduced, while the component of the forced convection increases. These plots were produced by applying the equations indicated above in a Matlab code see Appendix VIII.

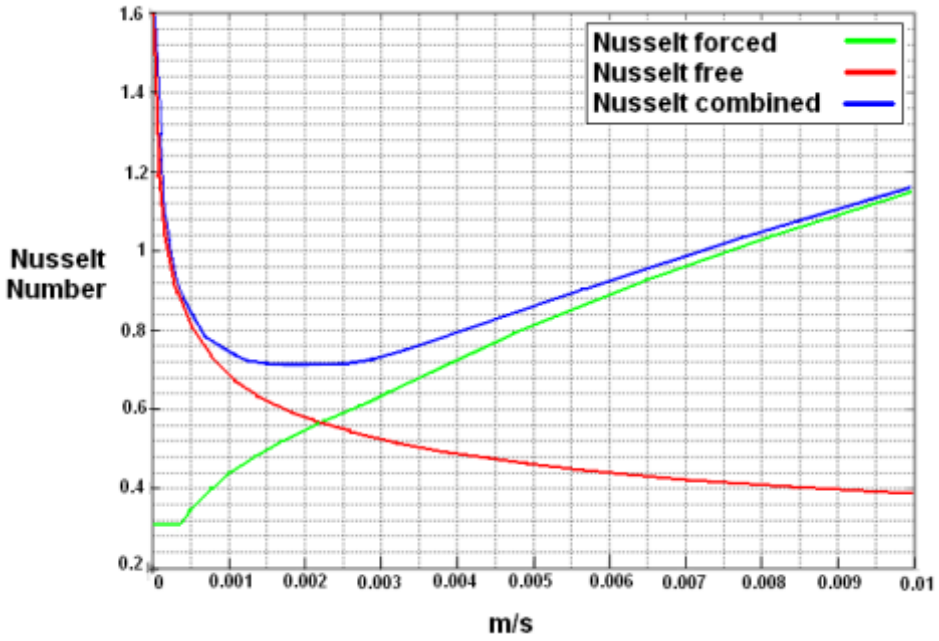

Figure 76: Nusslet number plots for free, forced and combined convection on a single cylinder.

Figure 76**Error! Reference source not found.** is an important plot as it shows, for a single cylinder, where roughly to expect the transition between fully free convection, mixed convection and fully forced convection dominated heat transfer. The combined Nusselt number will be used later to estimate the air temperature at the exit of a bundle of heated cylinders. These analytical results only give a very limited prediction of what to expect in reality for a single cylinder and indeed very little information of what to expect with an array of cells. This calculation does not include walls above and below the cylinder and nothing can be deduced regarding the exact flow regimes to expect around a single horizontal cylinder. It would be impossible to estimate heat transfer characteristics and flow regimes for a whole bundle of cylinders analytically.

However the results of this single cylinder test give an idea of what to expect. Important information to consider is that as the inlet flow velocity is increased the single cell temperature should drop almost instantaneously because the forced convection has a much more pronounced effect on heat removal from the cell compared to the free convective effects. However this should be slightly less severe in an array of cells because of the greater supply of heat to be removed, caused by the multiple number of the cells.

The chart in Figure 77 (Green) shows results for the exit gas temperature from the array as a function of the inlet gas velocity for an array of cylinders 3 rows deep. This analytical calculation was obtained by using a correlation from Von Böckh [122] using the combined free and forced Nusselt numbers acquired in Figure 76**Error! Reference source not found.**. Also included in the plot, Figure 77, is the same outlet temperature prediction from the CFD calculation (Blue) and this matches quite well to the analytical result. The minor deviation in the results seen between the methodologies, in Figure 77, was due to the fact that a single temperature is assigned to all the cells within the array in the analytical result. Refer to Von Böckh [122] for more information, however in practice the temperature of the cells in the first row should be lower than that of the cell in the last row. Also the flow effects induced on one cylinder by its neighbours is impossible to account for in an analytical calculation and this is also an advantage of the CFD method. The

analytical result was calculated via matlab and the code can be found in Appendix IX.

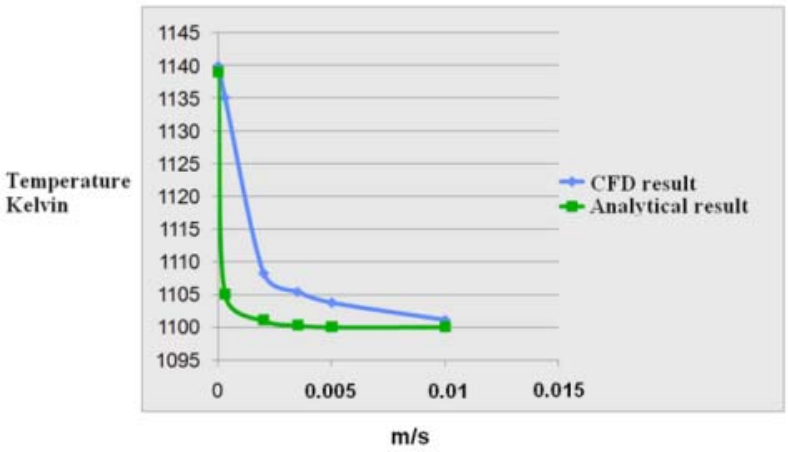

Figure 77: A plot of CFD and analytical results for the output temperature for a bundle of cylinders 3 rows deep versus inlet air velocity m/s.

Figure 78 (B) depicts the effects within a bundle of cylinders three rows deep for a highly buoyant flow predicted by the CFD simulation. The maximum wall temperature was about 1135 Kelvin (861.85°C) on the last row of cylinders and the inlet air velocity was 1.5 mm/s and 1100K (825°C). The units on the plot (A) are m/s in the Z direction, -Z being in the direction opposing gravity and Z being with the direction of gravity. An interesting prediction of this model was that for very low velocities for example below 1.5 mm/s, similar to Figure 78 there will be a non-uniform flow into the array.

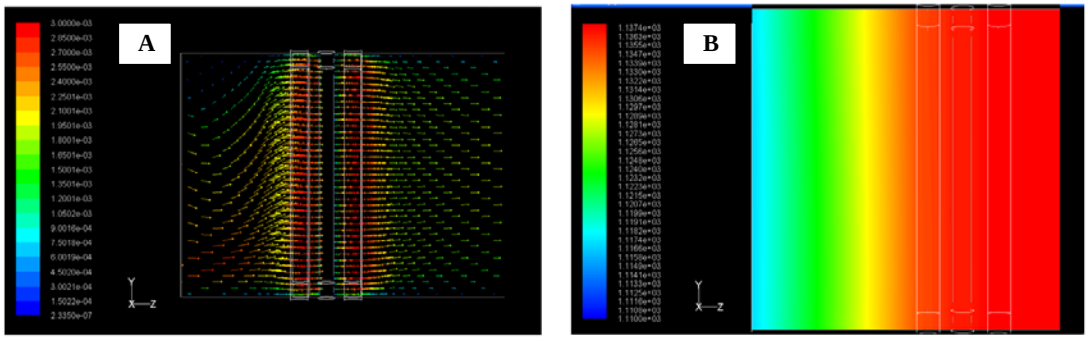

Figure 78: For the 1.5mm case (A) contours of z direction velocity on a plane situated in the middle of the bundle and flow path. (B) Contours of temperature on a plane located in the middle of the bundle and flow path.

This can be explained logically; because the array is a blockage in the duct that also conducts heat into the gas. In Figure 78 (B) the temperature profile through a section in the middle of the bundle is shown. Before the gas even enters the array it is being heated by the cylinders and this causes the buoyant non-uniform flows that can be seen in Figure 78 (A). When the gas eventually enters the array it speeds up because of the reduction in flow path volume caused by the cylinders in the way. This fact, combined with the fact the gas would have reached close to its maximum temperature after the first row, means that the flow then becomes more uniform and the viscous forces induced by gas, coming from the inlet, keeps the flow uniform through the rest of the array.

However the model predicted that there will still be some slight buoyant flows within the array, especially between the first row of cells. Figure 79 (A) shows the Z component velocity in m/s. The range is from 7 x 10^{-4} m/s meaning the maximum Z component in red is about 0.7 mm/s and given that the inlet velocity is 1.5 mm/s the buoyant forces were predicted to be quite high. Figure 79 (B) shows that between the first row of cells the model predicted a dominant upwards motion of the fluid. However at the very bottom of the cell there is a slight downward motion of the fluid as this is caused by the fact the very top and bottom 0.5cm zones are inactive and thus do not produce any heat. I.e. these zones are used for sealing and no cathode is situated in these zones.

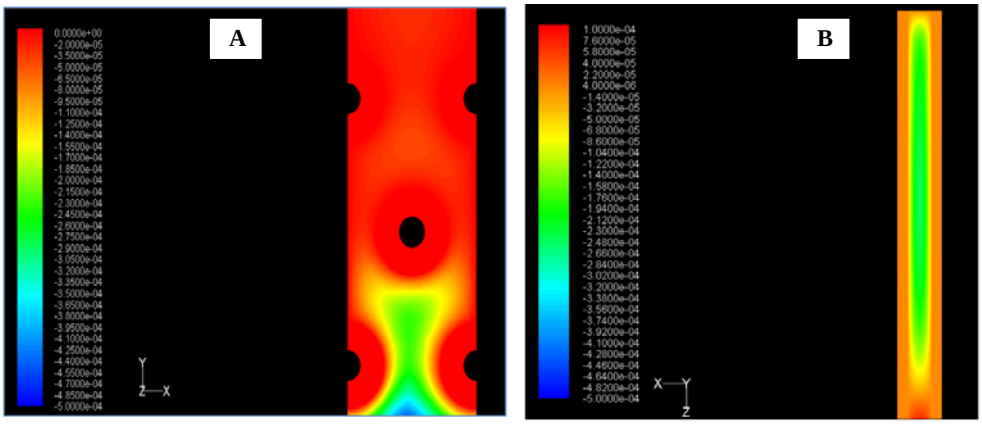

Figure 79: For the 1.5mm/s case (A) velocity contours on a plane situated in the middle of the bundle of cells. (B) Velocity contours situated on a plane located between the first two cells in the bundle

However as the gas flows into the array as seen in Figure 79 (A) this value

drops rapidly to 0.1 mm/s before the second row and then the buoyant effects cannot be observed. These effects are also supported as indicated by the Grasshoff number divided by the Re^2 (Gr/Re^2), which was applied to a single cylinder is cross flow. Gr/Re^2 numbers much above unity (e.g. in this bundle case below 3mm/s) indicate that highly buoyant effects are present while those much below unity (e.g. in this bundle case above 10mm/s) indicate little or no buoyant flows. For an array of cylinders these buoyant effects should be a bit more exaggerated and so the number indicated in Figure 80 by a value of 10 for a velocity of 1.5mm/s should be slightly higher for an array of cells.

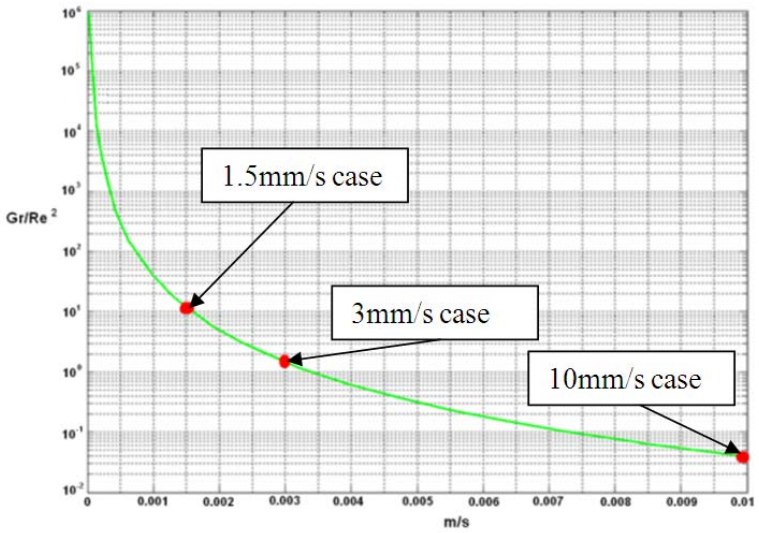

Figure 80 For a single cylinder vertical cylinder Gr/Re^2. The 3 red dots are the velocities mentioned in this section.

An interesting effect is observable when the inlet gas velocity is increased up to 3mm/sec. As seen in Figure 81 (A) only very small buoyancy flow is induced and this is predicted by the Gr/Re^2 plot shown in Figure 80 where for the 3mm/s case the free and forced convection forces should be equal. Figure 81 (B) shows the temperature distribution of the gas before it inters the bundle of cells and this temperature gradient is much less stark in contrast to the 1.5mm case, refer Figure 78 (B).

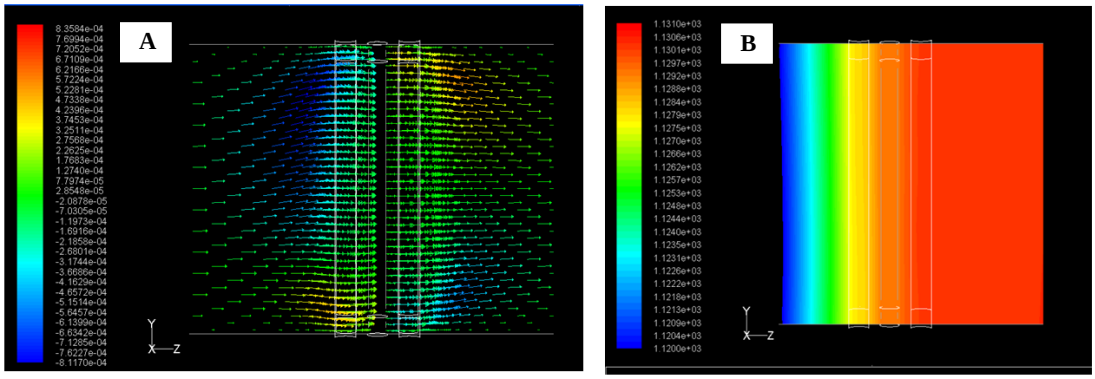

Figure 81: For the 1.5mm case (A) contours of z direction velocity on a plane situated in the middle of the bundle and flow path. (B) Contours of temperature on a plane located in the middle of the bundle and flow path.

Figure 82 (A) also shows the prediction of the model that between the first two cells in the first row, the free convection flows are almost totally un-observable and this shows that the forced convection forces are almost dominant. Figure 82 (A) for the 3mm/s case, which is a view looking at the velocity magnitude in the z direction, shows some minute up-ward and down-ward movements in the directions of the passive top and bottom zones of the cell.

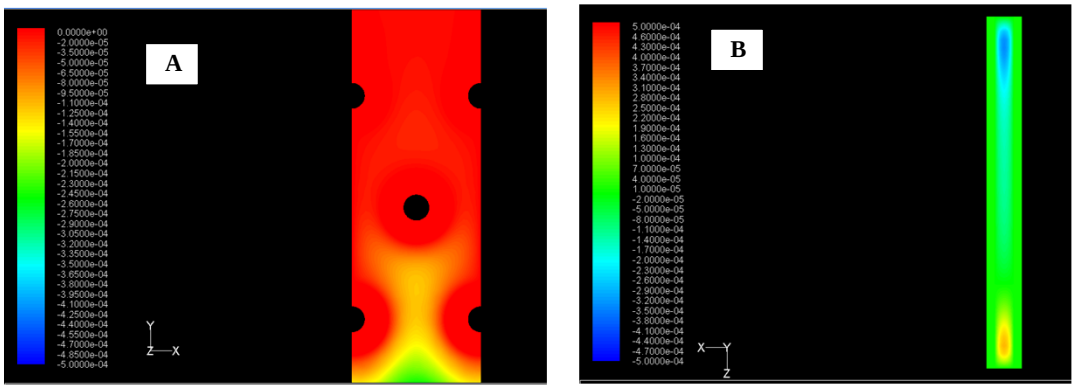

Figure 82: For the 3mm/s case (A) velocity contours on a plane situated on the middle of the bundle of cells. (B) Velocity contours situated on a plane located between the first two cells in the bundle

Figure 83 (A) shows the model prediction for 10mm/s case that the free convection flows are not observable. This is also predicted by the Gr/Re^2 plot shown in Figure 80, where for the 10mm/s case the result is a value much less than 1 indicating a totally force convection dominated flow. Figure 83 (B) shows that the temperature in the bundle of cells is decreased by the increased mass flow rate of air through the bundle. The combination of the lower temperature gradient between the incoming gas and cells' walls and increased mass flow are the cause of this reduction in free convection flow.

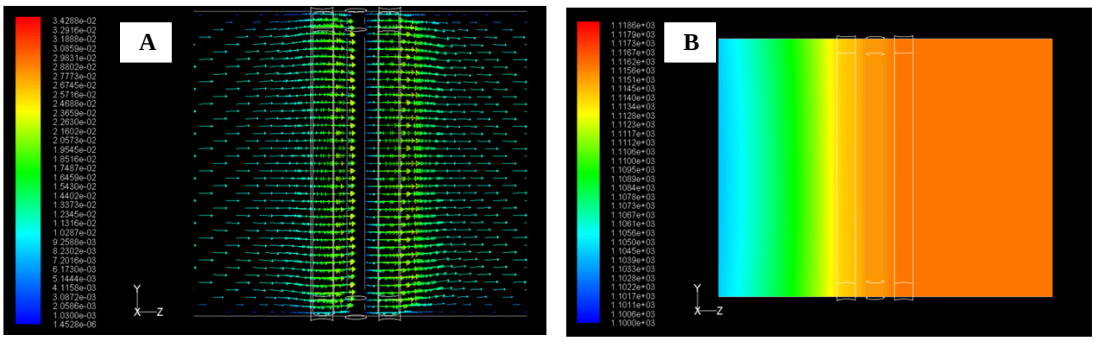

Figure 83: For the 1.5mm case (A) contours of z direction velocity on a plane situated in the middle of the bundle and flow path. (B) Contours of temperature on a plane located in the middle of the bundle and flow path.

Figure 84 (A) shows that buoyant flows inside the bundle are practically nonexistent and this is also confirmed by the contour plot of z velocity magnitude between the first two cells in the bundle shown in Figure 84 (B). Although these images appear to show a more defined zone of buoyant flows when the scales on the contour plots are checked these motions are actually insignificant.

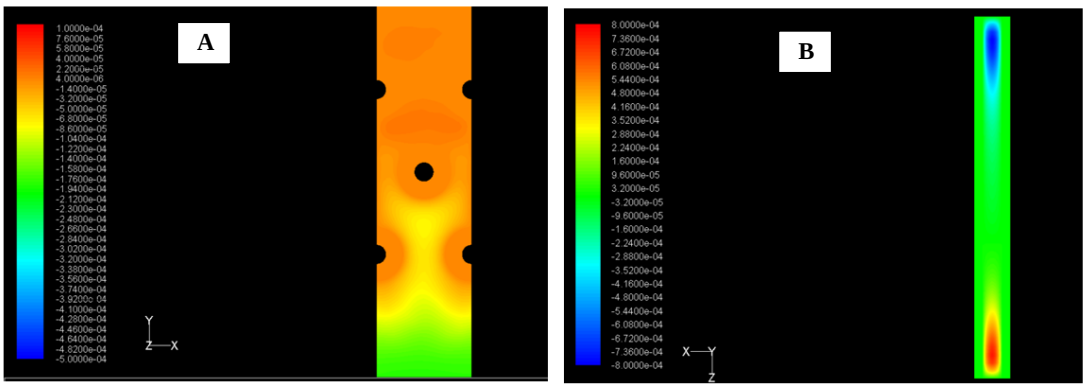

Figure 84: For the 10mm/s case (A) velocity contours on a plane situated on the middle of the bundle of cells. (B) Velocity contours situated on a plane located between the first two cells in the bundle.

Figure 85 (A) shows a contour plot of the Z component of the velocity vector and is a section taken between the first row of cells looking at the cells from a head on position. This is a fine example of how powerful CFD simulations can be. It even shows the effects of the air at the bottom of the cylinders, which is an area that does not produce heat in the model and the flow tends to move downwards. This is indicated by the red colour and is present. This feature is caused by the fact that the cathode length on the cylinders is 3.5cm long (the only heated area) while the cells are 4cm long which was included in the model. The model predicted that Z component in the rest of the air volume tends to move upward, except at the very top where there is again a slight downward movement.

It was found that increasing the inlet air velocity soon eradicated the effects of natural convection seen before the bulk flow enters the array. As the velocity is increased to even 3 mm/s the buoyant effects are dampened and this compares well to the plots of Figures 83 (B) and 85 (B) where the natural convective effects, caused by the temperature of the cylinder, is almost totally eclipsed by the forced convective regime. This is because the flowing gas removes the heat from the walls of the cylinders so fast that the temperature differences between the bulk flow and cell walls are very small. However these buoyant effects are not completely eradicated as even up to 10 mm/s the small effects at the top and bottom of the cylinders can be detected and seem to be more pronounced in definition whilst minimal in magnitude. Figure 85 (B) is a contour plot of these Z vector component velocities between the first row of cells for an inlet velocity of 10mm/s. It can be seen that the unheated

portions of the cells, at their ends, tend to pull up and down the flows respectively. This is because of the density differences caused by the lack of heating at the top and bottom of the cylinders. These effects are quite small less than 1 tenth of a mm/s in the + and – Z directions. It is interesting to compare this effect between the 3 mm/s case and 10 mm/s cases seen in Figure 85 (A and B)

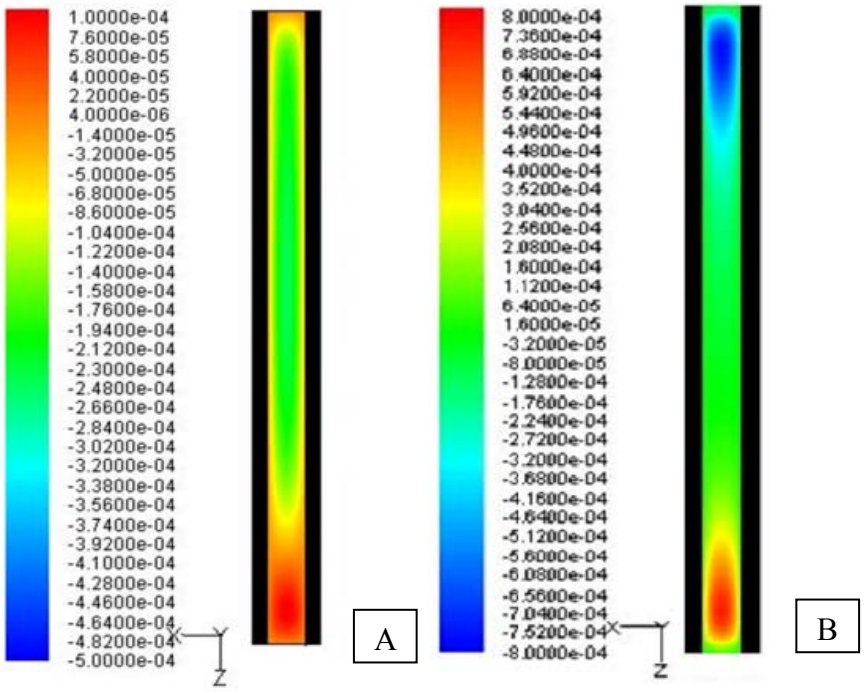

Figure 85: Looking between two cells the contours of Z velocity are displayed. (A) velocity is 1.5 mm/s and (B) is 10 mm/s.

6.2 Results of the method for temperature measurement of a MT-SOFC

This section will show how four different methods of temperature measurement can be used in combination to map a temperature profile for a passive or active MT-SOFC.

The set of two images in the centre of Figure 86 shows a thermographic camera image of a MT-SOFC in the wind tunnel and two images taken with a normal camera on either side of the middle positioned thermal camera image. The conditions for the measurement were left hand side 0 A/cm^2 (OCV) and right hand side 1.5 A/cm^2. The visual images clearly show that the cell heats up under this load and the thermal camera images quantify the amount. There are two interesting effects that should be noted in the thermal camera images. Firstly the line in the middle of the cell that appears to be colder than the sides of the cell in the thermographic camera image Figure 86.

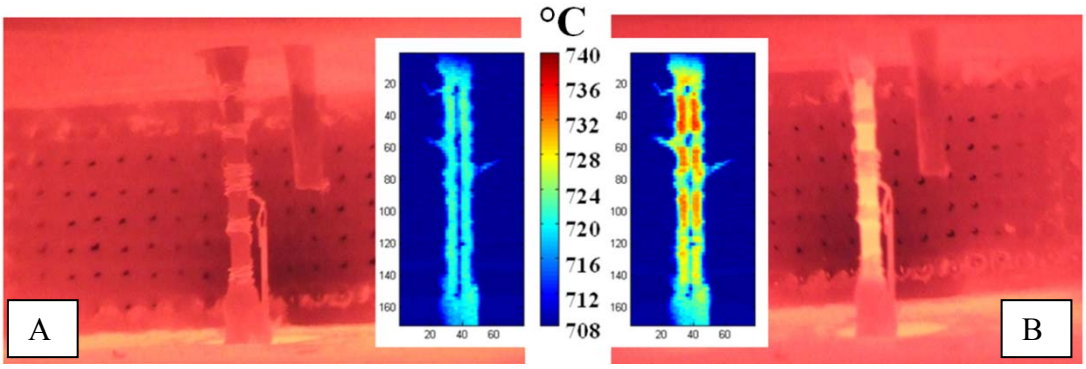

Figure 86: MT-SOFC under OCV conditions (A) and when producing 1.5 A/cm^2 (B) with colour scale showing the temperatures in °C in the middle.

In both cases the operational temperature of the test chamber where the cell is located is 725 °C, which is regulated by a thermocouple placed near the cell. Under OCV conditions (0 A/cm^2) the cell is passive regarding radiation and so the wind tunnel walls radiate heat to the walls of the MT-SOFC and this in combination with heat transfer from the gas flow determines the temperature of the cell. In the loaded case (1.5 A/cm²) the cell also produces heat internally and this combined with the previous effects determines the temperature of the cell.

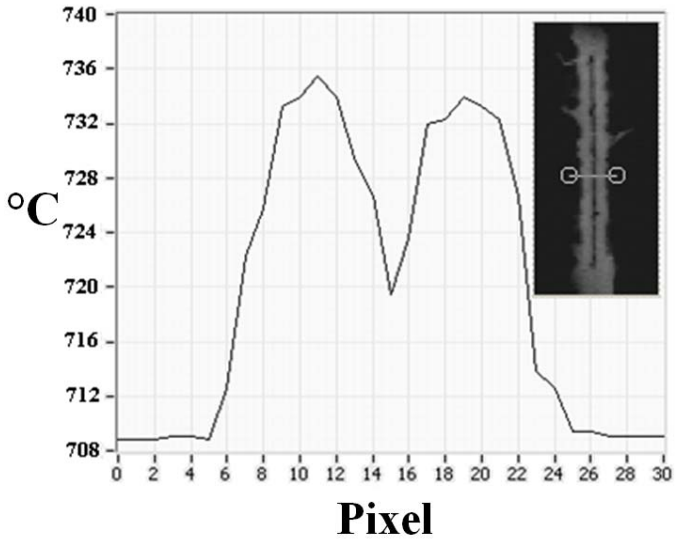

Figure 87: Temperature gradient around the perimeter of the cell caused by the wind tunnel slit.

The second point of interest with regard to the measurement of the MT-SOFC temperature is in relation to the silver wires that are wrapped around the cell. After some initial experimentation it was decided that the silver current collector should be wrapped around the cell in such a way that there are clear zones of cathode and silver exposed to the camera. This was achieved easily by wrapping the silver in such a way that all the connections to each silver zone were achieved by only crossing the silver from one ring zone to the next at the front of the cell (not visible region) and a conductive paste was also used improve the electrical contact.

It was found that the temperature reading of the camera varied quite a lot from the silver to the exposed cathode zones when the cell was under load. However if the thermocouple was used to measure the temperature of these regions, when the MT-SOFC was under load, the temperatures matched more closely to the expected temperature profiles of the cathode regions. However, it should be noted that there was no difference in the temperature readings when the cell was under OCV.

The reason why the silver and cathode appear to be the same temperature at OCV was because the wall temperatures of the wind tunnel were the dominant source of heat to the cell. Thus the wind tunnel wall temperatures had a massive effect on the temperatures radiated by the cell to the camera. However as soon as the temperature of the cell increased beyond the passive MT-SOFC state (OCV), when the cell became hotter than the wind tunnel enclosure walls, the emissivity difference of sliver and the black cathode played an important role. The camera was calibrated

using the cathode and the emissivity value was 0.97. The emissivity of silver should be much lower about 0.1 at these temperatures. However this value was contaminated in this case by parts of the cathode which "peek" through the silver wire wrappings and thus the emissivity value was substantially higher 0.83 when measured by the camera. For the thermal camera measurements this means that two temperature zones appeared, when in fact the temperatures of the silver regions are closer to their neighbouring open cathode zone temperatures. A solution to this effect may be to use software to apply emissivity values to specific regions of the MT-SOFC.

Displayed in Figure 88 is a plot of temperature values of points placed on the MT-SOFC when the total cell current density was stepped up to 1.5 A/cm^2 in steps of 0.3 A/cm^2 over a period of 250 seconds. Note that each step was made in conjunction with the natural temperature cycle of the wind tunnel. This natural temperature fluctuation cycle was observed by monitoring fluctuations recorded by a point placed on the diffuser behind the MT-SOFC. This is illustrated in Figure 88 by the bottom blue line. The top 3 lines in Figure 88 are points taken on the open cathode, while the middle 5 lines are points taken on each of the silver windings. At the beginning of this plot, at 0 s, the cell is at OCV and the silver windings and cathode appear to be roughly at the same temperature as the open cathode zones. However as the cell produces more power the temperature of silver and exposed cathode pieces deviate. A reading from the thermocouple showed that this deviation, in fact, does not really exist and the difference is just a measurement artefact. The temperatures of the silver and open cathode were actually similar. This difference in measurement is described previously and was due to the emissivity difference of the two materials when the cell is not in passive mode.

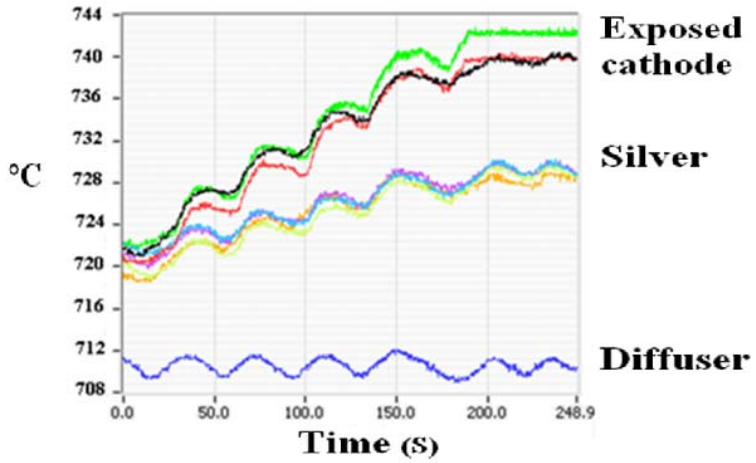

Figure 88: The effect of emissivity on the thermal camera measurements. Top 3 lines points on the cathode, middle 4 points on the silver. Bottom line shows the fluctuation in chamber temperature due to the PID heating control.

After the very first temperature measurements at OCV it was clear that the LGT (Laser Guided Thermometer) was unsuitable for this type of MT-SOFC. This was mainly because the measuring "spot" produced by the LGT was slightly bigger than the diameter of the cell. This meant that the temperature of the diffuser behind the cell, which was lower than the temperature of the cell, was included in many measurements. An advantage of this wind tunnel design for thermal camera measurements was that small flows of air through the diffuser lowered the temperature of the diffuser while the temperature of the cell under test was not affected up to flow rates of 30 cm/s. This characteristic greatly improved the contrast of the thermographic images.

The EIS (Electrochemical Impedance Spectroscopy) measurements were made in combination with a thermocouple placed on the outer wall of the MT-SOFC. A sample impedance measurement is shown in Figure 89. The thermocouple was held in position so that it was touching the exposed cathode zone above the middle silver zone (compare Figure 86). The temperature of the cell was increased by increasing the current produced by the cell and the ohmic resistance of the cell was measured via EIS using a four wire technique with separate voltage connections. Figure 90 is a plot that shows when the current produced by the cell is increased, the temperature measured via the electrochemical method (blue) was also increased. The cathode wall temperature, measured by the thermocouple, increases (red) but at a

much lower rate. These EIS measurements were taken when the cell was under load and the measured ohmic resistances were compared to values when the cell was in the OCV condition. It was found that, for example to get the same resistance values at OCV as when the cell was under load, the temperature of the cell had to be increased to much higher values (blue) than indicated by those measured at the cathode wall (red line) in Figure 90.

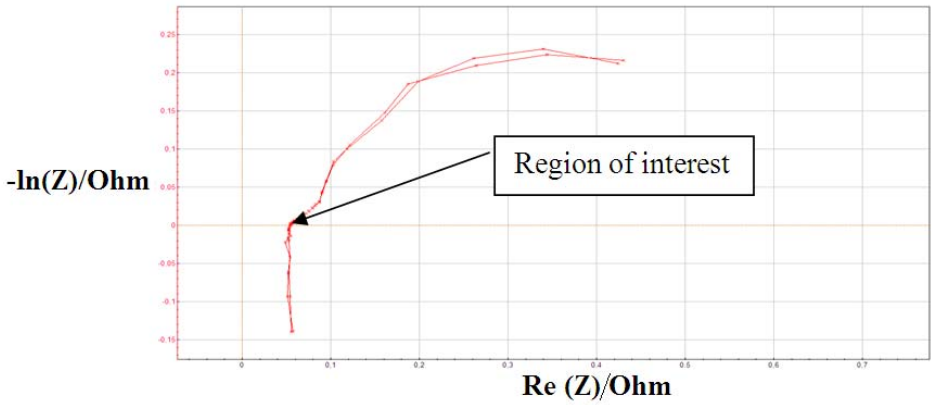

Figure 89: Sample impedance measurement made where the ohmic resistance is measured where the nyquest plot hits the x axis.

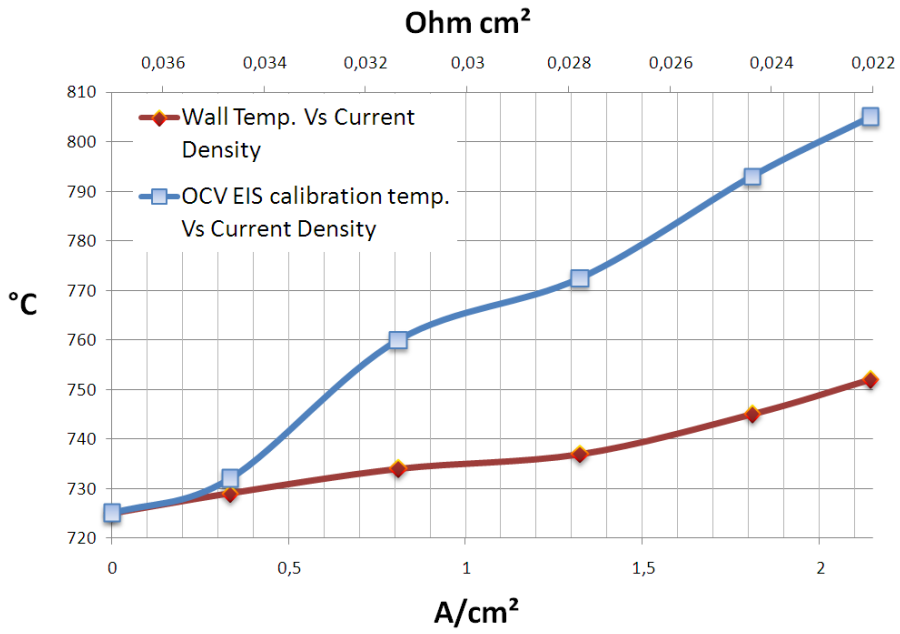

Figure 90: Comparison of the temperature calculated by the EIS method and wall temperature measured by a thermocouple.

Figure 91 shows a comparison of all the methods used in this work to measure the cell temperature. After calibration the thermocouple and thermographic camera gave very comparable results. This of course was expected because the EIS was originally calibrated with the thermocouple on the outer wall of the cell, in this case. The LGT on the other hand gave lower values than expected, because the cooler diffuser in the background of the cell that was included in its measurements. Another problem with this device was that separate measurements made on the cell in the same place resulted in temperature values that varied up to +/- 5 °C. The unreliability may be attributed to the fact that it was difficult to hold the device steady on such a narrow target. This device performed much better when the temperature of the diffuser is measured alone and agreed with thermal camera and thermocouple measurements. Therefore this tool should be quite effective for measuring the temperature of larger devices once calibrated. The thermal camera and thermocouple results were only calibrated at the 725°C point and this shows, because the increase of temperature matches quite well, that the emissivity value that was inputted into the camera must have been quite accurate. Otherwise the two plots shown for the thermocouple and thermal camera would not be as similar.

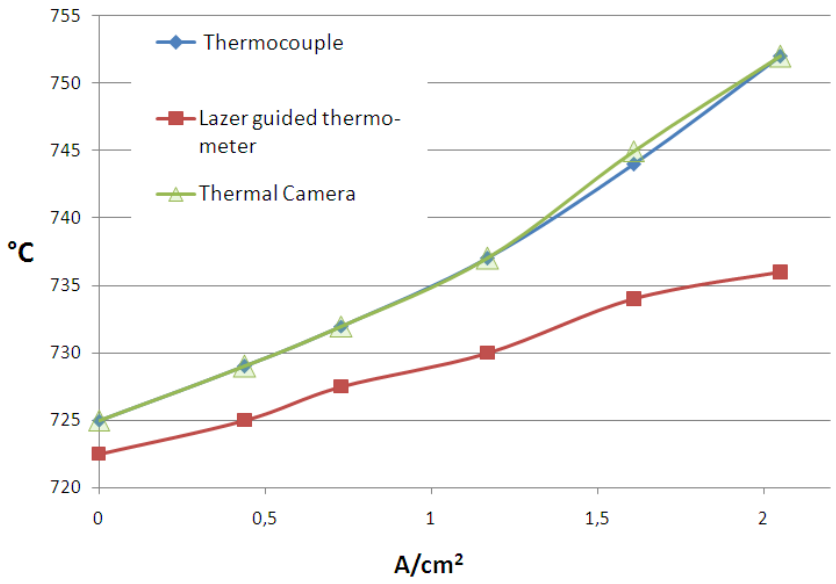

Figure 91: The methods are compared on the open cathode zone above the middle silver for a range of current densities produced by the cell.

6.3 Results from the modelling of a single MT-SOFC in cross-flow

6.3.1 Radiation and the model

During the course of the initial modeling of MT-SOFC's in cross-flow using the Fluent CFD software package with the SOFC module it was found that the temperature of the MT-SOFC was always 200°C or higher than the expected results as can be seen below in Figure 94. In the experiments made in the high temperature wind tunnel, such elevated temperatures were certainly not observed, at least on the outer wall temperature of the MT-SOFC. Initially 2D models were setup to investigate the radiation effects caused by the shape of the wind tunnel. This was subsequently followed by the addition of radiation to the previous 3-D models that included electrochemistry and is also outlined in the following sections.

6.3.2 2-D simulations and unrealistic radiation measurements

Before 3D models that included radiation were developed, initially models were made in 2D to establish the suitability of the radiation models provided by Fluent. This was also done to establish if the boundary conditions such as emmisivity on the walls of the testing apparatus and cell were correct. When modeling in 3D the itteration times are much longer than compared to the 2D models. Thus initially a 2D approach made more sense to begin with than a 3D approach.

Shown below in Figure 92 are the paramaters that were used in the 2D model. From earlier experimentation, using the thermal camera, it was found that the emmisivity value on the cathode wall should be 0.93. From the literature [125] it can be found that the emmisivity of a heavily oxidised surface similar to the inside of the wind tunnel should be 0.6. The exit of the the wind tunnel has a radiation temperature similar to the temperature of the room. The only obstruction that had a view factor to the cell, at the wind tunnel exit, was the thermal camera that was taking images. This means that the potential for radiation transfer between the cell

and the rear of the wind tunnel was quite significant. Fluent allows the user to set a radiation temperature that is uncoupled from the fluid temperature at inlets and outlets. In this simulation the radiation temperature at the outlet of the wind tunnel was set to 300 K. At the inlet the radiation and gas temperatures were coupled meaning that the radiation temperature was the same as the inlet gas temperature 998.15 K.

The internal walls of the wind tunnel was measured to be 998.95 K and this value was applied to all the walls inside the testing chamber. On the outlet channel a negative heat flux was applied to reduce the temperature of the out going gas to that which was measured experimentally 550 K. The velocity of the incomming gas was 20 cm/s. Figure 92 shows the boundary conditions applied inside the modelled wind tunnel. An inportant point to note in these simulations at OCV cell conditions the temperature of the cell is complety dependent on the heat transfer from the surroundings. This is statement is both true for the passive and active configeration of the cell. However in the cell internal heating must also be considered in the active state.

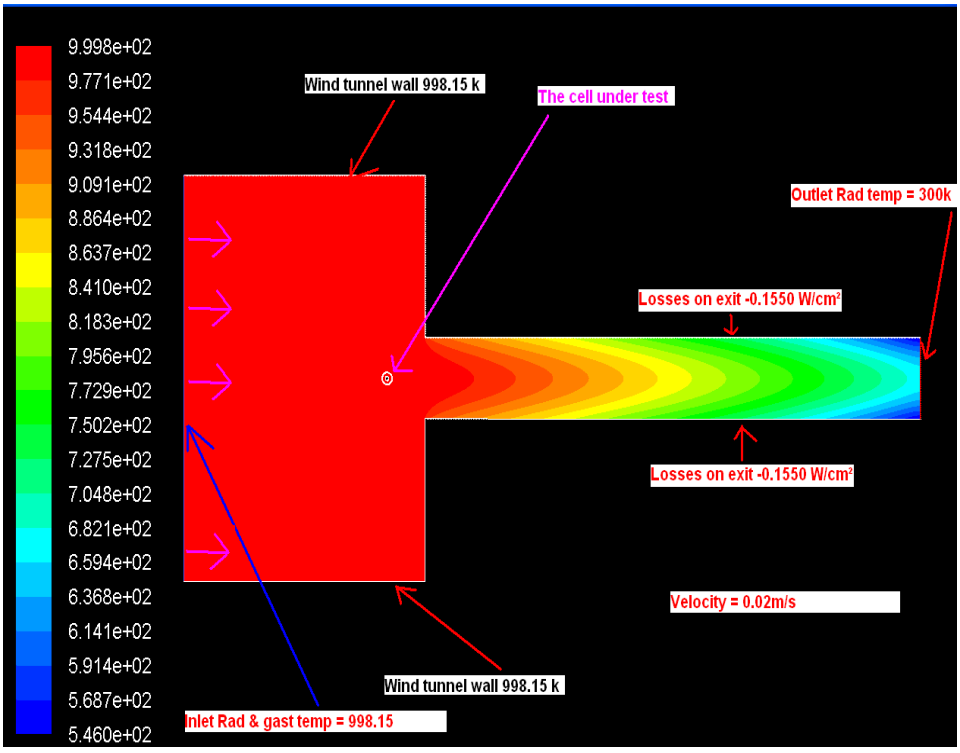

Figure 92: the boundary conditions applied to a 2-D model to investigate the effects of the wind tunnel profile on the temperature gradient around the cell.

To confirm the model was working correctly, initially simulations were performed without the radiation model. Figure 93 shows. as expected, that the temperature only decreases in the outlet channel, where heat is being removed through heat bridges. When a heat flux is applied to the cell, 2W/cm², as was the case when the MT-SOFC produced power, a 200°C temperature increase was observed in the 2D simulation see Figure 94. A simple energy balance calculation showed that this is a reasonable estimate if radiation is not included. This 200°C temperature increase was not observed it the experiments. This proved that radiation has to be included in these models.

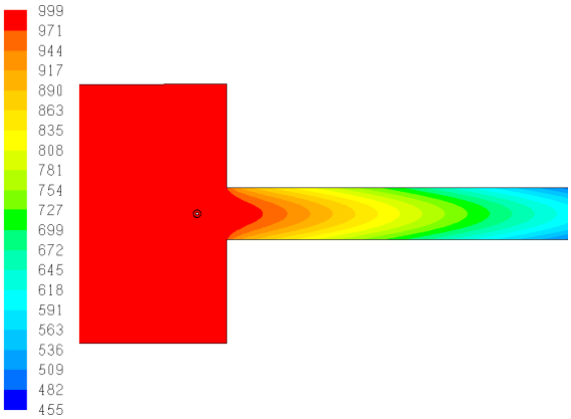

Figure 93: The temperature gradient when radiation model is not applied showing a broad temperature profile.

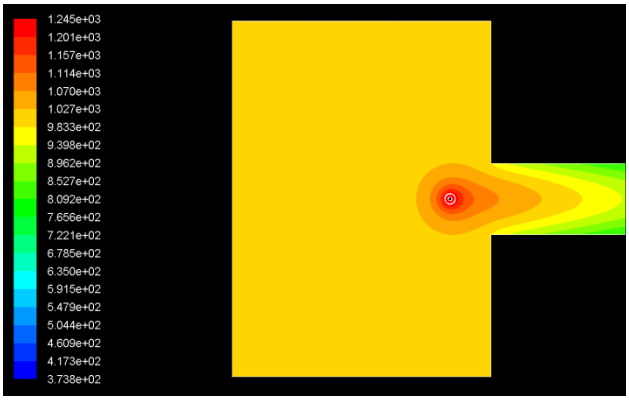

Figure 94: A case where a 2 w/cm² heat flux is applied to the cathode wall of the cell. As can be seen the temperature increases 200° above that which we would expect.

The next step in the iterative process to study radiation in the model with 2D models was to evaluate a model including radiation. The Discrete Ordinates (DO) model was chosen as it is a ray tracing model and is generally considered suitable for this type of modelling. The Phi and Theta values were selected as 5X5 and 5X5 which is more than enough resolution for this type of model. Figure 95 shows contours of temperature in the region around the cell. In comparison to the models where radiation was neglected, there is a massive temperature decrease. In fact the contours in Figure 95 suggest that the temperature of the cell should be even lower that the temperature of the gas. This would suggest that Fluent removes more heat from the cell through radiation out the back of the wind tunnel that is radiated to it from the side walls or supplied by the incoming gas. This result is of course unphysical and does not match the experimental results. Changing the emissivity and outlet radiation temperature did not increase the temperature of the cell substantially. In fact even changing the emissivity's of the cell to 1 (100% absorption) and wind tunnel walls to 0 (100% reflection) did not increase the cell temperature substantially and it still appeared to cool the gas.

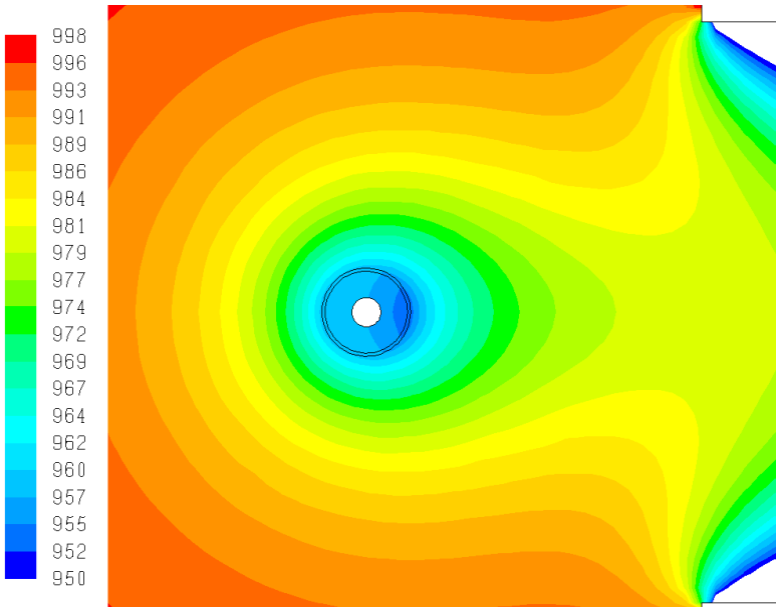

Figure 95: A simulation result for when a zero flux is applied to the outer wall of the fuel cell and there can be seen that the temperature profiles do not match the results of Figure 86

At this point to try to establish some additional information it was decided to add a heat flux to the cell to increase its temperature until it matched those of the experiments. Figure 96 shows that when a heat flux of 1.1W/cm² was added to the internal wall of the cell the temperature gradients around the cell appeared to match much more favourably in comparison to the experimental results. At this stage it was considered that the hydrogen flowing into the cell, on the fuel side, may be contributing this additional flux. A test was subsequently made in the wind tunnel for the same experimental conditions as stated for this model. The hydrogen gas flowing to the anode was switched off and the cathode wall temperature of the cell was monitored. It was found that the temperature of the cell did not change. Thus the hydrogen did not contribute this extra flux to the system.

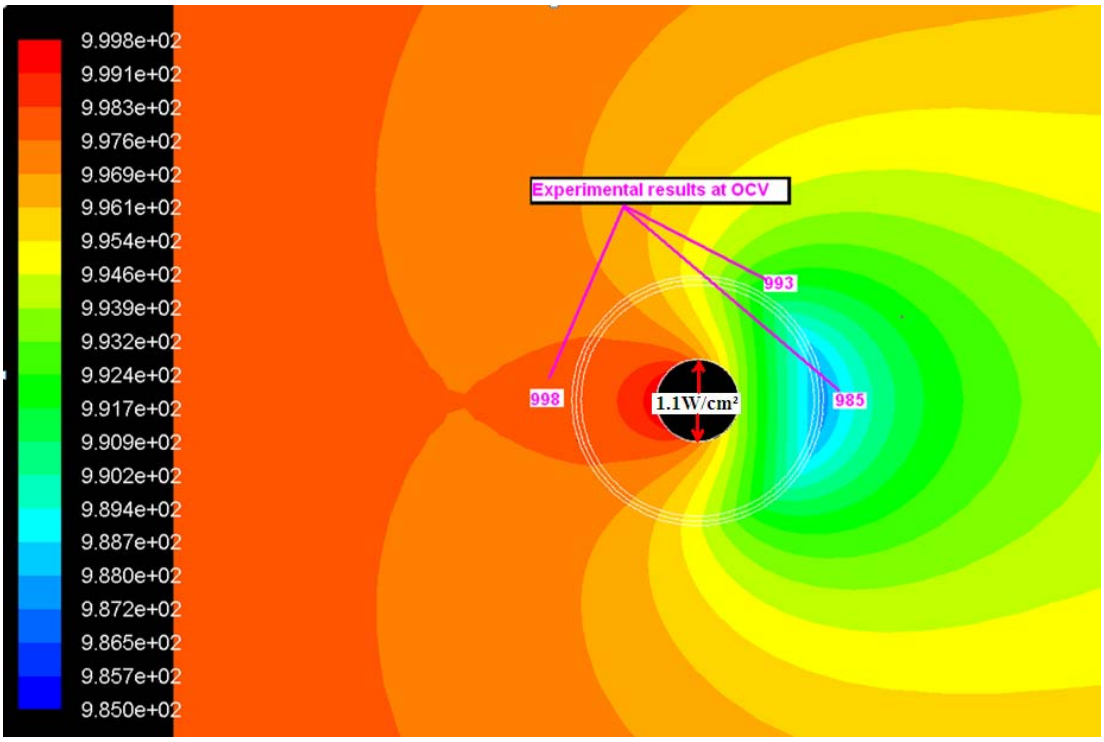

Figure 96: A flux of 1.1 W/cm² was placed on the inside of the cell because the cell temperature would be too low without it.

A heat flux of 2.8 x 10^8 W/m³ was then applied to the cell volume. Note that Fluent allows the user to inset volumetric heat fluxes into 2D models. These parameters are calculated on the basis that the 2D model is 1m thick. The results of the addition of this flux can be seen in Figure 97. This contour plot shows that the

change in temperature on the cell outer wall is very similar to the measurements made experimentally.

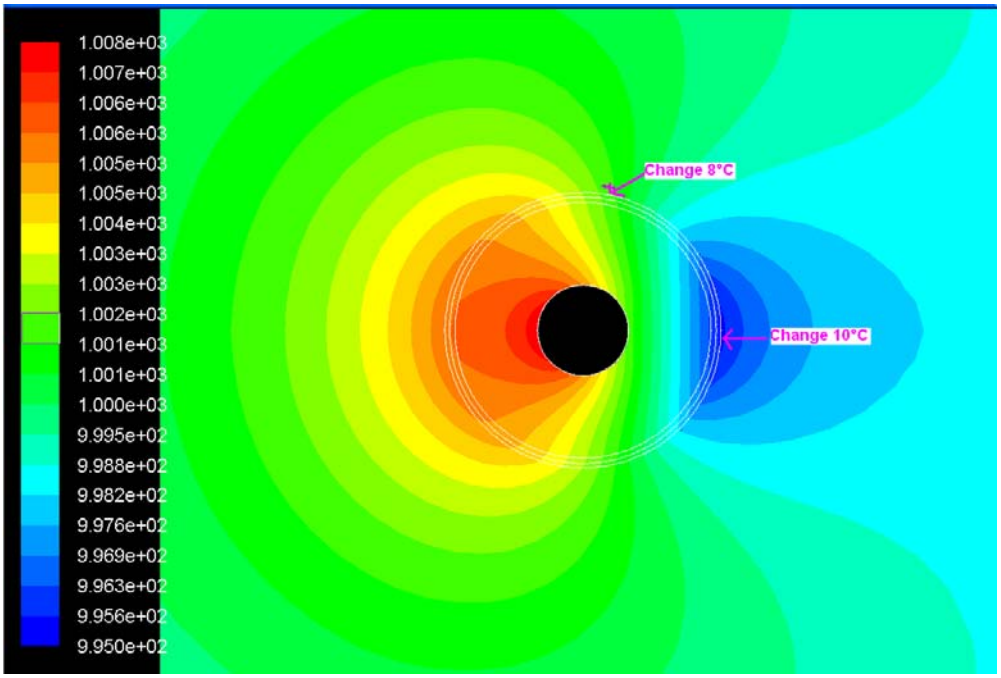

Figure 97: Temperature profile when a flux of 2e8 w/m³ on the electrolyte The simulation results match those of the experimental results.

However even though these profiles matched quite well it was considered that these results are unphysical and therefore do not represent the actual conditions inside the high temperature wind tunnel. Thus the only practical reason why the 2D model did not match the 3D case was that the top and bottom walls of the wind tunnel must also have supplied a heat flux to the cell. Thus 2D simulations do not allow for this attribute to be accounted for and this is why an additional heat flux had to be added to manipulate the simulation to give the correct results.

6.3.3 3-D simulations including radiation

Shown below, in Figure 98, are the parameters that were applied to the 3D model that included and accounted for radiation. The discrete ordinance model that was used in the 2D case was also used in this 3D case. The parameters such as emissivity and temperatures were measured using a combination of a thermographic camera and thermocouple inside the high temperature wind tunnel. Only half the cell was modelled to reduce the number of cells in the mesh. The cell was symmetrical, as shown below in Figure 98. The surface, which is hidden behind the displayed meshed, walls of the half cell, shown in "red", lies upon the symmetrical axis. This surface considers that all the flows and heat transfer that pass through it also pass back into it. This symmetry condition is often used for walls and boundaries with no friction. The important point to note, in this case, is that the DO model may be used. Other models such as the surface to surface model do not work with this symmetry condition.

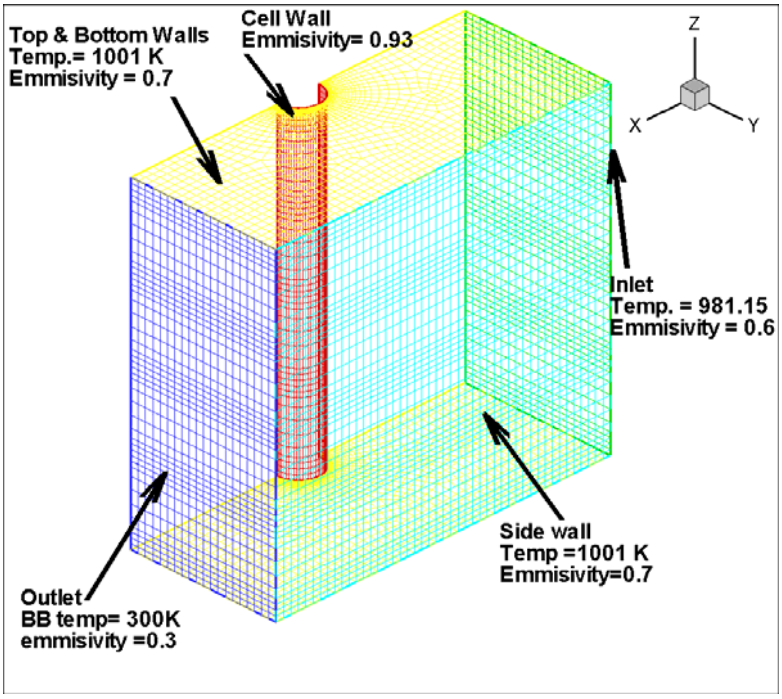

Figure 98: Only the fluid zone was included in the DO fluent model with the wall emissivity and temperatures set as shown.. Note that these values were obtained from experimental measurements using the thermo-graphic camera.

6.3.4 I/V and power curves comparison between model and experiment

The most important attribute that can be used to validate SOFC model simulations is the comparison of the modelled and experimentally measured I/V curves. The comparison should be made between the simulated and experimental curves. Shown below in Figures 99 and 100 are the I/V curves for a single MT-SOFC in cross-flow. To be certain that the models are variable the fuel flow rates were changed to see the effects of diffusion losses. Figure 100 shows the I/V curve for flow rates of 100 ml/m H_2 on the fuel side. In this case the I/V curves match quite well up to 1 watt/cm². The watts/cm² is calculated from the V multiplied by the A/cm² and the deviation towards the high powers is probably due to voltage losses in the experiment that are not accounted for in the model. These losses will occur in the wires connecting to the anode and cathode, which are in the high temperature zone and are not included in the simulation.

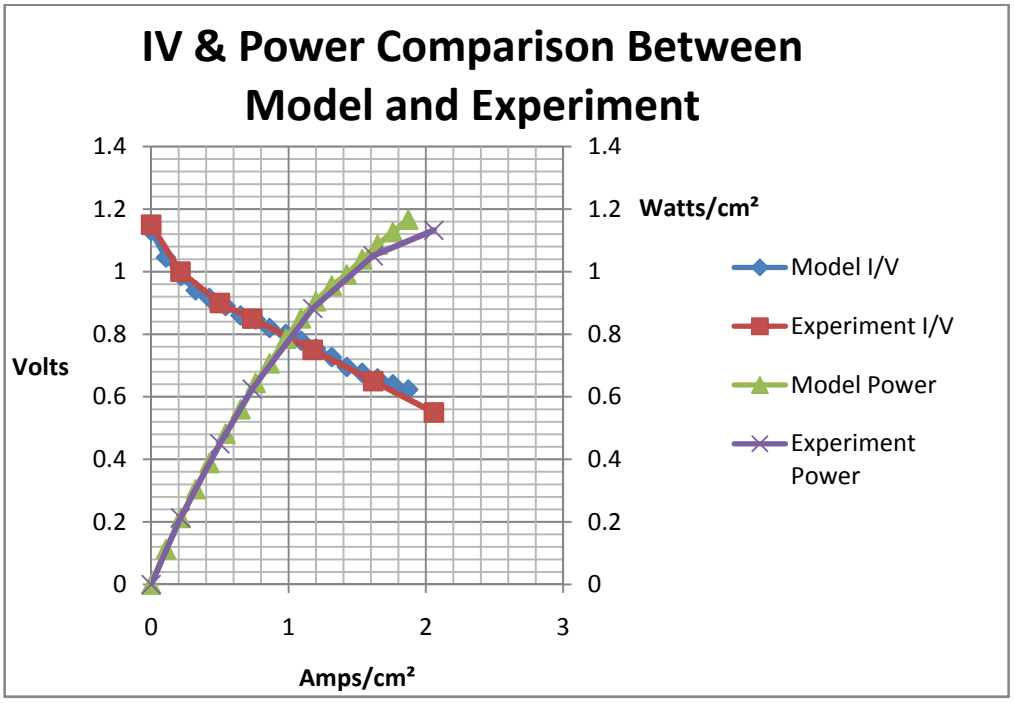

Figure 99: I/V and power curve comparison for the cell and the model at a flow rate of 100ml/min.

Shown in Figure 100 is the case when the fuel flow is 25 ml/min. With this fuel flow rate the experimental results clearly show cell losses because of diffusion. This is most clearly seen in the power plots where the plot bends down wards and indicates power losses. This occurs because the cell voltage is continually lowered by the load but the current produced by the cell does not increase. It does not increase because of shortages of reactants on the fuel side. Again the model and experiment powers match quite well up to the lower voltages/higher currents where the model power is slightly greater than the model result. As discussed previously this deviation can be attributed to losses in wires that are not included in the model but exist in the experimental setup.

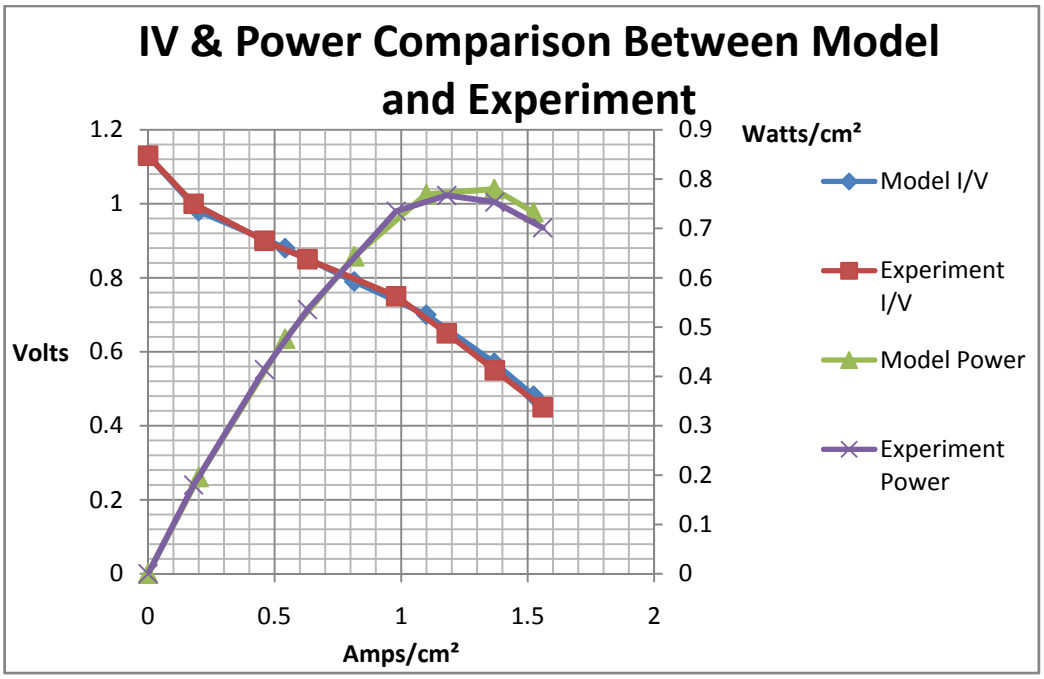

Figure 100: I/V and power curve comparison for the cell and the model at a flow rate of 25ml/min.

Shown below in Figure 101 is an image of the experimental setup with current and voltage contour plot inlays. The average current densities for these plots are 1.4A/cm². If the current and voltage plots are compared the effect of the silver wires and paste, which block the oxygen getting to the catalytic zones underneath them can be seen. The result is rings where the current density and voltage are considerably lower than on the exposed parts of the cathode. The highest current

density and lowest voltage drop occur at the top of the cell where the highest concentration of oxidant and fuel occurs. On the voltage plot the voltage is higher in the middle of the top cathode zone, uncovered by the silver wires and paste. This can be observed for example as the "red" spot of high voltage on the top of the cell. This high voltage occurs in this zone because of the lower current densities and high reactant concentrations located in this region. In regions nearer to the electrical connections more current travels towards the electrical connections. In these regions if the current is integrated, it is clear that the losses in the cathode increase as the current increases and thus voltage decreases.

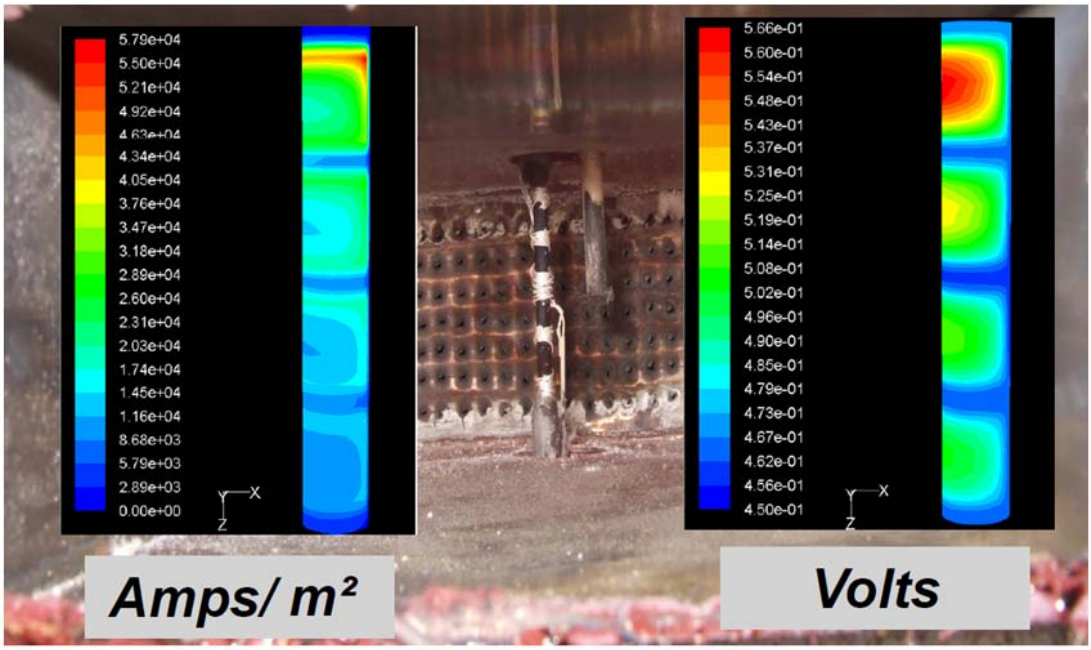

Figure 101: A sample comparison of the voltage and current plots on the outside cathode wall of the MT-SOFC in the wind tunnel.

6.3.5 Temperature at OCV conditions

In the following section simulation results are shown for a single MT-SOFC in cross-flow, like in the wind tunnel where electrochemical and radiation models are included. A key part of this validation component of the study was to try to get the temperature profiles of the simulated cell to match those measured with the thermographic camera as described and seen in section 6.2. Figures 102 and 103 show details about the temperature profiles that the thermographic camera cannot show. The temperature of the gas stream and internal sections of the cell can be seen in the simulations when no load is applied to the cell. The inlet oxidant gas flows from left to right and the effect of the top and bottom walls in heating the oxidant gas can be seen on the top and bottom planes. In comparison the middle plane remains colder until the heat has convicted into the gas at a point just beyond the cell. As the cell does not produce any current its temperature is solely dependent on the heat it receives from the gas and radiation from the walls of the wind tunnel.

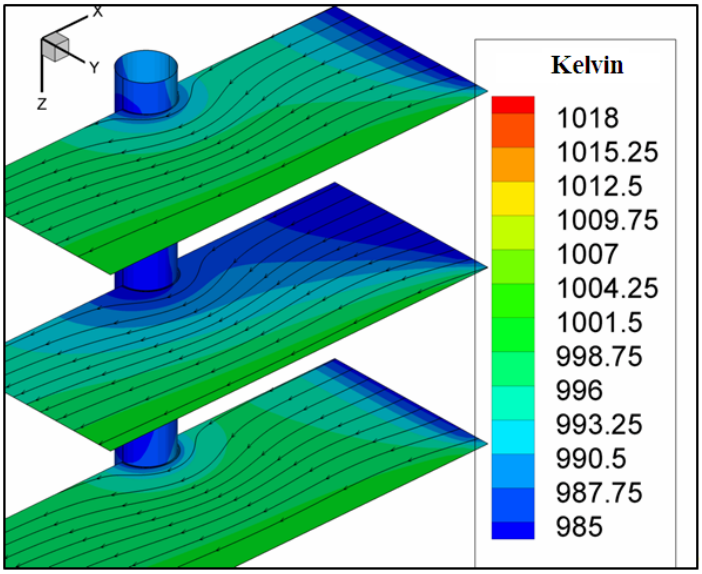

Figure 102: An illustration that shows the temperature profile (Kelvin) in three perpendicular sections along the length of a cell under test. Also the cell wall temperature and gas temperature is shown.

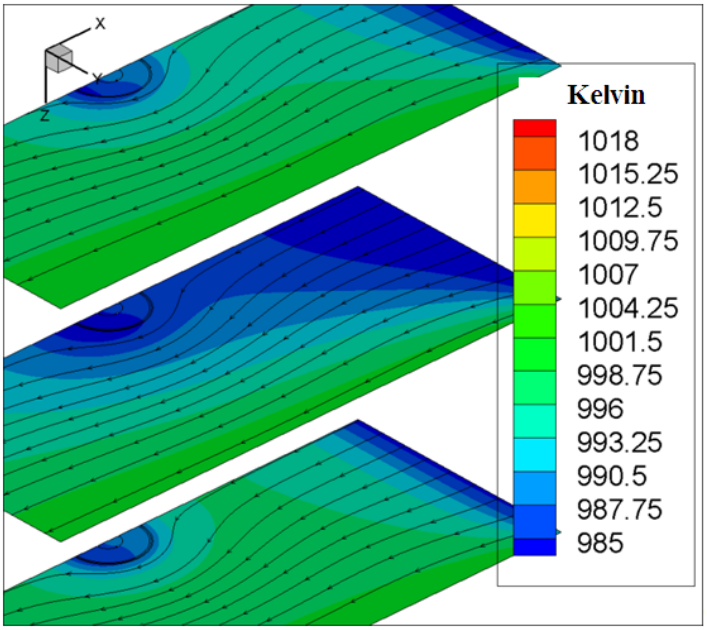

Figure 103: An illustration showing the temperature profiles (Kelvin) in the same order as above but without temperature profile on the cathode wall so that the radial temperature across the cell can be seen.

Figure 104 shows the temperature on the front and rear of the cell. The definition of the temperature contours in Figure 104 (A), show the effect of the radiation losses due to the losses out the exit of the wind tunnel. Figure 104 (B) does not show similar contours because of the radiation coming from the diffuser in the wind tunnel and side walls. An interesting observation in Figure 104 (B) is the increase in temperature at the top and bottom parts of the cell. This is due to heating from the top and bottom walls of the wind tunnel and no radiation losses on this side of the cell in comparison to the other side. Figure 105 shows a comparison between the experimental results (A) and simulated results (B) of the temperature profile on the outside wall of the MT-SOFC under test. Figure 105 (B), while it roughly shows the cold streak down the back of the cell, does not show this streak as defined as in the thermal camera image.

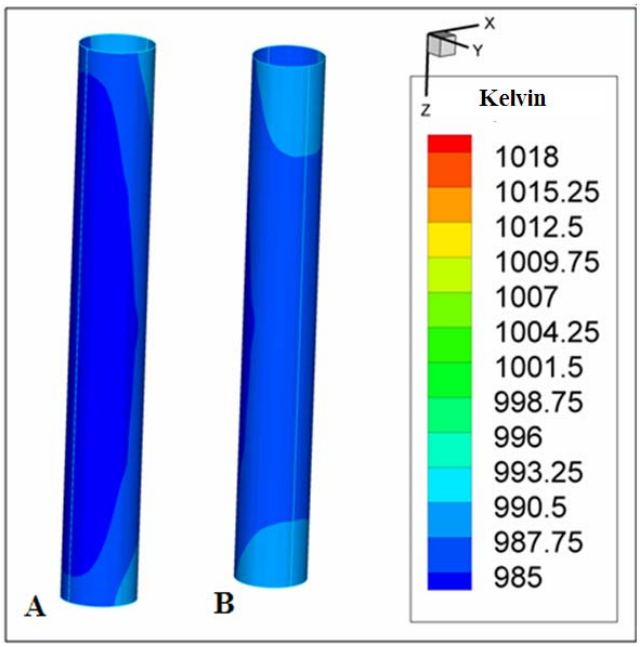

Figure 104: The temperature profile (Kelvin) on the outside wall of the cell. (A) depicts a view looking at the rear of the cell and (B) looking at the front.

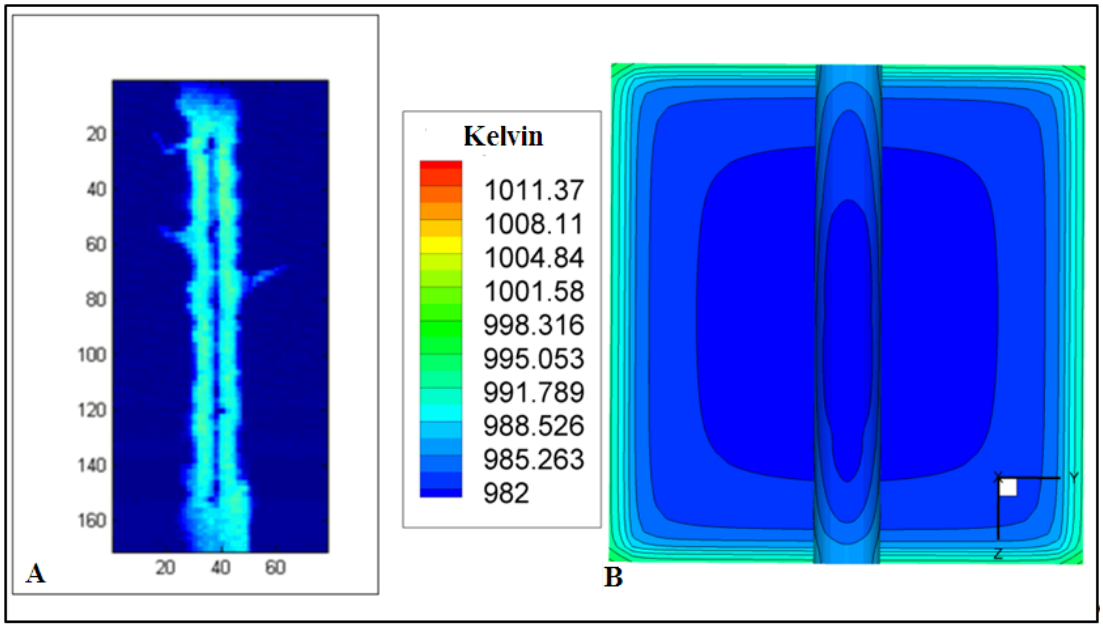

Figure 105: A comparison between a thermographic camera result (A) and a simulated result (B). Note that the temperature scale (Kelvin) applies to both.

6.3.6 Temperature at a loaded 1.5 A/cm² conditions

Simulation contour plots when the cell is delivering 1.5 W/cm² is shown in Figures 106 and 107. Again the temperature profiles of the gas flow and internal sections of the cell can be seen. It is interesting to note that the cell is clearly heating up some of the gas before it even reaches the cell and this is because of the low 4cm/sec flow rate. Also observable is the temperature gradient difference between the front and rear of the cell, which is about 8 K at the top of the cell, as seen in Figure 106. As displayed in Figure 107, the cell heats the gas about 15°C higher just before it reaches the cell in comparison to the OCV case. Refer to Figure 103 to see this contrast. This increase in temperature is due to the slow flow rate of the gas that allows conduction of heat into the oncoming flow and the high temperature of the cell wall that faces the hot diffuser and side walls. This orientation, that allows the temperature of the cell to increase so high, is in stark contrast to rear face of the cell, which suffers high temperature losses due to the opening at the end of the wind tunnel.

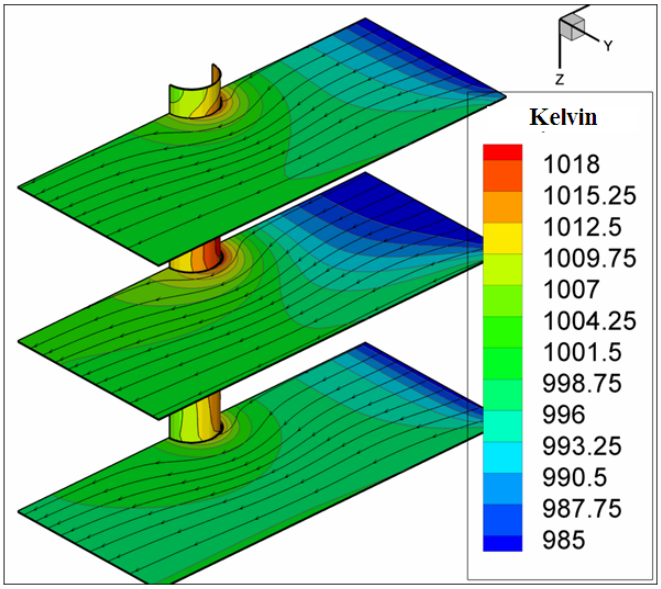

Figure 106: An illustration that shows the temperature profile (Kelvin) in three perpendicular sections along the length of a cell under test also the wall temperature and indirect gas temperature

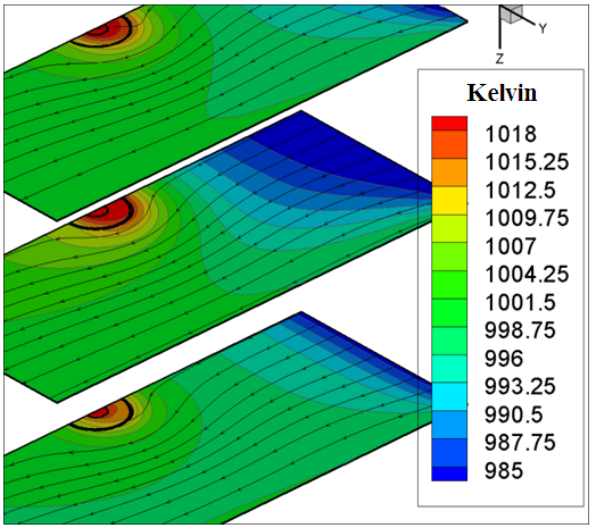

Figure 107: An illustration showing the temperature profiles (Kelvin) in the same order as above bust without temperature profile on the cathode wall so that the radial temperature across the cell can be seen.

Figures 108 and 109 show, in much better definition, the cold streak down the back of the cell, as was observed in the experimental results. The reason for why the cold streak definition does not "exactly" match the experimental result when the cell is not under load is not clear. But it may be that the shape of the model does not match exactly the shape of the wind tunnel as the wind tunnel surely has more imperfections in its wall smoothness compared to the model, which of course would be totally uniform. However further analysis by changing the shape of the model and re-simulating for slightly different radiation properties could tweak the results into giving a more agreeable definition. However as when the cell is hotter than the wind tunnel walls, as seen in the loaded cell case, the definition was much clearer and it was decided no further simulation was necessary.

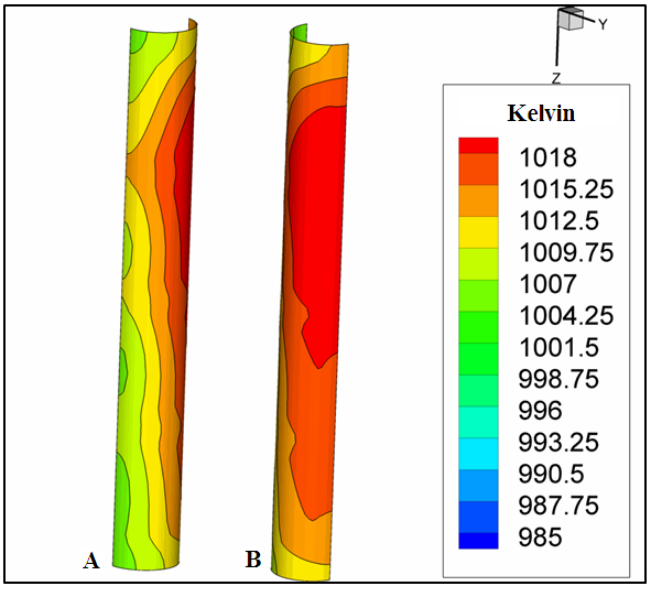

Figure 108: The temperature profile (Kelvin) on the outside wall of the cell. (A) depicts a view looking at the rear of the cell and (B) looking at the front.

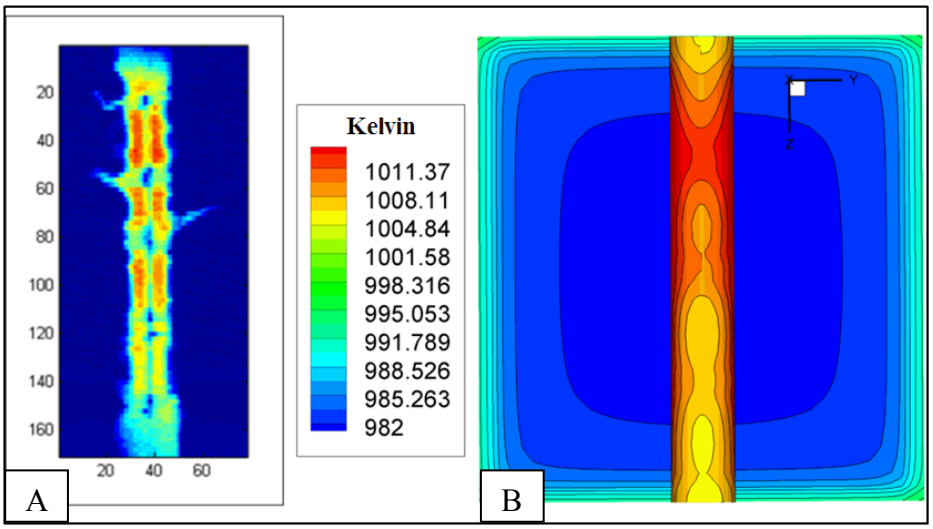

Figure 109: A comparison between a thermographic camera result (A) and a simulated result (B). Note that the temperature scale applies to both (Kelvin).

Figure 110 shows, when the cell is loaded and produces 1.5 A/cm², the heat flux that the cell produces. The temperature profile is also shown and such flux values are very usefully for simplified modelling of MT-SOFC like tubes, where the electrochemistry is not needed, for example when seeing temperature inside big stacks. An interesting feature of the heat flux and temperature plot shown in Figure 110 is that even though most of the heat is generated at the rear of the cell, where the contact resistance from the current collection connections has an influence, the temperature does not increase higher than the front of the cell. This is because of the high radiation losses that the rear of the cell endures, compared to the front, means that the cell temperature will not increase in an even proportion on both sides of the cell.

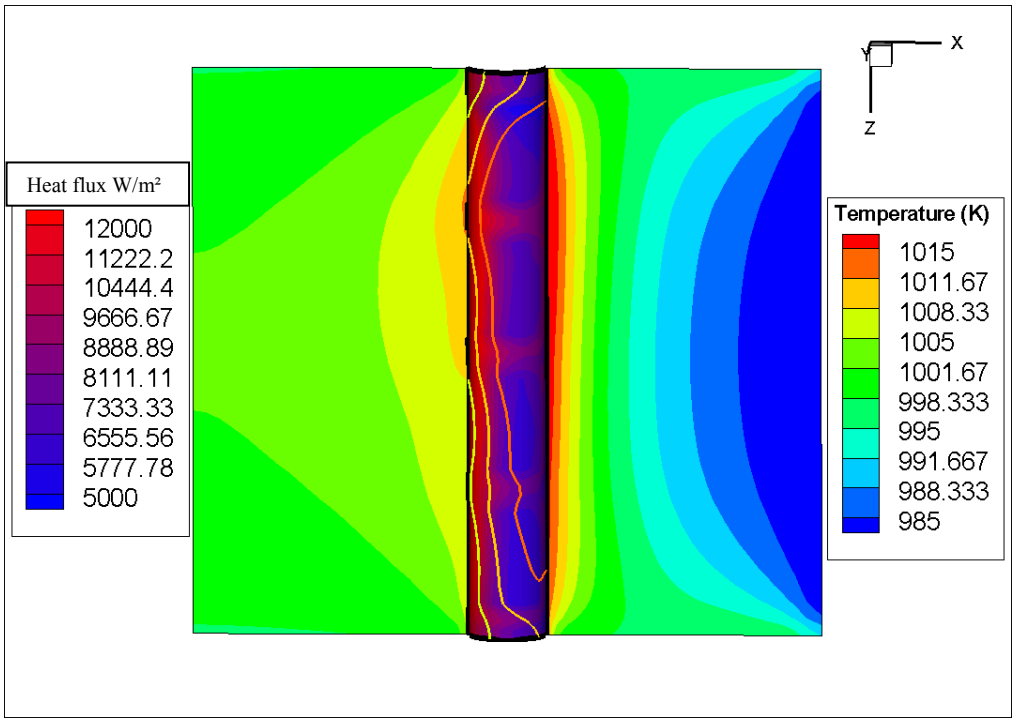

Figure 110: The thermal heat flux produced by the cell depicted by two colour scale and the resulting temperature profile in the oxidant gas shown in the rainbow scale. The lines seen on the outside wall of the cell refer to the temperature profiles (Kelvin).

6.3.7 Simulations showing specie concentrations

Because this study also deals with mass transfer to a cylinder in cross-flow a detailed species concentration analysis was also performed via the models. For the simulations below, the velocity on the oxygen inlet was 0.016 m/s meaning a Reynolds number of approximately 0.13. It can be seen in the simulation results in this section that the supply of oxidant was adequate. Thus for a single cell in cross flow, the flow regime will certainly be in creeping flow with little or no wake observable behind the cell. As a point of reference for the reader in all the following images the oxidant is travelling from right to left and the fuel is travelling from the top of the cell to the bottom.

Shown below in Figure 111 is the current production contours along the length of the cell with the mass fraction of oxygen superimposed on the background. The highest current density occurs at the top of the cell where the hydrogen concentration is at a maximum. This can clearly be seen in Figure 112 where the mole fraction of hydrogen is shown along the length of the cell. Notice how the hydrogen concentration depletes along the length of the cell. The molar concentration of oxygen along the length of the cell varies by about 30%. Although this means a low fuel utilisation the effect on the current density can clearly be seen when referring to Figure 111. The region of the cell with a high current density 40000 A/m² occurs because of the short path that the current on the cathode must travel to the current collector and high species concentrations. Notice that in this corner the current collection is made above this zone and to the right of this zone by the silver rings, where the current is collected by the wires and paste linking each of the rings. Refer to Figure 60 to see clearly how the current collection to the cathode was made. Such a high current density is not predicted to occur in the other open cathode zones because of the reduction in the hydrogen concentration. Refer to Figure 116 to see how small decreases in hydrogen concentration have a stark effect on the Nernst potential.

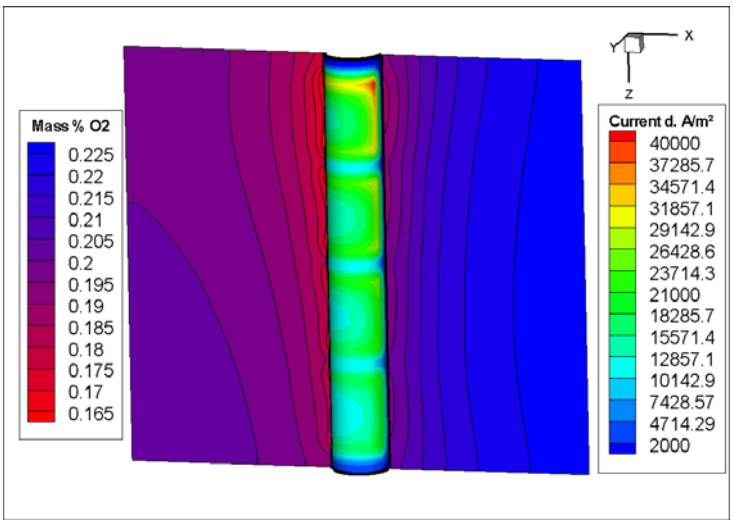

Figure 111: The current production of the cell into rainbow scale in the mass fraction of oxygen in the two colour scale

Figure 112 below shows a very interesting plot where the effects of the species concentrations on the current density can be seen. To see the current density refer to Figure 111. The hydrogen is depleted in the cell non-linearly around the perimeter of the cell as might be assumed. Because of the way that the current collectors are positioned on the cell, refer to Figure 60, and the way the oxidant is fed to the cell, the contours of hydrogen peak with a high utilisation of hydrogen at the front of the cell. The effect is most noticeably seen in Figure 112 at the top of the cell in the regions where the current density is high the hydrogen concentration is lower.

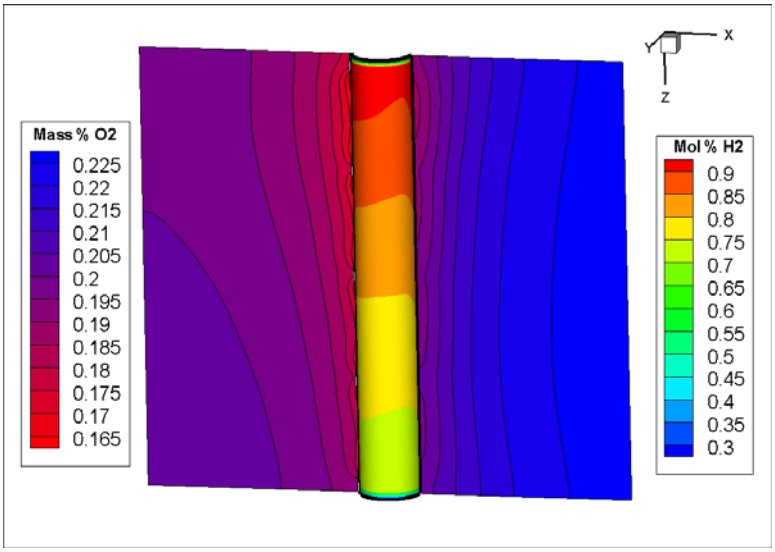

Figure 112: The mass concentration of oxygen in the fluid flow and molar faction of hydrogen at the electrolyte anode interface.

An importance point to be observed in Figures 112 and 113 is the depletion of oxygen along the length of the cell. Note that where the high concentrations of hydrogen exist high currents are produced in the modelled cell. Where these high currents exist, a substantial depletion of oxygen also occurs. The concentration of oxygen along the back of the cell ranges from 16% to 19% mass oxygen and 19% to 20% mass fraction along the front of the cell. The lower concentration of oxygen at the rear of the cell is in the wake region and because of the depletion of oxygen around the perimeter of the cell; the concentration of oxygen in this region will be lower. Notice that the highest difference in oxygen concentration between the front and rear of the cell is observed at the top of the cell where the hydrogen inlets and the reaction rate is highest. At the top of the cell the difference is 16% to 19% mass oxygen as opposed to 19% to 20% mass fraction of oxygen near the hydrogen outlet

The variation of oxygen around the perimeter of the MT-SOFC can be seen in Figures 113 and 114. When visually comparing these two images, that give a view looking at the front and rear of the cell, the effects of oxygen depletion can be seen.

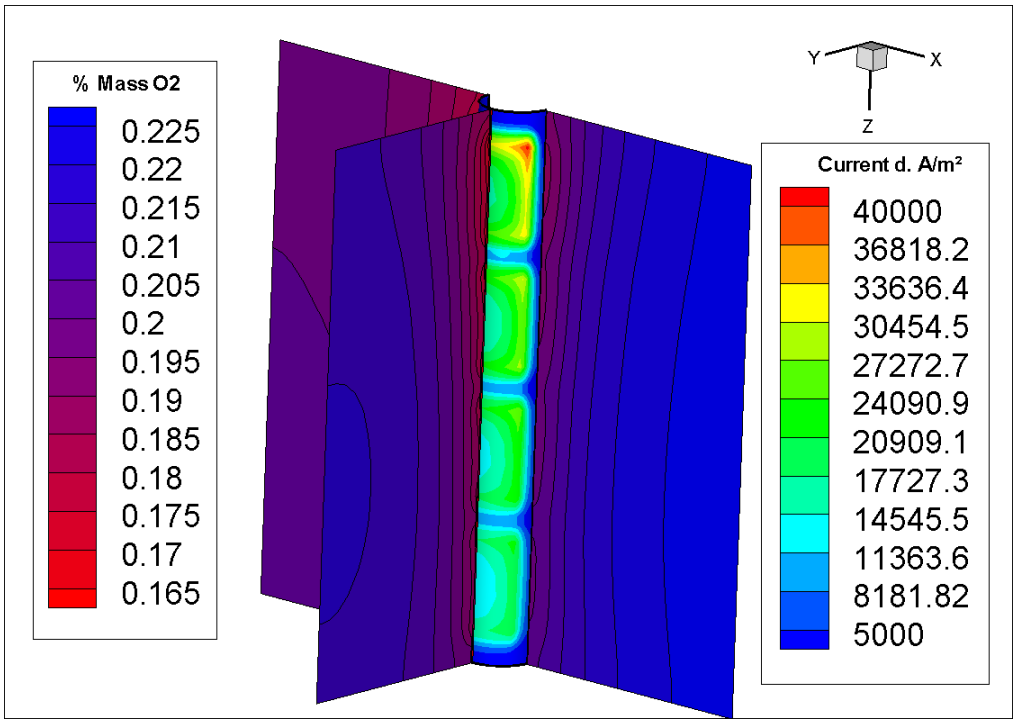

Figure 113: A three-dimensional plot of the mass fraction of oxygen in the gas flow looking at the front of the cell and the current density on the electrolyte cathode interface

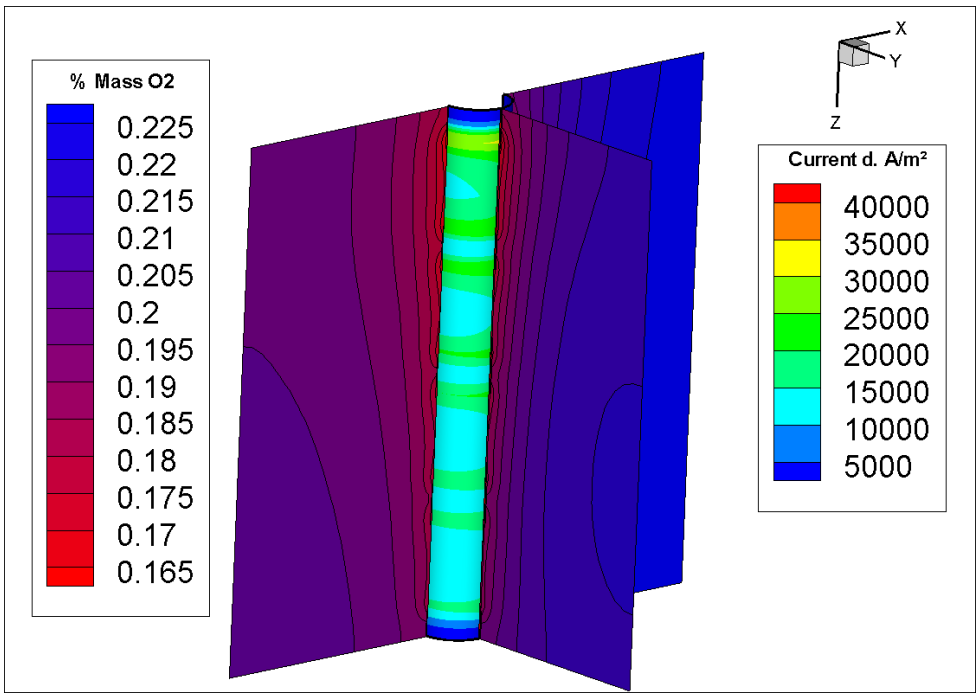

Figure 114: A three-dimensional plot of the mass fraction of oxygen in the gas flow looking at the back of the cell and the current density on the electrolyte cathode

6.4 Results of using MT-SOFCs to measure the rate of mass transfer to a cylinder electrode cross-flow

6.4.1 Determining the effects of electrical coupling between the two cathode strips

As can be seen in the results of the initial experiments, for example in Figure 115 (the graph) when-current is taken from the large cathode the open circuit voltage of the testing strip decreased and this is not an ideal case when highly accurate measurements are required. Table 6 shows in more detail this electrical dependence. It was realised that the partial pressure of hydrogen in the fuel flow can have a massive effect on the OCV of the cell.

As can be seen in Figure 116 the partial pressure of hydrogen in the fuel flow can have a massive effect on the OCV especially when fuelling the cell with almost

pure hydrogen. This means that when the large cathode is producing current also produced water and this caused the open circuit voltage of the testing strip to fall dramatically as can be seen on the right-hand side of Figure 116. It has been considered that the best method to reduce this electrical coupling is to reduce the partial pressure of hydrogen in the fuel flow by introducing water. For subsequent experiments partial pressure of 0.5 hydrogen and 0.5 water was selected to give the maximum reduction of the electrical coupling.

Table 6 Measurement of the electrical dependence of each of the testing strips

No Flow Conditions

	Testing Strip		Normal Cathode	
Test	Volts	Amps	Volts	Amps
both passive	0.604	0.35	0.6	0.97
Testing strip on	0.6065	0.3449	1.08	0
Normal cathode on	1.0798	0	0.6	0.97
both passive	1.13	0	1.13	0

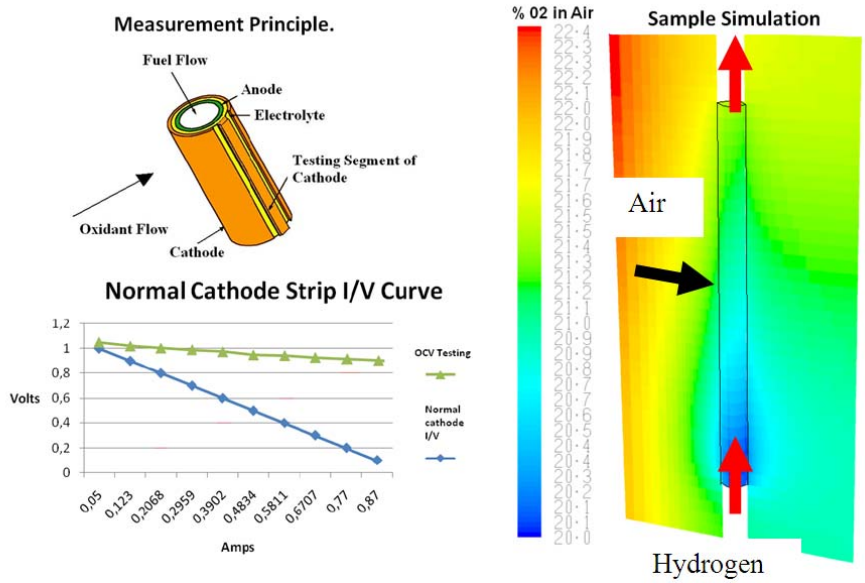

Figure 115: I/V curves showing how as more current is taken from a strip on the cathode the open circuit voltage of the other strip reduces and a initial simulation result for the concentration of oxygen around the cell.

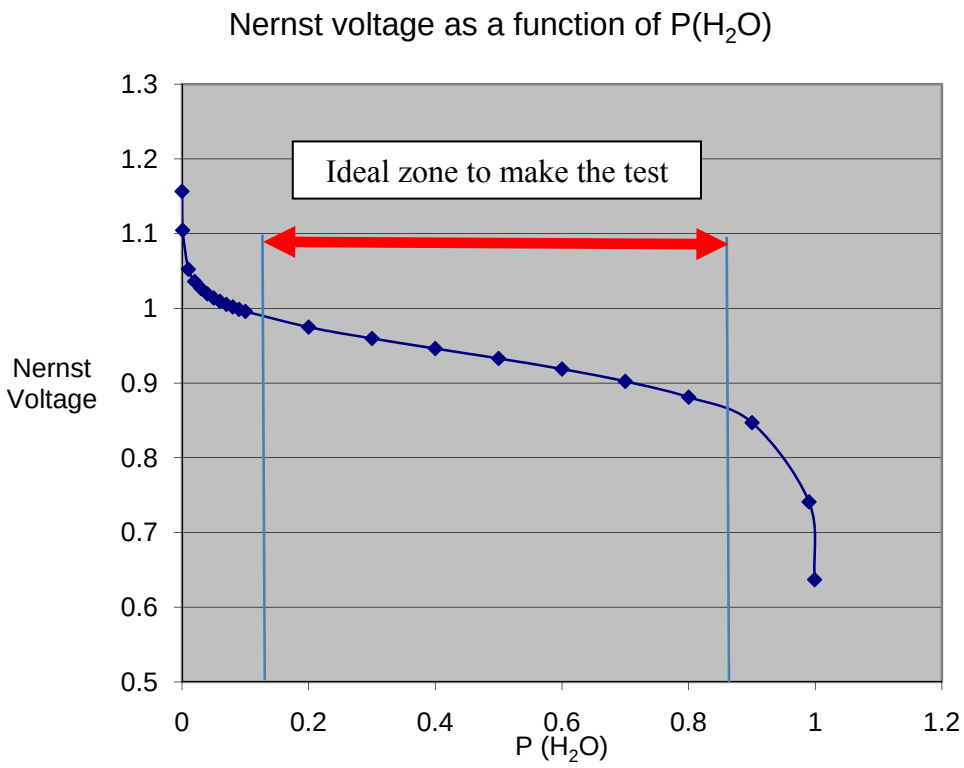

Figure 116: Plot showing the effect of the partial pressure of water in the flow on the Nernst potential.

6.4.2 Increasing the resolution that accuracy of the measurements.

As can be seen in Figures 113 and 114 and to a certain extent in Figure 115 (sample simulation) the concentration of oxygen along the length of the long cell is not constant. This means that accurate measurements would not be possible due to the poor resolution. To increase the resolution it was considered that a smaller cathode should be used. Using a smaller cathode means at the current production in the cell should be more or less constant along its length. Because the measurement of current density is directly related to the oxygen content, when the cell is running at low fuel utilisation, having a variable current profile along the length of the cell reduces the accuracy of the measurement. It was then decided that from this point the experimentation on smaller cathodes should be used.

As has been discussed in section 7.4.1, the smaller cathodes that were made tended to produce higher current densities. The original I/V curve for the cell shown in the remainder of this section also matched this trend. This effect is shown in Figure 117 where the "Testing strip" which is smaller than the "Normal strip" has a higher current density. The reason that the current density may appear higher on the small cathode was attributed to the smaller currents that flow from it through the connection wires and thus lower ohmic losses. Higher ohmic losses in the already hot wires will increase as the sum of the current increases and this may cause higher losses the larger the cathode which was indicated by a lower current density reading than expected. The reason that the current densities became the same in the later experimental section is not clear. However this may be attributed to degradation in the cell or movement of the current collection wires that increased the contact resistance.

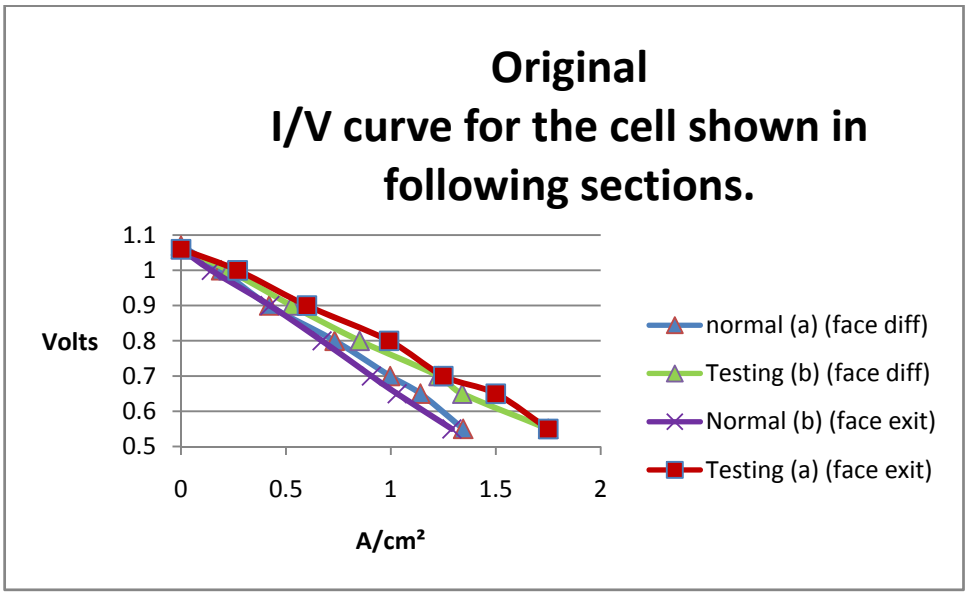

Figure 117: I/V plot for the cathode testing and normal strips the first time that the cell was tested. Notice that the testing strip produces higher current densities than the larger normal strip.

6.4.3 Determination of the extent of electrical dependence when using a smaller cathode.

Shown in Tables 7 and 8 are the experimentally measured effects of the electrical coupling between the cathode normal and testing strips for the anode supported cells with small cathodes. The effect of the fuel concentration depletion by the activated cathode is clear, particularly the effect of the activated normal cathode on the testing strip (OCV) is much larger at 100% P (H_2) than when at 90% P(H_2) 10% P (H_2O). Compare tables 7 and 8 to see this effect. Please note that it was originally aimed to get 50% P (H_2) and 50% P(H_2O). When the humidifier was set to supply this amount, the voltage of the cell only ever dropped to 1.05V and would not go lower. Referring to Figure 116 this means that the water content in the cell could not have been more than 10% P(H_2O).

When the value of humidification supplied to the cell was maintained at 50% P (H_2O) the voltage did not drop any lower than 1.05V and after a short period of time the OCV of the cells became erratic. It was noticed in the pipes leading into the fuel cell that water "back flowed" from the cell into the pipes (against the flow) in bursts every few minutes that became larger over time. 50 % P(H_2O) in hydrogen would mean that 90% of the mass was the water. So it seems that the orientation of the cell in the wind tunnel, fuel flowing from top to bottom, means that there is a maximum value of water that can enter the cell. In other cases where the cell was orientated horizontally this effect was not noticed. However this extra 10 % P(H_2O) seemed to have a good effect in reducing the coupling between the two strips.

Table 7: The effect of the testing strip and normal cathode on each others OCV when producing current at 100% P(h_2) @50ml/min 4ml/min air flow.

Normal Volts	Normal amps/cm²	Testing volts	Testing amps/cm²
1.223	0	1.221	0
1.08	0	0.55	1.16625
0.55	1.1095	0.55	1.4733
0.55	0.1654	1.01	0

Table 8: The effect of the testing strip and normal cathode on each others OCV when producing current at 90% P(h_2) @50ml/min and 90% P(h_20) 4ml/min air flow

Normal Volts	Normal amps/cm²	Testing volts	Testing amps/cm²
1.05	0	1.05	0
1.03	0	0.55	1.026
0.55	1.102	0.55	1.022
0.55	1.104	1.025	0

6.4.4 Determination of the extent of temperature dependence on the currents produced by the cell.

The temperature variations in the wind tunnel, as shown in section 6.2, may have also influenced the current densities that the testing strip produced. To quantify the current density measurement error, caused by temperature variations, the effect of temperature variations that occurred inside the wind tunnel, on the measurements made had to be established. As shown in Figure 118, condition (a) when the normal strip faces the diffuser and condition (b) when the normal faces the exit under 4cm/sec air flow, the temperature effects on the testing strip are negligible. However the temperature effect on the normal face is much more pronounced most probably

because of its larger area meaning that it is much more susceptible to even small temperature variations.

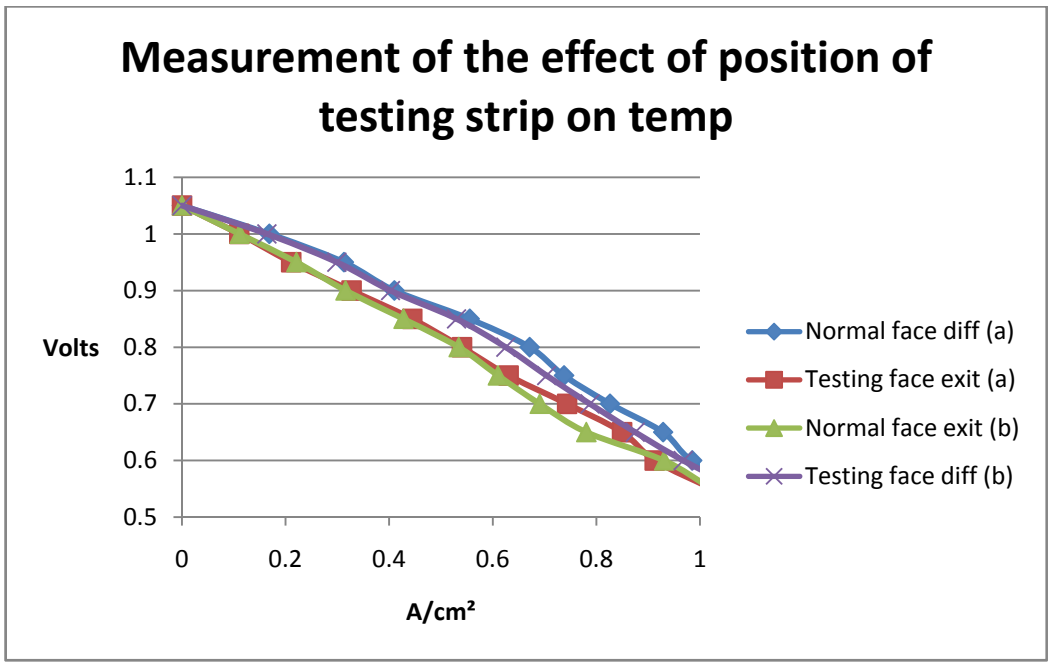

Figure 118: Measuring the effect of temperature variations within the wind tunnel with 0.9 P(H_20).

6.4.5 First attempts at oxygen concentration measurements.

Unfortunately as this was the last section to be researched in the thesis only the case of 1.5% oxygen in nitrogen at a flow rate of 16cm/s was chosen as a case that should be used to validate CFD simulations. Table 9 shows the results of the first attempt to establish the content of oxygen that remained in the gas fed to the cathode, even when 100% N_2 was fed to the cathode. Oxygen can diffuse through tiny leeks in the wind tunnel itself and also in the piping to the wind tunnel. As can be seen in Table 9 tiny traces of oxygen were in the supposed 100% gas feed. In this table the measurements under "testing face diff" refers to when the cell was orientated so that the small cathode strip faced the inside of the wind tunnel i.e. facing the oncoming gas. The measurements under "normal face diff" refers to the opposite condition when the larger cathode faces the oncoming gas. This measurement showed possible problems with the measurement method.

The results show to the contrary what should have been measured. For example the current density on the testing strip increases when the normal strip faces the diffuser. i.e. it changes from 0.017 A/cm² when it faces the diffuser and 0.075 A/cm² when it faces the exit of the wind tunnel.

Table 9: Measurements taken on the front and rear of cylinder for a flow rate of 16 cm/sec (100%N_2)

0.65v	**A**	**A/cm²**
Testing face diff.		
Testing	0.00134	0.01675
Normal	0.0036	0.0216138
Normal face diff.		
Testing	0.0060	0.075
Normal	0.0022	0.0132085

Because of time constraints these measurements were not finished successfully. The problems encountered in this experimental section are discussed in Section 7.4.2. It proved to be more difficult to make these measurements than initially anticipated however the information obtained in this section will provide a head start for any follow up work. The key components required for future experimental work are included in this section including humidification of the fuel, smaller cathodes. More improvements for the experiment design are also discussed in Section 7.4.2.

6.5 Results of detailed modelling of the concentration of oxygen around the perimeter of a MT-SOFC in cross flow and the fast solving model.

First of all a cell with a 4mm cathode ring around the cell was tested and compared to the simulated model. The conditions of the test were 23% oxygen in nitrogen flowing at a rate of 16 ml/min on the oxidant side of the cell. The fuel side the cell was fed with 50 ml/min hydrogen with 1% mass water. Details of the fluent simulation parameters can be found in Appendix XI. Figure 119 shows an I/V and power curve of this cell with high concentrations of hydrogen. As can be seen the plots match quite will up to the higher current densities where the experimental measurement and simulation result drift apart.

This is probably caused by the size of the small wires used to provide the electrical connection to the cell. As the current density passing through these wires increases their temperature the resistance of the wire will also increase. As the wires, which are also in the high temperature zone that connect to the silver wires and paste to the load, are not included in the model this effect will not be accounted for by the simulations. For this reason the lower cell power output at higher current densities can clearly be observed in Figure 119. Regardless the similarity in the experimental and predicted versions of the I/V and power curves provide evidence that the model provides a good estimation of the performance of the cell used in the experiment.

Figure 120 shows a comparison of the simulation and experimental results for the same cell used previously, but with a different concentration of hydrogen in the fuel flow. This cell was tested experimentally fed and simulated with 56% mass water or P (H_2O) 10%. It was initially planned that the cell should be fed with a mix of 50% P (H_2O) and 50% P (H_2). However it was found that the maximum amount of water that the cell could allow without blocking was about 10% P (h_2o).or 56% mass water.

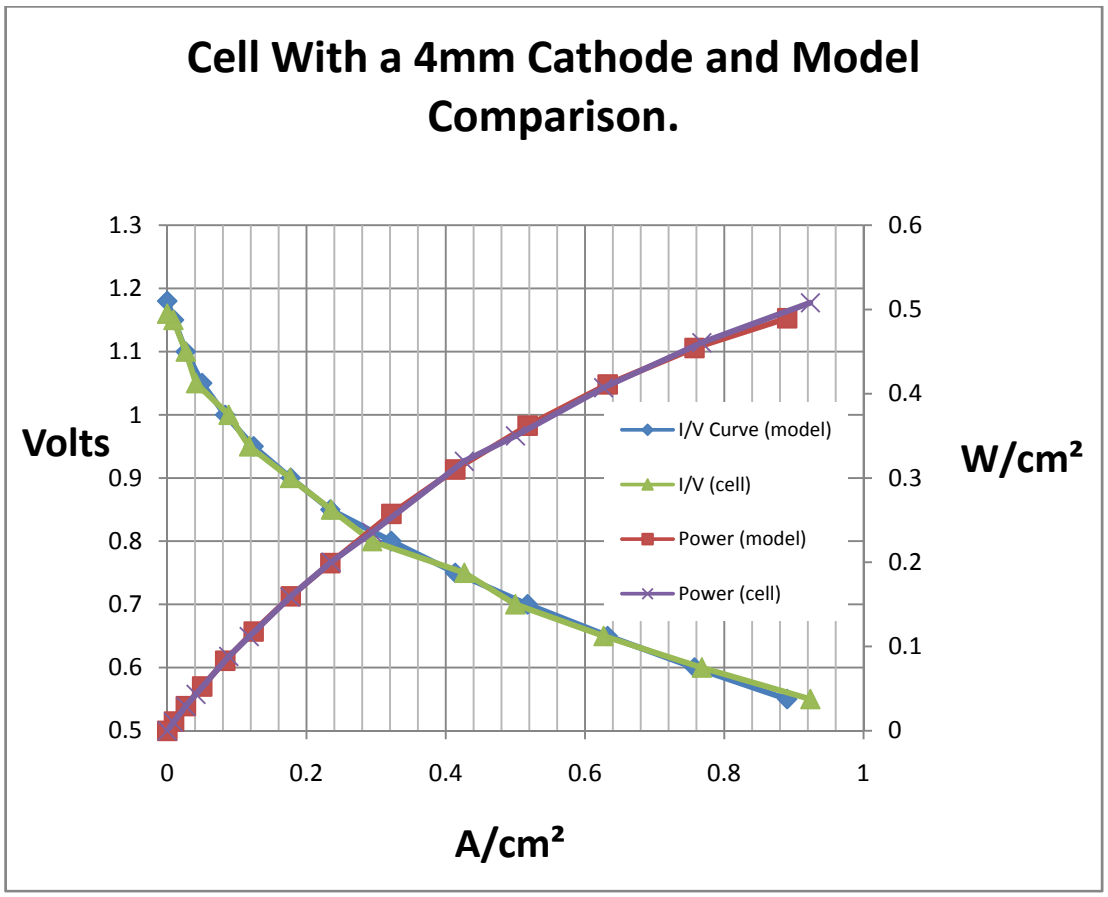

Figure 119: Comparison of a tested cell in the high temperature wind tunnel and the Fluent model.

This case was also tested experimentally and simulated with the parameter changes as seen in Appendix XI. The mass flow rate was 5.744 x 10^{-8} kg/sec and the specie contractions were 56% mass H_2O and 44% mass H_2 The mass flow rates were originally calculated by hand as two separate devices, the volumetric hydrogen flow regulator and mass vapor regulator, were used to feed the fuel gas to the cell. The mass flow rates of the hydrogen regulator and vaporizer were adjusted to provide 55% mass water and 45% mass hydrogen. Shown in Figure 120 is a comparison of the I/V curves for the simulated and experimented cell.

On the current density plot, shown in Figure 120, up to a current density of 0.4 A/cm² the results of the model and simulation match quite well. However at current densities above 0.4 A/cm² the current density of the modelled cell tends to be lower than the simulation result. This is probably caused by the ohmic losses in the current collection wires that are not included in the simulation. The results show that

simulations made with various concentrations of hydrogen and water are also accurate. An interesting observation that substantiates the validity of the model is the drop in OCV caused by the reduced potential of hydrogen, which was also most identical in the experiment and simulation. This is clearly seen when comparing the maximum voltage in Figures 119 and 120. This reduction in voltage is identical to that predicted in Figure 116 for a P(H_2O) of 10%. In Figure 116 the reduction of the OCV is predicted to be 1.05V for a P(H_2O) of 10%.and this is almost identical to the OCV value shown in Figure 120 which is also roughly 1.05 V.

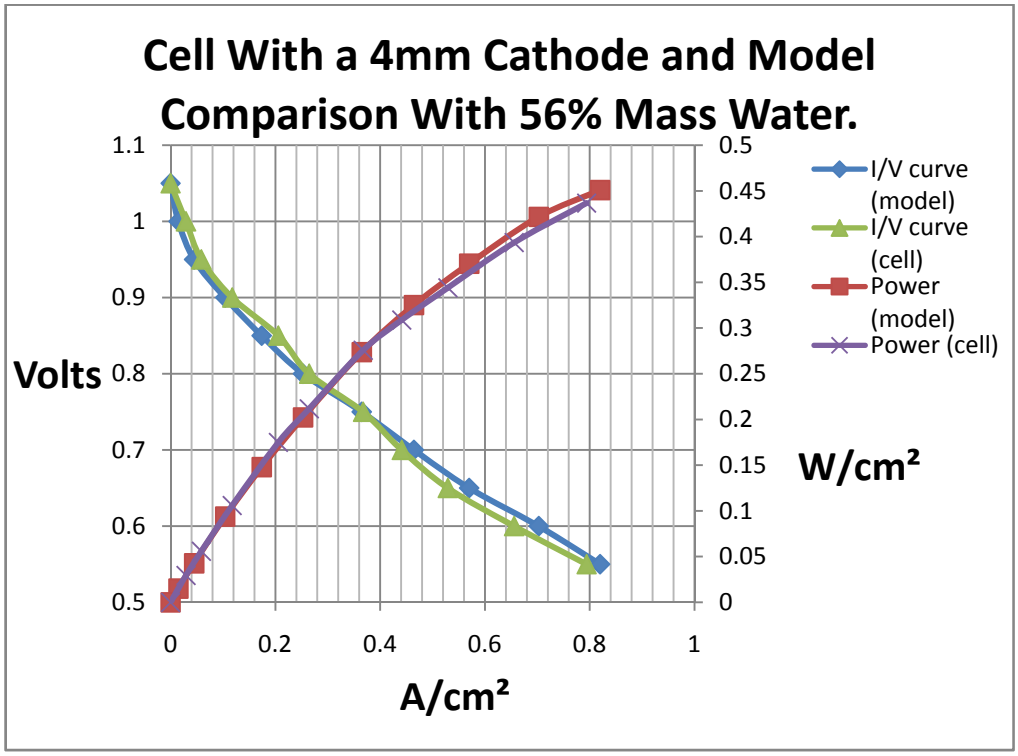

Figure 120: Plot comparing a simulated and tested cell with 56% mass water in the fuel.

To establish the accuracy of the model compared to experimental measurements for different oxygen concentrations on the cathode side this same cell with 56% vapor in the fuel flow was also tested with various mass fractions of oxygen in nitrogen in the oxidant flow. Figure 121 shows as plot of oxygen species concentration in the oxidant flow and the resultant current density produced by the cell. The comparison is made between the experimentally measured current densities as a function of the oxygen species concentrations. Figure 121 indicates that the model provides good predictions for various partial pressures of fuel and oxidant in

their respective electrodes. The slight deviation between the experimental and modeled results are probably caused by the fact that there may have been small leeks of oxygen in the wind tunnel as indicated in Table 9, which are not accounted for in the simulation. Thus the model shows slightly lower current densities compared to the experimental result. This is more noticeable at the lower concentrations of oxygen where even small changes in oxygen concentration will increase the current density.

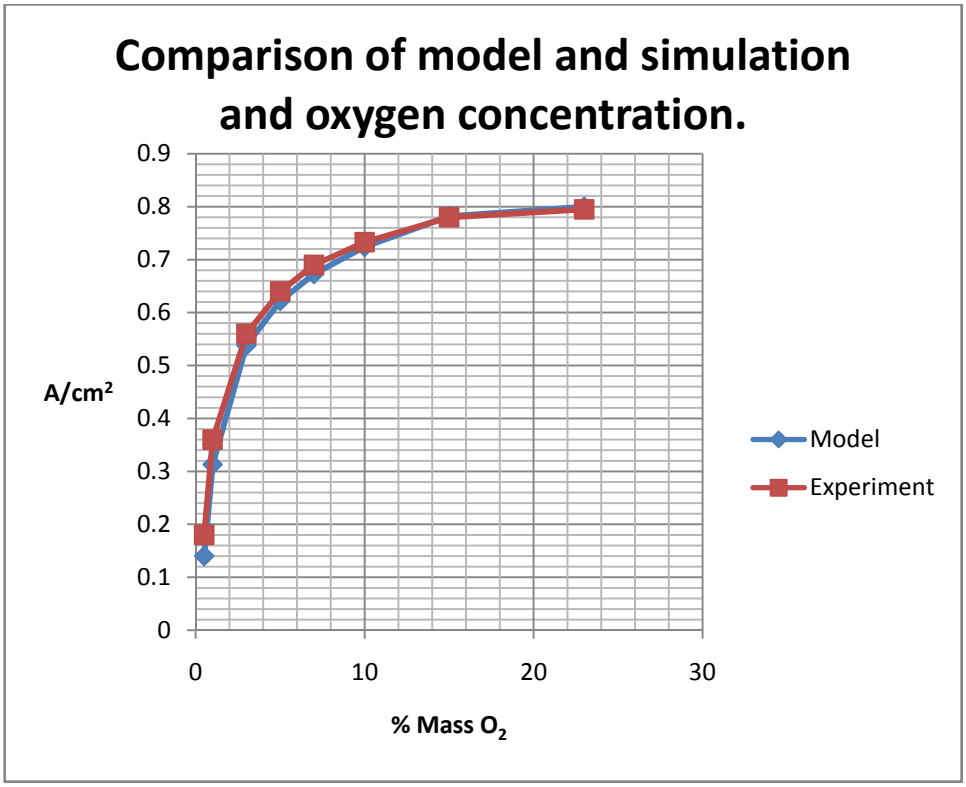

Figure 121: A plot showing a comparison of the tested cell in the wind tunnel under 50ml/min + 56% mass water and 16cm/sec oxygen/nitrogen mix.

Figures 122 and 123 show simulation results of the previously discussed case where the cell was fuelled with a gas containing 56% mass water and 44% mass hydrogen. In these contour plots, in the oxidant channel, 1.5% mass of oxygen was fed to the cathode at a rate of 16 cm/sec. Because the average current density of these models, shown in Figure 121, matches the well to the experimental results it can be assumed that the current density profiles shown in Figure 122 and 123 are probably correct. The gradient of the current density across the cell is affected by the

concentrations of hydrogen and oxygen. For example in Figure 122 the high current density seen on the top left hand corner, indicated by a red zone, is highest because of the high fuel and oxidant concentrations in this zone on the front of the cell. Also the proximity of this zone to the current collector, which is situated at the top of the cell will also have and influence.

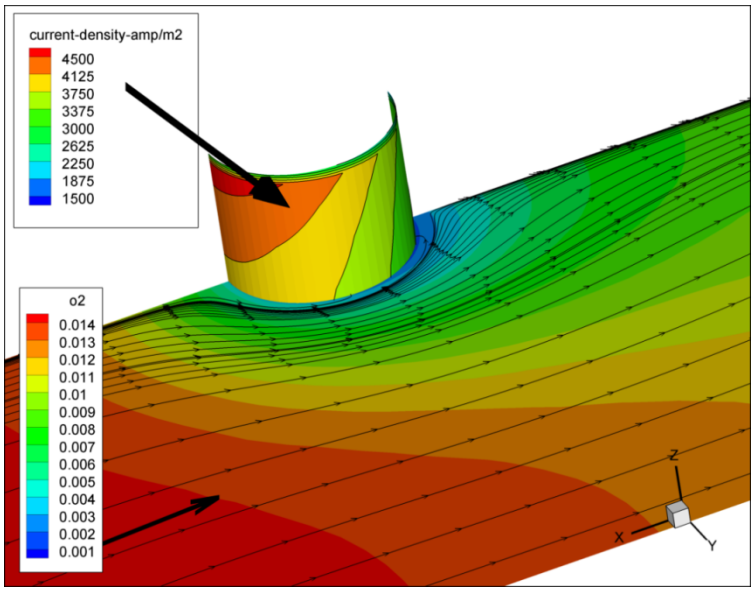

Figure 122: A simulation result showing the oxygen concentration on the flow plane and current density on the cell wall looking at the front of the cell.

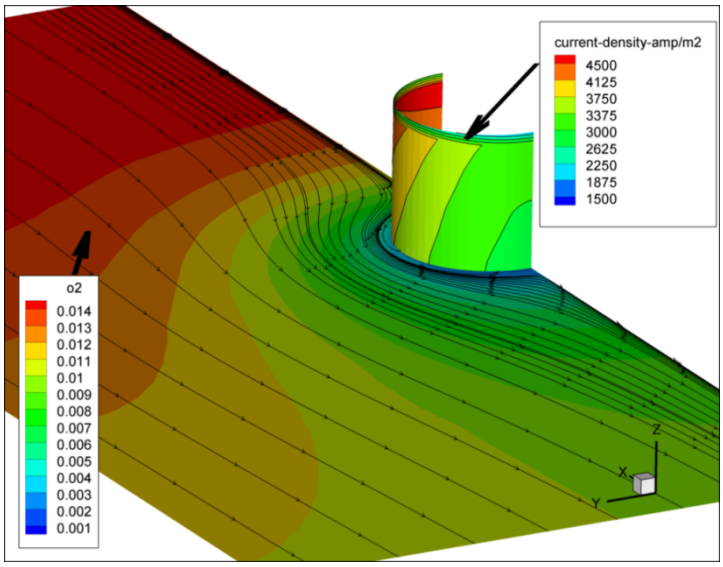

Figure 123: A simulation result showing the oxygen concentration on the flow plane and current density on the cell wall looking at the rear of the cell.

These simulations provide an important insight for the experimental results that were unfortunately not finished in this study. The attempted measurements are described in Section 6.4.5. What they show is the expected current densities and difference in current density between the front and rear of a MT-SOFC in cross flow. It may be deduced from this simulation that under the fuel and oxidant supply conditions described in this secion that the difference in oxygen concentration around the perimeter of the cell should vary as shown in Table 10

Table 10: Comparison of oxygen concentration and current density simulated with 1.5% mass oxygen in nitrogen flowing at 16cm/sec and with 55% mass water vapour in 44% mass hydrogen flowing at 5.7kg/s.

	A/cm²	**% mass O_2**
Front	≈ 0.4	≈ 1%
Rear	≈ 0.3	≈ 0.1%

The importance of these simulations is that they show the flow conditions and expected current densities that should occur on the front and rear of the cell. Should experimental work be performed in the future these simulations are a good starting point because of the proved reliability of the total current densities as a function of various fuel and oxidant concentrations. I.e. Further measurements with the dual cathode system are just validating the distribution of the current and oxygen around the perimeter of the cell.

6.6 Results of the development of the system incorporating MT-SOFC's to measure a concentration of oxygen around a larger high temperature electrode in cross-flow.

Figures 124 and 125 show contour plots of the mass concentration of oxygen, and velocity profiles behind the cylinder like body described in section 5.6. The mass sink rate around the wall of the body was 0.44032 kg/m^{3}s. This was calculated from previous experimental work with electrolyte supported MT-SOFCs placed in an oven. As the bulk flow velocity is increased the size of the wake of mass diffusion gradients reduces below a Re of 100. Then the form of the wake changes from a plume shape to a smaller structure with two small plumes at either side. Figure 125 shows that between the 80 and 100 Re cases, the eddies develop and these two rotating eddies then push into the centre of the wake flowing against the bulk flow and then change direction and flow in the direction of the bulk flow on the outside of the wake causing these two smaller plumes.

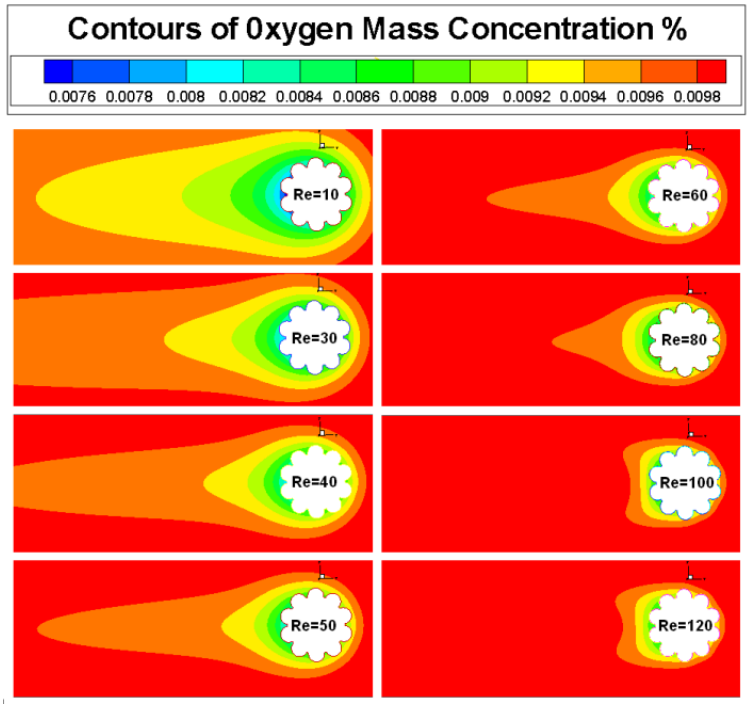

Figure 124: Variation of specie concentration in the wake of a cylinder in cross flow at a mass sink rate of 0.44032 kg/m^{3}s.

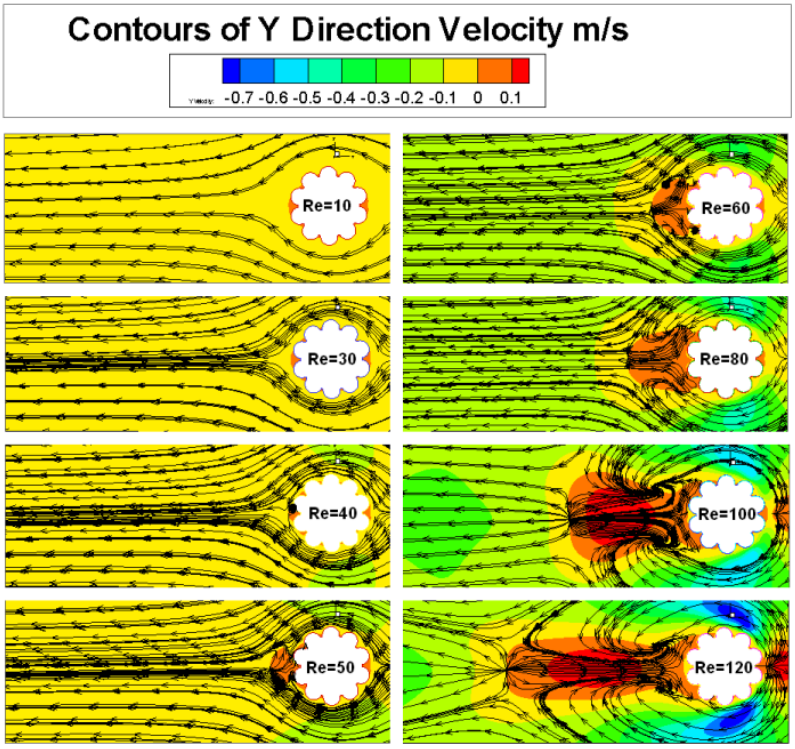

Figure 125: Contours of Y direction velocity (right to left being –Y) with an overlay of streamlines.

Unfortunately this is the cut-off point with regard to the experiments that were planned be performed in the wind tunnel described in Section 5.6. However simulations can be used to estimate what would happen at higher Reynolds numbers. However it is very clear from these results that by increasing the velocity of the flow even at low oxygen concentrations e.g. as shown here for 1 % oxygen in nitrogen, the difference in concentration between the front and the rear of the cells can be reduced up to Re=100.

This may indicate that by increasing the velocity of the oxidant through a bundle of cylinders this may reduce the concentration difference between the front and the rear of the cells. The velocity contours in Figure 125 show the normal development of the wake over the Re range of 10 to 120. It should be noted that the eddy development and size of the wake is retarded by the top and bottom walls, which have been included in these 3D simulations. The wake development may also be altered because of the fact that the body is not exactly a cylinder.

Figure 126 shows that as the flow rate is increased the oxygen available to the rear of the cylinder is increased. The aim of this study was to find out the effect of the wake evolution on the mass transfer to a cylinder in cross flow that sinks oxygen around its perimeter. The partial pressure of oxygen between the bulk flow and the wake is different as seen in Figure 124 and this will provide a potential to drive the oxygen into the wake.

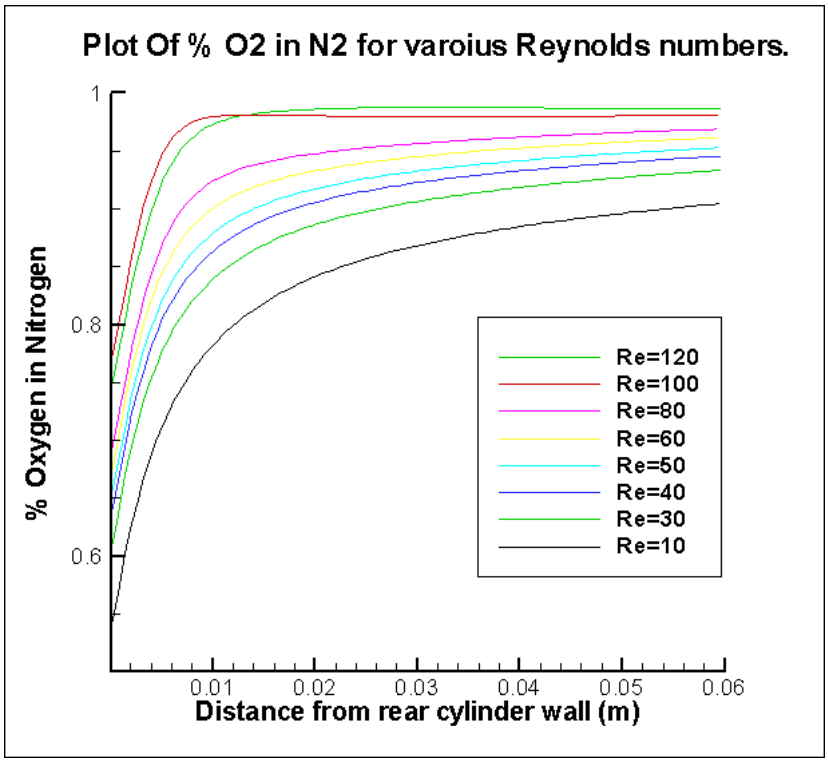

Figure 126: A plot of mass concentration of oxygen in nitrogen vs. Re.

The plots in Figure 127 can be used to describe what may occur in the near wake. As the bulk flow velocity is increased then so too does the velocity in the near wake and this also increases the supply rate of oxygen to the rear wall. An interesting observation in Figure 126 is that there is a reduction in the concentration of oxygen in the near wake between the plots at Re=100 and 120 and this is against the trend up to this point. The explanation for this is explained by the velocity contours in the region near the cell wall, which is situated in the wake.

From the contour plot of Figure 125 and the X-Y plot of velocities at various Reynolds numbers in Figure 127, it can be seen that size of the region of low velocity between the two sink walls at the rear of the cylinder increases between the Re of 100 and 120 and correspondingly in Figure 124 and Figure 126 the oxygen concentration in this zone is lower in the Re = 120 than in the Re = 100 cases. Figure 128 shows a zoomed in view of the velocities that the CFD simulations predict directly behind the cylinder in cross flow. It is interesting to note the rapid change in the velocity direction as soon as the Re becomes greater than 50. From this point to a Re of 100 the velocity in the near wake rapidly becomes larger in the –Y direction. This is because of the eddies are flowing towards the rear of the cell. Then above an Re of 100 the eddies begin to move away from the rear of the cylinder and this is observed by a reduction of velocity in the near wake seen for the Re = 120 plot.

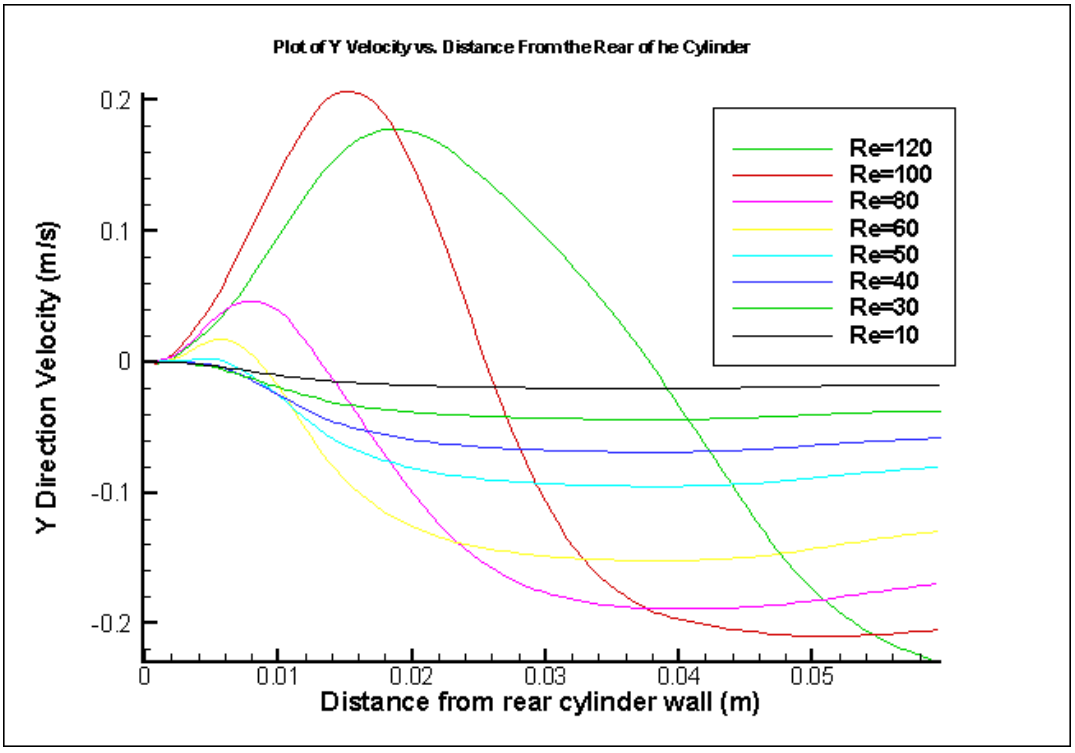

Figure 127: Velocity measurement along a line from the rear of the cylinder.

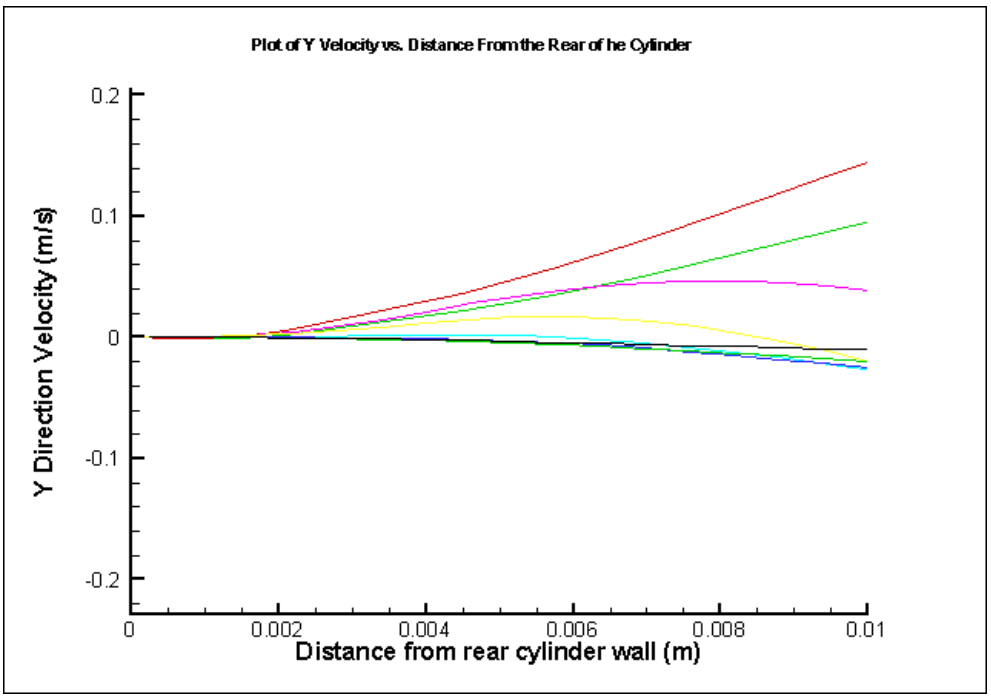

Figure 128 A view closer to the rear of the cylinder velocity at the rear wall of the cylinder (+Y: direction against the bulk flow) legend the same as Figure 127.

The velocity profile is also the reason that the oxygen concentration in the direct rear of the cylinder is reduced in the Re = 120 case, compared to the increasing trend up to the Re = 100 case. It seems that the velocity of the recirculation in the Re = 100 case is faster than in the Re = 120 case and this drives more oxygen into the near wake. It seems also that as the bulk flow increases above Re = 100 the region with low velocity is stretched outwards from the rear wall because of a decrease in recirculation velocity and strength in the wake and this would reduce the supply rate of oxygen to the rear wall. To really see how much a reduced concentration of oxygen at the rear of the cylinder contributes to any losses to the SOFC more detailed simulations should be performed in combination with experimental validations. Although this experimental work has not been performed in the duration of this thesis these simulations have introduced a hypothesis that is certainly of academic interest.

Chapter 7 Discussion.

7.1 Summary and discussion on CFD simulation and analytical calculation to estimate the effect of natural convection is a MT-SOFC reactor

The results of the simulations to indicate the type of flow regimes to be expected within a MT-SOFC stack show for the bundle configuration modeled, that natural convection effects should not be a problem. This means that naturally convective effects need not be a priority consideration when designing a MT-SOFC stack. This is clearly demonstrated, by the comparison of the CFD vector plots for the 1.5mm/s, 3mm/s and 10mm/s cases, as seen in Figure 78 (A) Figure 81 (A) and Figure 83 (A) and the plot of Gr/Re^2 shown in Figure 80. The relative effect and strength of natural convection flows in the CFD vector plots is predicted well by the Gr/Re^2 plot that was calculated in mat-lab. The Gr/Re^2 value is dimensionless and thus these values are purely superficial and provide a qualitative rather than quantitative measurement. Within the range of 1.5mm/s to 10mm/s the qualitative strength of the natural convective flows has been predicted by the estimation shown in Figure 80 and was quantified by the CFD simulations. As a rule of thumb it is recommended, for the configuration of cells described in Figure 52, with a distance of 1cm between each cell, that as long as the inlet oxidant velocity is greater than 3mm/s the flow will be dominated by forced convective flows. Factors that will alter this prediction include firstly, if the heat flux on the cells increased thus transferring more energy to the gas and secondly a closer cell to cell proximity in the bundle.

The Gr/Re^2 calculation and plot, which is shown in Figure 80, was calculated for a single cylinder in cross flow and this calculation was used to qualitatively describe the natural convection effects within a bundle of cylinders. In conclusion it can be stated that when the distances between the cells are greater than 1cm, from their centers, this Gr/Re^2 estimation plot, shown in Figure 80, calculated with a single model, will hold true and has relevance in qualitatively predicting the flow regime within a bundle of cells. Thus this simplified model can be used as a prediction tool for describing flow within bundles. This is possible with a single cell

calculation because the effect that each cell has on its neighbors, with regard to induced natural convection flows caused by the hot cells transferring energy to the gas, is negligible. Thus the flow regime, in the vicinity of each cell in the bundle is adequately estimated by a single cell model. This was clearly demonstrated by means of the comparison made in this study between this simplified estimation plot and the detailed CFD simulations.

Another very interesting feature and result seen in Figure 129 is the fact that the CFD shows, even at a relatively high velocity, which was 10 mm/s, that there is interesting evidence of a Z velocity magnitude component, indicating some natural convective influences. Figure 129 shows, through a comparison of a thermo graphic camera image, qualitatively showing the heated regions on the cell and a CFD model result, for the magnitude of Z velocity between the first two cells in the bundle, the passive and active heating regions and their effect on the flow regime. What this shows is that unheated areas even as short as 2.5 mm at the ends of the cells have an impact on the flow regime and that if a reactor is not carefully designed there could be some flows that may help or hinder the performance of the reactor. The effects could be positive by causing mixing of the inlet gas or indeed negative by causing in areas with poor concentrations of oxygen.

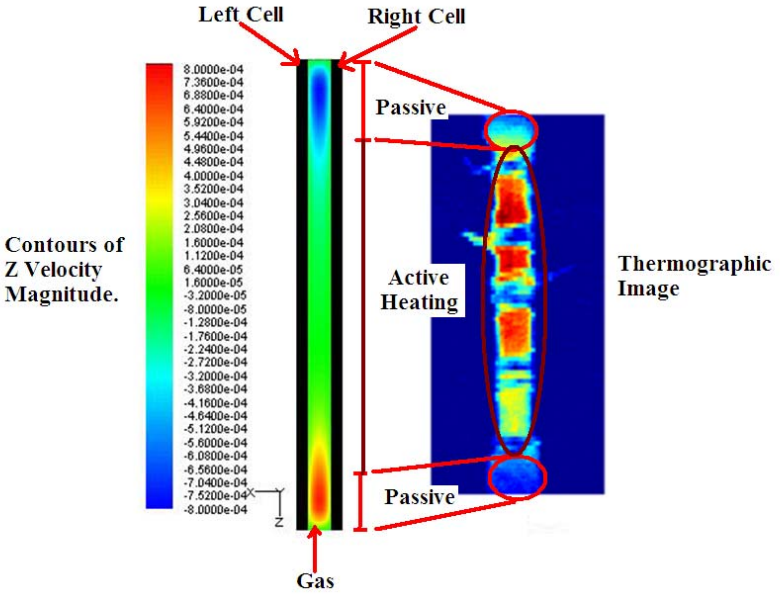

Figure 129: An image indicating passive and active heat production zones in the MT-SOFC model in the thermographic image. The convection effects at the top and bottom in the simulation can be noticed even at bulk velocities, around 10 mm/s. (Scale m/s of Z velocity component).

The analytical calculations made with the mat lab code found in Appendix IX proved to be a good indication, but the results from the CFD simulations really provided much more information. The CFD simulations cater for a much broader range of boundary conditions than possible with the mathematical model based on imperial equations and correlations. The fit between the CFD result and mathematical model based on the correlation of Von Böckh [122], for the exit gas temperature of a bundle of cylinders, match quit well. The offset on the results seen in Figure 77 where the CFD predicts a slightly higher exit temperature than the correlation based model is due the varying temperature of the cells through the bundle. This is not considered in the correlation of Von Böckh [122] where all the cells in the bundles are ascribed as single value.

Regardless the variation in the outlet gas temperature predictions is small when a comparison was made between the CFD and correlated result. A maximum variation of 5°C, predicted for the 2.5mm/s inlet velocity, was seen in Figure 77. A positive indication of the suitability of the correlation for MT-SOFC bundles, similar to that modelled is, that the temperature of the outlet gas, predicted for no gas flow condition and 10mm/s condition in both cases match almost identically. This means that the correlation and CFD can accurately point out two things. Firstly both the CFD and correlation agree on the value that the maximum temperature of the bundle should be, 1140 K, under the no flow condition. Secondly both models agree on the value that the inlet velocity should be to reduce the difference between the inlet and outlet gas temperature to a fraction of a degree, 10mm/s. This correlation of Von Böckh [122] is an extremely valuable tool for estimating what flow rate, through a bundle, operating at a certain temperature, is required to keep the outlet gas temperature low. The CFD result on the other hand provides a much more useful prediction for the operation of a MT-SOFC stack whereby the cells are cooled by the incoming gas and a temperature gradient through the bundle is accounted for.

It is clear that as soon as the electrochemistry and radiation models are included that CFD is an essential design tool to save both time and money in any design phase. In an actual reactor there will, of course, be struts for support, housing walls and temperature variations throughout the stack caused by the varying electrochemical reaction rates. Imperial models and correlations are far less useful when detailed models will be required.

Radiation is probably the dominant form of heat transfer within such a bundle as modeled in this section. This means that radiation and conduction through the metallic stack housing will probably be the primary means of heat removal. A major lacking in the models discussed in this section is the absence of the electrochemical processes. These phenomena produce heat and electricity depending on the temperatures, species concentrations and flow rates of both the fuel and oxidant.

Nonetheless the modeling work in this section has provided useful predictions regarding the flow regimes inside a stack. The modeling work in this section has also highlighted the potential and limitations of imperial equations and correlations with the clear result, that while they have uses, the CFD is a much more effective and detailed method of modeling a MT-SOFC stack.

7.2 Summary and discussion on methods of temperature measurement in MT-SOFCs

The purpose of the first part of this study was to compare four different temperature measuring methods. The application of these tools for possible temperature monitoring or calibration of monitors MT-SOFCs was explored. It was found that a thermographic camera was very useful to visualise the temperature gradient on the outside of a cell while an electrochemical impedance spectroscopy method was useful for estimating the core temperature of an operating cell. A standard thermocouple was also used in combination with the previous two methods. Furthermore an inexpensive laser guided thermometer was also tested for MT-SOFC temperature measurement.

This initial study has opened up a range of questions not only about the effect of the experimental apparatus on the measurement results but also about the radial temperature distribution through a MT-SOFC in a working mode. The discussed results are expected to be mainly temperature related, which should have direct consequences on power output and optimised gas inlet temperatures.

This study has shown how the combination of a high temperature wind tunnel and thermal camera may be used to measure the temperature gradient on the outside of a MT-SOFC. The problems that occur when observing a cell through an opening with a thermal camera have been shown. This reduces the amount of infrared reflection to the cell and provides a large temperature gradient that may affect the measurement, if compared to a cell in a bundle or at least insulated conditions. A method has been shown that negates these effects by subtracting images at OCV from images taken when the cell is under load. Also the effect of the different emissivity values of silver and LSM cathode on thermal camera measurements has been shown.

The comparison of four different temperature measurement techniques has shown that thermal camera and thermocouple values have been quite comparable once the emissivity value was calibrated. The big advantage of the thermal camera method is that one gets a detailed temperature profile all over the cell. Furthermore the potential of poisoning effects on the cathode caused by the thermocouple is avoided. During SOFC operation, volatile chromium (Cr) species, stemming from Cr-containing stack and system compounds, principally metallic interconnects and balance-of-plant components, tend to deposit at the cathode/electrolyte/air triple-phase-boundary blocking the active sites for oxygen reduction, known as Cr-poisoning. Already small quantities of Cr, at ppm level, can lead to a severe decrease of performance of standard state-of-the-art cathode. The used laser guided thermometer was not effective for accurate temperature measurement of the MT-SOFC. However, this was mainly caused by the size of the measurement spot. Larger devices or on the other hand LGTs with smaller measurement spots would provide better results. The electrochemical method shown by Hashimoto et al. [39] lead to much higher temperature values that measured on the outer cathode wall.

It is thought that these higher values, measured by the EIS method, are mainly due to the fact that the resulted temperature is mainly attributed to the core temperature of the cell and not to the wall temperature of the outer electrode measured by the thermocouple and the thermographic camera. It can be certain that this technique is very useful for estimating the core temperate of an operating MT-SOFC near the electrolyte and the triple phase boundaries. An accurate account of the temperature gradient radially across a MT-SOFC has been highlighted and questioned but not solved in this study. Several other authors including [41, 110,

111] show in their modelling results with much lower temperature gradients between the electrolyte and cathodes than these experimental measurements and indeed those of Hashimoto et al. [39].

The role of the experimental apparatus in causing this large gradient has not been established so far. A future study should be performed to establish the effect of the measurement apparatus on the temperature gradient radially through the cell. This can be performed by using a CFD software package to model the components of the MT-SOFC and experimental conditions. The version of Fluent used in this study however did not have a physical electrolyte and thus an alternative must be used for such models to account for the temperature profile in the electrolyte. The latest version of the fluent CFD software, Fluent 12 does allow this feature and should be used in any further modelling.

Measurements in this study have only been made with single cells but the EIS measurement should be very usefully when estimating the temperature of single cells within bundles should electrical connections cater for such measurements. When cells are stacked in tight bundles thermocouple measurements maybe impossible or undesirable and EIS or the current interrupt method described by Hashimoto et al. [39] should be useful for model validation.

Once calibrated the wall temperature of a cell can be estimated via the electrochemical method. It should be noted that this will only apply when this measurement is made in the same environmental conditions as the calibration. Unfortunately cell degradation may make this kind of measurement difficult to make within MT-SOFC stacks unless the degradation can be accounted for in the measurement.

A very important result of this study was that the wall temperature of the cell may not be a good estimation of the electrolyte temperature. It was found that by heating the cell under OCV conditions to the wall temperatures and making an EIS measurement that the ionic resistance was much higher than would have been expected. The reason for this must be that the electrolyte temperature is much higher than the outer wall temperature of the cathode. This high temperature in the electrolyte has also been shown by Hasimoto et al. [39] but did not appear in the modelling work performed in this thesis or indeed the modelling work reviewed during the course of this thesis.

A hypothesis for why the EIS measurements show lower resistance values and thus higher temperatures than would be expected, and indeed have been shown in some of the modelling work reviewed and simulation work performed in this thesis, is that when the temperature and resistance calibration curve is made when the cell is under OCV conditions and this may be misleading. What this in effect means is that only AC current passes through the cell and thus there is only an AC part in the measurement. This could mean that as the resistance of the cell is measured by applying only high frequency perturbations to the cell, the highest energy jump that an oxygen ion must have to move from an oxygen ion location to another may not be measured. This would mean that the resistance of the electrolyte would be measured lower than it actually is when a DC current is added to the system for any given temperature. This would mean that when the cell is producing current and a Nyquest plot is made, with an AC perturbation, the ohmic resistance of the cell may appear to be lower.

A second hypothesis, that may explain the low resistances when the cell produces power, is that the resistance of the electrolyte may have appeared to decrease because of leakage currents through the electrolyte. Although tests for leeks of hydrogen, which is a good indicator for holes in the electrolyte, were made by monitoring the temperature on the cathode wall with the thermographic camera when the cell was in the OCV condition and a comparison was made between the temperatures when high and low concentrations existed in the fuel. There may have been small short circuits. Normally this would be seen by a low OCV but in this case the OCV of the cell was high 1.15V. However if very thin regions of electrolyte were evident on the electrolyte, as soon as DC current was produced by the cell, these electrolyte zones my not have insulated the electrodes and the resistance of the electrolyte would have decreased more than it would with homogenous thick layers.

Further simulation and experimental work should be carried out to explain either the error in measurement or the reason for high temperatures in electrolyte zone.

7.3 Summary and discussion of detailed models of a single MT-SOFC.

7.3.1 2D simulations

As described in 6.3.6 initial models that were simulated of a single MT-SOFC in the high temperature wind tunnel always resulted with temperatures that were much higher than were measured. It was considered that the only plausible reason for these high temperatures, seen in the early simulations, see section 6.3.2, must be attributible to the neglection of radiation. Thus the discrete ordinates radiation model within fluent was applied to the following walls and zones of the MT-SOFC model. These boundary conditions are discribed in Figure 98. Because radiation is such a computationally intensive operation in CFD modeling, an initial attempt was made using 2-D simulations that just included a heat flux on the electrolyte wall. The reason for this artificial heat flux was to mimick the heat production of a MT-SOFC

However it was found that these 2D models did not output results similar to those obtained from the experimental measurements. The main problem with these measurements was that when all of the emmisivities were applied to the walls of the wind tunnel, and also to the wall of the cathode of the cell being modeled, the temperature of the cell reduced far below the experimental measurements. This occured when the cell had zero heat flux. A temperature similar to the wall temperature of the wind tunnel was expected as seen in the experimental case.

Clearly radiation in the 2D model causes losses on the wind tunnel walls. However as can be seen in Figure 94, if radiation is neglected and a flux of 2 W/cm² is applied to the cell wall, similar to the heat flux produced by a cell producing 1.5A/cm², then the temperature profiles in the wind tunnel become unrealistic. This meant that radiation losses were an important factor to consider. In this case the walls of the wind tunnel were considered as adiabatic, however emissivity losses and normal irradiative losses were not considered and this is why the temperature raises so much. In Figure 95 when the radiation model is activated, the temperature on the cell reduced to values much lower than those found in the wind tunnel in the experimental tests.

The experimental results, of the wall temperature of the cell under OCV and loaded conditions shown in Figure 86, are a very important reference to understand the results that were expected to be obtained from the CFD simulation. Figure 96 shows the case where zero flux is ascribed to the wall of the MT-SOFC in cross-flow. The model predicted a temperature profile around the perimeter of the cell that shows features such as the cold strip attributed to radiation losses out the back of the wind tunnel and an increasing temperature round the sides of the cell to the front facing the diffuser. This result can be seen in Figure 86. However quantitatively the temperature profile is totally unrealistic and does not compare well with the experimental measurements. With a certain amount of manipulation the results could be made to match those of the experiment. This was done more precisely by having a heat flux ascribed to the very inside of the cell and is illustrated in Figure 96 for the OCV case..

A Shown in Figure 97 is a simulation result displaying contour plots that demonstrated when the heat flux, as described above, is placed on the inside wall of the cell and the loaded condition is simulated, where the cell produces $2x10^8$ W/m³. The temperature profiles also match the experimental setup where the relative change in temperature caused by the load increases the wall temperature of the cell in line with the experimental results.

However even though these profiles matched quite well, it was considered that these results are unphysical and therefore do not represent the actual conditions inside the high temperature wind tunnel. This is because the additional 1.1W/cm² that was used to manipulate the temperature of the cell to match the experimental results was not accounted for in the 2D model. The only reasonable way that this heat flux could have been applied to the cell was by extra energy carried to the cell by the fuel which was not included in this model. A very quick test was made to measure the temperature of the hydrogen so that it could be ruled out for supplying a heat flux somehow to cell. It was found that the hydrogen certainly did not provide a heat flux. Thus the only practical solution could be that the top and bottom walls of the wind tunnel must also apply an additional heat flux to the cell and 2D simulations do not allow for this attribute to be accounted for.

The main conclusion of this section is that 2D simulations did provide good predictions for radiation heat transfer that occurred in the 3D domain. This error may

have been intensified in the 2D simulations by the heating arrangement of the wind tunnel in the experimental setup. The wind tunnel is heated from the top and the bottom by the radiating light bulbs. The outer shell of the wind tunnel body conducts the heat through the sheet metal housing on the top and bottom and this energy is then radiated into the inside of the wind tunnel. Some of this energy is also transferred into the gas flowing inside the wind tunnel. To model the gas flow inside the wind tunnel the orientation of the 2D plane must be as modelled as in this section. Thus the radiation effects from all the walls in the wind tunnel were not accounted for and it is hypothesised that this is the reason for the error in the simulation predictions presented in this section.

7.3.2 3D Models including radiation

Following the 2D simulations discussed in the previous chapter, simulations that included radiation in a 3D model including electrochemistry were performed. Two specific attributes of the MT-SOFC that was tested were used to validate the CFD simulations with experimental measurements. Firstly I/V curves were selected as the obvious method to assess the performance of the models in relation to the experimental setup. From I/V curves the ultimate electrical performance of the cell can be compared to experimental results. The electrical performance is a function of temperature, material properties, reaction kinetics, geometry species concentrations and temperature. If the I/V curves predicted by the CFD simulation matches those produced by the experimented MT-SOFC, this is a good indication that the models are valid. Secondly as temperature is an important attribute in MT-SOFC stack design, the model has also been validated by comparing the temperature gradient that was measured with a thermo graphic camera on the cell wall with the temperature profile predicted by the model.

With reference to the I/V curve validation, as can be seen in Figure 99, the experimental and simulated I/V and power curves were compared. In this case the cell is provided with adequate fuel to eliminate the effects of diffusion losses in the cell. Up until the higher current densities the models compare extremely well with an

error of under 1%. In the higher current density region, above 1.5A/cm², the models begin to diverge. At the highest generated current density the error in current density between the model and simulation is 15%.

This error has been attributed to the current losses in the wires, which are not included in the simulation and could cause this reduction in the MT-SOFC output power. The temperature dependence of the exchange current densities may also play a role in this error at the higher current densities. Obviously a single I/V curve is not enough to prove the validity of the prediction ability of the simulations and a second I/V curve was also made when the cell was fuelled with less fuel. In this case as seen in Figure 100 the diffusion losses caused by the inadequate supply of fuel is clearly distinguishable by the arc at the end of the power curve. Again the experimental result and simulation prediction match very favourably. In this case as the maximum current densities are lower than in the previous case and the variance of the model and simulation in the region is small, maximum 1%. From these two initial I/V curves and experimental results, also confirmed by the simulation predictions that are discussed in section 6.5, the CFD adequately predicts the current densities based upon both the oxidant and fuel species concentrations provided to the cell.

The second characteristic used to validate the predictions of the CFD models, was to compare experimentally produced, quantitative, thermographic images with the CFD predictions. In this case not only is the MT-SOFC performance accounted for but also the effect of the testing apparatus, which has a huge effect, via radiation, on the temperature profile on the cell outer wall. Two cases were used to assess the validity of the CFD predictions. Firstly the case when the cell was not producing current and its temperature profile is determined solely by its surroundings. Secondly the case when the cell produced a high current and thus heat was produced which also was also used to validate the temperature profile on the outer wall of the cathode.

Figure 105 shows a comparison between the experimentally quantified temperature profile measured by the thermo graphic camera and the temperature profile predicted by the CFD simulation for the case when the cell was not loaded. In comparison to the results for when the cell is loaded, seen in Figure 109, the temperature profile on the cell produced only a reasonable match. The average temperature was certainly about 5°C lower in the CFD prediction compared to the

experimental measurement. In this unloaded case, the temperature of the cell is totally determined by the radiation and gas heating rates supplied to it. In the loaded case, Figure 109, the match between the simulation prediction and experimental measurement of the temperature profile on the cell wall was much better. The only parameter change in the simulation was the voltage applied to the cell, which in turn increased the current density and this increased the temperature of the cell. The effect of the radiation losses is seen clearly in the thermo graphic images and can also be seen in the simulation predictions in the unloaded and loaded cases.

The fact that the predicted and measured temperature profiles do not match not well in the unloaded case may be caused by the extremity of the temperature gradient between the cell and the outlet of the wind tunnel radiation temperature. This outlet temperature was set to 300K, which meant that the temperature gradient between the cell and outlet was about 700°C. Seen in Figure 103 is the radial temperature through the cell and temperature in the gas. It seems in this contour plot that the predicted temperature of the gas is the reason that the cell appears to slightly colder than the experimental values. It may have been the case in the experimental setup that the temperature of the wind tunnel was on a cycle high point. This means that there was an duty cycle involved in the control of the wind tunnel and thus its temperature can potentially differ by about 6 °C i.e.3°C < set point < 3°C. In other words if the measurement of the wall temperatures was taken on a high point in the temperature cycle and the thermal camera image was taken on a low point such an error could occur. This or a numerical error, such as the high radiation heat transfer potential between the outlet and cell, which is extremely hard to define, or the fact that the wind tunnel walls were not smooth and in fact were extremely notched and bumpy, may have affected the radiation properties. The grid was checked for independence by increasing the cell count by a factor of 8 and no significant differences in temperature contours or current densities was observed.

The accurate prediction produced by the CFD model for the loaded case supports the claim that the model makes an accurate prediction under loaded conditions at high current densities. However it is hypothesised that when such measurements and CFD simulations are made for a case where the stark temperature gradient between the cell and outlet of the wind tunnel does not exist, i.e. for example if measurements and simulations are made for a cell in an 6 walled box, the anomaly in the un loaded case will not appear.

7.4 Summary of discussion of results of measuring the concentration of oxygen around the perimeter of a MT-SOFC in cross flow.

7.4.1 Smaller cathodes in general seem to produce higher current densities.

As seen in Figure 117, which is an example of a general I/V curve for most of the dual cathode cells, the smaller cathode always tended to produce a higher current density. While at first this seems very unusual, similar results were found in a very informative thesis by Hyde [126] during the closing stage of this thesis. Hyde found that segmenting the cathode coatings on the electrolyte increased current density from 150 mA/cm^2 for un-segmented cathode to 210 mA/cm^2 and power density from 70 mW/cm^2 to 100 mW/cm^2 when cells were run at 885°C with 60 ml/min hydrogen. Hyde attributes the increased performance to two effects. Cathode current collection may be improved as each cathode segment had its own current collection wires. Alternatively, any un-reacted fuel and product gases can mix without electrochemically reacting in the short distance between each cathode segment, moving water and carbon dioxide from the three-phase boundary and opening up other active sites so fuel could react with the incoming oxygen-ion flux. In Hydes experiments the cathodes were segmented in series along the length of the cell while in the case in this study, for example one of the segments being further segmented around the perimeter of the cell was the case. This means that Hydes second suggestion that the fuel mixes better cannot be the dominant case. So the extra wires seem to be the reason why smaller cathodes produce more power.

In fact later in the study from Hyde [126] it is also shown that the current densities increased significantly on cells with single cathodes from 70 mA/cm^2 for one wire, to 165 mA/cm^2 for two wires, and to 275 mA/cm^2 for four additional current collection wires. This means that the extra wires have a massive effect on the output current of a cell. What was not performed in this study but what would have been interesting would be to keep increasing the number wires up to the point when no significant current density is seen.

Hydes thesis [126] was found towards the very end of this thesis work but should be regarded as essential reading for fuel cell researchers and stack designers as a lot of the basic optimization questions such as, cathode current collection, anode current collection, and various other parameters are explored. When the optimizations suggested in this thesis are all included on a final cell in the thesis, compared to a standard cell, the power density of the cells used was doubled.

7.4.2 Summary and conclusion of the measurements and simulations.

Making an assumption that the CFD results in Figure 122 and Figure 123 are correct then the difference between the front (0.4181 A/cm²) and rear (0.2941 A/cm²) is 0.124 A/cm². The average value reported by the simulation was 0.3576 A/cm². These values for the front and rear are taken from a line drawn down as in Figure 130 and Figure 131. These values may be a bit misleading, because they are taken on points on a line and not an average over an area. It may be possible to make these measurements in the CFD software. What this in effect means is that the average value on the cathode and testing strip, as reported above, is probably too high and thus the measurements taken in the experiment, taken over an area, are possibly more realistic as measured.

One way to prove that the reduction in current on the cathode is cause by oxygen concentrations is to use the power of impedance spectroscopy, but time did not allow for these measurements. Attempts to make the impedance measurements were made but it was extremely difficult to get good measurements with the dual cathode system. For such measurements electronic loads may not be used and potentiostats not connected to a mains supply should be used.

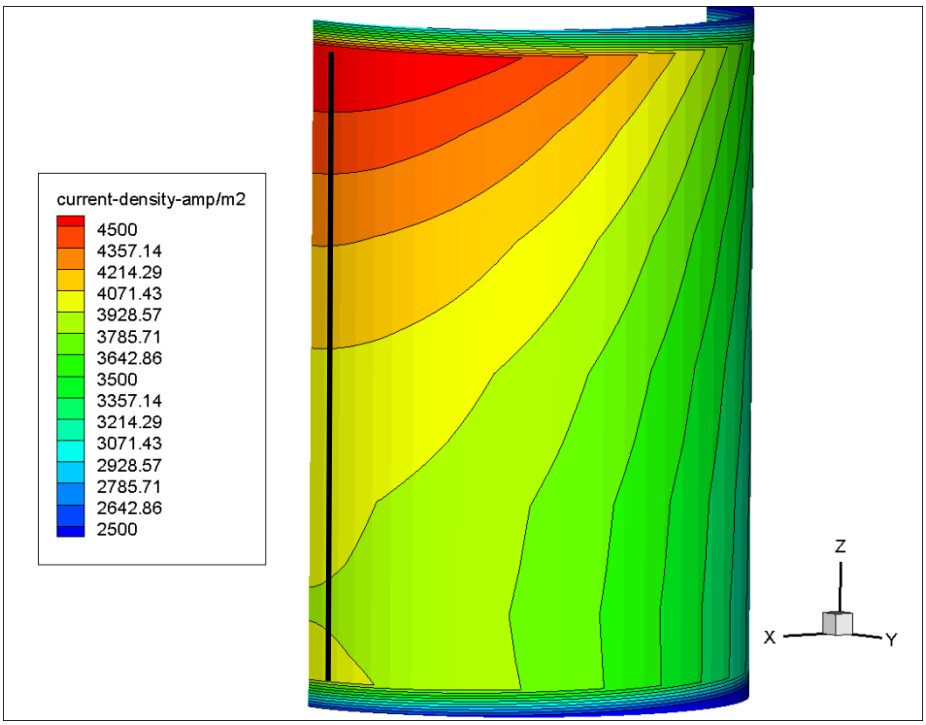

Figure 130: A view from the simulations where the front of the cell can be seen showing current density. Please refer Figure 122 for O_2 values.

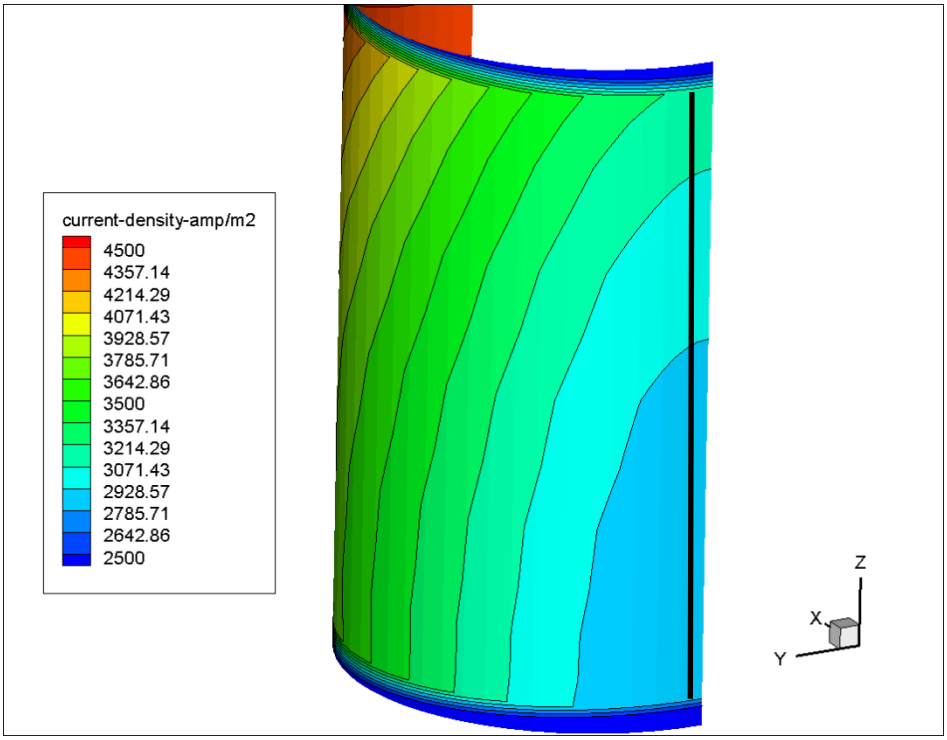

Figure 131: A view from the simulations where the rear of the cell can be seen showing current density. Please refer Figure 123 for O_2 values.

Should impedance fail to show the losses another solution would be to make two strips with each having the same area. Then the two areas are related and the effects of different area cathodes may be negated. This way the effects of oxygen depletion may be easier to recognise even while making the experiments from just Amp values and not Amp/m². The fact that in the measurements performed the testing strip shows a higher current density compared to the normal makes it difficult to compare these results with simulation results and is an argument in favour of the segments being similar in size. Also the CFD does not take into consideration the fact that two segmented cathodes exist in the experiment, the un-cathoded segments had a combined area of the testing strip.

While the experiments to validate the current distribution on the cathode as a function of oxygen concentration have not been an outright success, they show that there is potential for the method used to provide the measurements to be developed. The fact the comparison of I/V curves measured and simulated for a single cathode 4mm long, that were made for various species concentrations, match extremely well means that at least the average current densities have been validated as a function of oxygen concentration. It is extremely likely that the current density profiles predicted by the CFD were an accurate account. If the average current density predicted by the CFD and measured via the actual cell are the same, it makes sense that the distributions of current density and oxygen concentration should be correct. So even though the distributions were not successfully measured it is hypothesised that the CFD predictions are suitable.

As an extra note it was noticed at the end of these experiments that the shape of the wind tunnel had changed quite dramatically. Please note the buckle as seen in Figure 132. It is presumed that this occurred over a period of time but clearly shows that the metals used as supports in MT-SOFC reactors also need to be studied. It is 100% certain that this wind tunnel was not under any other stresses than those applied thermally.

Figure 132: Buckle on the wind tunnel after the course of 7 months testing.

7.5 Summary and discussion of the 4 mm cathode and suggestion for a new modelling strategy.

The results of the modelling section were the CFD I/V curve predictions were compared to experimental I/V curves, made on 4mm long un-segmented cathodes, showed the versatility and accuracy of the Fluent SOFC module in predicting these curves. In this experimental and CFD modelling section, the ratios of N_2 versus O_2 and H_2 versus H_2O. in the oxidant and fuel supplies were varied. Figure 119 shows a comparison between an experimental I/V curve made on a 4mm long cathode cell and the predicted CFD result. Figure 120 show a comparison between an experimental I/V curve made on a 4mm long cathode cell and the predicted CFD result for a cell with 56% mass water in the fuel channel. Both simulations match quite well but the fluctuation in the experimental I/V curve for the cell in the 56% mass water case was likely due to fluctuations in the water constituent.

Figure 121 shows that the model is also valid for when the oxygen concentration of the cell is varied. This is very important for the dual cathode measurements where the model and measurement data would need to be closely matched.

Figures 122 and 123 clearly show the capability of CFD, whereby it is easy to visualise the effect of the oxygen concentration on the I/V curve produced by the cell. This set of simulations and experimental results on the 4mm cathode in this section shows that these smaller models were extremely useful and credible tools. A result of this section is not only the results shown but also the realisation that new strategy for model tuning that should be employed in future MT-SOFC modelling activities using this CFD software. The speed that the model solves is very impressive requiring only about 25 minutes for an initial solution and 2 to 3 minutes thereafter for predicting each point on an I/V curve. In comparison to the larger, full cell, models, see 6.3.3, that that took about 10 hours to produce full I/V curves, these smaller models converge extremely fast. The key benefit of these smaller models is that they may be used to tune the larger models via the exchange current density parameters. The values should be and were found to be identical for the 4mm cathode and full cell models. This means with regard to the simulation strategy that

smaller models should be simulated initially and then larger simulations should be ascribed to the current exchange densities as the final step in setting the large model parameters.

7.6 Summary and discussion of simulations for a larger bundle of cells to increase the cylinder diameter.

Because the bundle of cells was too difficult to build, no experimental data was produced for the following simulation results. Without experimental data it is difficult to assess the preciseness of the numerical results. However a finding in the simulations was that up to a Reynolds Number of 100, in the case of this wind tunnel, the concentration of oxygen at the rear of the bundle increases. But after 100 the oxygen concentration decreases meaning the some kind of wake effect is occurring. The reason for this was attributed to the velocity profile directly behind the cylinder that causes the oxygen concentration in the direct rear of the cylinder to be less. In conclusion from the numerical study performed, it seems that the wake structure does have an effect on the concentration of oxygen in the direct rear of the cylinder. Up to a Reynolds number of 100 the numerical analysis predicts that the oxygen concentration at the rear of the cylinder sinking a defined amount of oxygen, will experience an increase of available oxygen in proportion to the Reynolds number.

In this numerical analysis the Reynolds number was varied by varying the oxidant inlet velocity. Thus as the velocity increased so also did the concentration of oxygen at the rear of the cylinder. This statement was true up to a Reynolds number of 100 where the concentration of oxygen bucked the trend and the concentration reduced. This was clearly observed in Figure 126 where green plot showing the percentage mass of oxygen available to the direct rear of the cylinder is decreased compared to the red plot for Reynolds number of 100. This buck in the trend was explained by monitoring the velocity of the gas flow in the near wake region.

Predicted by the numerical simulation is that up to the Reynolds number of 100 the velocity of the air in this near wake region is increasing proportionately with the inlet air velocity. As seen clearly in Figures 15 16 and 19 the shape of the wake

changes as the Reynolds number increases. When the Reynolds number reaches 100 the two rotating eddies in the wake elongate and also the ends of the eddies move away from the rear of the cylinder which begins to form a zone of stagnation between the eddies and the rear wall of the cylinder. This was illustrated with contour plots seen in Figure 124 showing the predicted species profile and Figure 125 showing the velocity profile. As discussed in Section 2.2.8 these effects on the velocity profiles have been observed by others in the near wake. These observations were made by others for Reynolds numbers in the range of 35 to 60, but because of the effect of the enclosure walls, in the numerical simulation, the wake evolution as a function of the Reynolds number was retarded. This meant that the wake developed over a wider span of Reynolds numbers.

In conclusion the numerical simulation performed, predicted that mass transfer to the cylinder in cross flow is affected by the evolution of the wake. The model predicted that when the Reynolds number increases to a high enough value, which causes the eddies in the wake to begin to move away from the rear of the cylinder, a stagnation in the region directly behind the cylinder wall will occur. This stagnation zone, which begins at the cylinder wall and reaches out as far as the eddy recirculation limit, is the reason that the oxygen concentration begins to reduce. An interesting further study would be to use the same simulations and to keep increasing the Reynolds number to see if this reduction in oxygen concentration continues to increase and up to what point does this occur. It is expected that as soon as vortex shedding occurs these stagnation zones will exist for short periods of time and unsteady concentration at the rear of the cylinder will occur and be a function of the shedding frequency.

It may be argued that the “flower” shape design of the big bundle of cells is not a cylinder and therefore the Reynolds numbers cannot be the same as a real cylinder. However a cell with such a large diameter was not available and because the Reynolds numbers achievable with a small cell were not appropriate only numerical predictions were calculated. For validation experiments are needed to make the simulated results conclusive. However the predictions of the simulations are reasonable and can be explained with logic reason as describes above. This indicates that mass transfer effects are influenced by the wake development as hypothesised

Chapter 8 Thesis Conclusions.

8.1 Overall Conclusions with reference to the original goals in Section 2.6

Aim 1: Establish if and when natural convective flows are likely to occur in a bundle of MT-SOFCs

- The effect of natural convection in arrays of cylinders can soon be negated with even relatively low flow velocities of air more than 3 mm per second in bundles where the cells are spaced 1cm apart from each centre.

Aim 2: Design and build an apparatus capable of creating the conditions for MT-SOFC testing. These conditions should include variable fuel and oxidant flows to the cell, the ability to test the cell at various temperatures up to 850°C and should allow thermo graphic images to be taken either through a window or opening.

- A high temperature wind tunnel apparatus capable of generating testing conditions up to 850°C was designed built and used for experimental measurements.
- The oxidant exhaust was used as a window/opening to allow thermo graphic images operating cells.
- The ability to test cells under variable oxidant and fuel conditions was achieved.

-

Aim 3: A variety of measurement techniques to measure the temperature profiles on a MT-SOFC in cross flow should be performed

- Temperature profile on a MT-SOFC was mapped by using a combination of a thermo graphic camera, a thermocouple and impedance spectroscopy.

Aim 4: CFD models should be developed that accurately predict the behaviour of an MT-SOFC in cross flow. Experimentally acquired I/V curves and temperature measurements should be realised to compare and asses the validity of the CFD predictions.

- Single cell MT-SOFC models were developed that included electrochemistry and radiation.
- The experimentally acquired I/V curves and temperature profiles measured in the high temperature wind tunnel were used to assed the accuracy of the CFD predictions.
- It was found that the accuracy of the models for predicting the electrical performance of the cell as a function of the species concentrations is extremely accurate. The predictions that the CFD models made for the temperature profiles on the cell, when under load, was also very accurate. However the temperature profiles predicted on the cells in the OCV (no load) condition was not as accurate. This error was attributed to a measurement error.
- The combination of the high-temperature wind tunnel and CFD simulation analysis is an excellent way to observe the effects of the multi-physical phenomena on the performance of a MT-SOFC that may otherwise be unobservable or at least to a lesser extent.
- The Fluent 6.3 CFD software may not provide an accurate account of the radial temperature across the cell particularly within the electrolyte which cannot be drawn. Future research should be made with the Fluent 12 where the electrolyte may be drawn. Experiments regarding the suitability of the impedance methodology should also be performed.

Aim 5: The concentration of oxygen and current density profiles on the cathode electrolyte interface should also be predicted using the CFD software and experimentally validated.

- A dual cathode method was developed for measuring the concentration of oxidant around the perimeter of a MT-SOFC in cross-flow.
- It was found that smaller cathodes, like the testing strip that was created in this method, generate higher current densities than larger cathodes. This effect was attributed to the wires that are connected to the strips and that the larger cathode produces, in sum, more current which in turn causes more ohmic losses in the wires.
- These losses made it impossible to compare the experimental reading with simulations and in future work the cathodes used to measure the concentration around the perimeter of the cell should all have the same area.
- The simulation predictions for the I/V curves for single cathode 4mm models matched the experimental results indicating that even though the oxygen distribution was not actually measured the CFD probably gave a good prediction.

Aim 6: The effect on mass transfer to a cylinder in cross flow as the wake develops behind the cylinder as a function of the Reynolds number should be assessed.

- With regard to larger high temperature electrodes in cross-flow, as the Reynolds is increased, so also does the supply of oxygen to the rear of the cylinder. However up to Re=100, if the velocity is increased further, a reduction in the rate of mass transfer to the rear of the cylinder was observed in simulations.
- This effect was explained by the air velocities around the cylinder and by the stagnant zones that evolve as the wake develops at Reynolds numbers higher than 100.

8.2 Thesis Contribution.

This thesis has contributed the following information to the micro tubular solid oxide fuel cell field.

- A review paper during the course of this thesis which is the first of its kind on this specific topic has been published.

- An apparatus capable of measuring the multi-physical phenomena that affect the performance of MT-SOFCs in cross-flow has been built and several publications on this topic have been published.

- When modelling and testing a single MT-SOFC in cross-flow, the experimental apparatus has to be considered as the temperature effects due to radiation are extremely important.

- The difference in concentration between the front and the rear of an MT-SOFC in cross-flow would be negligible under normal operating conditions.

- High flow rates can be used to negate the effect of natural convection in MT-SOFC reactors.

- The models developed and validated during the course of this thesis provide a powerful tool for future development such as bundles of cells.

The thesis has contributed to the fluid dynamics field in the following way

- Simulations show that from a Re of zero to 120 the development of the wake is subject to the effects of the side walls and also the top and bottom walls. As a Res increased to about 100 the supply of oxygen to the rear of the cylinder in the wake increases. However above a Re of 100 the wake seems to stretch and this reduces the concentration of oxygen supply to the rear of the cylinder in cross flow.

- When a heated or unheated cylinder is paced in cross flow inside of a body like the high temperature wind tunnel described in this study, a cold line can be seen on the rear of the cylinder which can be seen with a thermographic camera and CFD simulations.

8.3 Recommendations for Further work.

One of the original goals specified for this project was that the wind-tunnel should be capable of testing bundles of MT-SOFC's in cross-flow. However due to problems with the design this goal was dropped in favour of a more targeted scientific study on a single MT-SOFC in cross-flow. This thesis provides a launch-pad of information develops single MT-SOFC models in CFD software that should surely be developed to the stacks scale.

Also a method should be figured out by either using lookup tables are smart functions that could be used in place of the detailed Fluent electrochemical model. This model in many instances is unnecessary for the fluid dynamic design of MT-SOFC reactors. However its role in the current collection and widening of the stack is extremely important.

To discover more information about the radial temperature in a MT-SOFC simulating single MT-SOFCs, like in this thesis but with the Fluent 12 software, that allows the user to actually draw the electrolyte, could give more temperature related information to the field.

More work needs to be done on the dual cathode method to measure the concentration of oxygen around the perimeter of a cylinder but he method and wind tunnel are key elements that can achieve this goal. Impedance measurements need also to be taken to validate the method.

The biggest suggestion for the advancement of this topic should be a targeted investigation of MT-SOFCs in bundles. This is the obvious next step and this thesis certainly provides a cauldron of valuable information to this aim.

The main recommendations are contained in the following bullet point list

- A high temperature wind tunnel should be developed to include bundles of cells.
- The MT-SOFC module in Fluent should also be expanded to include bundles of cells in an investigation into possible alternatives to the fuel and fuel cell module should be undertaken.
- Instances when radiation can be neglected should be investigated and put it into any future high-temperature wind tunnel design.

References:

[1] **Boukamp, B.** Fuel cells: Anodes sliced with ions. *Nature Materials*, 2006, **5**, pp. 517-518.

[2] **Bessler, W.G.,** Electrochemistry and Transport in Solid Oxide Fuel Cells (Habilitationsanschrift) Fakultät für Chemie und Geowissenschaften der Ruprecht-Karls-Universität Heidelberg 2007

[3] **Baur, E. and Preis, H.** Über Brennstoff-Ketten mit Festleitern. *Z. Elektrochem.*, 1937, **43**, pp. 727-732.

[4] **Finnerty, C., Cunningham, R. and Ormerod, R.** Development of a novel test system for in situ catalytic, electrocatalytic and electrochemical studies of internal fuel reforming in solid oxide fuel cells. *Catalysis Letters*, 2000, **66**(4), pp. 221-226.

[5] **Minh, N.Q. and Takahashi, T.** *Science and technology of ceramic fuel cells*. Elsavier, Amsterdam, 1995.

[6] **S.C. Singhal, K.K.** *High Temperature Solid Oxide Fuel Cells*. Elsevier, Oxford, 2003.

[7] **Kee, R.J., Zhu, H. and Goodwin, D.** Solid-oxide fuel cells with hydrocarbon fuels. *Conference Papers, Proceedings of the Combustion Institute*, 2005, **30**, pp. 2379–2404 K.

[8] **Möbius, H.-H.** On the history of solid electrolyte fuel cells. *Journal of Solid State Electrochemistry*, 1997, **1**(1), pp. 2-16.

[9] **Minh, N.Q.** Ceramic Fuel Cells. *Journal of the American Ceramic Society*, 1993, **76**(3), pp. 563-588.

[10] **Riess, I.** Mixed ionic-electronic conductors-material properties and applications. *Solid State Ionics*, 2003, **157**, pp. 1-17.

[11] **Jacobson, A.J.** Materials for Solid Oxide Fuel Cells. *Chemistry of Materials*, 2009, **22**(3), pp. 660-674.

[12] **Tatsumi, I.** *Perovskite Oxide for Solid Oxide Fuel Cells*. Springer, 2009.

[13] **Zhu, B., Yang, X.T., Xu, J., Zhu, Z.G., Ji, S.J., Sun, M.T. and Sun, J.C.** Innovative low temperature SOFCs and advanced materials. *Journal of Power Sources*, 2003, **118**(1-2), pp. 47-53.

[14] **Singhal, S.C. and Kendall, K.** *High-temperature Solid Oxide Fuel Cells: Fundamentals, Design and Applications* 2004.

[15] **Kreuer, K.D.** Proton-conducting oxides. *Annual Review of Materials Research*, 2003, **33**(1), pp. 333-359.

[16] **Alston, T., Kendall, K., Palin, M., Prica, M. and Windibank, P.** A 1000-cell SOFC reactor for domestic cogeneration. *Journal of Power Sources*, 1998, **71**(1-2), pp. 271-274.

[17] **Kendall, K. and Prica, M.** Integrated SOFC tubular system for small-scale cogeneration Proceedings of 1st European Solid Oxide Fuel Cell Conference Lucerne, Switzerland 1994 pp 163-170

[18] **Van herle, J., Ihringer, R., Sammes, N.M., Tompsett, G., Kendall, K., Yamada, K., Wen, C., Kawada, T., Ihara, M. and Mizusaki, J.** Concept and technology of SOFC for electric vehicles. *Solid State Ionics*, 2000, **132**(3-4), pp. 333-342.

[19] **Winkler, W. and Lorenz, H.** Design studies of mobile applications with SOFC-heat engine modules. *Journal of Power Sources*, 2002, **106**(1-2), pp. 338-343.

[20] **Tompsett, G.A., Finnerty, C., Kendall, K., Alston, T. and Sammes, N.M.** Novel applications for micro-SOFCs. *Journal of Power Sources*, 2000, **86**(1-2), pp. 376-382.

[21] **Bujalski, W., Dikwal, C.M. and Kendall, K.** Cycling of three solid oxide fuel cell types. *Journal of Power Sources*, 2007, **171**(1), pp. 96-100.

[22] **Du, Y., Finnerty, C. and Jiang, J.** Thermal Stability of Portable Microtubular SOFCs and Stacks. *Journal of the Electrochemical Society*, 2008, **155**(9), pp. B972–B977.

[23] **Sammes, N.M., Du, Y. and Bove, R.** Design and fabrication of a 100 W anode supported micro-tubular SOFC stack. *Journal of Power Sources*, 2005, **145**(2), pp. 428-434.

[24] Funahashi, Y., Shimamori, T., Suzuki, T., Fujishiro, Y. and Awano, M. Fabrication and characterization of components for cube shaped micro tubular SOFC bundle. *Journal of Power Sources*, 2007, **163**(2), pp. 731-736.

[25] Funahashi, Y., Suzuki, T., Fujishiro, Y., Shimamori, T. and Awano, M. Improvement of Micro Tubular SOFC Bundles. *Fuel Cell Seminar & Exposition* Phoenix Convention Center Arazona (USA), 2008).

[26] Lee, S.-B., Lim, T.-H., Song, R.-H., Shin, D.-R. and Dong, S.-K. Development of anode supported micro-tubular SOFC stack for APU application ECS Transactions - 10th International Symposium on Solid Oxide Fuel Cells, SOFC- 2007 pp **187-191**

[27] Zheng, R., Rho, H., Yamarte, L., Kovacik, G.J. and Sarkar, P. Controlling Solid Oxide Fuel Cell Operation. Alberta Research Council Inc., ed. International, 2004).

[28] Aspen-aerogels-inc. [Online] Products. http://www.aerogel.com/products/overview.html Date of Access: November 20-2008

[29] Sarkar, P., Rho, H., Yamarte, L. and Kovacik, G.J. Heat exchanger for fuel cell stack. 2004).

[30] Acharya, N., Sen, M. and Chang, H.-C. Analysis of heat transfer enhancement in coiled-tube heat exchangers. *International Journal of Heat and Mass Transfer*, 2001, **44**(17), pp. 3189-3199.

[31] Jayakumar, J.S., Mahajani, S.M., Mandal, J.C., Vijayan, P.K. and Bhoi, R. Experimental and CFD estimation of heat transfer in helically coiled heat exchangers. *Chemical Engineering Research and Design*, 2008, **86**(3), pp. 221-232.

[32] Krasnikova, O., Komarova, L. and Mishchenko, T. Coiled smooth-tubular heat exchanger with improved heat properties. *Chemical and Petroleum Engineering*, 1997, **33**(4), pp. 377-380.

[33] Prabhanjan, D.G., Raghavan, G.S.V. and Rennie, T.J. Comparison of heat transfer rates between a straight tube heat exchanger and a helically coiled heat exchanger. *International Communications in Heat and Mass Transfer*, 2002, **29**(2), pp. 185-191.

[34] Liu, M., Dong, D., Peng, R., Gao, J., Diwu, J., Liu, X. and Meng, G. YSZ-based SOFC with modified electrode/electrolyte interfaces for operating at temperature lower than 650 °C. *Journal of Power Sources*, 2008, **180**(1), pp. 215-220.

[35] Liu, Y., Hashimoto, S.-I., Nishino, H., Mori, M., Funahashi, Y., Fijishiro, Y., Hirano, A., Imanishi, N. and Takeda, Y. Development of micro-tubular SOFC with an improved performance via nano-Ag impregnation for intermediate temperature operation. *ECS Transactions - 10th International Symposium on Solid Oxide Fuel Cells, SOFC-X,*, pp. 615-622 Japan, 2007).

[36] Serincan, M.F., Smirnova, A. and Sammes, N.M. Modeling and analysis of a micro-tubular solid oxide fuel cell operating at intermediate temperatures 10th International Symposium on Solid Oxide Fuel Cells, SOFC-X Japan 2007 pp 1955-1965

[37] Yamaguchi, T., Shimizu, S., Suzuki, T., Fujishiro, Y. and Awano, M. Fabrication and characterization of high performance cathode supported small-scale SOFC for intermediate temperature operation. *Electrochemistry Communications*, 2008, **10**(9), pp. 1381-1383.

[38] Suzuki, T., Yamaguchi, T., Fijishiro, Y. and Awano, M. Improvement of SOFC performance using a microtubular, anode-supported SOFC. *Journal of the Electrochemical Society*, 2006, **153**(5), pp. A925-A928.

[39] Hashimoto, S., Nishino, H., Liu, Y., Asano, K., Mori, M., Funahashi, Y. and Fujishiro, Y. The electrochemical cell temperature estimation of micro-tubular SOFCs during the power generation. *Journal of Power Sources*, 2008, **181**(2), pp. 244-250.

[40] Sammes, N.M., Bove, R. and Pusz, J. Ch. 1.5.3, *Design of an SOFC stack. The case of the Micro-tubulal Solid Oxide Fuel Cell. Fuel cel Technology: Reaching towards Commercialisation*. (2006), pp. 16-19.

[41] Serincan, M.F., Pasaogullari, U. and Sammes, N.M. Computational thermal-fluid analysis of a microtubular solid oxide fuel cell. *Journal of the Electrochemical Society*, 2008, **55**(11), pp. B1117-B1127.

[42] Hashimoto, S., Nishino, H., Liu, Y., Asano, K., Mori, M., Funahashi, Y. and Fujishiro, Y. Development of Evaluation Technologies for Microtubular SOFCs Under Pressurized Conditions. *Journal of Fuel Cell Science and Technology*, 2008, **5**(3), pp. 31208-31205.

[43] Lessing, P. A review of sealing technologies applicable to solid oxide electrolysis cells. *Journal of Materials Science*, 2007, **42**(10), pp. 3465-3476.

[44] Raj, N.S. Sealing Technology for Solid Oxide Fuel Cells (SOFC). *International Journal of Applied Ceramic Technology*, 2007, **4**(2), pp. 134-144.

[45] Singh, P., Yang, Z., Viswanathan, V. and Stevenson, J. Observations on the structural degradation of silver during simultaneous exposure to oxidizing and reducing environments. *Journal of Materials Engineering and Performance*, 2004, **13**, pp. 287-294.

[46] Abernathy, H.W., Koep, E., Compson, C., Cheng, Z. and Liu, M. Monitoring Ag−Cr Interactions in SOFC Cathodes Using Raman Spectroscopy. *The Journal of Physical Chemistry C*, 2008, **112**(34), pp. 13299-13303.

[47] Tucker, M.C., Jacobson, C.P., De Jonghe, L.C. and Visco, S.J. A braze system for sealing metal-supported solid oxide fuel cells. *Journal of Power Sources*, 2006, **160**(2), pp. 1049-1057.

[48] Kim, J.Y., Hardy, J.S. and Weil, S. Dual-atmosphere tolerance of Ag-CuO-based air braze. *International Journal of Hydrogen Energy*, 2007, **32**(16), pp. 3655-3663.

[49] Kim, J.Y., Choi, J.-P. and Scott Weil, K. Mechanical properties and dual atmosphere tolerance of Ag-Al based braze. *International Journal of Hydrogen Energy*, 2008, **33**(14), pp. 3952-3961.

[50] Janardhanan, V.M. and Deutschmann, O. CFD analysis of a solid oxide fuel cell with internal reforming: Coupled interactions of transport, heterogeneous catalysis and electrochemical processes. *Journal of Power Sources*, 2006, **162**(2), pp. 1192-1202.

[51] Janardhanan, V.M. and Deutschmann, O. Numerical study of mass and heat transport in solid-oxide fuel cells running on humidified methane. *Chemical Engineering Science*, 2007, **62**(18-20), pp. 5473-5486.

[52] Lockett, M., Simmons, M.J.H. and Kendall, K. CFD to predict temperature profile for scale up of micro-tubular SOFC stacks. *Journal of Power Sources*, 2004, **131**(1-2), pp. 243-246.

[53] Jasinski, P., Suzuki, T., Dogan, F. and Anderson, H.U. Impedance spectroscopy of single chamber SOFC. *Solid State Ionics*, 2004, **175**(1-4), pp. 35-38.

[54] Lehnert, W., Meusinger, J. and Thom, F. Modelling of gas transport phenomena in SOFC anodes. *Journal of Power Sources*, 2000, **87**(1-2), pp. 57-63.

[55] Qi, Y., Huang, B. and Luo, J. Dynamic modeling of a finite volume of solid oxide fuel cell: The effect of transport dynamics. *Chemical Engineering Science*, 2006, **61**(18), pp. 6057-6076.

[56] Tanaka, T., Inui, Y., Urata, A. and Kanno, T. Three dimensional analysis of planar solid oxide fuel cell stack considering radiation. *Energy Conversion and Management*, 2007, **48**(5), pp. 1491-1498.

[57] Bhattacharyya, D., Rengaswamy, R. and Finnerty, C. Isothermal models for anode-supported tubular solid oxide fuel cells. *Chemical Engineering Science*, 2007, **62**(16), pp. 4250-4267.

[58] Ivers-Tiffée, E., Weber, A., Schmid, K. and Krebs, V. Macroscale modeling of cathode formation in SOFC. *Solid State Ionics*, 2004, **174**(1-4), pp. 223-232.

[59] Xue, X., Tang, J., Sammes, N. and Du, Y. Dynamic modeling of single tubular SOFC combining heat/mass transfer and electrochemical reaction effects. *Journal of Power Sources*, 2005, **142**(1-2), pp. 211-222.

[60] Hong, C.W. Fuel Cell Power Research for Transportation. *ICAT Internationl Conference on Automative Technology "Future Automotive Technologies on Powertrain and Vehicle* (Automative Manufacturers Association, Istanbul, Turkey, 2004).

[61] Hussain, M.M., Li, X. and Dincer, I. Mathematical modeling of transport phenomena in porous SOFC anodes. *International Journal of Thermal Sciences*, 2007, **46**(1), pp. 48-56.
[62] VanderSteen, J.D.J. and Pharoah, J.G. Modeling Radiation Heat Transfer With Participating Media in Solid Oxide Fuel Cells. *Journal of Fuel Cell Science and Technology*, 2006, **3**(1), pp. 62-67.
[63] Daun, K.J., Beale, S.B., Liu, F. and Smallwood, G.J. Radiation heat transfer in planar SOFC electrolytes. *Journal of Power Sources*, 2006, **157**(1), pp. 302-310.
[64] Murthy, S. and Fedorov, A.G. Radiation heat transfer analysis of the monolith type solid oxide fuel cell. *Journal of Power Sources*, 2003, **124**(2), pp. 453-458.
[65] Damm, D.L. and Fedorov, A.G. Spectral Radiative Heat Transfer Analysis of the Planar SOFC. *Journal of Fuel Cell Science and Technology*, 2005, **2**(4), pp. 258-262.
[66] Recknagle, K.P., Williford, R.E., Chick, L.A., Rector, D.R. and Khaleel, M.A. Three-dimensional thermo-fluid electrochemical modeling of planar SOFC stacks. *Journal of Power Sources*, 2003, **113**(1), pp. 109-114.
[67] Lawlor, V., Hochenauer, C., Buchinger, G., Griesser, S., Olabi, A. and Meissner, D. Numerical Simulation and Experimental Validation to Design an Optamised Micro-Tubular SOFC Reactor 2. Forschungsforum der österreichischen Fachhochschulen Upper Austria University of Applied Sciences. Wels. Austria. 2008 pp 327-334
[68] Lawlor, V., Buchinger, G., Hochenauer, C., Cordinor, S., Griesser, S., Olabi, A. and Meissner, D. EFC2007-39060 Design of a Microtubular SOFC Reactor with CFD and Validations. The Second European Fuel Cell Technology and Applications Conference Rome Italy 2007 pp 168-170
[69] Chouikh, R., Guizani, A., El Cafsi, A., Maalej, M. and Belghith, A. Experimental study of the natural convection flow around an array of heated horizontal cylinders. *Renewable Energy*, 2000, **21**(1), pp. 65-78.
[70] Chouikh, R., Guizani, A., Maâlej, M. and Belghith, A. Numerical study of the laminar natural convection flow around an array of two horizontal isothermal cylinders. *International Communications in Heat and Mass Transfer*, 1999, **26**(3), pp. 329-338.
[71] Suzuki, T., Funahashi, Y., Yamaguchi, T., Fujishiro, Y. and Awano, M. Fabrication of Micro-Tubular SOFC Stack Using Ceramic Manifold 10th International Symposium on Solid Oxide Fuel Cells (SOFC-X) Japan 2007 pp 477-482
[72] Serincan, M.F., McPhee, W.A.G. and Sammes, N.M. Mass transport effects of current collector coated on the entire cathode surface of a micro tubular solid oxide fuel cell. *Journal of the Electrochemical Society*, 2007, **3**(33), pp. 35-43.
[73] Zdravkovich, M.M. *Flow Around Circular Cylinders Volume 1: Fundamentals* Oxford University Press, USA, 1997.
[74] Shapiro, A. [Online] Flow Visualization. http://web.mit.edu/hml/ncfmf.html Date of Access: 13-11-2009
[75] Bouard, R. and Coutanceau, M. Étude théorique et expérimentale de l'écoulement engendré par un cylindre en translation uniforme dans un fluide visqueux en régime de Stokes. *Zeitschrift für Angewandte Mathematik und Physik (ZAMP)*, 1986, **37**(5), pp. 673-684.
[76] Coutanceau, M. and Defaye, J.-R. Circular Cylinder Wake Configurations: A Flow Visualization Survey. *Applied Mechanics Reviews*, 1991, **44**(6), pp. 255-305.
[77] White, C.M. The Drag of Cylinders in Fluids at Slow Speeds. *Proceedings of the Royal Society of London. Series A. Mathematical and Physical Sciences*, 1946, **186**(1007), pp. 472-479.
[78] Barker, M. On the Use of Very Small Pitot-Tubes for Measuring Wind Velocity. *Proceedings of the Royal Society of London. Series A*, 1922, **101**(712), pp. 435-445.
[79] Thom, A. The flow past a circular cylinder at low speeds, Series A. *Proceedings of the Royal Society of London,*, 1933, **141**, p. 651.

[80] Underwood, R.L. Calculation of incompressible flow past a circular cylinder at moderate Reynolds numbers. *Journal of Fluid Mechanics Digital Archive*, 1969, **37**(01), pp. 95-114.

[81] Homann, F. Einfluß großer Zähigkeit bei Strömung um Zylinder (Influence high strength flows around cylinder). *Forschung im Ingenieurwesen*, 1936, **7**(1), pp. 1-10.

[82] Nisi, H. and Porter, A.W. On eddies in air. *Philosopical Magazine series 6*, 1923, **46**, pp. 754-770.

[83] Taneda, S. Experimental investigations of wakes behind cylinders and plates at low Reynolds numbers. *Journal Physical Society Japan*, 1956, **11**, pp. 302-307.

[84] Coutanceau, M. and Bouard, R. Experimental determination of the main features of the viscous flow in the wake of a circular cylinder in uniform translation: part one steady flow. *Journal of Fluid Mechanics*, 1977, **79**, pp. 231-236.

[85] Camichel, C. On it is produced by an obstacle immersed in a stream of liquid. *Comptes Rendus Acadime Sciences*, 1927, **185**, pp. 1536-1560.

[86] Trinatfyllou, G.S., Trinatfyllou, M.S. and Chryssostomidis, C. On the formation of vortex streets behind stationary cylinders. *Journal of Fluid Mechanics*, 1986, **170**, pp. 461-477.

[87] Munsen, B., Young, D. and Okiishi, T. *Fundamentals of Fluid Mechanics*. Edition 5Don Fowley, New York, 2005, pp. 299-371.

[88] Fage, A. Photographs of fluid flow revealed with an ultra microscope. *Proceedings of the Royal Society of London,*, 1934, **A-144**, pp. 381-387.

[89] Teissie-solier, M., Castagneto, L. and Sabathe, M. On the beating that accompanies the formation of Bernard Karman alternate eddies. *compte rendu. Acad. Sci.*, 1937, **205**, pp. 23-28.

[90] Gerrard, J.H. The wakes of cylindrical bluff bodies at the low Reynolds numbers. *philosophical transactions of the Royal Society of London, Series A*, 1978, **288**, pp. 351-382.

[91] Roshoko, A. On the development of turbulant wakes from vortex streets *NACA Rep.*, 1954, p. 1191.

[92] Gerrard, J.H. Numerical study of the instabilities in the near wake of a circular cylinder at low reynolds number. *Journal of Fluids and Structures*, 1997, **11**(3), pp. 271-291.

[93] Shair*, F.H., Grove, A.S., Petersen, E.E. and Acrivos, A. The effect of confining walls on the stability of the steady wake behind a circular cylinder. *Journal of Fluid Mechanics Digital Archive*, 1963, **17**(04), pp. 546-550.

[94] Slater, J. [Online] [Online] Aeroelasticity phenomenon (figure 2). http://www.cs.wright.edu/~jslater/SDTCOutreachWebsite/aeroelasticity.htm Date of Access: 17-11-2009

[95] Newman, J. Mass transfer to the rear of a cylinder at high schmidt numbers. *Indus & Eng Chem-Fundamentals*, 1969, **8**(3), pp. 553-557.

[96] Todd, B. and Young, J.B. Thermodynamic and transport properties of gases for use in solid oxide fuel cell modelling. *Journal of Power Sources*, 2002, **110**(1), pp. 186-200.

[97] Zald, M.M., Nirdosh, I. and Sedahmed, G.H. Natural convection mass transfer behaviour of long vertical annuli. *International Communications in Heat and Mass Transfer*, 2000, **27**(3), pp. 435-442.

[98] Cordiner, S., Mariani, A. and Mulone, V. An integrated CFD-approach to design micro-tubular solid oxide fuel cells. *Thermal Issues in Emerging Technologies, ThETA 2,*Cairo, Egypt,, 2008).

[99] Michal P. Sobera, Kleijn, C.R., Akker, H.E.A.V.d. and Brasser, P. Convective heat and mass transfer to a cylinder sheathed by a porous layer. *AICHE Journal*, 2003, **49**(12), pp. 3018-3028.

[100] Serincan, M.F., Pasaogullari, U. and Sammes, N.M. Effects of operating conditions on the performance of a micro-tubular solid oxide fuel cell (SOFC). *Journal of Power Sources*, 2009, **192**(2), pp. 414-422.

[101] Brett, D.J.L., Aguiar, P., Clague, R., Marquis, A.J., Schöttl, S., Simpson, R. and Brandon, N.P. Application of infrared thermal imaging to the study of pellet solid oxide fuel cells. *Journal of Power Sources*, 2007, **166**(1), pp. 112-119.

[102] Pomfret, M.B., Steinhurst, D.A., Kidwell, D.A. and Owrutsky, J.C. Thermal imaging of solid oxide fuel cell anode processes. *Journal of Power Sources*, **195**(1), pp. 257-262.

[103] Suzuki, T., Funahashi, Y., Yamaguchi, T., Fujishiro, Y. and Awano, M. New Stack Design of Micro-tubular SOFCs for Portable Power Sources. *Fuel Cells*, 2008, **8**(6), pp. 381-384.

[104] N. M. Sammes, Y.D. Fabrication and Characterization of Tubular Solid Oxide Fuel Cells. *International Journal of Applied Ceramic Technology*, 2007, **4**(2), pp. 89-102.

[105] Buchinger, G., Kraut, J., Raab, T., Griesser, S., Lawlor, V., Haiber, J., Hiesgen, R., Sitte, W. and Meissner, D. Operating Micro-Tubular SOFCs Containing Nickel Based Anodes with Blends of Methane and Hydrogen International Conference on Clean Electrical Power, 2007. ICCEP '07. 2007 pp 450 - 455

[106] Campana, R., Merino, R.I., Larrea, A., Villarreal, I. and Orera, V.M. Fabrication, electrochemical characterization and thermal cycling of anode supported microtubular solid oxide fuel cells. *Journal of Power Sources*, 2009, **192**(1), pp. 120-125.

[107] Suzuki, T., Funahashi, Y., Hasan, Z., Yamaguchi, T., Fujishiro, Y. and Awano, M. Fabrication of needle-type micro SOFCs for micro power devices. *Electrochemistry Communications*, 2008, **10**(10), pp. 1563-1566.

[108] Zitouni, B., Moussa, H.B., Oulmi, K., Saighi, S. and Chetehouna, K. Temperature field, H2 and H2O mass transfer in SOFC single cell: Electrode and electrolyte thickness effects. *International Journal of Hydrogen Energy*, 2009, **34**(11), pp. 5032-5039.

[109] Daan, C. and Mojie, C. Numerical analysis of thermal and electrochemical phenomena for anode supported microtubular SOFC. *AICHE Journal*, 2009, **55**(3), pp. 771-782.

[110] Fischer, K. and Seume, J.R. Location and Magnitude of Heat Sources in Solid Oxide Fuel Cells. *Journal of Fuel Cell Science and Technology*, 2009, **6**(1), pp. 11002-11011.

[111] Kanamura, K., Yoshioka, S. and Takehara, Z.-i. Temperature distribution in tubular solid oxide fuel cell. *The Chemical Society of Japan*, 1991, **64**(6), pp. 1828-1834.

[112] Çengel, Y.A. and Cimbala, J.M. *Fluid mechanics fundamentals and applications*. McGraw-Hill education, 2006, pp. 819-883.

[113] Apsely,D.[online] Introduction to CFD . http://personalpages.manchester.ac.uk/staff/david.d.apsley/lectures/comphydr/index.htm Date of Access: 2-11-2009

[114] Bhaskaran, R. and Collins, L. [Online] Introduction to CFD Basics http://courses.cit.cornell.edu/fluent/cfd/ Date of Access: 14-july-2010

[115] University_of_Sydney. [Online] [online] Aerodynamics for students. http://www-mdp.eng.cam.ac.uk/web/library/enginfo/aerothermal_dvd_only/aero/fprops/pipeflow/node9.html Date of Access: 14-July-2010

[116] Fuel.cell.handbook. *Fuel Cell Handbook*. U.S. Department of Energy EG&G Technical Services inc., Virginia, 2004.

[117] Fuel_cell_Norway_ANS. [Online] Fuel Cell Theory. Date of Access: 14-july.-2010

[118] Fluent.Inc. [Online] Chapter 3 SOFC Model Theory. http://my.fit.edu/itresources/manuals/fluent6.3/help/pdf/fuelcells/chp03.pdf Date of Access: 17-Nov-2009

[119] Lawlor, V., Hochenauer, C., Buchinger, G., Griesser, S., Olabi, A. and Meissner, D. Towards an optimized Microtubular S.O.F.C. reactor core design. 3. Forschungsforum der Österreichischen Fachhochschulen Villach, Austria 2009 pp 288-293

[120] Zdravkovich, M.M. *Flow around circular cylinders Vol: 2 Applications* Oxford University Press, USA, 2003.

[121] Fowler, A.J. and Bejan, A. Forced convection in banks of inclined cylinders at low Reynolds numbers. *International Journal of Heat and Fluid Flow*, 1994, **15**(2), pp. 90-99.

[122] P. Von Böckh. Ch. 3-4, *Wärmeübertragung: Grundlagen*.(Basics of heat transfer) (Springer, 2006)

[123] Costamanga, P. and Honegger, K. Modeling of solid oxide heat exchanger integrated stacks and simulation at high fuel utilization. *Journal of the Electrochemical Society*, 1998, **145**(11), pp. 3995-4007.

[124] Zhu, H., Kee, R., Janardhanan, V., Deutschmann, O. and Goodwin, D. Modeling elementary heterogeneous chemistry and electrochemistry in solid-oxide fuel cells. *Journal of the Electrochemical Society*, 2005, **152**, p. A2427.

[125] Incropera, P.F. and David, D.P. *Fundamentals of heat and mass transfer 5 ed.* 2002.

[126] Hyde, A.J., A Portable Generator Incorporating Mini-Tubular Solid Oxide Fuel Cells. The University of Waikato 2008 pp 76-77

Appendix

Appendix I Experimental techniques used to improve cell performance.

A modern experimental technique, used by Izzo et al. [1] which use computed X-ray computed tomography (XCT) and some modelling techniques in an attempt to quantify the gas concentrations can be used to estimate the gas concentrations within the anode electrode and triple phase boundary region. Specifically the hydrogen inside the electrolyte interface region/electrochemically active region of the anode. They take a 6.3 µm cubic segment of the anode and assume a fuel species concentration of 47% H2, 3%H2O and 50% N2 is known at $x^* = 0$ the gas region. The hydrogen fuel is consumed at the triple phase boundary to generate an equal-molar amount of H_2O at the prescribed current density of the cell at $x^* = 1$. Figure 133 shows their result using multi-component mass transport through the XCT reconstructed the anode geometry is modelled using the lattice Boltzmann method (LBM). Substantial lateral species variation can be seen especially near the TPB, indicating the importance of proper structural representation in analyzing gas transport in SOFCs.

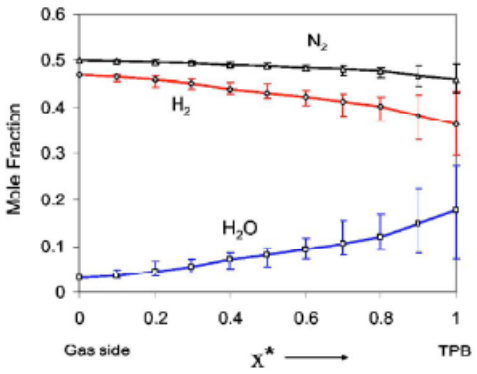

Figure 133: Average species mole fractions from the gas side to the triple phase boundary zone [1].

Figure 134 illustrates a typical distribution of hydrogen inside the porous anode obtained by Izzo et al. using LBM is shown and images like this from the methods from Izzo et al. methodologies are extremely informative on the gas concentrations within the anode. A similar study on the concentrations within the cathode electrode may also be very interesting in the future. They also explain that this kind of information will be valuable in pore-scale SOFC transport models,

examples of which are presented in this work. With increasing availability of supercomputers and parallel computing platforms, detailed pore-level models will be at the forefront of SOFC analysis and optimization in the near future.

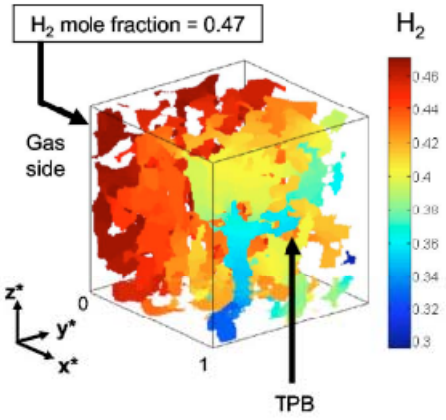

Figure 134: Application of the XCT reconstructed geometry to predict the pore-scale species distribution of hydrogen in an SOFC anode using LBM (62).

Another state of the art experimental approach for visualising the tracks of local oxygen transport at interface has been investigated by Kishimoto et al. [2] using the oxygen stable isotope labelling and subsequent secondary ion mass spectrometry analyses (SIMS). The reader is pointed to Horita et al.[3] for more information on this technique They found that the activation of oxygen exchange reaction was clearly observed as a strong 18O− intensity at Au or Pt/YSZ electrode/electrolyte interface treated at T=973 K. It's stated that this indicates that the oxygen to oxygen ion reaction dominantly occurs at gas/electrode/electrolyte triple phase boundary.

Figure 135 is an interesting image and example of how the SIMS analysis can be used to determine the reaction zones within an electrode. It shows the 18O-isotope images around Au/YSZ interface treated at 773 K in p(O2)=7 kPa with and without cathodic polarization. When the sample was treated without cathodic polarization, Figure 135 (a), the 18O− intensity was very low so that little oxygen exchange and dissolution occurred in the whole area. When the sample was treated under a cathodic polarization (E=−0.3 V) Figure 135 (b), a bright line was observed along Au/YSZ interface which the authors recommend indicates that the electrochemical reduction of oxygen and dissolution of oxide ions into YSZ mainly occur around the TPB. The same investigation was also tried for Pt/YSZ, Figure 135 (b) however, it was difficult to observe clear evidence that the oxygen exchange was enhanced around TPB. As shown in Figure 135 (c) the 18O− intensity around

Pt/YSZ interface was very low and no line was observed even under a cathodic polarization E=−0.3 V. A very beneficial study could be done similar to this for Ni/YSZ and LSM electrodes would be very interesting and compliment the work of Izzo et al. [1]and other modellers

The previously mentioned modelling and experimentation in this section relates to state of the art single cell modelling but for commercialisation and so a product can be developed a more engineering orientated rather than scientific approach to modelling is discussed below from the works of authors dealing with stacks of micro-cells rather than single cells.

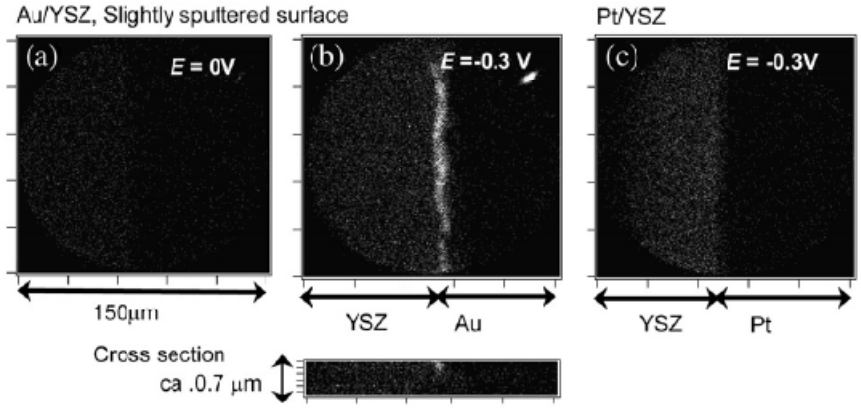

Figure 135: 18O- ion images on the surface around Au/YSZ and Pt/YSZ interfaces treated at different cathodic polarization T=773 K, p(O2)=7 kPa for 300 s: (a) Au/YSZ E=0 V, (b) Au/YSZ E=−0.3 V, (c) Pt/YSZ, E=−0.3 V. The depth of the images ranges from ca. 150 nm in YSZ region.

[1] Izzo, J.J.R., Joshi, A.S., Grew, K.N., Chiu, W.K.S., Tkachuk, A., Wang, S.H. and Yun, W. Nondestructive Reconstruction and Analysis of SOFC Anodes Using X-ray Computed Tomography at Sub-50 nm Resolution. *Journal of the Electrochemical Society*, 2008, **155**(5), pp. B504-B508.

[2] Kishimoto, H., Sakai, N., Yamaji, K., Horita, T., Brito, M.E., Yokokawa, H., Amezawa, K. and Uchimoto, Y. Visualization of oxygen transport behavior at metal electrode/oxide electrolyte interface using secondary ion mass spectrometry. *Solid State Ionics*, 2008, **179**(9-10), pp. 347-354.

[3] Horita, T., Yamaji, K., Sakai, N., Yokokawa, H., Kawada, T. and Kato, T. Oxygen reduction sites and diffusion paths at La0.9Sr0.1MnO3-x/yttria-stabilized zirconia interface for different cathodic overvoltages by secondary-ion mass spectrometry. *Solid State Ionics*, 2000, **127**(1-2), pp. 55-65.

Appendix II Level of research in micro-tubular SOFCs and what is being researched in the field.

To compare the quantity of research in larger SOFCs with the micro-tubular version the Compendex database on the Engineering Village web site [1] was used in November 2008. This site contains a data base of scientific and engineering publications from the most popular journals around the world. It was found that while comparisons can easily be made between the levels of research between larger SOFCs and the micro-tubular type, when these are subsequently broken into paper themes it is difficult to make a direct comparison. This is because the larger SOFC papers tend to be more specific while the papers relating to the MT-SOFC tend to include several topics in a single paper, especially in stack design papers.

The following results were found for the number of publications which had solid oxide fuel cell or SOFC in their abstracts, titles or subject fields. Using different inclusion and exclusion parameters in the advanced search engine on the site, these results were broken down into their main themes. It is clear that there has been a recent surge in the interest in general SOFC research as shown in Figure 136. These results are also broken down into the themes of the research papers and indicate a good spread of research over the whole topic. It should be noted that while these papers are not directly related to the MT-SOFC, many of them may be applied such as control systems, sealing and interconnects. It seems that as the interest in SOFCs increases so also has the interest in the peripheral devices such as sealing, interconnects, control systems and stack design. It may be the case that these peripherals become of more interest to SOFC groups and groups of other disciplines as the quality of the cells improve and the role of the different peripherals become more necessary for fully functioning stacks.

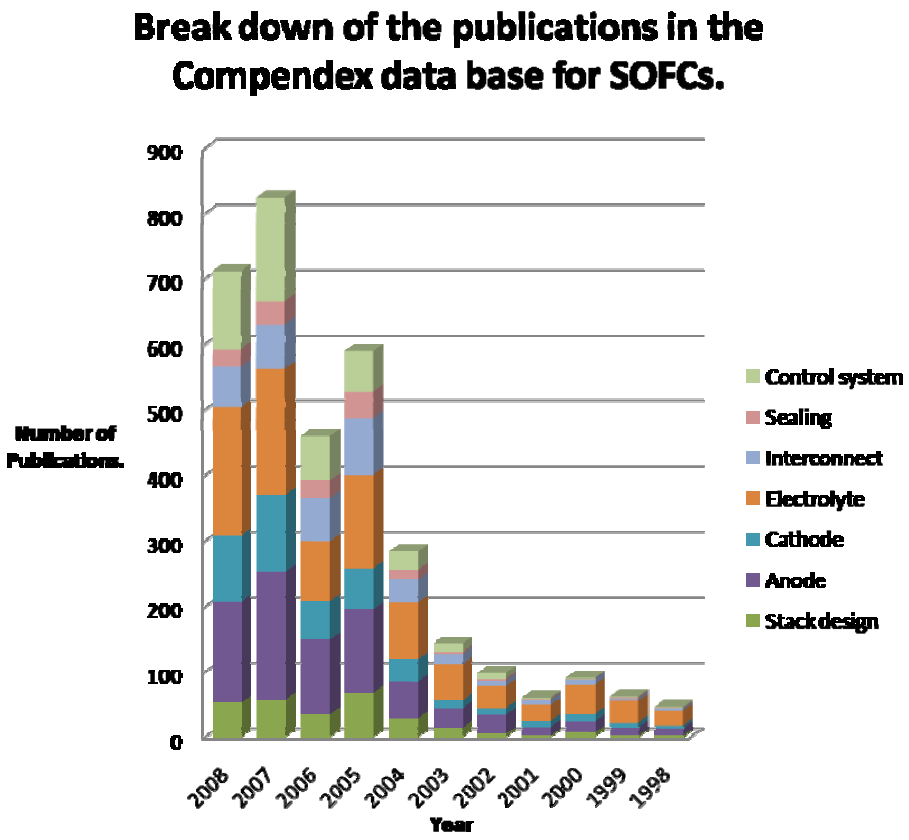

Figure 136: Search results from [1] for articles with the terms c (AND/OR/NOT) a theme in their titles abstracts or subject fields..

Figure 137 illustrates the percentage of the total for each year of publications from each of the major contributing nations. It is clear from this plot that China and Korea seem to be continually expanding their research. Also the contribution numbers of all the major contributors in the last 7 years has continually eaten into the percentage contributed by the non major contributors. This could be an indication that the major contributors, because of their previous research activities, are becoming much more specialised and therefore will be the dominant proprietors of the SOFC know how and intellectual property.

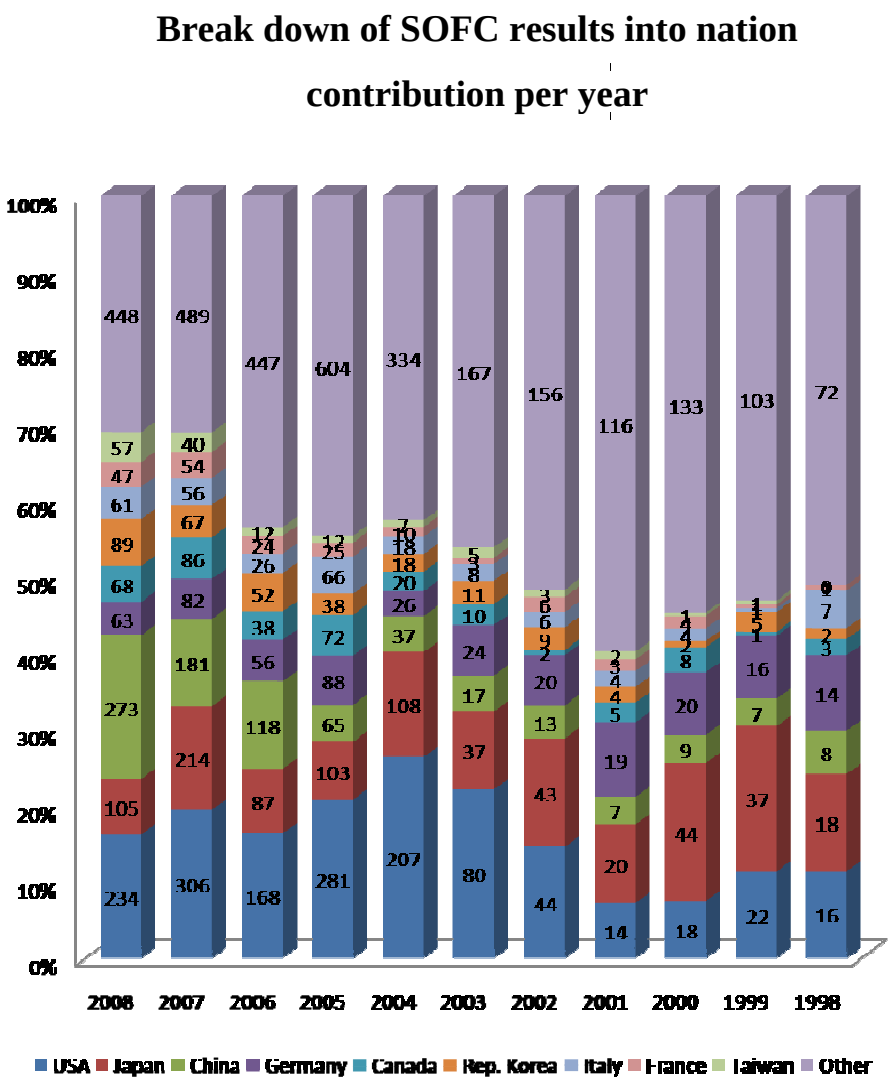

Figure 137: Break down of the search results in Figure 136 into the countries of origin of the major contributors.

This review has focused more specificaly with the micro-tubular SOFC and so a more sutible search query was inserted into the engineering village's Compendex data base search. The result can be seen below in Figure 138, which is broken down into the main topic of the publications. It was found that the MT-SOFC publications tend to be much more general. For example there is not any literature that deals specifically with the sealing of these cells. However some information about sealing can be found within texts based on other themes. So for example a single paper can include several topics such as fabrication of the anode cathode and electrolyte, with some manifold design, sealing techniques and stack arrangment.

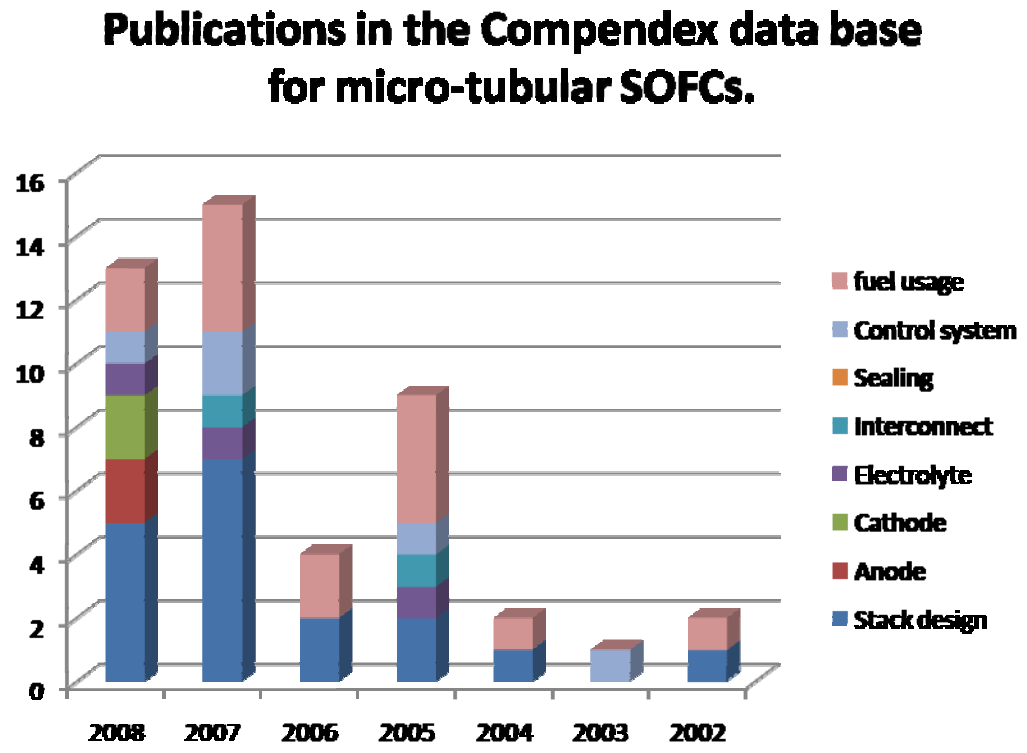

Figure 138: Break down of the search results in [1] using an advances search more specific to MT-SOFCs.

It can be seen from the results Figure 12 and Figure 138 that only a small proportion of the overall publications related to SOFCs deal specifically with the MT-SOFC. It should be remembered that some of the topics included in the general SOFC do not also apply to the micro-tubular version. Because of the much lower numbers of publications it was also noticed that many papers for the MT-SOFCs dealt specifically whith the theme of running the cells on different fuels.

From Figure 139, which is a breakdown of these results into their nation of origin, it can be seen where most of the development is taking place in this field. This does not account for non-published research but it should still be a good indication. Breaking these results down shows that 38% of the publications in the past 7 years came from Japan alone, 21% from America and Canada and 20% came from E.U. members.

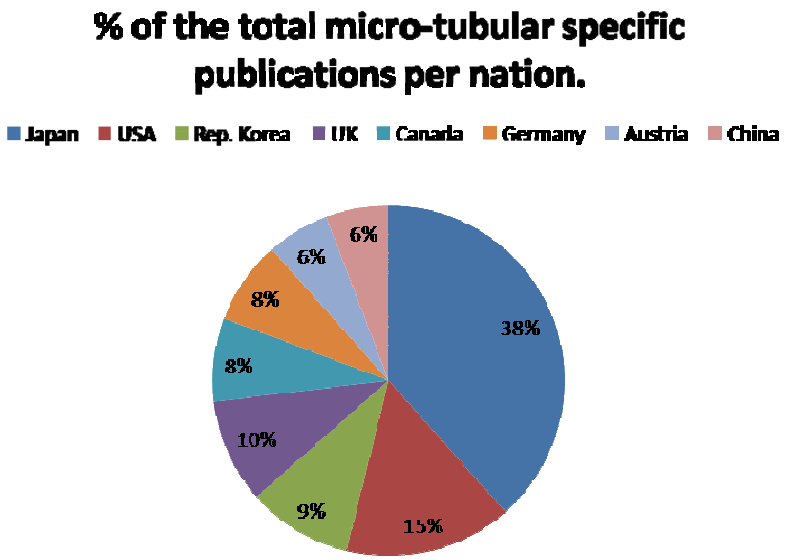

Figure 139: Break down of the search results from Figure 138 into percentage publications per nation since 2002.

Winkler in 2004 [2] researched a worldwide survey and review of research taking place dealing with micro scale SOFCs. Also outlined in this document are substantial projects for micro-tubular and micro-planar SOFCs. Four were found in the U.S, two each in the E.U. zone, Japan, Canada and Rep. of Korea. It is very clear that the points and advantages raised by Van Herle et al. [3] in 2000 about the potential of MT-SOFCs for portable applications have been certainly proved. While the larger type of SOFC may be closer to large scale commercialization than the MT-SOFC the potential of the micro-tubes seems to be over looked by the broader SOFC community.

[1] Elsevier-Inc. [Online] Engineering Village web-based discovery. http://www.engineeringvillage2.org Date of Access: 24 November -2008

[2] Winkler, W. Analysis of actual RTD on SOFC architectures in Japan and US and conclusions. 2004 Hamburg University of Applied Sciences

[3] Van herle, J., Ihringer, R., Sammes, N.M., Tompsett, G., Kendall, K., Yamada, K., Wen, C., Kawada, T., Ihara, M. and Mizusaki, J. Concept and technology of SOFC for electric vehicles. *Solid State Ionics*, 2000, **132**(3-4), pp. 333-342.

Appendix III-(A) An Initial Study to Design a Device to Test Single MT-SOFCs and Stacks.

Specifications for the Design of an Initial Testing Device

Prior to the concept of a high temperature wind tunnel a study was performed to see what kind of apparatus could be built for testing single or multiple SOFCs. After a brief search for available equipment it was decided that an apparatus could be built out of the following components.

- A PID controller (LABVIEW) and solid-state relays (Type D2410 Crydom.inc)
- Heating Tapes (HSQ - 900 °C Horst Gmbh Germany)
- Three flow controllers to supply the fuel, purge gas and oxidant (Vögtlin Instruments AG Smart series 10, 0.2 and 0.1l (H2)/min.)
- An insulation compartment for the reactor (Superwool 607™ MAX Blanket Morgan Crucible company plc UK.)
- Lab view was given as the preferred method for data acquisition and control.

The original device/housing that was used to contain a single MT-SOFC or stack was a simple welded steel box and the shape of it may be seen in Figure 145 and Figure 146. A simple set of guidelines were suggested for the minimum requirements that this system should meet. It was decided that it should be regulated up to a temperature of 850°C with the possibility of using single cells or stacks. It was also proposed at this stage that the supplied heat to the standalone single cell or reactor holding device should be supplied by the air supply at the cathode side of the single MT-SOFC or stack. This means that the flow of air into the housing would be used to heat the housing and stack up to the operational temperature or at least this was the original concept.

Flow control

Figure 140 below is a picture of the type of flow controller used (Vögtlin Instruments AG Smart series 10 l (H2)/min.). The 10 litre per minute controller was calibrated for use with air.

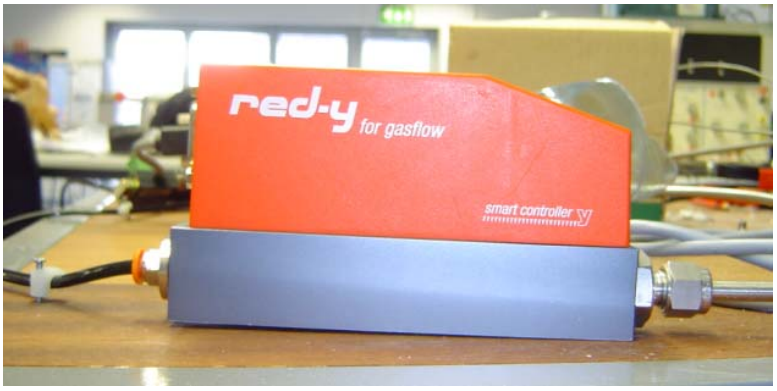

Figure 140 Picture of a gas flow controller used.

The red-y mass flow meter has a constant heating power and ensures a temperature difference that is directly proportional to the gas flow rate. Inside the flow channel of the flow controller a temperature measurement is followed by a heater and then a temperature measurement again. Figure 141 below illustrates this process.

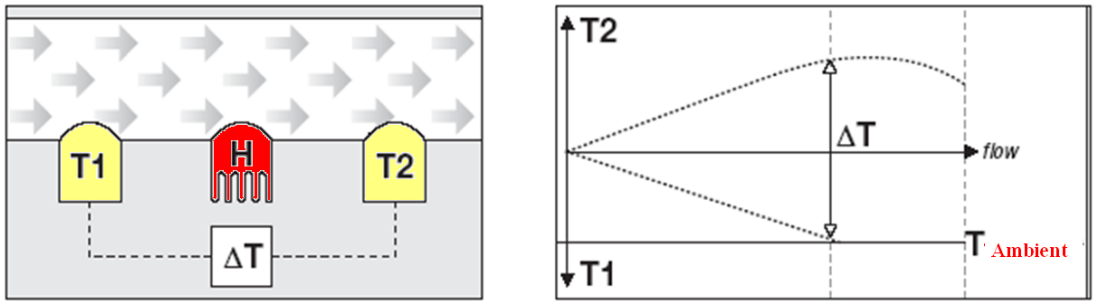

Figure 141 the method of measuring the flow rate in the mass flow controllers.

If there is no gas flowing through the controller the heater "H" uniformly distributes the heat, and the temperature difference T1-T2 equals zero. The mass flow rate is proportional to the temperature difference between T1 and T2. This means that the faster the gas flows through the controller, the greater temperature of difference between T1 and T2 as seen in Figure 141 (right). This type of controller has an advantage over volumetric principles of measurement because pressure and temperature do not have to be additionally measured to obtain an accurate flow rate.

The flow controllers use a CMOS semi conductor chip that allows high sensor precision, as well as digital intelligence, reliability, a dynamic measuring range and a fast response time. CMOS is a standard technology for the manufacture of integrated circuits. With the CMOS technology, the sensor element, the amplifier and the A/D converter form a unit on the same silicon chip. The digital intelligence linked to the CMOS sensor permits the emission of a fully calibrated temperature-compensated output signal.

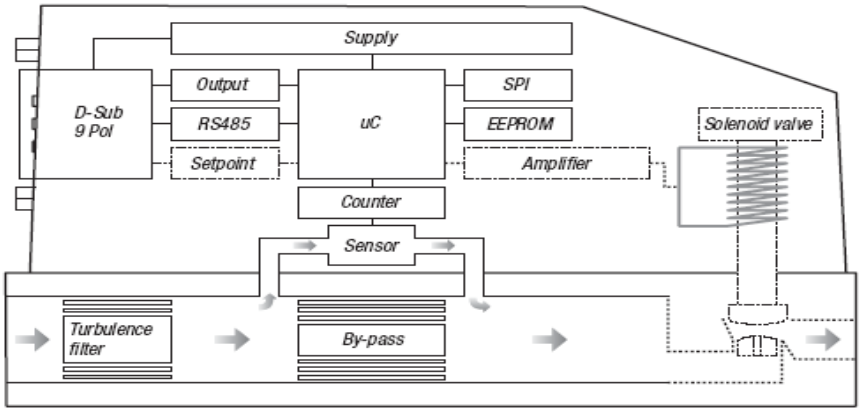

Figure 142 A schematic of the components inside the flow controllers

The pipes to hold the gases.

For the initial study Figure 143 below illustrates the piping routes of the gases and processes they are involved in along the route. In internal diameter of the pipe was 5.2 mm and heated length of the pipe was 0.1 m. pipes were made of high temperature stainless steel.

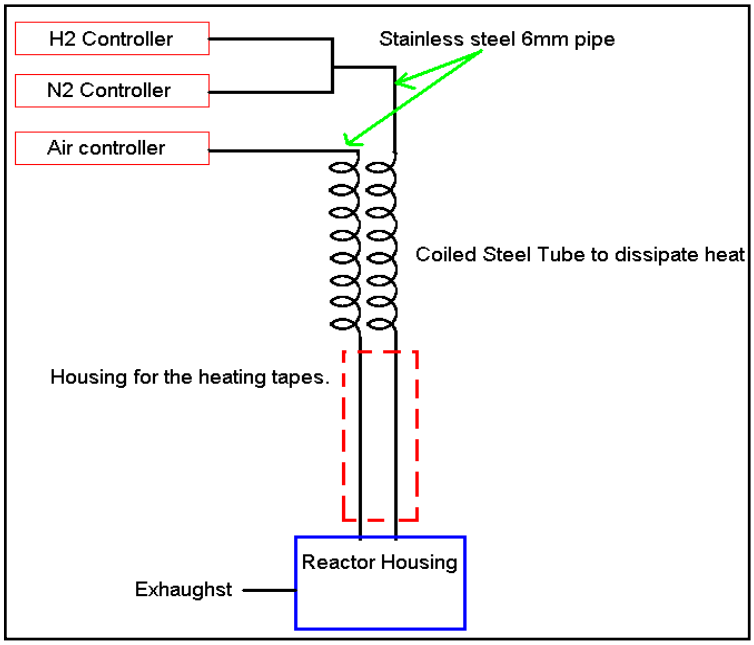

Figure 143: An illustration depicting the flow of the gases in the initial experimental apparatus.

As a safety precaution it was decided to make sure that the flow controllers did not get damaged from the heating by the heating cable that the length of the steel pipes should be long. To keep the components in a small space it was decided to coil the steel pipes as shown in Figure 143. It was quite simple to coil the pipes; a three meter long piece of 6mm tubular stainless steel was placed into a stake as shown in (1) Figure 144. The stainless steel was gripped in the stake by a slit which was cut into the steak and some U-shaped tacks and the stainless steel bar was heated as it was wrapped around the wooden stake as seen in (2) Figure 144. Figure 144 (3) was the finished coiled stainless steel tubes which had to be bent a little more to get a better finish on the coils. Figure 144 (4) shows the two finished stainless steel pipes with the coils and wrapped with the heating tape. The coiling of the high temperature steel

was later achieved by wrapping the steel around an empty gas bottle using 2 people to hold the bottle and steel pipe in place, to heat the section of the pipe being bent and to apply force vial leverage to the steel pipe to bend it.

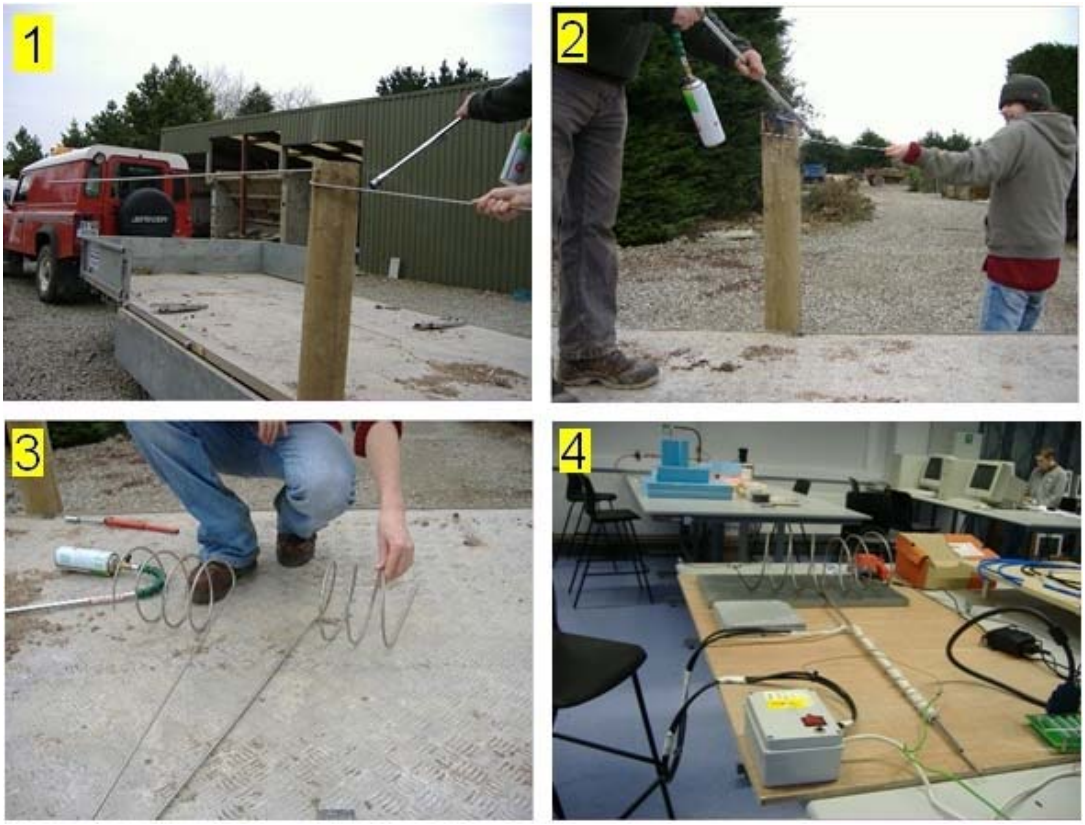

Figure 144 making the coils on the end of the stainless steel bars.

Appendix III-(B) Heat transfer calculations for designing and proofing.

Heat transfer estimations.

Before the concept of a high temperature wind tunnel had been envisaged the original concept was to build simple stand-alone testing device that would heat single MT-SOFCs or small stacks two 850°C. The following section deals with the calculations associated with inputting heat into the system and heat losses from various parts of the test rig. The aim of making these calculations was to gain a deeper understanding of what is going on in the system with regard to heat. The following section explains the theory behind the equations used in a MAT-LAB code contained in Appendix III-(E) Code used to estimate the temperature of the first attempt system.. The Matlab code listed in could have been written in any computer compiler program.

Lots of effort was put into the code to make it as easy as possible to read and in most cases the parameters are explicitly named in the units are shown on the right-hand side. Because many of the properties of air change in relation to temperature a lookup table was generated so that depending on the temperature of the wall of the pipe. It may be argued that this is not an accurate representation of the temperature gas but for the simple initial calculations this measurement was deemed good enough. This effect will be discussed more in the results section of this chapter.

The code was simply put into “for” and “while loops” to change certain parameters of the code which were essentially changing parameters of formulas discussed in the next section, which provided sets of results such as gas outlet temperature, losses through installation and in the effect of gas velocity on the outlook temperature of the pipes.

Symbol	Definition	Units
V	Voltage	Volts
I	Current	Amps
R	Resistance	Ohms
P	Power	Watts
q	Heat transfer rate	kJ/sec
L	length	meters
k	Thermal conductivity	W/ m K
Tw	Wall temperature	Deg C
Tb1	Inlet gas temperature	Deg C
Tb2	Outlet gas temperature	Deg C
Cp	Specific heat capacity	kJ/kg K
m	Mass	kg
S	Conduction shape factor	m
x	Wall thickness	m
W	Width	m
H	Height	m
di	diameter	m
Re	Reynolds number	No units

Pulse width modulation and heating tape power.

The heating tape (HSQ - 900 °C Horst Gmbh Germany) was wrapped around both the oxidant and fuel stainless steel inlet pipes. For the purposes of the following calculations each inlet pipe was considered separately. It is assumed that the heating tape is wrapped fully around each inlet pipe separately. Over a 6m length the power output of the heating tape is 1000 watts and the voltage applied is roughly 230 Volts.

$$I = \frac{P}{V} = \frac{1000}{230} \approx 4.34\_Amps$$

$$R = \frac{V}{I} = \frac{230}{4.34} \approx 50\_Ohms$$

With pulse with modulation only the current changes in the circuit, the voltage and resistance remain constant. The resistance of the heating tape changes slightly with varying temperature but at 900 °C the rated temperature of the heating tape is 1000 Watts. From experience it is suggested that when the heating tape is coiled around a small radius and under compact and relatively thick insulation the temperature of the heating tape rises up to values greater than 900 °C and this causes the mains switches to trip. It was found that a pulse with modulation value of 0.6 was sufficient to ramp up the temperature of the cables up to 850 ° C without any interruptions to the mains current supply or damage to the heating tapes. Table 11 below contains a list of the heating cable specifications.

Table 11. The heating tape's specifications.

Length	6M
Resistance	50 Ohms
Max power	1000W
Nominal temperature	900 Deg C
Minimum bending radius	10 mm

The amount of power that gets to the heating tape is controlled by pulse width modulation. The voltage stays constant as it comes from the mains and the resistance of the heating tape is assumed to stay constant. Therefore only the value of current

varies between 0 amps at 0 percent pulse width and 4.34 amps at 100 percent pulse width. So for example at 50 % pulse width the current is equal to 2.18 amps over any period of time doubled the pulse width.

The output of the heating tape is calculated from the following formula

$$Power = I^2 * R \qquad (1)$$

The power output to the heating tape is also determined by the length of the heating tape wrapped around the pipe. So for 1 m of tape wrapped around the pipes the output would be roughly $1/6^{th}$ of the total power output.

Heat losses through the insulation around the pipes

Figure 145 shows a side view and end view and the view without insulation of the pipes leading into the heating chamber. The side view image shows terms for the dimensions of the pipes and heated length (Ro, Ri & L), the mass flow rate through the pipe ($\dot{m}$), The heat supplied by the heating tape (Tw) and heat loss through the insulation (q insulation). The end view shows the orientation of the pipe wall, the heating tape wrapped around this and the insulation wrapped around both of these. The view without insulation shows the pipes leading into the heating chamber and the heating cables wrapped around the pipes. This system basically contains two pipes leading into a containment box. Both the pipes a containment box are insulated and this is explained in more detail further on.

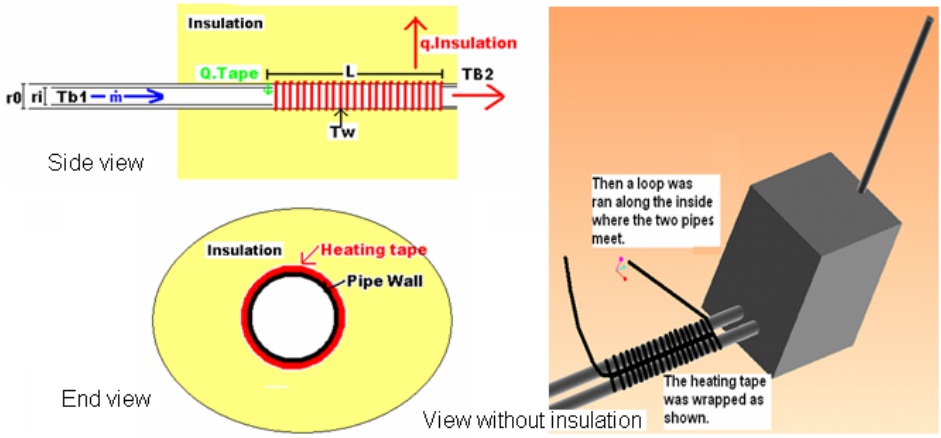

Figure 145 Side view end view and a view showing the system without any insulation.

To calculate the heat lost to the installation wrapped around the pipes the following equation is used [1]. The K value of the insulation was assumed to be 0.13 w/m.K, which is the value stated by the manufactures of (Superwool 607™ MAX Blanket Morgan Crucible company plc UK.) at 800°C.

$$q.insulation = \frac{2 * \pi * (q.tape / L.pipe\_with\_tape)}{\ln(ro/ri) \Big/ k.insulation} \qquad (2)$$

Where q.insulation is the heat loss through the installation (w), q.tape if the heat supplied by the heating tape (w), L.pipe_with_tape is the length of the heated part of the pipe (m) and ro and ri are the pipe inner and outer diameters (m). It is assumed that no heat is loosed through conduction in the steel pipe. An estimation of the wall temperature may be calculated through the following equation [1]

$$Tw = Tb1 + (q.tape - q.insulation \ /(Cp.steel * m.steel)) \qquad (3)$$

Where Tw is the pipe or temperature (°c), Tb1 is the temperature of the gas coming into the pipe (°C), q.tape is the heat generated by the heating tape (w) q.insolation is the heat lost through the installation, Cp. Steel is the specific heat capacity of the steel (J/kg.K) and M.steel is the mass of the steel pipe under the heating tapes (kg).

The addition of the reactor chamber.

Hydrogen or nitrogen will flow through a the second pipe and it will enter the fuel cell stack directly and exhausts out without really mixing in the chamber and therefore the heat it gives is not really relevant to the overall temperature of the chamber as it is assumed to flow at a rate $1/5^{th}$ of that of the air. It is assumed that the heated air that flows into the chamber is used to heat it up. The flow rate will roughly be 0.75 L/min for a stack containing 15 cells.

Heat loss through the insulation around the chamber

There will also be heat losses from the reactor chamber; it is calculated similarly to the heat losses around the heating tapes insulation. The conduction shape factor for a body can be calculated from the following equation [2],

$$q = K * S * \Delta T_{overall} \quad (4)$$

Where q is conducted energy (w). K is the thermal conductivity of the material (w/m.K) and Delta T is the temperature difference across the conduction region. Figure 146 below shows a diagram of the pipes leading into the system and the energy losses from the housing chamber itself. The characteristics of the insulated housing are also listed in the table in the figure.

Characteristics of the Insulation box

Length	0.12 m
With	0.09 m
Hight	0.12 m
Volume	0.013 Cubic meters
Wall thickness	0.004 m
Density	7870 Kg/ Cubic meter
Mass	2.26 Kg
K value for steel	0.45 W/m.K

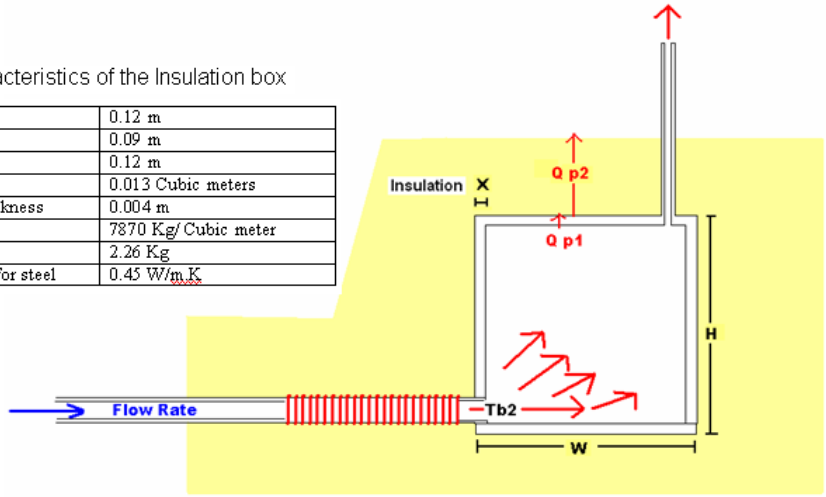

Figure 146. An illustration and characteristics of the insulation chamber.

The values for S (conduction factor) have been determined experimentally elsewhere and were extracted from [3].The insulation chamber is assumed to be constructed of 6 plates, 12 edges and 8 corners and of steel. From these characteristics the shape conduction factor can be calculated.

$$S\_for\_plates = 2 * \frac{L*W}{x} + 2\frac{W*H}{x} + 2\frac{L*H}{x} \quad (5)$$

$$S\_for\_edges = 4*(0.54*L) + 4*(0.54*W) + 4*(0.54*H) \quad (6)$$

$$S\_for\_corners = 8*(0.15*x) \quad (7)$$

$$S = S\_for\_plates + S\_for\_edges + S\_for\_corners \quad (8)$$

Where *x* is the wall thickness of the steel case and where L,W and H and the length width and height of the box. Please refer to Figure 146 to get an idea of the orientation of the box.

Calculating the temperature of the gas after being heated.

With any fluid or thermo-fluid problem the flow regime must be determined. The Re is the ratio of inertial forces ($v_s\rho$) to viscous forces (μ/L) and is used for determining whether a flow will be laminar or turbulent. Laminar flow, is when a fluid flows in parallel layers, with no disruption between the layers, turbulent flow is a flow regime characterized by chaotic, stochastic, property changes. The Re for this case is calculated as shown below and has no units. Using the Re plot it is possible to determine the flow regime. For the flow rates expected in the problem stated it was found that the regime is always laminar inside the heated inlet pipes even for elevated air temperatures to 850°C.

$$\mathrm{Re}.d = \frac{\rho * v.mean * di}{\mu.air} \quad (9)$$

Where ρ is the density (kg/m³), v mean is the mean velocity in the pipe (m/s), di is the internal diameter of the pipe and $\mu.air$ is the dynamic viscosity of air.

The Nusselt number is a dimensionless number which measures the enhancement of heat transfer from a surface which occurs in a 'real' situation, compared to the heat transfer that would be measured if only conduction could occur. Typically it is used to measure the enhancement of heat transfer when convection takes place. There are many different equations for calculation this number but due to the relatively small size of the inlet pipe for this calculation the following equation was found to suit [3].

$$Nu.d = 3.66 + \frac{0.0668 * \left(\frac{d}{L}\right) * \mathrm{Re}.d * \mathrm{Pr}}{1 + 0.04 * \left[\left(\frac{d}{L}\right) * \mathrm{Re}.d * \mathrm{Pr}\right]^{\frac{2}{3}}} \qquad (10)$$

The Pr term above is the Prandtl Number and it is a dimensionless number approximating the ratio of momentum diffusivity and thermal diffusivity, the ratio of thermal conductivity to volumetric heat capacity.

The convection heat transfer coefficient is defined in Newton's law of cooling [4]

$$q = h.A(Tw - T\infty) \qquad (11)$$

The heat transfer coefficient "h" (W/m².K) is normally calculated experimentally but can be estimated using the Nusselt number.

$$h = \frac{k}{d} * Nu.d \qquad (12)$$

The bulk temperature is the energy average fluid temperature across a tube. It can be calculated from the following [5].

$$\mathrm{Tb} = \frac{\int_0^{r0} \rho * 2 * \pi * dr * u * Cp * T}{\int_0^{r0} \rho * 2 * \pi * dr * u * Cp} \qquad (13)$$

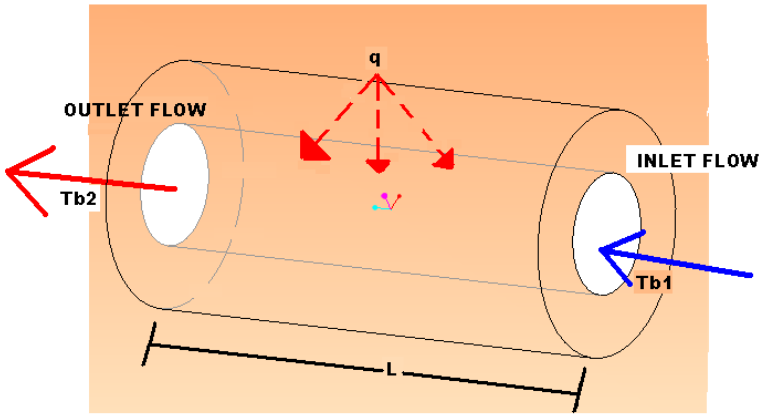

Figure 147 Flow of gas through a tube.

For the flow of gas through a tube as shown in Figure 147 above, the total energy added can be expressed (14) in terms of bulk temperature difference or in terms of the heat transfer coefficient. Where Tb1 is the inlet gas temperature and Tb2 is the outlet gas temperature L is the heated length of the pipe and d is the diameter of the pipe. This equation can be re arranged to give equation where the outlet temperature of the gas can be estimated as in equation (15).

$$q = h * \pi * d * L * \left(Tw - \frac{Tb1 + Tb2}{2} \right) = \dot{m} * Cp * (Tb2 - Tb1) \qquad (14)$$

$$Tb2 = \frac{2 * Tw + 2 * \frac{\dot{m} * Cp}{h * \pi * d * L} * (Tb1) - Tb1}{\left(1 + 2 * \frac{\dot{m} * Cp}{h * \pi * d * L} \right)} \qquad (15)$$

[1] Holman, J.P. *Heat Transfer.* 7th Edition in SI units(McGraw-Hill Book company, London, 1992), pp. 29-29.

[2] Holman, J.P. *Heat Transfer..* 7th Edition in S.I. Units(McGraw-Hill book company, London, 1992), pp. 77.

[3] Holman, J.P. .*Heat Transfer.* 7th Edition in S.I. Units(McGraw-Hill cook company, London, 1992), pp. 285.

[4] Holman, J.P. .*Heat Transfer*. 7th Edition in S.I. Units(MacGraw-Hill book company, London, 1992), pp. 11.

[5] Holman, J.P. *Heat. Transfer.* 7th Edition in S.I. Units(McGraw-Hill book company, 1992), pp. 257.

Appendix III-(C) Numerical Results and Comparison to Experimental Data

Results Related to Pipe Wall Temperature & Outlet Temperature.

Using the mat lab code in Appendix II (E) outlet temperature of the pipe when a 0.1 meter length of the inlet pipe was set to a range of values was simulated. Under an internal flow rate of air of 0.75 L/min air (room temp), it was found that for this low flow rate that no matter what the wall temperature up the pipe was the outlet temperature match this. This means that because the gas was travelling so slowly it had lots of time to absorb heat from the walls. However the amount of heat energy that would be transferred from the heated walls of the pipe to the stack reactor housing would be very low. In fact a quick calculation shows that the amount of energy provided by air ait this flow rate at 800°C is about 0.0034 kw/sec.

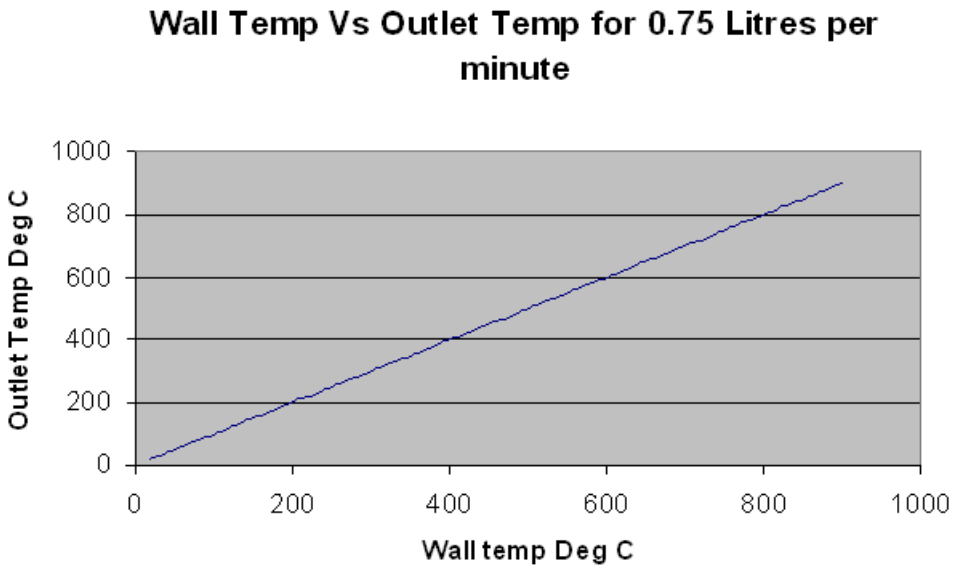

Figure 148: For a 0.75 l/min flow rate of air through the heated pipe the outlet temperature should always equal the pipe wall temperature.

If the flow rate of the gas is increased to 1 Litres per minute at the higher wall temperatures it can be seen that the difference in the wall and outlet gas temperature

can be seen. This means that the air does not get enough time to absorb enough energy from the heated walls to increase its temperature to that of the heated walls of the pipe.

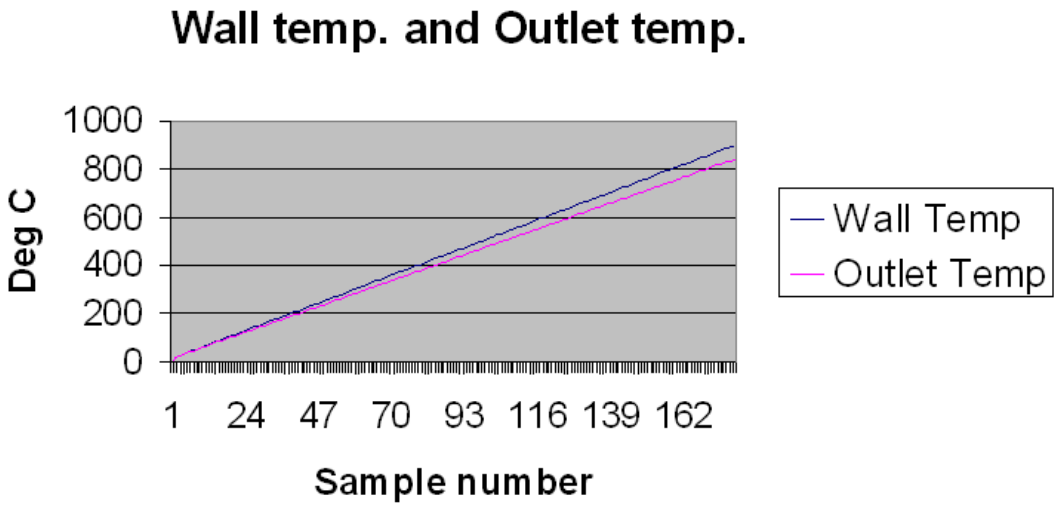

Figure 149 for a flow rate of 1 litre per minute the outlet gas temperature begins to drop off.

If the flow rate of the gas is increased to 2 litres/min the simulations suggest that the temperature of the gas at the outlet should be about 300°C lower than the wall temperatures of the pipe if they are maintained at 900°C. This result is shown below in a new Figure 1.

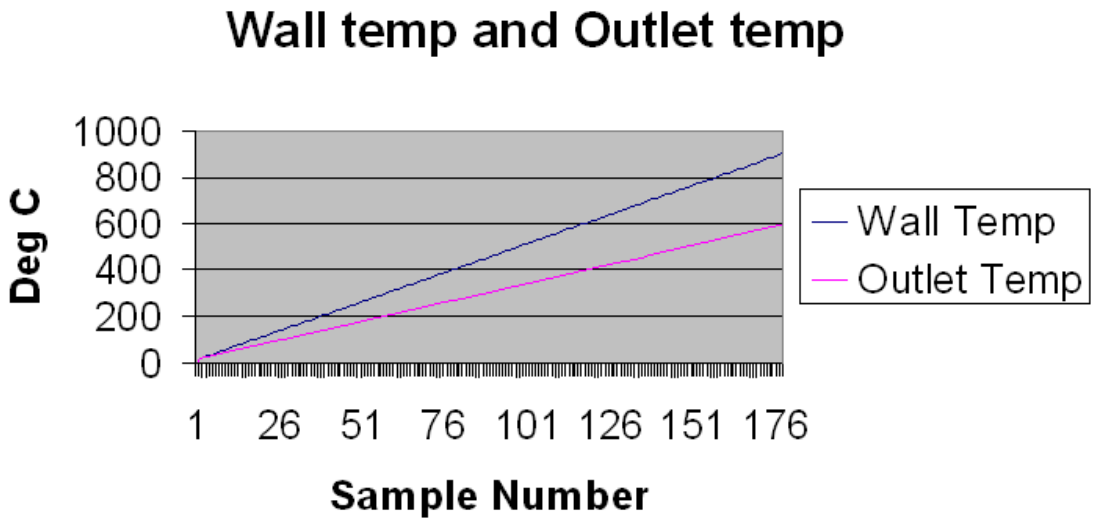

Figure 150 For a flow rate of 2 litres per minute the outlet gas drops well below the wall temperature.

The following simulation result shown in Figure 151, also for a flow rate of 2l/min shows, shows that if the heated length of the pipe is doubled to 0.2m in length that this reduction in temperature of the gas at the outlet is reduced to about 50°C. An interesting point to note is that at 2 litres per minute the air would supply about 0.0357 kw/sec of heat to the chamber at the end of the pipe.

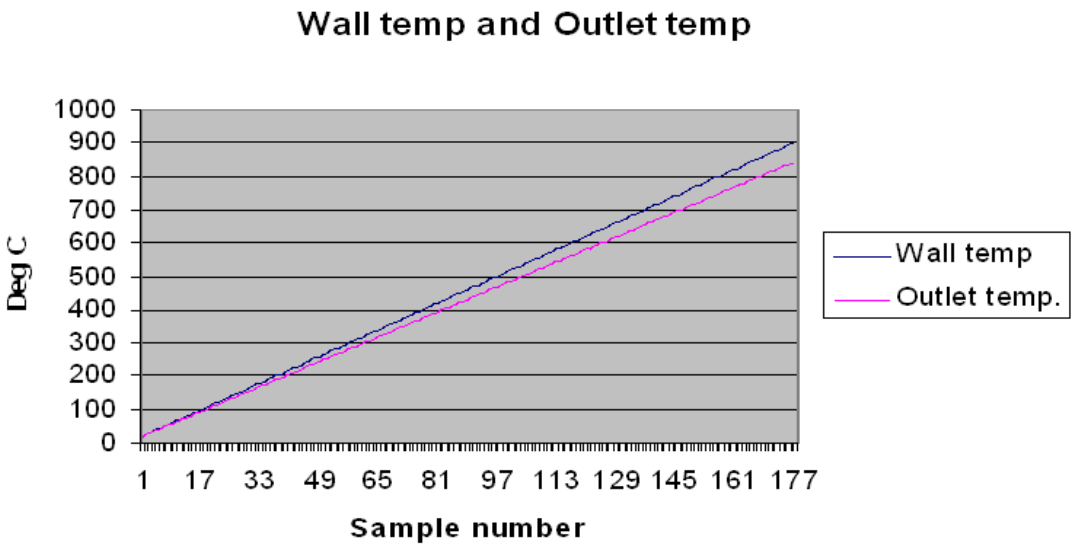

Figure 151 For a flow rate of 2 litres per minute the outlet gas drops only by a small amount below the wall temperature.

Discussion

For a flow rate of 0.75 litres per minute and for the tape wrapped over a length of 0.1m the heat transferred into the air would be sufficient to heat the air to the same temperature as the wall temperature of the pipe see Figure 148. However if the flow rate is increased even slightly the outlet air temperature begins to deviate from that of the wall temperature see Figure 149 and Figure 150. This is because the rate at which heat is being transferred into the pipe and then gas is fast enough to provide enough energy to heat the air up to the same temperature as the wall temperature.

The calculations indicate that for a flow rate of two litres per second the tape would have to be wrapped around the pipe over a length of 0.24m. The tape will wrap around a length of 0.68 m along the inlet pipes and the calculations suggest that the max flow rate that the whole tape could heat up to the same temperature to that of the wall temperature is 5.8 litres per minute. However if the maximum flow rate

available to heat the chamber is 5.8 litres per minute this would mean that 0.18 Kw/sec of heat energy could be transferred to the heating chamber.

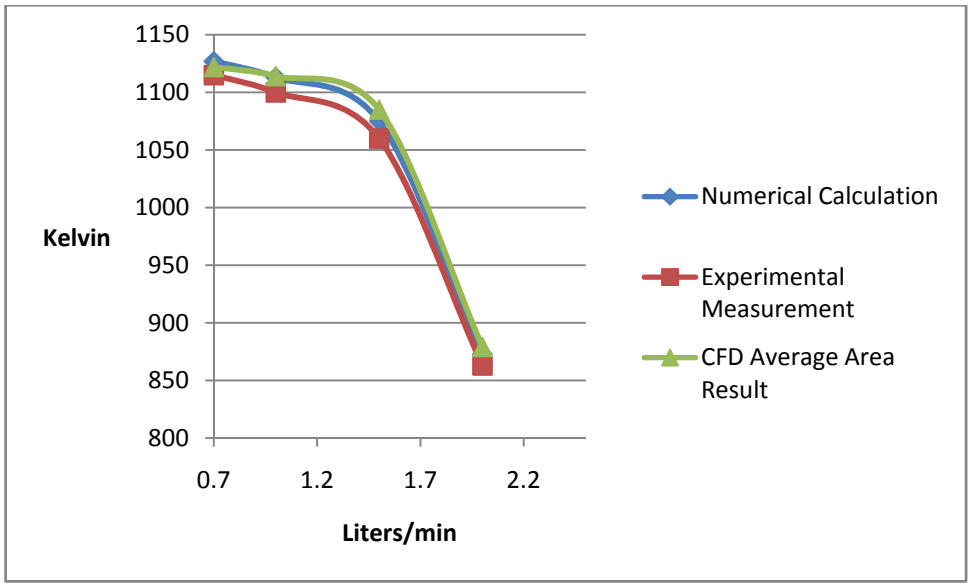

Figure 152: Comparison of experiment, numerical and a quick CFD simulation for the outlet temperature of the pips wrapped with heating tape and PID regulated 1127 Kelvin pipe wall temperature.

Conclusion

It seems extremely unlikely that at the assumed flow rates and required rise in temperature that the steel chamber will heat up at an acceptable rate. Indeed several quick tests were made to see if the reactor holding chamber could be heated up to anywhere near 850°C. It was found however that this was impossible in the temperatures in the heating chamber for flow rates up to 2 L per minute never even exceed 80°C. It is impossible that for such low flow rates that heating chamber could be heated up to 850°C.

The following plot illustrates the heat losses in the plant for 0.12m wall thickness around the chamber and for a radius 0.12m of insulation around the heating tapes. It can be seen that heat losses are greater from the insulation and heating tapes (cylinder) than from a shape such as the chamber (cubeoid). Please appendix II (E)

for the mat-lab code for this calculation and for more information on the formulas used.

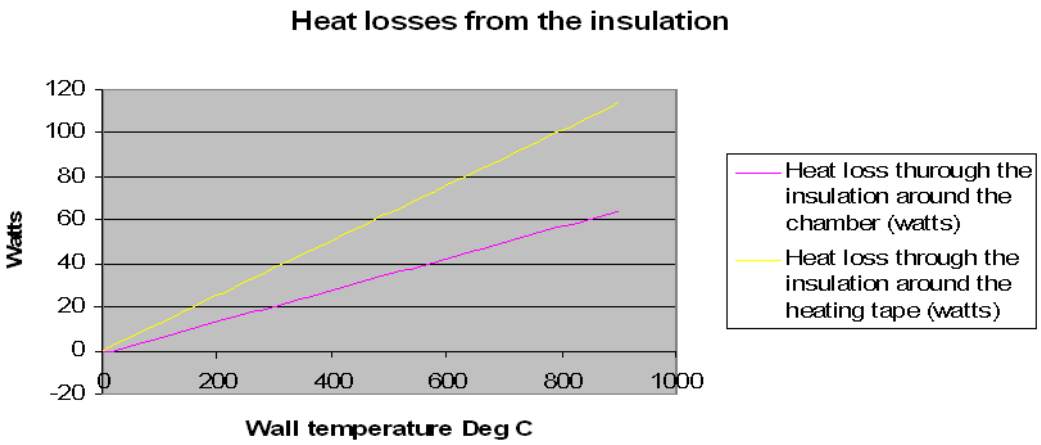

Figure 153 Heat losses through the insulation encasing the heated gas.

A further Quick calculation using the thermal energy transfer equation shows that if 2 L per minute of air at 900°C is feed to the reactor chamber the energy storage ability of the air is certainly too low to heat the chamber up to the required temperatures. Also using the thermal energy transfer equation a total of 1021 K watts is needed to heat 2.26 Kg of steel to 900°C and considering the losses from the isolation when the wall temperatures would be 900°C shown in Figure 153 not enough heat gets transferred to the air to increase the temperature of the reactor chamber to anything near the specified 850°C.

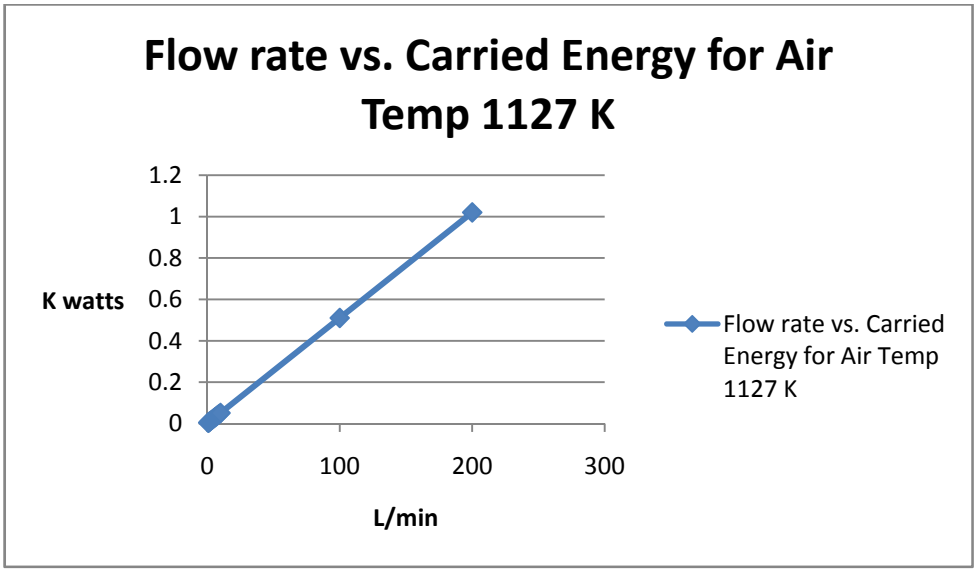

Figure 154: Simple calculation shows that to make the air deliver large amounts of energy high flow rates would be needed.

A final result of this section is that equation 15 maybe used to estimate the initial outlet temperature fall of the gas when the wall temperature of a heated pipe is know.

Implications of such a heating system on temperature control.

Even though the system described in the previous section would not work, some valuable information about the system heating properties relating to temperature control has been observed. A copy of the LabVIEW code that was used to control the heating tapes and thus the wall temperature of the pipe can be found in Appendix II (D).

Figure 155 and Figure 156 show some of the dynamic heating up and cooling down properties of the system. It would later be found and is described in section (XX) that the nonlinearity of the cooling down of the system means that a single set of PI and D terms for the PID controller to cover the temperature range from the room temperature to 850°C.

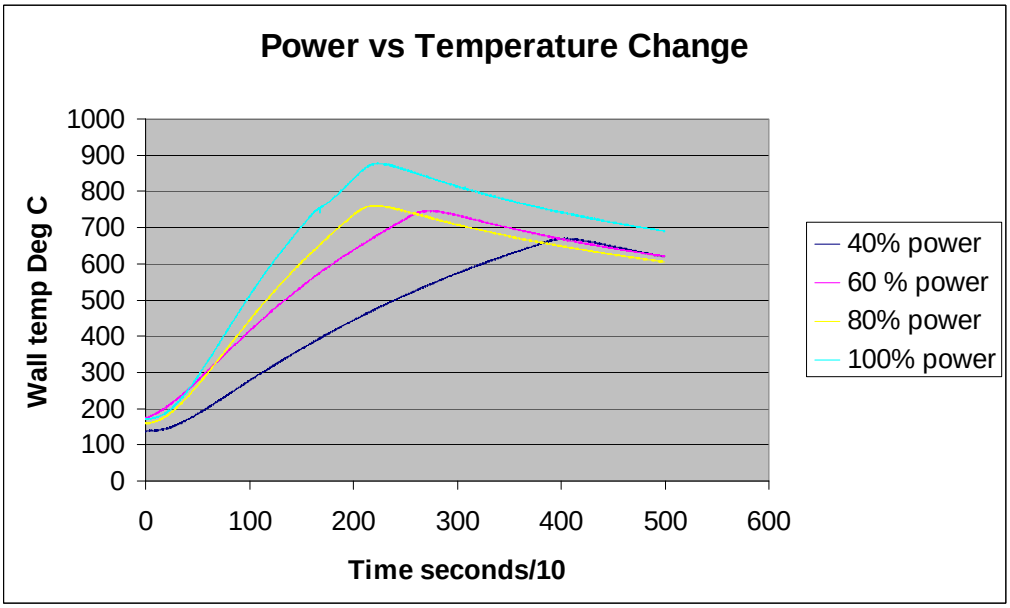

Figure 155 rates of change of temperature for zero flow rate and the heating tape wrapped around 0.68m of the pipes.

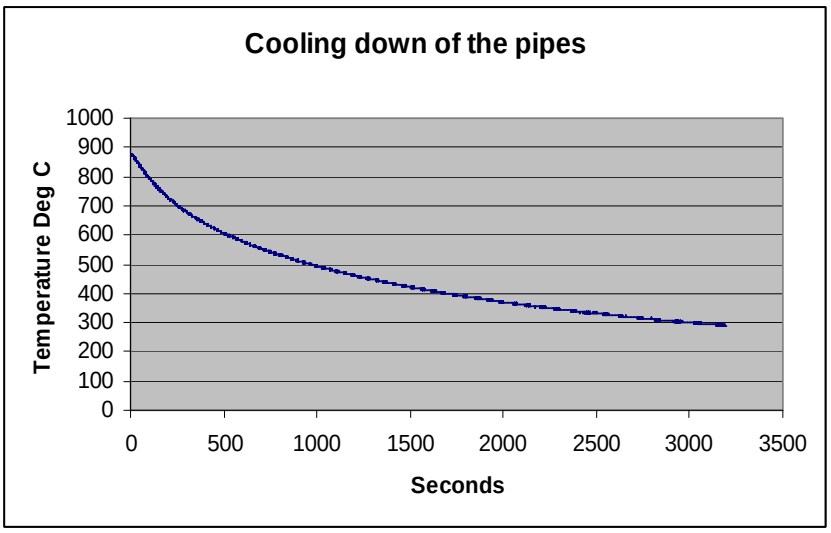

Figure 156 Shows how the pipes cool when no heat flux is applied over a period a time.

Appendix III-(D) Lab view code to control the experiments for initial design

A copy of the locking code used to control the very first inlet gas heated reactor housing. The code consists of reading and writing polling of flow controllers and called for the regulation of the PID control of the heating tape. Unfortunately at this period in time optimum parameters for the PID terms were not found in default terms provided by LabVIEW were used. The effect of these terms under the control system were +5 and –10°C meaning that the system was never properly tuned. Measurements were always taken when the sinusoid was around the -10°C because it tended to hover on this point for a longer period of time making it easier to take measurements.

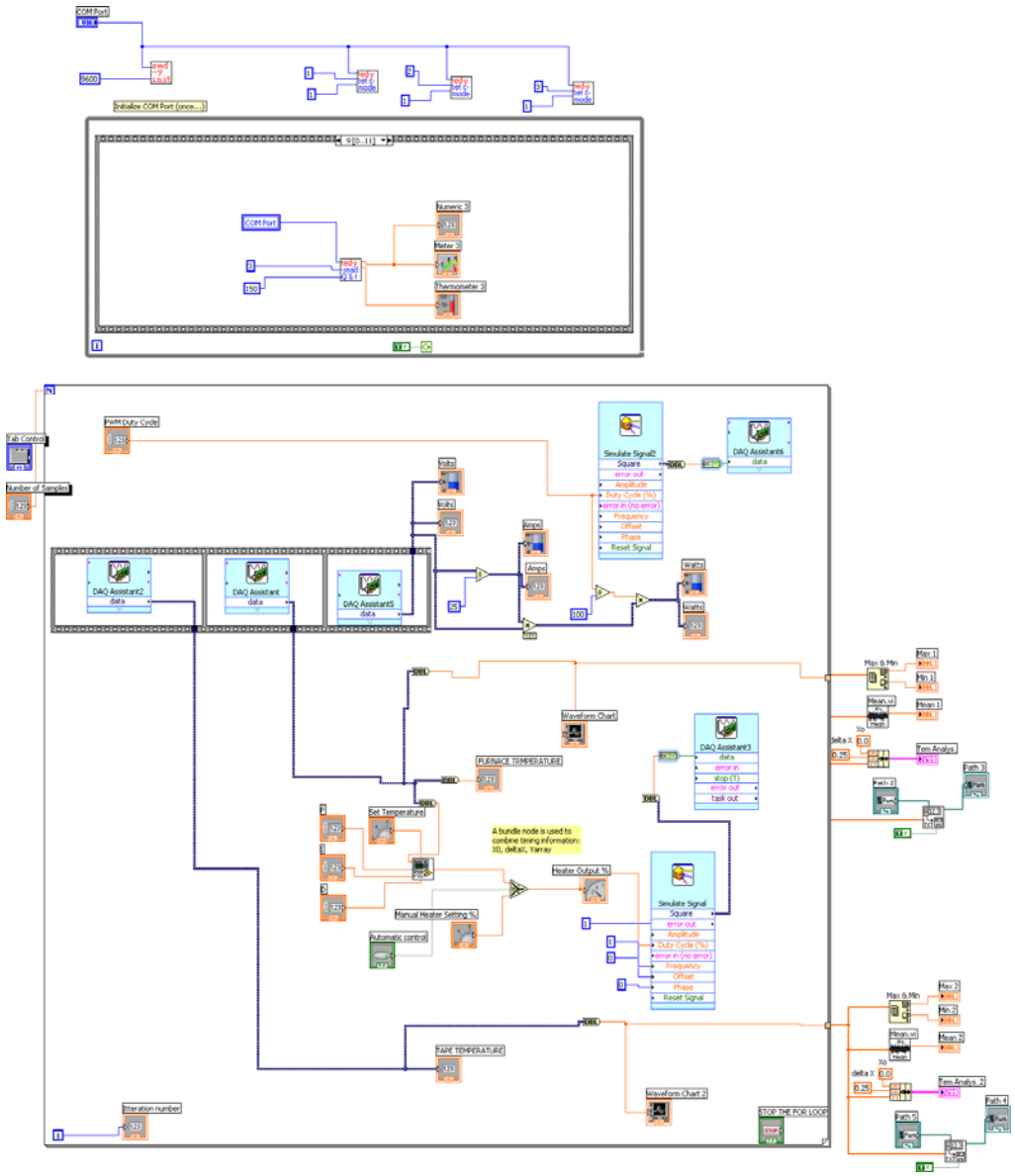
COM Port
9600
Initialize COM Port (once...)
COM Port
Numeric 3
Meter 3
Thermometer 3
PWM Duty Cycle
Tab Control
Number of Samples
DAQ Assistant2
DAQ Assistant
DAQ Assistant5
Simulate Signal2
DAQ Assistant6
Volts
Amps
Watts
Waveform Chart
FURNACE TEMPERATURE
DAQ Assistant3
Set Temperature
A bundle node is used to combine timing information: Xt0, deltaX, Yarray
Heater Output %
Manual Heater Setting %
Automatic control
Simulate Signal
TAPE TEMPERATURE
Waveform Chart 2
Iteration number
STOP TIME FOR LOOP
Max & Min
Mean.vi
Tem Analys
Path 3
Max & Min
Mean.vi
Tem Analys 2
Path 4
Path 5

Appendix III-(E) Code used to estimate the temperature of the first attempt system.

```
n=1

%-------------------------Constants--------------------------------
----


inlet_temp = 20         % deg C

flow_rate_Lmin= .75 %l/min

flow_rate_Lsec = flow_rate_Lmin/60      %L/s

diameter = .0052        %M

length_of_heating_tape_over_pipe = 0.1 %M


%-------------------------power to heating tape--------------------
---




% 1cm of coiled heating tape = 9cm of tape

actual_length_of_heating_tape = length_of_heating_tape_over_pipe*9

power_from_heating_tape_over_the_pipe=10




for wall_tempe=20:20:900


wall_temp = wall_tempe


%-------------------------To calculate the mean velocity

flow_rate_M = flow_rate_Lsec * .001
```

```
mean_velocity = flow_rate_M/((pi*(diameter/2)^2))



%-------------------------------------------------------------------
-------

%------------calculation of heat losses-----------------------------
-------

%-------------------------------------------------------------------
-------



%--------------------------heat loss through insulation-------------
-------------



r_inner=.01

r_outer=.2

k_for_insolation = 0.05

heat_loss_through_insolation                                        =
(2*pi*(power_from_heating_tape_over_the_pipe))/((log(r_outer/r_inner
))/(k_for_insolation))



%-------------------------------------------------------------------
-------

%------------picking  out  temperature  dependent  variables  from  a
table-----

%-------------------------------------------------------------------
-------



% -------------------------Inatilasing the values-------------------
-----
```

```
%          temp      density  Cp         dyn-visc  k-visc  k-val   pr_num
emisivity_air

 t = [  26.5      1.1774      1005.7      .0000185    .0000157    .0262
.708 .00002216;

        76.5      0.998 1009  .0000208     .0000208     .0300     .697
.00002983;

        126.5     0.8826      1014  .0000229   .0000259   .0337   .689
.00003760;

        176.5     0.7833      1020.7      .0000248    .0000317    .0337
.683 .00004222;

        226.5     0.7048      1029.5      .0000267    .0000379    .0371
.680 .00005564;

        276.5     0.6423      1039.2      .0000285    .0000443    .0404
.680 .00006532;

        326.5     0.5879      1055.1      .0000302    .0000513    .0436
.680 .00007512;

        376.5     0.543 1063.5      .0000318   .0000585   .0466   .682
.00008578;

        426.5     0.503 1057.2      .0000333   .0000663   .0495   .684
.00009627;

        476.5     0.4709      1085.6      .0000348    .0000739    .0523
.686 .00010774;

        526.5     0.4405      1098.7      .0000363    .0000823    .0578
.689 .00011959;

        576.5     0.4149      1095  .0000377   .0000908   .0603   .692
.00013097;

        626.5     0.3925      1121.2      .0000390    .0000993    .0628
.696 .00014271;

        676.5     0.3716      1132.1      .0000402   .000108     .0653
.699 .00015510;

        726.5     0.3524      1141.7      .0000415   .000118     .0675
.702 .00016779;
```

```
        826.5     0.3204      116   .0000444   .000139     .0732   .704
.0001969;

        926.5     0.2947      1179  .0000469   .000159     .0782   .707
.0002251;

        1026.5    0.2707      1197  .0000493   .000182     .0837   .705
.0002583;

        1126.5    0.2515      1214  .0000517   .000206     .0891   .705
.0002920]




if 1.45 < wall_temp <51.5


    density = t(1,2)

    specific_heat_capacity = t(1,3)

    viscosity = t(1,4)

    k_value = t(1,6)

    pr_number = t(1,7)

    emisivity_air = t(1,8)


elseif 51.5< wall_temp <=101.5


    density = t(2,2)

    specific_heat_capacity = t(1,3)

    viscosity = t(2,4)

    k_value = t(2,6)

    pr_number = t(2,7)

    emisivity_air = t(2,8)
```

```
elseif 101.5< wall_temp <= 151.5

    density = t(3,2)
    specific_heat_capacity = t(3,3)
    viscosity = t(3,4)
    k_value = t(3,6)
    pr_number = t(3,7)
    emisivity_air = t(3,8)

elseif 151.5< wall_temp <=201.5

    density = t(4,2)
    specific_heat_capacity = t(3,3)
    viscosity = t(4,4)
    k_value = t(4,6)
    pr_number = t(4,7)
    emisivity_air = t(4,8)

elseif 201.5< wall_temp <=251.5

    density = t(5,2)
    specific_heat_capacity = t(5,3)
    viscosity = t(5,4)
    k_value = t(5,6)
    pr_number = t(5,7)
    emisivity_air = t(5,8)
```

```
elseif 251.5< wall_temp <=301.5

    density = t(6,2)
    specific_heat_capacity = t(6,3)
    viscosity = t(6,4)
    k_value = t(6,6)
    pr_number = t(6,7)
    emisivity_air = t(6,8)

elseif 301.5< wall_temp <=351.5

    density = t(7,2)
    specific_heat_capacity = t(7,3)
    viscosity = t(7,4)
    k_value = t(7,6)
    pr_number = t(7,7)
    emisivity_air = t(7,8)

elseif 351.5< wall_temp <=401.5

    density = t(8,2)
    specific_heat_capacity = t(8,3)
    viscosity = t(8,4)
    k_value = t(8,6)
    pr_number = t(8,7)
    emisivity_air = t(8,8)
```

```
elseif 401.5< wall_temp <=451.5

    density = t(9,2)
    specific_heat_capacity = t(9,3)
    viscosity = t(9,4)
    k_value = t(9,6)
    pr_number = t(9,7)
    emisivity_air = t(9,8)

elseif 451.5< wall_temp <=501.5

    density = t(10,2)
    specific_heat_capacity = t(10,3)
    viscosity = t(10,4)
    k_value = t(10,6)
    pr_number = t(10,7)
    emisivity_air = t(10,8)

elseif 501.5< wall_temp <=551.5

    density = t(11,2)
    specific_heat_capacity = t(11,3)
    viscosity = t(11,4)
    k_value = t(11,6)
    pr_number = t(11,7)
    emisivity_air = t(11,8)
```

```
elseif 551.5< wall_temp <=601.5

    density = t(12,2)
    specific_heat_capacity = t(1,3)
    viscosity = t(12,4)
    k_value = t(12,6)
    pr_number = t(12,7)
    emisivity_air = t(12,8)

elseif 601.5< wall_temp <=651.5

    density = t(13,2)
    specific_heat_capacity = t(1,3)
    viscosity = t(13,4)
    k_value = t(13,6)
    pr_number = t(13,7)
    emisivity_air = t(13,8)

elseif 651.5< wall_temp <=701.5

    density = t(14,2)
    specific_heat_capacity = t(1,3)
    viscosity = t(14,4)
    k_value = t(14,6)
    pr_number = t(14,7)
    emisivity_air = t(14,8)
```

```
elseif 701.5< wall_temp <=751.5

    density = t(15,2)
    specific_heat_capacity = t(15,3)
    viscosity = t(15,4)
    k_value = t(15,6)
    pr_number = t(15,7)
    emisivity_air = t(15,8)

elseif 751.5< wall_temp <=801.5

    density = t(16,2)
    specific_heat_capacity = t(1,3)
    viscosity = t(16,4)
    k_value = t(16,6)
    pr_number = t(16,7)
    emisivity_air = t(16,8)

elseif 801.5< wall_temp <=851.5

    density = t(16,2)
    specific_heat_capacity = t(16,3)
    viscosity = t(16,4)
    k_value = t(16,6)
    pr_number = t(16,7)
    emisivity_air = t(16,8)
```

```
elseif 851.5< wall_temp <=901.5

    density = t(17,2)
    specific_heat_capacity = t(1,3)
    viscosity = t(17,4)
    k_value = t(17,6)
    pr_number = t(17,7)
    emisivity_air = t(17,8)

elseif 901.5< wall_temp <=951.5

    density = t(17,2)
    specific_heat_capacity = t(1,3)
    viscosity = t(17,4)
    k_value = t(17,6)
    pr_number = t(17,7)
    emisivity_air = t(17,8)

elseif 1001.5< wall_temp <=1051.5

    density = t(18,2)
    specific_heat_capacity = t(18,3)
    viscosity = t(18,4)
    k_value = t(18,6)
    pr_number = t(18,7)
    emisivity_air = t(18,8)
```

```
    else 1051.5< wall_temp <=1101.5


    density = t(18,2)
    specific_heat_capacity = t(18,3)
    viscosity = t(18,4)
    k_value = t(18,6)
    pr_number = t(18,7)
    emisivity_air = t(18,8)
end




%-------------------------To calculate the mass flow rate-----------
-------
mass_flow_rate = density*mean_velocity*((pi*diameter^2)/4)


%-------------------------To calculate the h_value-----------------
-------
re_number = (density*mean_velocity*diameter)/viscosity


nu_number                  =                  3.66                  +
(((0.0668)*(diameter/length_of_heating_tape_over_pipe)*(re_number*pr
_number))/(1+(0.04*((diameter/length_of_heating_tape_over_pipe)*re_n
umber*pr_number)^(2/3))))


h_value = ((k_value*nu_number)/diameter)
```

```
%--------------------------The outlet temperature-----------------
-------

a = (2)*(wall_temp)



b
=(2)*((mass_flow_rate)*(specific_heat_capacity))/((h_value*pi*diamet
er*length_of_heating_tape_over_pipe))*(inlet_temp)




outlet_temp_of_air_numerator = a + b -(inlet_temp)



outlet_temp_of_air_denomenator                                    =
(1)+((2)*(mass_flow_rate*specific_heat_capacity)/(h_value*pi*diamete
r*length_of_heating_tape_over_pipe))




OUTLET_TEMP=
outlet_temp_of_air_numerator/outlet_temp_of_air_denomenator



%------if the temperature of the gas = the wall temperature then
there exists no way for more heat to be transfered

%      and so temp wall = temp of gas



if OUTLET_TEMP > wall_temp

    OUTLET_TEMP=wall_temp

end



%-------------------------heat loss from around the heating tapes
through

%insulation
```

```
r_inner=.01

r_outer=.12

k_for_insolation = 0.05

heat_loss_through_insolation                                    =
(2*pi*(wall_temp))/((log(r_outer/r_inner))/(k_for_insolation))


%----------------------------area and volume of the box

temp_dif_between_box_and_insolation=1

density_of_box = 7870

k_for_iron = 73

specific_heat_capacity_of_iron=0.45

box_length =  .090

box_with   =  .120

box_height  =  .120

wall_thickness_of_box=.004

volume_of_box = box_length*box_with*box_height

capacity_of_box = volume_of_box/1000 % 1000 = conversion factor m^3
to meter

time_to_fill_box = capacity_of_box/flow_rate_Lsec



total_area_of_box        =        (2*(box_length*box_with))        +
(2*(box_with*box_height)) + (2*(box_length*box_height))

mass_of_box                                                     =
(total_area_of_box*wall_thickness_of_box)*(density_of_box)


%----------------------------calculating the thermal conductivity--
-------
```

```
heat_transfer_rate=(OUTLET_TEMP-
inlet_temp)*((k_for_iron*total_area_of_box)/(wall_thickness_of_box))



S_for_6_plates   =(2*(box_length*box_with)/wall_thickness_of_box)   +
(2*(box_with*box_height)/wall_thickness_of_box)                     +
(2*(box_length*box_height)/wall_thickness_of_box)

S_for_12_edges                                                      =
(4*(0.54*box_length))+(4*(0.54*box_with))+(4*(0.54*box_height))

S_for_8_cornors = 8*(0.15*wall_thickness_of_box)



total_shape_factor_steel_box=S_for_6_plates+
S_for_12_edges+S_for_8_cornors



Heat_flow_from_insolation                                           =
k_for_iron*total_shape_factor_steel_box*(OUTLET_TEMP-(OUTLET_TEMP-
10))



wall_thickness_of_insolation = .12



S_for_6_plates_insolation
=(2*(box_length*box_with)/wall_thickness_of_insolation)             +
(2*(box_with*box_height)/wall_thickness_of_insolation)              +
(2*(box_length*box_height)/wall_thickness_of_insolation)

S_for_12_edges_insolation                                           =
(4*(0.54*box_length))+(4*(0.54*box_with))+(4*(0.54*box_height))

S_for_8_cornors_insolation = 8*(0.15*wall_thickness_of_insolation)
```

```
total_shape_factor_insolation=S_for_6_plates_insolation+
S_for_12_edges_insolation+S_for_8_cornors_insolation


Heat_flow_from_insolation                                          =
k_for_insolation*total_shape_factor_insolation*(OUTLET_TEMP-
inlet_temp)


%---------------------------heat transfer from air to the chamber

gas_temp=OUTLET_TEMP

absorbavity_air =emisivity_air

boltzmanns_constant =.000000056704

bwall_temp=gas_temp-10

heat_flow_air_box                                                  =
(total_area_of_box*(emisivity_air*gas_temp*boltzmanns_constant*(gas_
temp)^4))-
(total_area_of_box*(absorbavity_air*bwall_temp*boltzmanns_constant*(
bwall_temp^4)))


n=n+1


output(n,:)=
[OUTLET_TEMP,heat_flow_air_box,Heat_flow_from_insolation,heat_loss_t
hrough_insolation]


end
```

Appendix IV: Development of a single inlet singlet outlet manifolding system.

Title: Method to fuel a Micro Tubular Solid Oxide Fuel Cell that combines, heat exchange, current collection and can increase the overall efficiency of any stack design that incorporates it and sample stack designs.

(Patent Pending)

Background

Solid Oxide Fuel Cells are devices that convert hydrogen enriched fuels into electricity electrochemically. They consist of three layers a cathode, an electrolyte and an anode. They operate at high temperature in the range of 850 Deg C. An oxygen enriched gas is fed to the cathode where at triple phase points, where a catalyst, an electrical contact to an external circuit and an oxygen meet, each oxygen gains two electrons and becomes an oxygen ion. This ion is conducted through the solid electrolyte and pass through to the anode, where at triple phase points there, requiring 2 oxygens, a hydrogen and a nickel catalyst and electrical contact to the external circuit all to meet, a water molecule is formed and in the process electrons are released that are free to do work. These electrons generated on the anode side are fed through an external circuit that will be loaded and they flow from the anode to the cathode. These electrons are driven by the voltage generated between the negative and positive electrodes. This voltage is a function of the Nernst equation, which provides a relationship between the ideal standard potential for a cell reaction and the ideal equilibrium potential at other partial pressures of reactants and products. For the overall cell reaction, the cell potential increases with an increase in the partial pressure, gas concentration of the reactants and/or a decrease in the partial pressure of products.

SOFCs are becoming of ever more interest to both the academic and industrial sectors because of several key characteristics. Firstly the materials required to build the cell components are relatively cheap compared to other types of fuel cell

that for example require platinum catalysts. They also have the possibility of being substantially more efficient than both the combustion based engines and indeed other types of fuel cells and can even be coupled with Stirling engines and gas turbines. Operating at high temperatures also increases the types of fuels that can be used because to use fuels such as methane, wood gas and petrochemicals they have to be reformed at temperatures above 700 Deg C. Both the fact that the heat produced by the SOFC can be used in this reforming process and because the cells themselves can internally reform the fuel makes them much more resilient and versatile to fuels other than pure hydrogen.

The Micro Tubular-SOFC (MT-SOFC) is a variation of the larger SOFC and they have only recently been going through a R&D phase by about 10 different institutions around the world. The MT-SOFCs have diameters that are the size of needles (sub mm) up to cells that are 1cm in diameter. They operate exactly the same as the large type but have several key advantages that make them even more attractive. As they are much smaller they can be started up extremely fast. The most impressive start-up times have been shown by Bujalsk et al. [1]. This makes them attractive for auxiliary power units and maybe even vehicle power. Tompsett et al. [2] have highlighted many ways that a MT-SOFC can be integrated into devices such as electric wheel chairs, lawn mowers and camping cooking apparatus. For more information on the MT-SOFCs and the current level of stack and manifold designs please see the review paper by Lawlor et al. [3]. In the conclusions of this review paper it is clear the MT-SOFC, while becoming more attractive, is largely over shadowed R&D wise by its large predecessor. This means that there should be a wide range of patentable possibilities with regard to stack design, fuel and oxidant manifolding, current collection methods and control methods. A last introductory point that is worth noticing is that it is very possible that when it comes to manifold and stack design that the first patents could be simply the single best way to perform certain functions.

Reason for and description of the idea.

The following idea that is believed to be patentable is related to the manifolding of fuel to the anode and a combined current collection system. The idea has come from the work of the applicant during the past two years and has been developed and briefly tested during the past few months. Normally the MT-SOFCs tested by the previous fuel cell group led by Prof. Dieter Meissner and presently by Dr. Gerhard Buchinger were fuelled with a "fuel in one end of the anode" and "exhaust out the other end" method when testing in large ovens. However the applicant has found that this method is unsatisfactory when the cells are placed in enclosed small spaces.

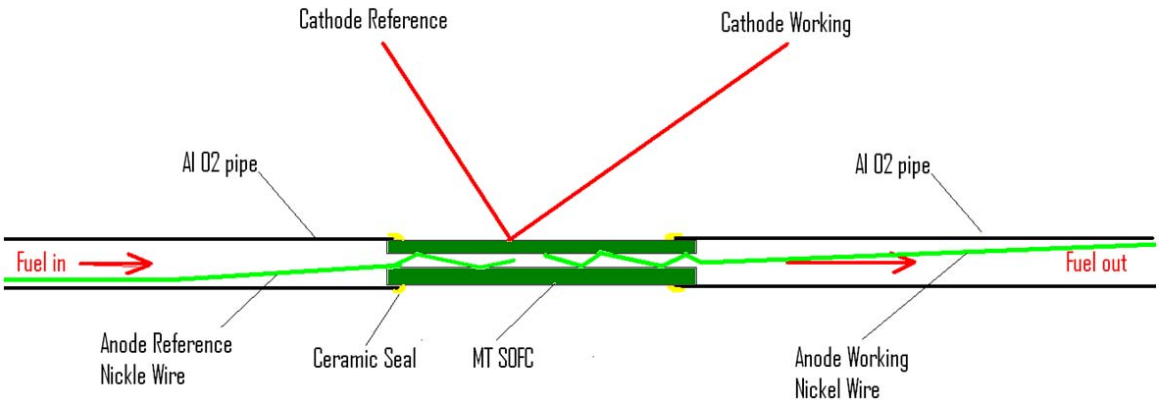

Figure 157: Normal method to fuel and collect current from a cell.

This is a key point considering that to be highly efficient the stacks of cells should be thermally self sufficient. It was found that even though a small test chamber was heated up to 825 Deg C that the cells only performed as expected up to 25% of their optimal fuel flow rate. For flows above this it was found the power output of the cells decreased. Tests have indicated that this is because the extra heat removed by the increased fuel flow. Decreasing the temperature of a MT-SOFC dramatically reduces the ionic transfer through the electrolyte and the quantity of the red-ox reactions taking place.

The solution to the loss in temperature from the cell has been to use the cell outlet gas to heat the incoming fuel gas by inserting a stainless steel capillary pipe

that has been grinded in a specific way to avoid blocking the cell while also making a tight connection to the anode. This means that the current produced by the anode can be collected by the fuel manifold. The proposed patentable solution is shown below.

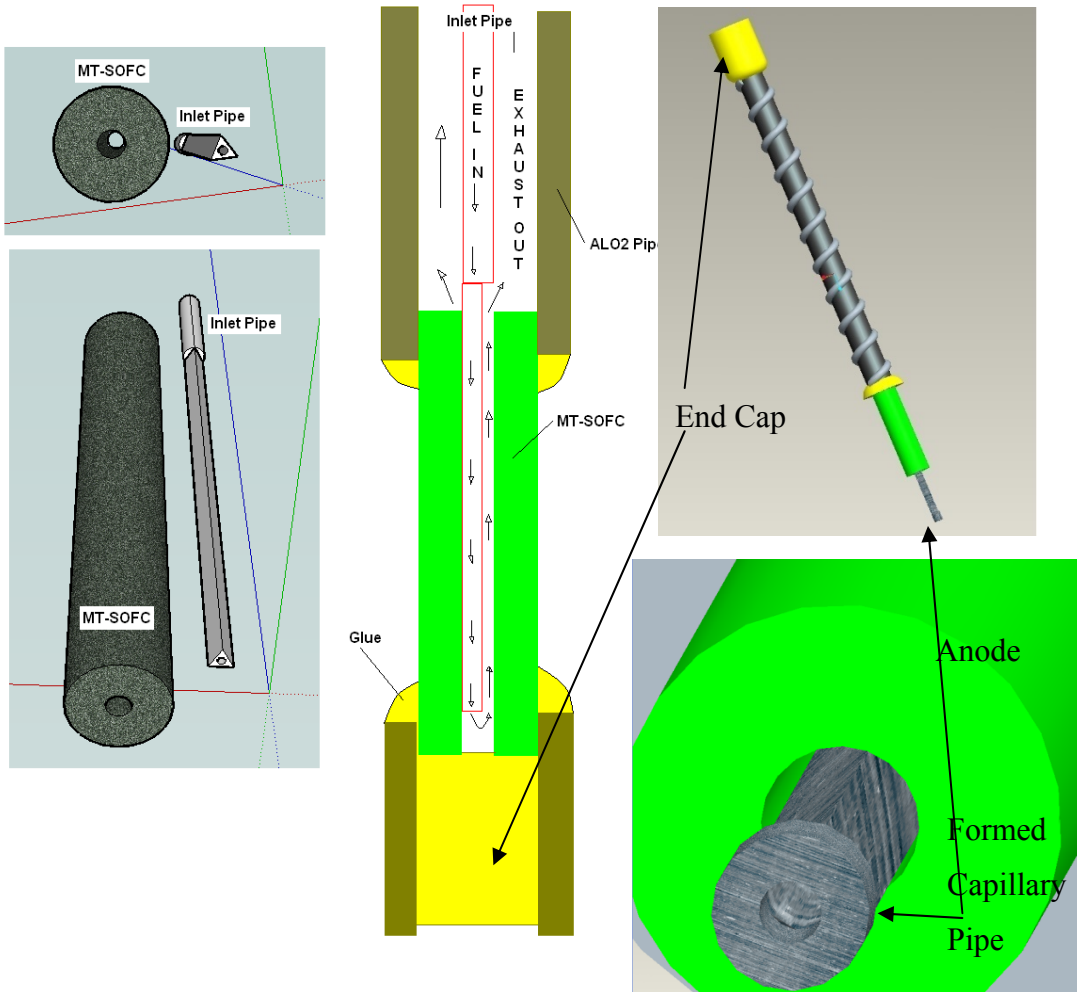

Figure 158: Proposed patentable method to collect current from the anode while fuelling it in a way that reduces temperature losses.

The method proposed is the first method that worked with in the SOFC group in Wels and is the first suggested in both the literature for MT-SOFCs under 3mm in diameter. Another similar method have been proposed by Lee et al. [4], but their method is for cells on the scale of cm and they use a nickel felt and extra wires to make sure that the cell does not become blocked. The proposed method does not involve any other features than the capillary pipe which could make it ideal for mass manufacture.

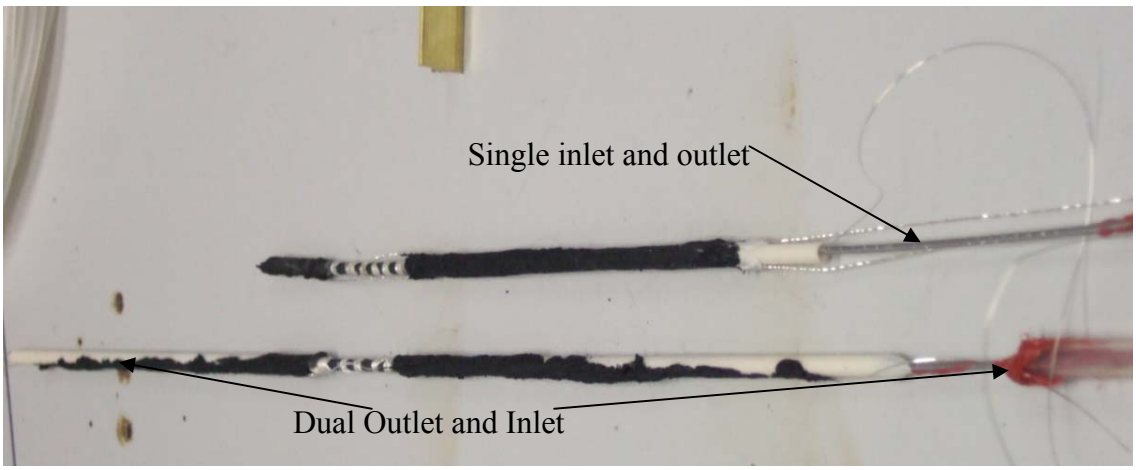

Figure 159 Picture with a single inlet and outlet fuelling design and the dual inlet outlet design.

Suggested Development

The applicant sees this simple first attempt as the first concept that can be developed in several ways that could increase the value of any patent with either included clauses or indeed following patents.

- The first suggestion is to change the material of the capillary pipe to nickel or copper because of their excellent performance in a reducing environment and stainless steels inherent chromium poisoning effect.

- The second suggestion is to put an oxide coating on the capillary pipe so that both the anode working and reference can be held inside the fuel exhaust pipe. Meaning that if the capillary pipe is coated then the reference wire will not touch the working capillary pipe which is important for an accurate voltage reference value. It may also be possible to use a coated exhaust pipe with sections that connect to the anode that are conductive on the inside of the pipe with points that could be connected to at the other end of the pipe. Methods like this should be very interesting for easy manufacture.

- The third suggestion is to reverse the flow of the fuel, i.e. To feed the fuel through the larger formally named exhaust pipe and force the fuel to exhaust through the capillary pipe. This would increase the pressure in the anode which should also increase the cells performance as shown as S. Hashimoto et al. [5] who used another method to increase the pressures in the anodes.

These ideas could be of interest to MT-SOFC companies around the world and as the idea is fundamental, a good patent could force these companies to pay to use this method. The applicant is of the opinion that they will discover this method is necessary especially for cells in the 3mm diameter up to 1cm diameter when they try to make thermally self sustaining reactors. There are not any reports in the literature of experiments or simulations with the aim of achieving a thermally self sustaining reactor. Also eZelleron Gmbh linked to Dr. Gerhard Buchinger and FHÖO Campus Wels may also have some interest in such patents.

Development of the idea to make a larger reactor.

To increase the purpose of the patent it was suggested that the afore mentioned design should be developed into a multi cell system. The basic concept is that instead of the fuel and exhaust going in one end of the cell and out the other it should leave at the same end of the cell as it enters. Two concepts have been developed that are distinctively different but are based upon this simple principle.

When designing a MT-SOFC reactor the electrical connections between each cell are an important consideration. The cells may be connected in parallel or series just like batteries however serial and parallel MT-SOFC connections have advantages and disadvantages. Connecting the cells in Parallel causes the voltage to remain the same. But the current produced increases incrementally from cell to cell. High currents passing through the connection wires is an undesirable feature of parallel connection of MT-SOFCs at high temperatures as the resistance of the wires increases with temperature.

The alternative is to connect the cells in series and while this may seem more desirable by reducing the high currents passing through the wires the drawback is that should one cell cease to function or should a connection between the cells disconnect then all the cells in series will stop working. This means that a combination of Parallel and Series connections will be the most likely solution and also the capabilities and costs of any power electronics such as inverters should be considered. In an effort to apply the single in single outlet approach to the series and parallel connection problem the following two designs are proposed.

Design A: Parallel connection design.

This design as seen in Figure 160 incorporates a novel approach to the problem of providing each cell with its appropriate supply of oxygen as within an air supply. In this design each cell has its own regulated control path that can be made of Crofer, Allochrome or Conichrome. These are materials that are easy to weld and have low chromium evaporation attributes which is important to prevent poisoning of the cells. So that each cell receives the same amount of oxidant the end caps on the cells, as can be seen in Figure 162, can be used to build up some pressure in the oxygen inlet at the top of the cells. This should work then like a shower head whereby the same amount of or passes by each cell no matter where it is located in the bundle. The oxidant inlets via the cell end caps and exhausts at the bottom of the cells. This zone where the air exhausts may be a good position for a heat exchanger to heat up the incoming oxidant and fuel flows with some simple apparatus and redirecting of the inlet pipes.

The hydrogen/fuel supply can be sent in through the capillary pipes connected to the H2 inlet pipe as seen in Figure 162. These pipes should all be electrically connected to each other forming the anode side parallel connection. This connection can easily be made within the larger supply pipe where are the pipes are joined by a soldering technique. The cells can be sealed to hydrogen containment chamber with ceramic or glass seals that are either spot seals or a sheet that is formed around all of the cells. Another option would be a silver seal whereby each cell is connected to the others in parallel via this seal either through the hydrogen containment chamber or

through a separate plate. The Allochrome and Conichrome materials are high temperature resistant steals that form coatings on their outer surfaces that do not conduct electricity. Corofer on the other hand is also a High temperature resistant steal but it forms a highly conductive layer on its outer surface. Using a combination of these materials which may also be welded together the reactor body should be built. Another way to make the electrical connections on the cathode side would be to simply take the electrical wires out through the air inlet holes and then out through the air in pipe. An example of how the current can be taken from the cell is shown below in Figure 161.

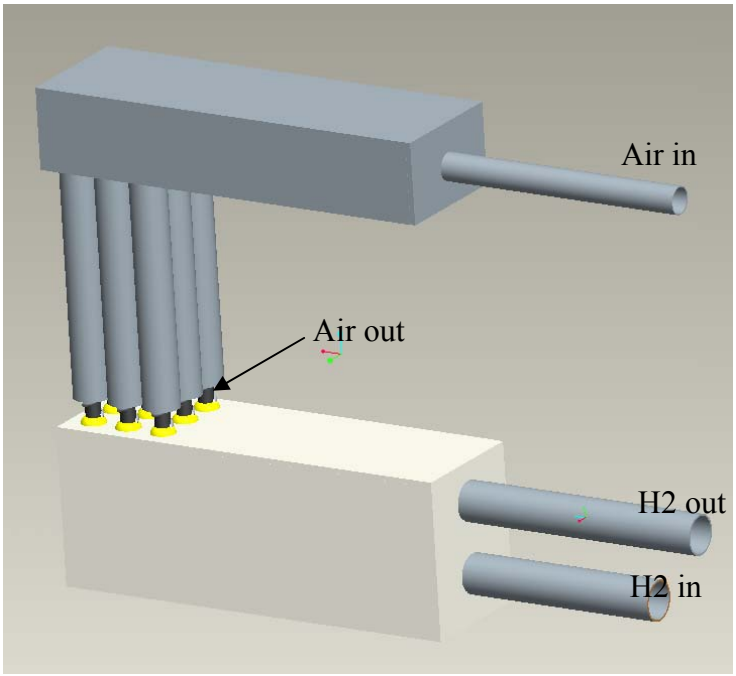

Figure 160: Outer view of the parallel connected MT-SOFC stack module.

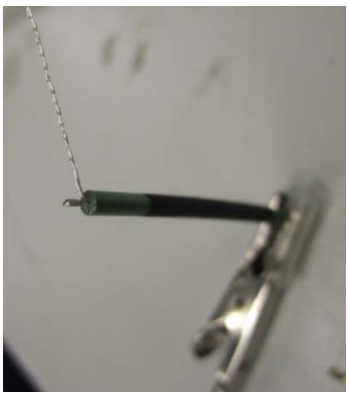

Figure 161 The current can be taken from the cell by blocking the end of the cell with a nickel pin thus jamming the silver wire into the cell. A glued cap is then placed over this.

Because these wires will inevitably carry large currents regulation of the stack voltage must be performed via a four point measurement. This means that at least one cell per module must have a separate two electrical connections and two probe wires. This could also be done for every cell but increases the complexity of the design many times. The anode side probe wires can be wrapped around the open anodes inside the hydrogen basin, these wires can be coated and they can be fed out through the H2 outlet. With regard to the cathode side probes by using individual wires fed out through the holes in the air inlet basin and out through the air inlet pipe for the reference and using a conductive crofer plate or the H2 basin itself or with an electrical surface coating in contact with the cathodes the electrical connections can be made to the cathode. It should be noted that both the air and hydrogen supplies can be reversed to increase the pressure on the anode and cathode sides. Such an approach would be a very novel MT-SOFC reactor design.

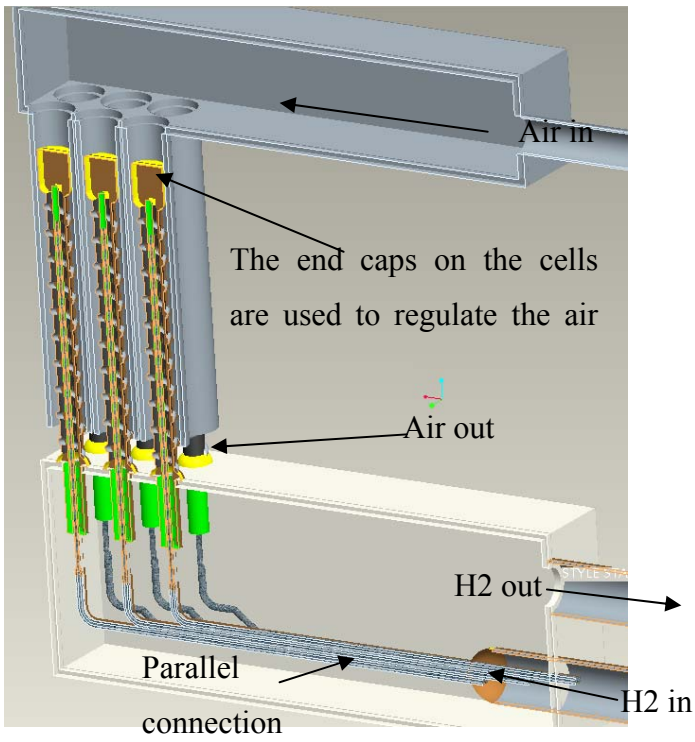

Figure 162: Section view of the Parallel MT-SOFC module sown in Figure 161.

Design B: Serial connection design.

The serial connection design is quite similar to the previous parallel connection design and the two may indeed be incorporated with some minor changes. Seen below in Figure 163 is the serial connection method. The red pipes are the anode capillary pipes that carry the flow downwards through the pipes and back up into the cells as can be seen more clearly in the sectional view on Figure 164. The flow through the cells is the same as depicted in Figure 158. What is unique about this design is that the serial connection is made from the cathode to the capillary pipe with small plates that are connected to the capillary pipe and cathode via a silver braze. In this way the current flows in serial from cell to cell and the voltage is increased rather than the current and this will reduce the ohmic losses through the wires. If we take for example the first row. The first red pipe on the left side of the picture is connected to the anode of the first cell. The cathode of this cell is connected to the anode of the next through the capillary pipe via an inter-connect. This connection is used for the remaining cell on this line. If wires are connected to the anode connection on the far left and cathode on the far right we would have a

series of fuel cells. These serial stacks can then be connected in serial to the other rows of cells and then these modules can connected in serial and parallel to other modules.

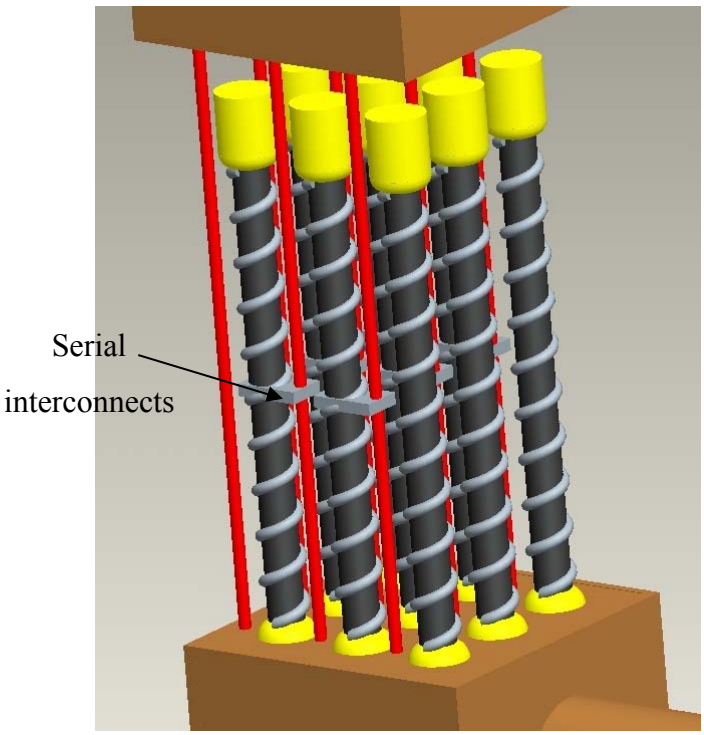

Figure 163: View of the serial connection cells.

Again using a combination of materials like Crofer, Allochrome or Conichrome with their conductive and non conductive properties the stack can be assembled as Figure 163 and Figure 164. Sealing may be made as mentioned in the parallel stack design. This is only one of several ways of using the capillary pipe to make the serial connection with the cathode of a neighbouring cell. Placing the capillary pipes directly beside the cells may help to increase the temperature of the hydrogen or indeed lower the temperature of the oxidant flowing through the cells. Radiation and forced convective heat transfer should be the dominant means of heat transfer in such a case.

The oxidant inlet approach of the parallel module mentioned could also be incorporated into this design. This would require a rerouting of the fuel inlet capillaries. The fuel capillaries could be inleted through the side of the bottom hydrogen basin and a 45° bend used to flow the fuel into the cells. Then if a rod is connected to the open portion of the anode in the basin and then passed through the

top wall of the basin for a defined length along the path of the capillary pipes shown in Figure 164 with an identical connection made from it to the neighbouring cathode then air could be supplied to the cells as in Figure 160. In this case each of the flow separators encloses the cell and the electrical connection via the rod and connector plate. Electrical wires can then be taken identically as previously mentioned in the parallel stack arrangement except the fuel capillaries would be the 4 point probes and a connection via the rods and cells would make the power delivery circuit.

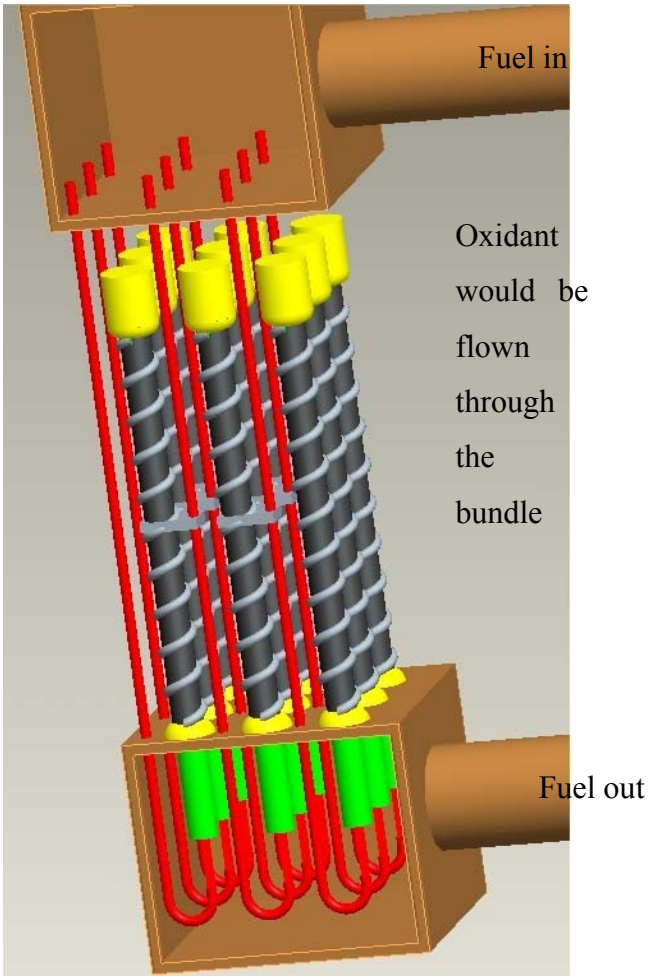

Figure 164 Sectional view of the serially connected cells.

References

[1] G. A. Tompsett, C. Finnerty, K. Kendall, T. Alston and N. M. Sammes, Novel applications for micro-SOFCs, J. Power Sources, 86, (2000), pp. 376-382

[2] W. Bujalski, C. M. Dikwal and K. Kendall, Cycling of three solid oxide fuel cell types, J. Power Sources, 171, (2007), pp. 96-100

[3] V. Lawlor, S.Griesser, G. Buchinger, A. G. Olabi, D. Meissner Review of the micro-tubular solid oxide fuel cell (part I: Stack design issues and research activities) J. Power Sources (2009), In Press, Accepted Manuscript (version available online),
[4] S.-B. Lee, K.-S. Yun, T.-H. Lim, R.-H. Song and D.-R. Shin, Development of anode supported micro-tubular SOFC stack for APU application, in: ECS Transactions - 10th International Symposium on Solid Oxide Fuel Cells, SOFC-,(2007)

[5] S. Hashimoto, H. Nishino, Y. Liu, K. Asano, M. Mori, Y. Funahashi and Y. Fujishiro, The electrochemical cell temperature estimation of micro-tubular SOFCs during the power generation, J. Power Sources, 181, (2008), pp. 244-250.

Appendix V Introduction to Methods of Temperature Control.

This section is an investigation into using PID controllers to control temperature. It is relatively easy to find plenty of information on this topic and there is an abundance of information on the internet. A good general understanding of PID control is essential for creating an experimental system that should be both reliable and controllable to a high degree of accuracy. Normal high temperature ovens for sintering for example generally fluctuate around fractions of a degree of their set points and they generally use the PID control system. The following section gives an introductory account of this control method. As this controller would be built into LABVIEW an understanding is needed. Another option would be to simply buy an off the shelf PID controller but implementing one in LABVIEW is a cheaper and more customisable approach.

The On/Off control method.

This system is often used for very simple systems for example room temperature control with thermostats or fridge temperature control. It works on the basis that the power is either "on" full power or "off" no power. Thus the pulse width, the time the full power is on, determines the heating rate. A set point is used to indicate at what temperature the heat value should fluctuate around.

The turn-on and turn-off temperatures are deliberately set to a value above and below the set point. This difference is used to prevent the heater switching on and off fast when in steady state operation and is called the hysteresis value. This switching in more complicated applications that require rapid switching would be wasteful and if a relay is being used to switch on and off then the relay lifetime would be unnecessarily short. If Figure 165 and Figure 166 below are compared it can be clearly seen that by changing the hysteresis value would cause a relay not burn out so fast but accuracy is lost and this is the trade off. The other alternative to a relay is a transistor which would not burn out so fast. The following Simulation figures were

investigated by the Author of this thesis using the online teaching simulation tool provided by the University of Exeter [1].

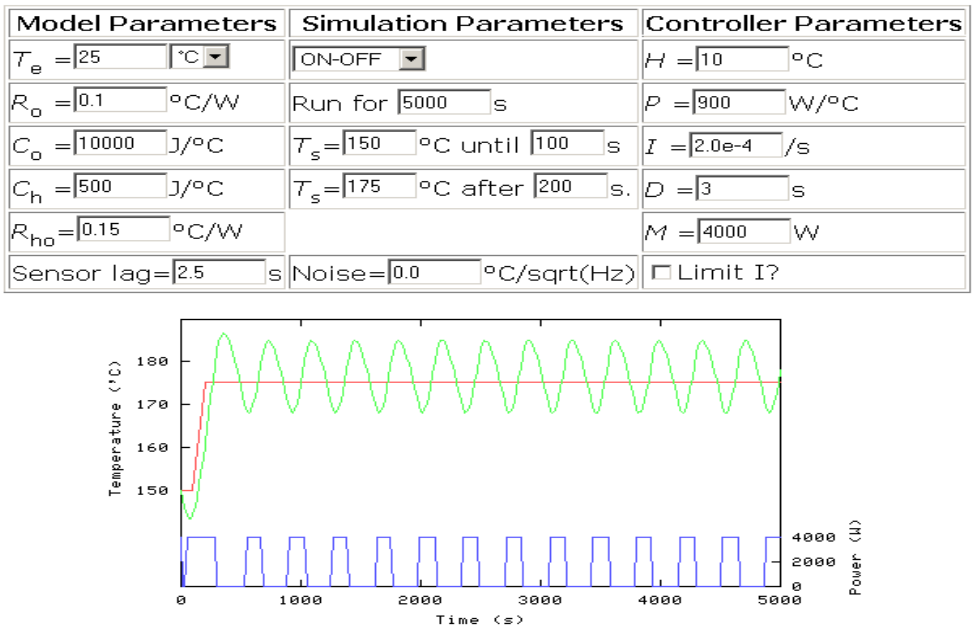

Figure 165 A simulation result showing on off control with a high hysteresis value and thus low relay switching rates [1].

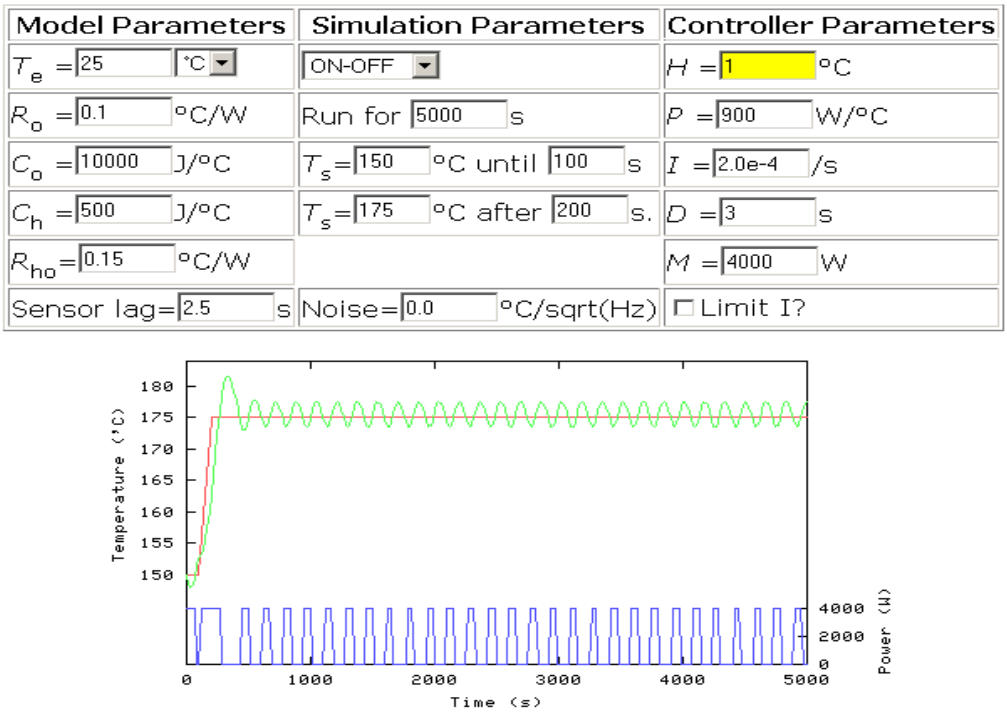

Figure 166 Simulation result with reduced hysteresis value and thus a higher switching rate [1].

Proportional Control

Another form of control is called proportional control or P-control. P-control is an improvement on the “on” “off” control in that a proportional controller applies power to the heater in proportion to the difference in temperature between the heater and the set point.

$$Power\,(W) = P \times (Ts - To)$$

Where “P” is the proportional gain of the controller, “Ts” is the set point and “To” is the current temperature at a given time. As the “P” term value is increased the system responds faster to changes in the set point. The problem with a P controller is that as the P value is increased the output becomes progressively under damped. The final temperature value will eventually settle below the set point. This final out put value ends up below the set-point for this system because a difference is required to keep the heater supplying power. The heater power must always lie between zero and the maximum power because it can only be a source heat and not a sink of heat.

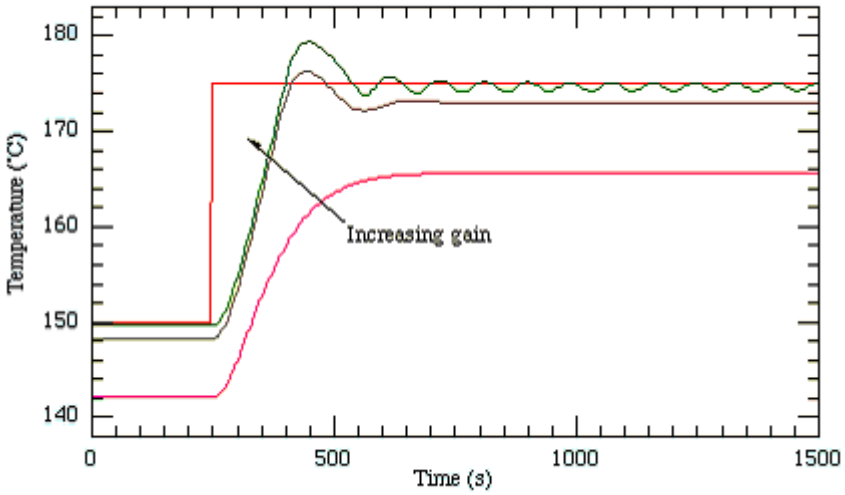

Figure 167: Proportional control where it can be seen that increasing the gain "P" to a value under that which would cause instability causes the temperature to fluctuate under the set point. [2].

Proportional + Derivative Control

The stability and overshoot problems that arise when a proportional controller is used at high gain as seen in Figure 167 can be reduced by adding a term proportional to the time-derivative of the error signal,

$$W = P \times [(Ts - To) + Dx \frac{d}{dt} (Ts - To)]$$

This technique is known as PD control. The value of the damping constant, D, can be adjusted to achieve a critically damped response to changes in the set-point temperature, as shown in the next figure.

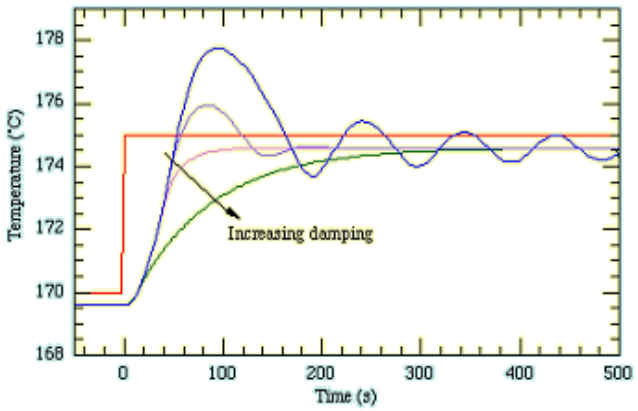

Figure 168 Proportional + Derivative control where increasing the "D" term reduces the ringing in the system but still does not make the controller meet the set point. [2]

Too little damping results in overshoot and ringing, too much causes an unnecessarily slow response. PD control is not commonly used in temperature control. Although PD control deals neatly with the overshoot and ringing problems associated with proportional control it does not solve the problem with the steady-state error as seen in Figure 168.

Proportional+Integral+Derivative Control

Fortunately it is possible to eliminate this while using relatively low gain by adding an integral term to the control function which becomes

$$W = P \times [(Ts - To) + D \times \frac{d}{dT}(Ts - To) + I \times \int (Ts - To)dt]$$

Where I, is the integral gain parameter is sometimes known as the controller reset level. This form of function is known as proportional-integral-differential, or PID, control. The effect of the integral term is to change the heater power until the time-averaged value of the temperature error is zero. The method works quite well but complicates the mathematical analysis slightly because the system is now third-order.

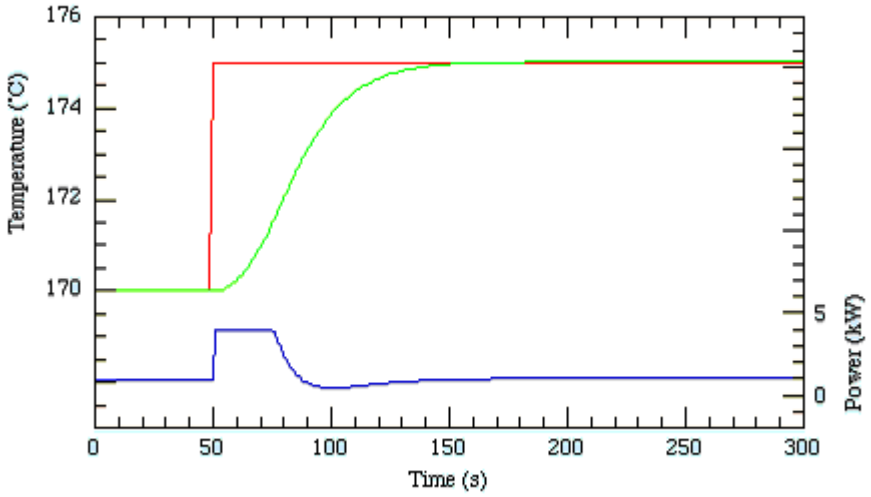

Figure 169 PID control where the integral term forces the controller to meet the set point and eliminates the ringing effect in this case [2]

Figure 169 shows that, as expected, adding the integral term eliminates the steady-state error. The slight undershoot in the power suggests that there may be scope for further tuning.

Proportional + Integral Control

Sometimes when the sensor measuring the temperature is susceptible to noise or other electrical interference, the derivative action can cause the heater power to fluctuate wildly. In such circumstances it is often sensible use a PI controller or set the derivative action of a PID controller to zero.

Tuning of PID Controllers.

For PID controllers to operate they require Proportional, Integral and Derivative terms. Picking numbers for these terms for a beginner is very difficult as found during the course of this study by the author. However if one understands what each term does the operator should be able to tune the PID controllers to a very high degree of accuracy. In the literature there is an abundance of texts that make suggestions for how to manually or use systems to select the P,I and D terms.

One of the most informative documents found by Wescott [3] titled “PID without a PhD” is an article and describes how the P, PI and PID controllers work. Wescott is an electrical engineer, author of "Applied Control Theory for Embedded Systems" and owner of Wescott Design Services, an embedded systems design company. He has been setting up control loops in embedded software for over 15 years. He uses a Voltage driven motor, precision actuator and a heating system to show system responses for a given type of controller. Although the responses of the voltage driven motor and the precision actuator are extremely interesting, the system with most relevance to the given project was the heating system.

Wescott explains that thermal systems tend to have very complex responses. He explains that unless a system’s requirements are severe, then an accurate model of the system isn’t necessary. Using time constants of t = 0.1s and t = 0.3s he shows the following plot Figure 170.

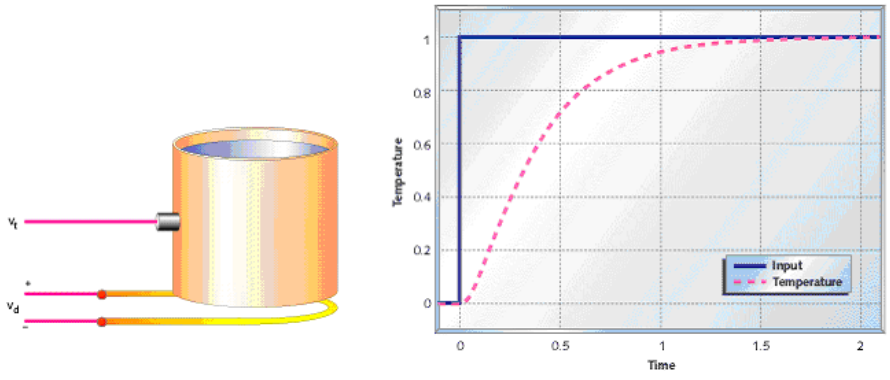

Figure 170 Heater system and its response against time [3].

Temperature like the other systems settles at a constant value for a given input. The most notable difference between the heating system and the others is that the heating system takes a relatively longer time to rise and settle when a step input is applied.

As explained previously in the prior section proportional control alone will never get the temperature up to the set point value. Increasing the gain value of the P controller helps and increasing the gain results in a large over shoot value that is undesirable in most systems involving temperature for obvious reasons. This idea is illustrated in the Figure 171 on the next page. The P controller is useful for plants with very low delay times like a voltage controlled motor when the motor needs be driven at extremely high speeds the P controller is not suitable. The P controller is definitely not suitable for temperature control.

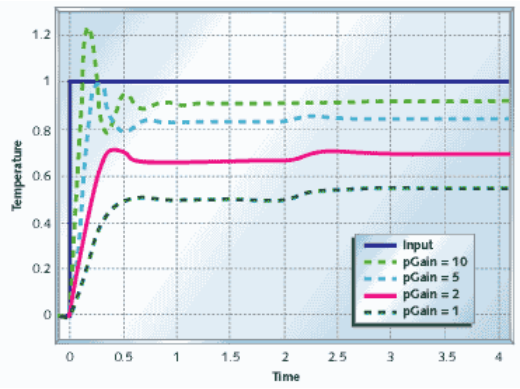

Figure 171 Temperature controller with proportional feedback [3].

A temperature controller under pure integral control will settle to the required set point but will take a long time to settle with plenty of ringing beforehand. A disturbance has little effect on the output as can be seen at time = 2. The integrator uses previous values of the output which have come before and this allows the controller to cancel out any errors on the output. If a system does not need a fast settling time then pure integral control may be an option but there are better solutions.

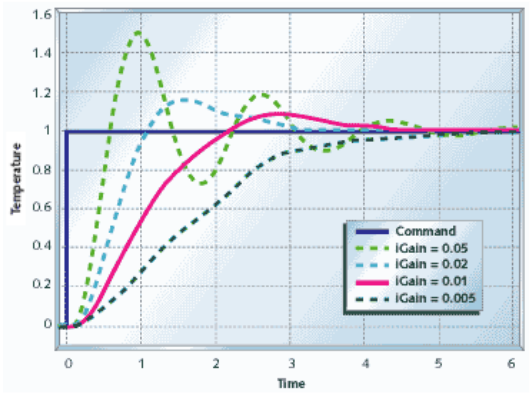

Figure 172 Temperature control system with integral control [3].

Using a PI controller results in a much faster settling time up to 3 times faster than the previous examples of controller configurations. Once again he points out that disturbance is minimised because of the integral component of the controller. This can be seen on the figure below, noting that the disturbance occurs at t = 2s. If a plant cannot be controlled by P control then it is impossible to control it via PI control [3].

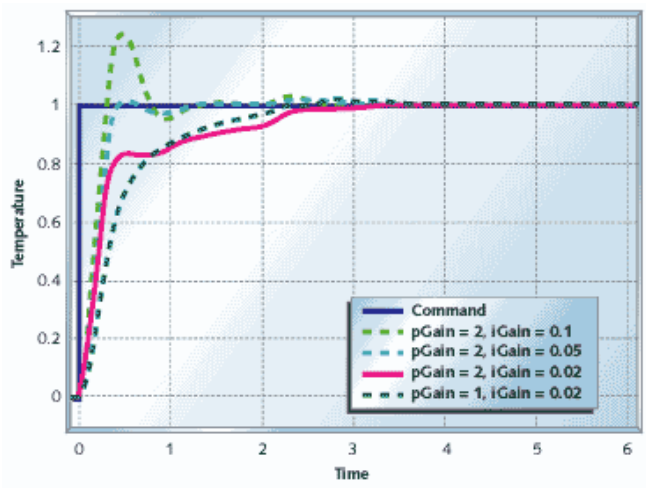

Figure 173 Heater with PI control

The following is a very good way to understand the different elements of a controller. A proportional controller deals with the present behaviour of an output, an integral controller deals with the past behaviour of an output and a differential controller predicts future plant behaviour. PID control involves all the above elements. It is a very powerful tool available to the control engineer but it can be

very problematic. In the following figure it can be clearly seen that the response of the heating system with the PID controller is the best covered so far. With PID control, the result is slight over shoot but the temperature value never strays far from the set point and it eventually reaches and stabilises at it. In the literature it is commonly stated that around 90% of closed loop controller applications perform very well even if tuned only fairly well. Often for certain systems including temperature systems often PI control is enough and this un-complicates the tuning process a bit.

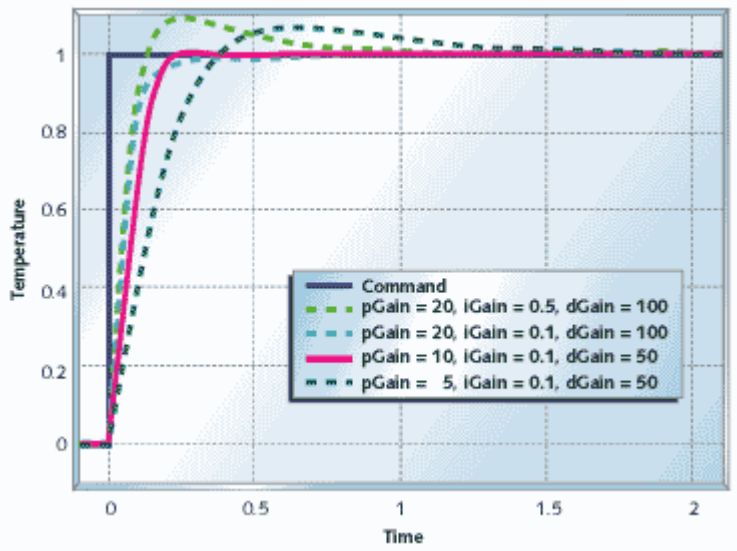

Figure 174 Heating system with PID control [3].

Wescott also discusses the problems with differential control like sampling irregularities, noise and high frequency oscillations and the reader is pointed to the following text for more information [3]. The real treasure of this document was his advice for oh a PID controller. Of course it would be possible to tune the controllers in the plant for this project with mat-lab and zeiglor-nichols, grid search or ultimate stability methods but this would require a transfer function which would take time to create and perfect therefore the following information is extremely relevant and useful.

Wescot suggests the following steps to tune a PID controller.

1) Set the proportional gain to one or less.

2) Check and see how the system works

3) If oscillation occurs it can be cured by differential gain. Begin with about 100 times more differential gain than proportional gain. Watching the drive signal, increase the differential gain until oscillation, excessive noise or more than 50 percent overshoot on the drive or plant output.

4) Oscillation from too much differential gain is much faster than the oscillation from not enough

5) He suggests, to push the upwards until the system on the verge of oscillation and then back the gain off by a factor of two or four.

6) Then when the system acts close to the desired output, fine tune the proportional gain by factors of two until one likes what one sees on the output.

7) Then increase the integral gain beginning at 0.0001 up to 0.01 until again one likes what one sees.

Wescott recommends that gains within a factor of two of the ‘correct’ value should be sufficient.

Coon [4] has written a document entitled, how to find a controller setting from process characteristics. This document is well know and is widely known be

people in the control field. In this document written in 1956 however it is an excellent introduction to the PID controller and summarises all the methods of tuning a controller. Some were already familiar but her explanations are clear concise and she includes plenty of plots and graphs to help the reader understand. This document contrasts nicely with Wescots PID without a PhD and when the two are combined a good understanding of the PID controller should be achieved.

Coon discusses in depth four different methods of finding a controllers P I and D terms. The controller's settings can be found from the reaction curve produced by a step response, by closed loop cycling, by the frequency response obtained by experimental tests or by a quarter decay ratio. All these methods are discussed with the aid of clear and easy to follow charts. Once the reader understands that rate action is derivative or the D-term and that reset or sensitivity action is the integral or I-term the reader should follow this document easily. Coon also discusses Zeigler-Nichols formulas and states that the quality of control from this method is good to fair.

It is interesting to contrast Coons [4] document with the online document written by Wescot, PID without a PhD [3] which has been used as the main source to outline the operation of PID control of temperature control. Wescott offers a trial and error online setup of the controller. It is interesting to note the two different approaches to tuning. Certainly Coons approach is more formulised and exact where as Wescot suggests a more liberal trial and error approach. It would be interesting to see how all the different methods proposed of tuning would compare. It would be interesting to see results for how long to tune, robustness of the result and compare the different P,I and D terms found in the results. Both documents lack information on when to use any of the methods discussed and what advantages and disadvantages are associated with each. Without a doubt these two documents were extremely interesting and are valuable sources of information with regard to tuning of PID controllers.

[1] University_of_Exeter. Temperature Controller Simulation (online simulation learning tool). http://newton.ex.ac.uk/cgi-bin/metaform?http://newton.ex.ac.uk/teaching/CDHW/Feedback/OvSimForm-gen.html Date of Access: 26-10-2009

[2] Williams, C. Types of Feedback Control. http://newton.ex.ac.uk/teaching/CDHW/Feedback/ControlTypes.html Date of Access: 26-10-2009

[3] Wescott, T. PID Without a PhD. http://www.embedded.com/2000/0010/0010feat3.htm Date of Access: 10-10-2006

[4] Coon, G.A. How to find a controller settings from a process characteristics. *Control Engineering*, 1956-a, pp. 66-76.

Appendix VI Control circuitry for the high temperature wind tunnel control.

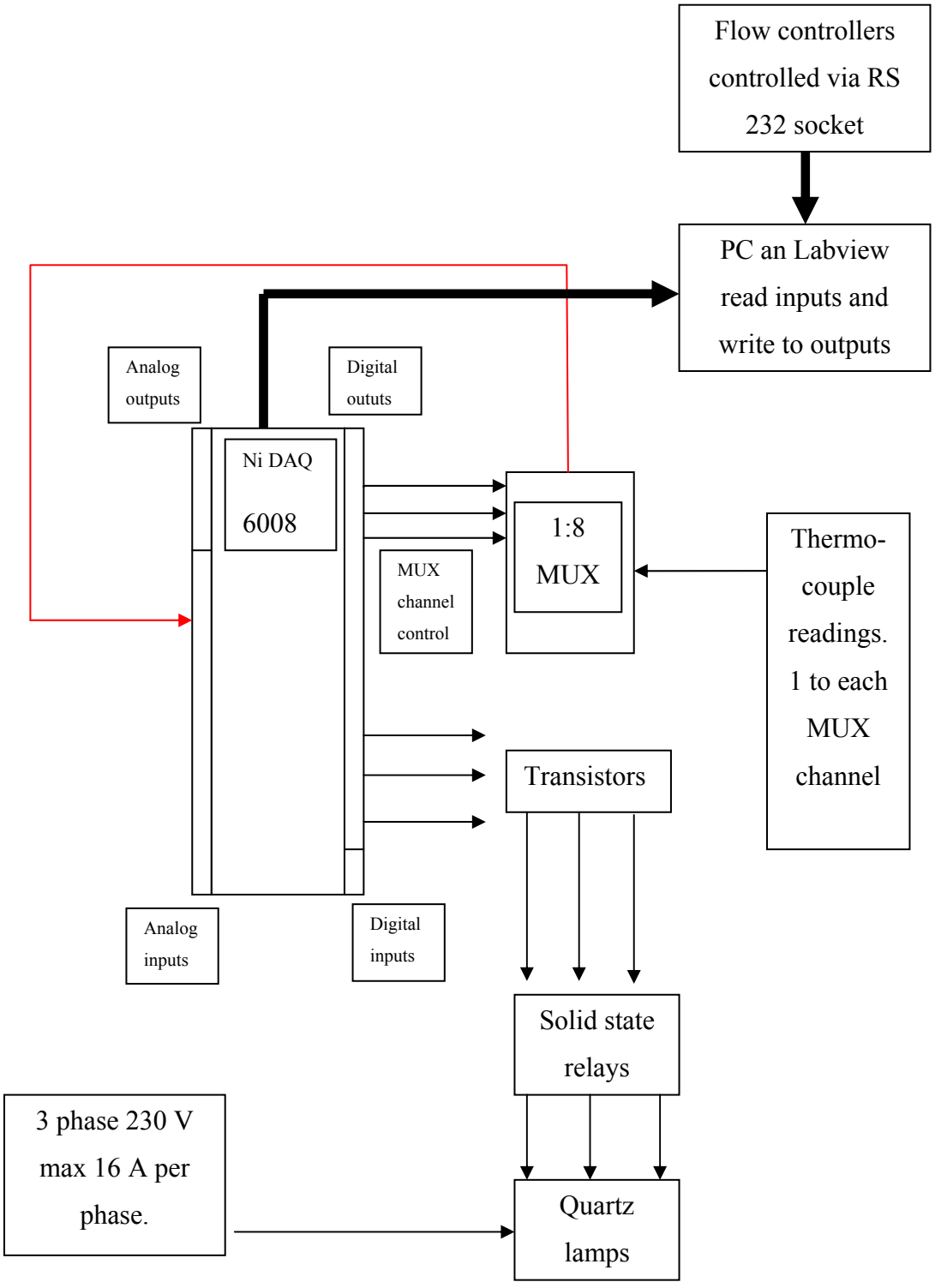

Appendix VII Labview code for the final version of the high temperature wind tunnel.

Labview code is not suitable for A4 sheet printing because of the large spatial dimensions of the pictorial code. Anyway the code used to control the wind tunnel is quite complex to describe and would take at least 20 pages to describe properly. Thus the functions in the graphical user interface to control the wind tunnel will be described.

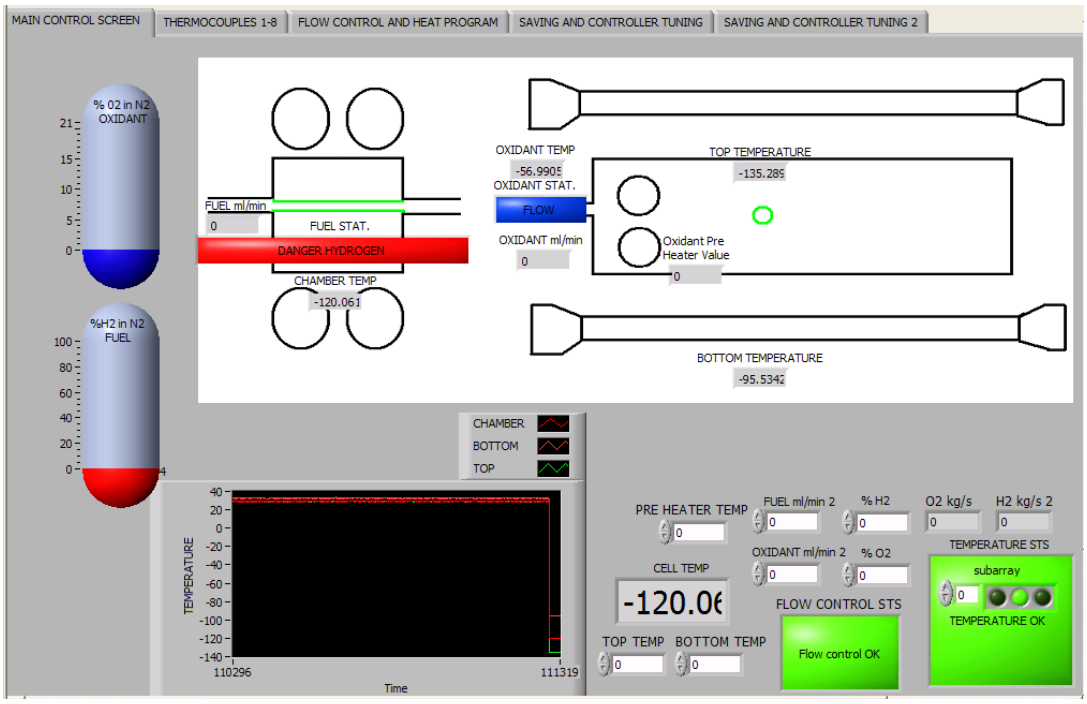

Figure 175 shows the main control screen where the concentrations of oxidant and fuel in their respected channels are controlled.

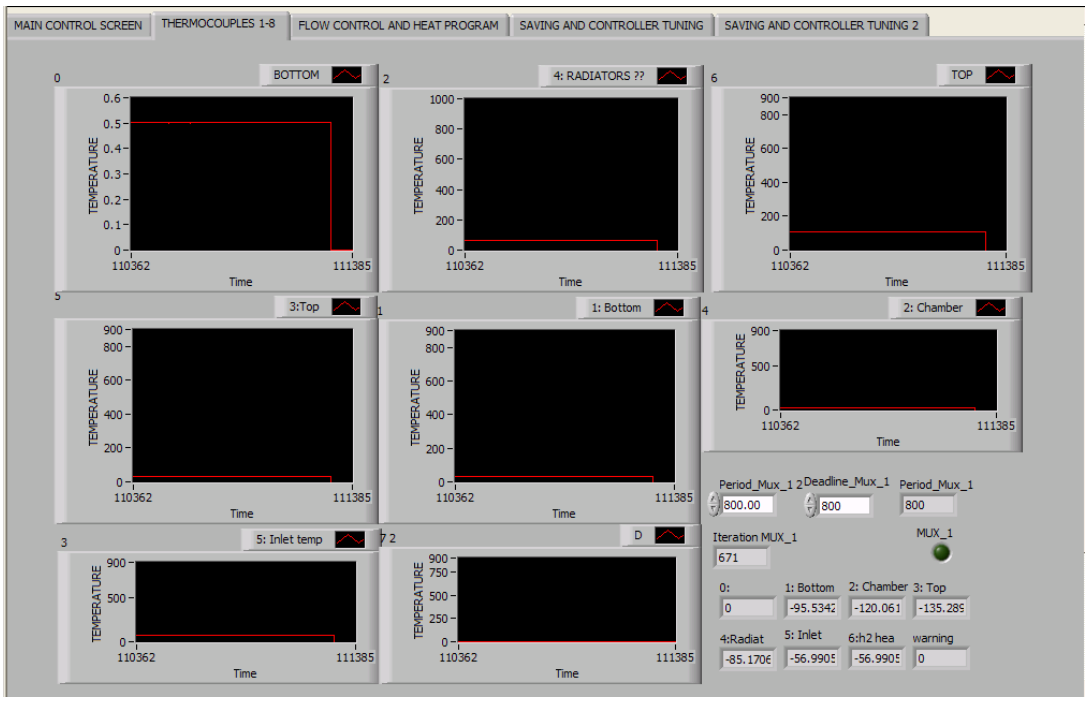

Figure 176 On this screen several thermocouples can be monitored via a multiplexer built on a separate circuit board.

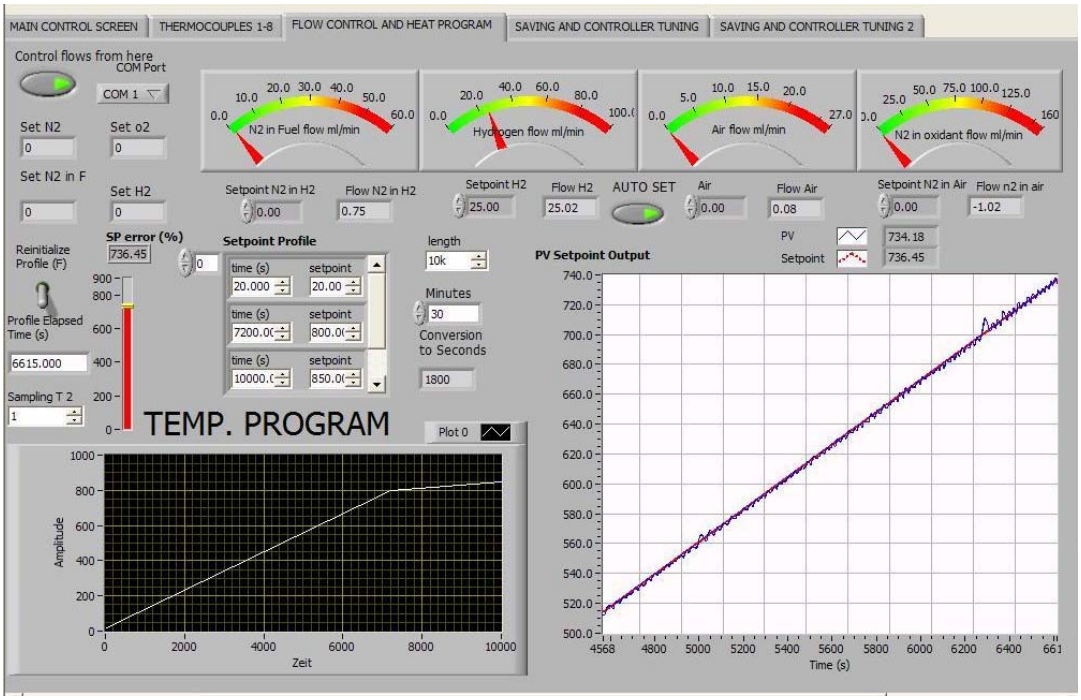

Figure 177 This is where temperature programs be programmed into, that the wind tunnel follows. The operate can monitor the temperature profile (big white graph). The oxidant and fuel concentrations may also be manually controlled from this screen.

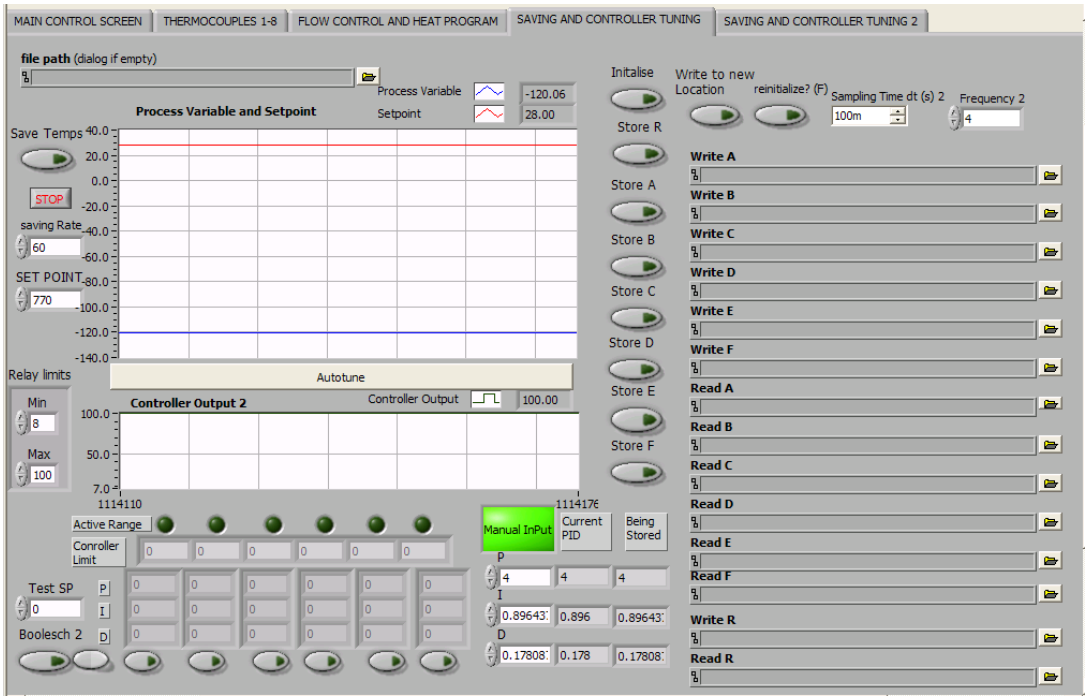

Figure 178 Probably the most complicated screen. The PID controller is tuned here either manually or with an auto tuning function. Regardless of the wind tunnel type this program can be applied to all and tuning parameters may be saved. Also thermocouple readings are saved to disk on this page.

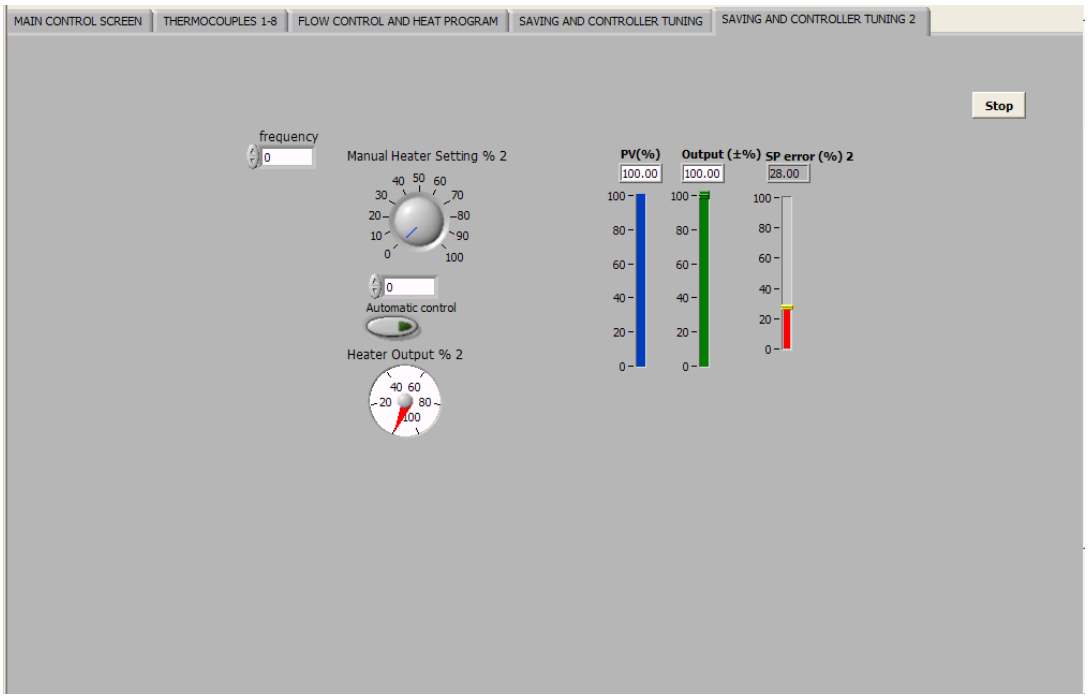

Figure 179 This page allows proportional control or just % on off control.

Appendix VIII: Drawings for the final high temperature wind tunnel

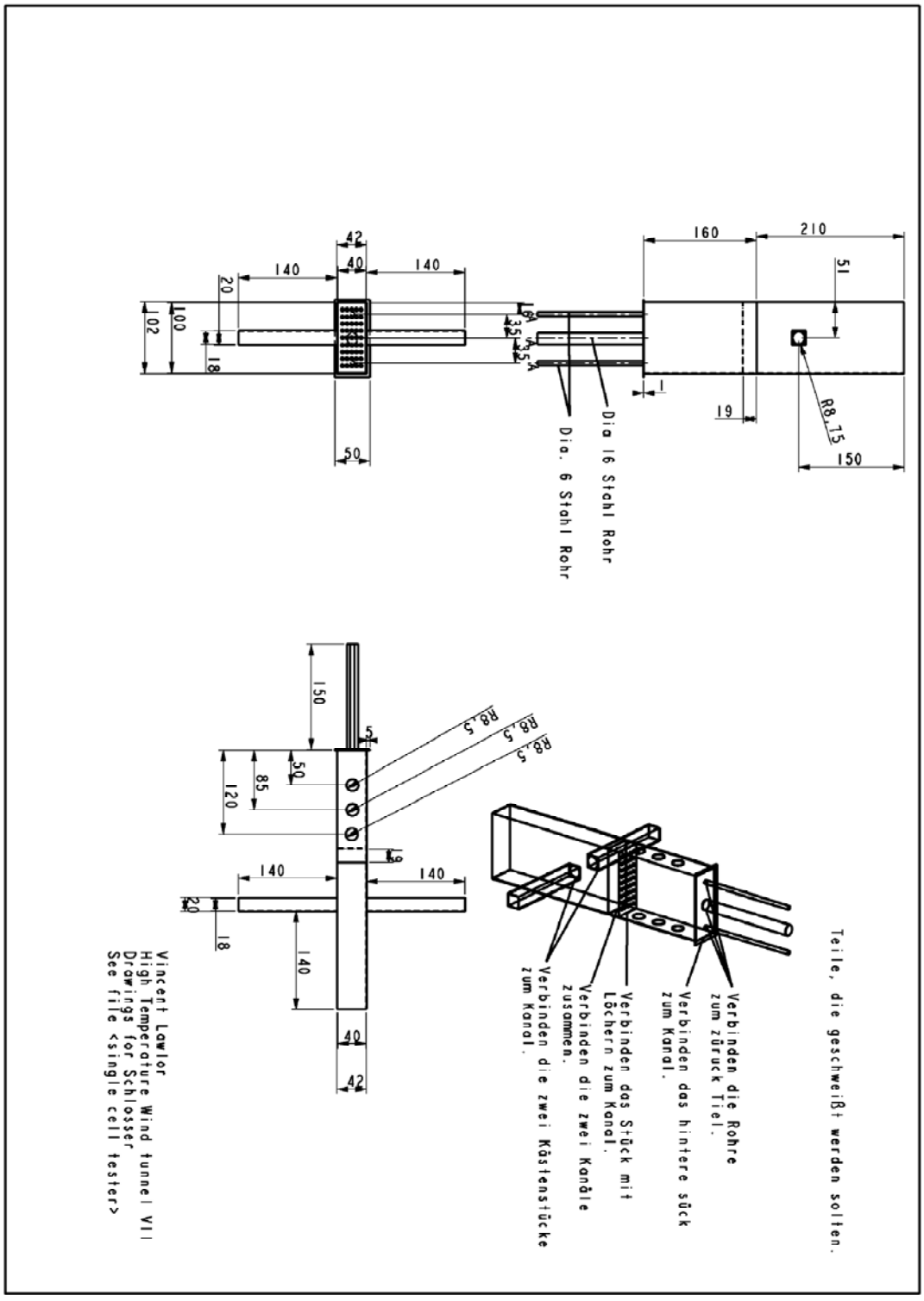

Appendix IX Code for single cylinder and bundles in forced and free convection regimes.

```
%XXXXXXXXXXXXXXXXXXXXXXXXXXXXXXXXXXXXXXXXXXXXXXXXXXXXXXXXXXXXXXXXXXXX
XXXXXXX
%XXXXXXXXXXXXXXXXXX To measure the free convection effects
XXXXXXXXXXXXXXXX
%XXXXXXXXXXXXXXXXXXXXXXXXXXXXXXXXXXXXXXXXXXXXXXXXXXXXXXXXXXXXXXXXXXXX
XXXXXXX

clear all

format long e

%-------------------------------Itteration--------------------------
------
%pointer 1
N=1;
out=0;

%--------------------------------------------------------------------
------
%-------------------------------Fuel Cell output--------------------
------
%--------------------------------------------------------------------
------

     %The required amount of air.


     %The amount of heat given off.


%--------------------------------------------------------------------
------
%-------------------------------Variables---------------------------
------
%--------------------------------------------------------------------
------

%--------------------------------------------------------------------
------
%-------------------------------Geometry----------------------------
------
%--------------------------------------------------------------------
------

staggered = 1 ;

C_lth    =0.04;       %M
C_dia    =0.003;      %M
C_n      =1;
C_n_t    =1;
Sl       = 0.01;
St       = 0.01;
L        =(Sl*(C_n/C_n_t)+Sl);
C_Area= pi * C_dia * C_lth;

C_nr    =C_n/C_n_t;
```

```
num = C_n/C_n_t;

NOTE = St/Sl;


%-------------------------------------------------------------------
------
%------------------------------Flow conditions----------------------
------
%-------------------------------------------------------------------
------

         %M/s

         step=0.00001;
         for A_vel=0:step:0.1

             %  The  following  equations  to  establish  the  maximum
velocity
             % for both staggered and in-line arrays comes from Pg
439 and
             % 440 in Incropera.

        %maximum fluid velocity

        % a=(((Sl^2)+ (St/2)^2))^.5;

        %b=((St + C_dia)/2);

        %Sd=a;

        %Max_vel_where=0;

 %if staggered == 1 && (a < b)

    %thus V_max occurs at A2
  %          V_max = St/(2*(Sd-C_dia))*A_vel;
   %             Max_vel_where=2;

 %elseif staggered==1 && (a > b);

    %thus V_max occurs at A1 similar to normal array
  %          V_max = (St/St-C_dia)* A_vel;
   %             Max_vel_where=1;
 %else
    %V_max occurs at A1 directly between two cells

  %          V_max = (St/St-C_dia)* A_vel;
   %             Max_vel_where=1;

 %end
%-------------------------------------------------------------------
-------
%------------------------------Heat transfer----------------------
-------
%-------------------------------------------------------------------
-------

% Cell temperatures
K_temp      =1173;
C_temp      =K_temp-273;         %°C
```

```
% Inlet air temperature
KA_temp     =1123;
A_temp      =KA_temp-273;        %°C


%-------------------------------------------------------------------
-------
%-----------------To calculate the average temp--------------------
-------
%-------------------------------------------------------------------
-------

avg_temp    =((C_temp+A_temp)/2);


%-------------------------------------------------------------------
-------
%------------picking   out   temperature   dependent   variables   from
polymomials--
%-------------------------------------------------------------------
-------
 T           =     avg_temp ;
 T1          =     C_temp ;


% The following polynomials came from trendline plots which I made
in excel

density     =(-0.000000002*T^3)+(0.000004*T^2)-(0.003*T)+(1.207);
Cp_kj       =(-.0000000003*T^3)+(.0000004*T^2)+(.00005*T)+(1.003);
Cp          =(Cp_kj*1000);
Dyn_vis     =(-0.00000000001*T^2)+(0.00000004*T)+(0.00002);
Kin_vis     =(0.00000000006*T^2)+(0.0000001*T)+(0.00001);
K_val       =((0.00005*T) + 0.027);
Ther_diff   =(0.00000000007*T^2)+(0.0000002*T)+(0.00002);



%-------------------------------------------------------------------
-------
%------------To estimate the Reynolds number-----------------------
-------
%-------------------------------------------------------------------
-------

%The following reynold's numbber comes from Page 438 in Incropera.

%Re_d_max = ((density*V_max*C_dia)/Dyn_vis);

%-------------------------------------------------------------------
-------
%------------Calcualtion of the prandtal number--------------------
-------
%-------------------------------------------------------------------
-------

%The following Prandtl number comes from Incropera and is the Pr
number for
%1100 Kelvin.

Pr= 0.7;
Prs= 0.7;
```

```
%-------------------------------------------------------------------
----
%----------------- to calculate the Nusselt number -----------------
----
%-------------------------------------------------------------------
----


%-------------------------------------------------------------------
-------
%--------------------------Christoph's book-------------------------
-------
%-------------------------------------------------------------------
-------

%Pages 91 and 92 note that the reynold's number here is is different
than
%that suggested by Incropera for such problems of flow arround a
cylinder.

L_dash  = (pi*C_dia)/(2) ;
Re_L_dash = ((density*A_vel*L_dash)/Dyn_vis);


%------The correction factors and alterations to the reynolds
number.-----

% These are values which decide which dimensions should be used in
the the
% following correction factors. page 9s in Christoph's book (3.38)
and
% (3.40)

 a_Chr=St/C_dia;
 b_Chr=Sl/C_dia;

    if b_Chr>1

        c_Chr=(1-(pi/(4*a_Chr)));


    else



        c_Chr=(1-(pi/(4*b_Chr*a_Chr)));

    end



% These are correction factors



Kfr1=1+(2/3*a_Chr); %Pg 97(3.43) for staggered arrays
```

```
% I used a polynomial of bild. 3.10 on page 97 to pick out a second

%correction factor

Kfr2=(0.000006*num^5)-(0.008*num^3)+(0.096*num^2)+   (0.475*num)   +
(0.238);


 %A different Reynold's Number is calculated from that proposed by

 %Incropera, it's on page 97 (3.41).


Vel_C_cr=(A_vel/c_Chr);



Re_L_dash_BUN =((Vel_C_cr*L_dash)/Kin_vis);


%Then to establish the Nusselt the suggested corolations on page 92
were

%utalised


% The Eval term is used to determine if more that a single cylinder
is

 %involved in the the array because if a single cylinder is involved




eval=C_n/C_n_t;



if  0 <= Re_L_dash && Re_L_dash < 0.1
```

```
      Nu_d_Chr=0.3;

      Nu_BUN = 0.3;

     out=1;

elseif 0.1 < Re_L_dash&& Re_L_dash <= 2;




      Nu_d_Chr=0.745*((Re_L_dash*Pr)^0.333333333);

      Nu_BUN = Nu_d_Chr*Kfr1*Kfr2;

      out=2;



else

      Nu_d_Chr = 0.664*((Pr)^.33333333)*((Re_L_dash)^0.5);

      Nu_BUN = Nu_d_Chr*Kfr1*Kfr2;

      out=3;

end

%see page 430 chapter 7 in Incropera



%-------------------------------------------------------------------
-------

%-----------------To acount for natural convection-----------------
-------
```

```
%-------------------------------------------------------------------
-------



%The following for natural convection on a vertical plate on page
568.


g_Pr=       (0.75*Pr^0.5)/((0.609+(1.221*Pr^.5)+(1.238*Pr))^(0.25));
%(9.20)


g= 9.81;


T_exp_coef=1/(C_temp); %(9.9)


Gr_nc=  ((T_exp_coef)*(g)*(C_dia  ^3)*(C_temp-avg_temp))/(Kin_vis^2);
%(9.12) Pg. 565

%Gr_nc= 9.81*((1/avg_temp)*(C_temp-A_Cor)*C_lth^3)/(Kin_vis);


Nu_nc= (4/3)*((Gr_nc/4)^.25)*(g_Pr); %(9.21)


%-------------------------------------------------------------------
-------

%-----------------free and forced convection combination-----------
-------

%-------------------------------------------------------------------
-------


if Re_L_dash < 0.1
```

```
     Nu_cor=0.3;

else

Nu_cor = ((Nu_nc*Nu_nc*Nu_nc)+(Nu_BUN*Nu_BUN*Nu_BUN))^(1/3);

end




test=Gr_nc/(Re_L_dash_BUN*Re_L_dash_BUN);
%-------------------------------------------------------------------
-------
%-----------------heat transfer coefficient-------------------------
-------
%-------------------------------------------------------------------
-------

HTCF_Chr= Nu_d_Chr*(K_val/L_dash);
HTCF_BUN= Nu_BUN*(K_val/L_dash);
HTCF_Cor= Nu_cor*(K_val/L_dash);




%-------------------------------------------------------------------
-------
%------To calculate heat transfer rate per unit length of the tubes-
-------
```

```
%-------------------------------------------------------------------
-------



%A= Ts-To

%B= Ts-Ti


%Temp= C_temp-A_temp;

%A= Ts-To

%B= Ts-Ti


Temp= C_temp-A_temp;


%see incropera page 442 for the following formula  (7.67)


%lost temp = (cell temp - outlet temp)

lost_temperature=Temp*exp(-
1*(pi*C_dia*C_n*HTCF_BUN)/(density*Vel_C_cr*C_n_t*St*Cp));


% If we then know the cell surface temp and the lost


T_out = C_temp-lost_temperature;


%Please 7.66 and 7.68 in incropera page 442

%Temp=(C_temp-A_temp)/(C_temp-T_out);

%dt_per_length_Fow= ((C_temp-A_temp)-(C_temp-T_out)/log(Temp));
```

```
%HTR_P_UL_Fow=C_n*(HTCF_BUN*pi*C_dia*dt_per_length_Fow);




%Gr_l_Chr= 9.81*((1/avg_temp)*(C_temp-A_Chr)*C_lth^3)/(Kin_vis);

%Gr_l_Cor= 9.81*((1/avg_temp)*(C_temp-A_Cor)*C_lth^3)/(Kin_vis);




%-----------------------------------------------------------------
-------

%---measure of the boyancy forces to visvous forces acting on the
fluid.---

%-----------------------------------------------------------------
-------







%proof_Chr=Gr_l_Chr/(Re_d_max^2);

%proof_Cor=Gr_l_Cor/(Re_d_max^2);




%On page 594 Icnopra suggests that that free convection is neglible
if this

%proof number is much less than 1 and that forced convection is
neglible

%when this number is much greater than 1. So when around the 1 value
mixed
```

```
%convection is evident and must be taken into account for heat
transfer.




A(N,:)                                                                =
[Re_L_dash,Nu_d_Chr,HTCF_Chr,Nu_BUN,HTCF_BUN,HTCF_Cor,Nu_cor,Nu_nc,t
est,Re_L_dash_BUN,A_vel];




N=N+1;

end



%-------------------------------------------------------------------
-------
%-----------------------------Plots---------------------------------
-------
%-------------------------------------------------------------------
-------


figure(1)

clear figure(1)
plot (A(:,1),A(:,2),'g')
hold on
plot (A(:,1),A(:,4),'y')
plot (A(:,1),A(:,7),'b')
%plot (A(:,1),A(:,8),'r')

title('reynolds number Vs Nusselt number')
xlabel('reynolds number')
ylabel('Nusselt number')
legend('just forced convection on a No. of rows','free and
forced','single cylinder','free')

hold off

figure(2)
clear figure(2)
title('reynolds number Vs Nusselt number')
xlabel('reynolds number')
```

```
ylabel('Watts/m^2.k')
legend('free and forced','single cylinder','just forced convection
on a No. of rows')

hold on
plot (A(:,1),A(:,3),'g')
plot (A(:,1),A(:,5),'y')
plot (A(:,1),A(:,6),'b')



figure(3)
title('reynolds number Vs Nusselt number')
xlabel('reynolds number')
ylabel('grashof/re^2')
clear figure(3)
semilogy(A(:,10),A(:,9),'g')
grid minor


legend('grasshoff/re^2')
figure(4)
clear figure(4)
semilogy(A(:,11),A(:,9),'g')
grid minor
title('reynolds number Vs Nusselt number')
xlabel('M/sec')
ylabel('grashof/re^2')
%-------------------------------------------------------------------
-------
%--------------------Convection between parallel plates in the duct-
-------
%-------------------------------------------------------------------
-------

%g= 9.81;
%h=0.04;
%Tb=850;
%Tt=900;
%T_exp_coef=1/((Tt+Tb)/2);

%Gr= (T_exp_coef*g*h^3*(Tt-Tb))/Kin_vis;

%Ra= Gr/Ther_diff;
% pointer
```

Appendix X Modelling parameters for the Full cathode simulations.

Modelling Parameters for small cathode	Value	Units
SOFC modeling paramaters		
Electrochemically active area	9.29-05	m^2
Anode Thickness	0.00085	m
Cathode Thickness	0.00005	m
Electrolyte Thickness	0.00001	m
Anode exchange current density	2400000	A
Cathode exchange current density	1000	A
All mol fraction values	1	
All stoichoimetric values	0.5	
All Butler-Volmer transfer coefficients	0.5	
Electrolyte restivity	0.5	ohm-m
leekage current	0	A/m^2
Electrical Properties		
Anode conductivity	333330	1/ohm
Cathode Conductivity	7937	1/ohm
Nickel and silver conductivity	1.50E+07	1/ohm
Silver touch cathode resistance	1e-8	ohm-m^2
Nickel touch anode resistance	1e-7	ohm-m^2
Material properties		
Anode		
Density	3310	kg/m^3
Cp	430	j/kg-K
Thermal conductivity	1.86	w/m-K
Porosity	0.3	
Cathode		
Density	3030	kg/m^3
Cp	470	j/kg-K
Thermal conductivity	2.16	w/m-K
porosity	3	
Current collectors		
Density	8900	kg/m^3
Cp	446	j/kg-K
Thermal conductivity	72	w/m-K
porosity	0	

Flow regime managment		
Fuel mass flow (h2)	3.54E-08	Kg/s
fuel is (hydrogen)	97	% mass
fuel is (water)	3	% mass
Fuel inlet temperature	1025	K
Oxidant inlet temperature	1025	K
Oxidant inlet velocity	0.016	m/s
Oxidant is (oxygen)	23	% mass
Modeliing Parameters		
Gas mixture		
Mixture species	o2 n2 h2o h2	
Reaction	Finite-Rate	
Mechanism	reaction-mechs	
Density	Inc. Ideal gas	
CP	mixing law	
Thermal conductivity	ideal gas mixing law	
Viscosity	ideal gas mixing law	
Mass diffusivity	User-defined	
Thermal diffusion coefficiant	Kinetic theory	
UDS diffusivity	defined per uds	
solver	Pressure based	
formulation	Implicit	
Time	Steady	
velocity formulation	Absolute	
Gradient option	green gauss cell based	
porous formulation	superficial velocity	
Energy equation	on	
Viscous model	laminar	
Species model		
Model	Species transport	
Reactions	volumetric	
Options	diffusion energy source	
	Full multicomponent diffusion	

	Thermal diffusion	
SOFC model control panel options		
	Enable SOFC model	
	Enable surface energy source	
	Enable species sources	
	Disable CO electrochemistry	
	Enable volumetric energy	
Radiation		
	Discrete Ordinates	
Flow itterations per radiation itteration	5	
Theta Divisions	5	
Phi Divisions	5	
Theta Pixels	5	
Phi Pixels	5	
Residual solving criteria		
Continunity	7.00E-05	
x-velocity	1.00E-06	
y-velocity	1.00E-06	
z-velocity	1.00E-06	
energy	1.00E-07	
do-intensity	1.00E-06	
h20	1.00E-06	
o2	1.00E-06	
h20	1.00E-06	
uds-0	1.00E-08	
Solution controls		
Pressure-velocity coupling	SIMPLE	
Under relaxation factors		
Pressure	0.3	
Density	0.7	
Body forces	0.7	
Momentum	0.4	
H20	1	
02	1	
H2	1	
Energy	1	
Discrete Ordinates	1	
User Scaler 0	1	
Discritisation		
Pressure	standard	

Momentum	First order upwind	
H20	First order upwind	
O2	First order upwind	
H2	First order upwind	
Energy	First order upwind	
Discrete ordinates	First order upwind	
User Scaler 0	First order upwind	

Appendix XI Modelling parameters for the small cathode simulations.

Modelling Parameters for small cathode	Value	Units
SOFC modeling paramaters		
Electrochemically active area	1.77E-05	m^2
Anode Thickness	0.00085	m
Cathode Thickness	0.00005	m
Electrolyte Thickness	0.00001	m
Anode exchange current density	7000	A
Cathode exchange current density	200	A
All mol fraction values	1	
All stoichoimetric values	0.5	
All Butler-Volmer transfer coefficients	0.5	
Electrolyte restivity	0.5	ohm-m
leekage current	0	A/m^2
Electrical Properties		
Anode conductivity	333330	1/ohm
Cathode Conductivity	7937	1/ohm
Nickel and silver conductivity	1.50E+07	1/ohm
Silver touch cathode resistance	1.00E-07	ohm-m^2
Nickel touch anode resistance	5.00E-06	ohm-m^2
Material properties		
Anode		
Density	3310	kg/m^3
Cp	430	j/kg-K
Thermal conductivity	1.86	w/m-K
Porosity	0.3	
Cathode		
Density	3030	kg/m^3
Cp	470	j/kg-K
Thermal conductivity	2.16	w/m-K
porosity	3	
Current collectors		
Density	8900	kg/m^3
Cp	446	j/kg-K

Thermal conductivity	72	w/m-K
porosity	0	
Flow regime managment		
Fuel mass flow (h2)	3.54E-08	Kg/s
fuel is (hydrogen)	97	% mass
fuel is (water)	3	% mass
Fuel inlet temperature	1025	K
Oxidant inlet temperature	1025	K
Oxidant inlet velocity	0.016	m/s
Oxidant is (oxygen)	23	% mass
Modeliing Parameters		
Gas mixture		
Mixture species	o2 n2 h2o h2	
Reaction	Finite-Rate	
Mechanism	reaction-mechs	
Density	Inc. Ideal gas	
CP	mixing law	
Thermal conductivity	ideal gas mixing law	
Viscosity	ideal gas mixing law	
Mass diffusivity	User-defined	
Thermal diffusion coefficiant	Kinetic theory	
UDS diffusivity	defined per uds	
solver	Pressure based	
formulation	Implicit	
Time	Steady	
velocity formulation	Absolute	
Gradient option	green gauss cell based	
porous formulation	superficial velocity	
Energy equation	on	
Viscous model	laminar	
Species model		
Model	Species transport	
Reactions	volumetric	
Options	diffusion energy source	

	Full multicomponent diffusion	
	Thermal diffusion	
SOFC model control panel options		
	Enable SOFC model	
	Enable surface energy source	
	Enable species sources	
	Disable CO electrochemistry	
	Enable volumetric energy	
Radiation		
	Discrete Ordinates	
Flow itterations per radiation itteration	5	
Theta Divisions	5	
Phi Divisions	5	
Theta Pixels	5	
Phi Pixels	5	
Residual solving criteria		
Continunity	2.20E-05	
x-velocity	1.00E-06	
y-velocity	1.00E-06	
z-velocity	1.00E-06	
energy	1.00E-07	
do-intensity	1.00E-06	
h20	1.00E-06	
o2	1.00E-06	
h20	1.00E-06	
uds-0	1.00E-08	
Solution controls		
Pressure-velocity coupling	SIMPLE	
Under relaxation factors		
Pressure	0.3	
Density	0.7	
Body forces	0.7	
Momentum	0.4	
H20	1	
02	1	
H2	1	
Energy	1	
Discrete Ordinates	1	
User Scaler 0	1	
Discritisation		

Pressure	standard	
Momentum	First order upwind	
H20	First order upwind	
O2	First order upwind	
H2	First order upwind	
Energy	First order upwind	
Discrete ordinates	First order upwind	
User Scaler 0	First order upwind	